Control of rheology on the development of structures in layered gneissic rock

Thesis submitted to Jadavpur University, Kolkata by

DEBOJYOTI BASU MAJUMDER

For the Degree of Doctor of Philosophy (Science)

Index no. 21/20/Geol. Sc./26

Registration No: SOGE01102120

Department of Geological Sciences

Jadavpur University

Kolkata-700032

2025

Control of rheology on the development of structures in layered gneissic rock

Thesis submitted to Jadavpur University, Kolkata by

DEBOJYOTI BASU MAJUMDER

For the Degree of Doctor of Philosophy (Science)

Index no. 21/20/Geol. Sc./26

Registration No: SOGE01102120

Department of Geological Sciences

Jadavpur University

Kolkata-700032

2025

Dedicated to my family

যাদবপুর বিশ্ববিদ্যালয়
কলকাতা - ৭০০০৩২, ভারত

JADAVPUR UNIVERSITY
KOLKATA-700 032, INDIA

FACULTY OF SCIENCE : DEPARTMENT OF GEOLOGICAL SCIENCES

CERTIFICATE FROM SUPERVISOR

This is to certify that the thesis entitled "**Control of rheology on the development of structures in layered gneissic rock**", submitted by **Mr. Debojyoti Basu Majumder**, who got his name registered on **07.10.2020** for the award of **Ph.D. (Science)** degree of Jadavpur University, Kolkata Vide Ph.D. Registration Number **SOGE01102120,** is absolutely based upon his own work under the supervision of **Dr. Susanta Kumar Samanta (Professor, Dept. of Geological Sciences)** and that neither this thesis nor any part of it has been submitted for either any degree/ diploma or any other academic award anywhere before.

30/12/2025

Dr. Susanta Kumar Samanta
Professor
Department of Geological Sciences,
Jadavpur University,
Kolkata-700032, India

Dr. Susanta K Samanta
Professor
Department of Geological Sciences
Jadavpur University
Kolkata-700032, W.B., INDIA

Website : https://jadavpuruniversity.in
E-mail : hod.geology@jadavpuruniversity.in

Phone (HOD) : +91 33 2457 2719
Phone (Office) : +91 33 2457 2268

CONTENTS

Abstract

This thesis presents an integrated investigation into the deformation mechanisms of layered metamorphic rocks within the Chhotanagpur Granite Gneissic Complex, employing a combination of field observations, analogue experiments, and advanced numerical modelling. The study critically examines the evolution of complex structures—including boudinage structures, folding, and flanking features—in order to elucidate the interplay between rheological contrasts, mechanical anisotropy, and strain partitioning under diverse tectonic regimes.

The work begins by exploring the development of segmented, elongated boudinage structures that serve as natural strain markers. This study investigates the influence of viscosity on the formation of rectangular torn boudins, categorized based on the curvature of their exterior and face margins. Finite Element Method-based numerical simulations using Maxwell viscoelastic materials were conducted in ANSYS, exploring seven viscosity combinations among boudin, inter-boudin, and matrix materials. The findings highlight that the relative viscosity of the inter-boudin material critically affects boudin morphology. Bone-shaped boudins form when the inter-boudin is more competent than the boudin, with enhanced development when the matrix is also stronger than the boudin but weaker than the inter-boudin. In contrast, when boudins are stiffer than the inter-boudin, barrel- or fish-head shapes with concave faces emerge. Straight margins are observed when the boudin is more rigid than the matrix or when viscosity contrasts between boudin and inter-boudin are minimal. Thus, field-based boudin shape analysis can provide qualitative estimates of relative viscosity contrasts.

The investigation then turns to the processes underlying fold formation in layered rock under layer-parallel compression. Folds in layered rock systems are key to understanding deformation history and rheological behaviour. This study uses finite element modelling to examine fold development in such systems, emphasizing how thinner layers influence the folding of adjacent thicker layers. Results reveal that initially harmonic folds may evolve into polyharmonic or disharmonic patterns due to complex strain interactions within the contact zones of thinner layers. The geometry of resulting folds is strongly shaped by the mutual influence between thinner and thicker layers, where folding in one layer initiates deformation in the other. These interactions often diverge from outcomes predicted by simpler models, as noted in previous research. The study also suggests that higher-order fold geometries may serve as qualitative indicators for estimating relative viscosity contrasts between layers and the surrounding medium.

Subsequently, the research addresses the deflection of pre-existing fabrics adjacent to cross-cutting elements. By focusing on the mechanisms by which linear and planar fabrics are dragged and reoriented in response to local perturbations, the study distinguishes between open and closed flanking geometries within layered gneissic rocks. Using two-dimensional finite element modelling, the effects of cross-cutting element (CE) orientation, kinematic vorticity number (W_k), and anisotropy factor (δ) were analysed. Results show that the geometry, offset, and drag patterns of flanking structures are strongly influenced by anisotropy, particularly by the CE's orientation relative to stress axes and anisotropy pole. CE shape, offset magnitude, and tip displacement serve as qualitative indicators for estimating mechanical anisotropy in deformed layered rocks. The analysis further demonstrates that an increase in the degree of simple shear, as well as variations in the anisotropic factor,

systematically alters both the normalized aspect ratios and offset lengths of these features, thereby providing deeper insights into the kinematic implications of shear-induced deflections in heterogeneous media.

Overall, the thesis advances our understanding of deformation processes in high-grade metamorphic rocks by systematically linking microstructural observations with rigorous numerical analyses. The integrated approach adopted herein provides a comprehensive framework for interpreting the interdependence of material properties, strain conditions, and structural evolution in tectonically active regions.

List of Notations

Chapter 1: General Introduction

CE	Cross-cutting element
CGGC	Chhotanagpur Granite Gneissic Complex
δ	Anisotropy factor
η_N	Normal viscosity
η_S	Shear viscosity
d	Total thickness of layers
d_a	Thickness of individual layer
η_a	Viscosity of individual layer
α	Angle of the flow apophyses
W_k	Kinematic vorticity number
ζ	Orientation of principle stress axes
A_p	Pole of anisotropy
Type I	Flanking structure (open CE)
Type II	Flanking structure (closed CE)
W	Wavelength factor

Chapter 2: Study Area

CGGC	Chhotanagpur Granite Gneissic Complex
NSMB	North Singhbhum Mobile Belt
TTG	Tonalite–Trondhjemite–Granodiorite
UHT	Ultra-high temperature
SPSZ	South Purulia Shear Zone
Dx	Phases of deformation (x = 1, 2, 3, 4)
Fx	Fold axis (x = 1, 2, 3, 4)

Chapter 3: Boudinage Structures in Layered Gneissic Rock

R_B	Aspect ratio of boudin
L_B	Length of boudin
W_B	Width of boudin
L_I	Length of separation zone (Inter-boudin)
N_R	Separation factor
ε	Instantaneous strain
σ	Instantaneous stress
μ	Maxwell shear modulus
η	Viscosity
t	Time

FEM	Finite element modelling
U_x	Displacement along X-axis
U_y	Displacement along Y-axis
A1	Area of boudin
A2	Area of inter-boudin
A3	Area of matrix
W_k	Kinematic vorticity number
k	Percentage of shortening in decimal
η_{BM}	Ratio of viscosity (boudin / matrix)
η_{IM}	Ratio of viscosity (inter-boudin / matrix)
η_{BI}	Ratio of viscosity (boudin / inter-boudin)

Chapter 4: Folds in Layered Gneissic Rock

ε	Instantaneous strain
σ	Instantaneous stress
G	Maxwell shear modulus
η	Viscosity
t	Time
t_h	Initial thickness of central thin layer

s	Spacing between two consecutive layers
n	Spacing factor
λ_{dv}	Viscous dominant wavelength
λ_{de}	Elastic dominant wavelength
R	Ratio of dominant wavelength (viscous/elastic)
η_L	Viscosity of competent layer
η_M	Viscosity of incompetent embedded medium
η_R	Viscosity ratio (layer / medium)
P_o	Initial layer parallel stress
U_x	Displacement along X-axis
U_y	Displacement along Y-axis
k	Percentage of shortening in decimal
λ_{ob}	Wavelength from the numerical simulation
λ_f	Expected wavelength after 30% shortening
W	Wavelength factor (λ_{ob}/λ_f)

Chapter 5: Flanking Structures in Layered Gneissic Rock

CE	Cross-cutting element
θ	Initial orientation of CE

δ	Anisotropy factor
ξ	Orientation of the principal stress axis
CGGC	Chhotanagpur Granite Gneissic Complex
Dx	Phases of deformation (x = 1, 2, 3, 4)
Type I	Flanking structure (open CE)
Type II	Flanking structure (closed CE)
O	No drag
0	Neutral roll
S type/*s* type	Contractional synthetic flanking structure
Sh type/*sh* type	Extensional synthetic flanking structure
A type/*a* type	Contractional flanking structure
N	Normal drag
R	Reverse drag
FEM	Finite Element Method
ε	Instantaneous strain
σ	Instantaneous stress
G	Maxwell shear modulus
η	Viscosity
t	Time
A_p	Pole of anisotropy

η_C	Viscosity of competent layer
η_I	Viscosity of incompetent layer
η_N	Normal viscosity
η_S	Shear viscosity
G_C	Shear modulus of competent layer
G_I	Shear modulus of incompetent layer
E_C	Elastic modulus of competent layer
E_I	Elastic modulus of incompetent layer
W_k	Kinematic vorticity number
α	Angle between two flow apophyses
U_x	Displacement along X-axis
U_y	Displacement along Y-axis
k	Percentage of shortening in decimal
γ	Effective shear strain
φ	Degree of simple shear
l_a	Long axis of CE
l_b	Short axis of CE
l_s	Offset length
R_N	Normalized aspect ratio
L_N	Normalized offset length

σ_1	Maximum principal stress axis
σ_2	Minimum principal stress axis
a_1	Extensional flow apophyse
a_2	Compressional flow apophyse
θ'	Final orientation of CE
β	Shifting of tip points

Chapter 6: Flanking Structures in Simple Shear Regime

CE	Cross-cutting element
Type I	Flanking structure (open CE)
Type II	Flanking structure (closed CE)
ξ	Orientation of the principal stress axis
δ	Anisotropy factor
W_k	Kinematic vorticity number
U_x	Displacement along X-axis
U_y	Displacement along Y-axis
γ	Shear strain
ψ	Degree of simple shear
θ	Initial orientation of CE
R_N	Normalized aspect ratio

L_N	Normalized offset length
S type/*s* type	Contractional synthetic flanking structure
Sh type/*sh* type	Extensional synthetic flanking structure
A type/*a* type	Contractional flanking structure
θ'	Final orientation of CE
ω	Orientation factor

Chapter 7: Discussions and Conclusions

CE	Cross-cutting element
δ	Anisotropy factor
W_k	Kinematic vorticity number
Type I	Flanking structure (open CE)
Type II	Flanking structure (closed CE)
L_N	Normalized offset length
ω	Orientation factor
W	Wavelength factor
FEM	Finite Element Method

Chapter 1

General Introduction

The deformation of layered rocks in the Earth's crust is a subject of enduring interest in structural geology because it encapsulates the interplay between lithological heterogeneity, rheological contrasts, and complex strain partitioning during tectonic events. The features that emerge during ductile deformation—such as boudinage, folds and, flanking structures—are not only visually striking but also provide crucial insights into the strain history and mechanical behaviour of the crust. This thesis aims to investigate these interrelated structural phenomena through a combination of analogue observations, numerical simulations and field studies. In this introductory chapter, we outline the geological context, review the state of knowledge as represented in the literature, and present the objectives and scope of the research.

1.1 Geological Background and Motivation

Layered gneissic rocks are high-grade metamorphic formations characterized by pronounced banding or foliation, created when intense pressure and temperature reorganize minerals into alternating light (quartz and feldspar) and dark (biotite, amphibole) layers. This compositional layering reflects differential segregation of mineral phases during deformation and recrystallization, often driven by tectonic forces deep within continental crust. The resulting boudinaged bands and folds record episodes of strain and metamorphic smearing, making gneisses valuable archives of crustal evolution and deformation history.

When these layers are subjected to extensional forces, they may fragment into discrete blocks—a process known as boudinage, where the effect of anisotropy is negligible and only the rheology plays remarkable role on the final geometry.

Conversely, compressional forces tend to bend and buckle the layers, leading to the development of folds, where both the rheology and layer thicknesses (in case of multilayer folds) are important, but it is not in terms of mechanical anisotropy as discussed earlier. In addition, the presence of cross-cutting elements (CEs), such as fractures or small intrusions, can deflect or "drag" preexisting fabrics, resulting in the formation of flanking structures, where layered or mechanical anisotropy plays a great role on the final geometric patterns. Each of these deformation styles provides independent yet complementary information about the conditions that prevailed during tectonic events.

Layered rocks often record the history of tectonic processes, particularly in regions where alternating beds of competent (strong) and incompetent (weak) materials respond differently to applied stresses. This creates a kind of anisotropy, which is known as mechanical anisotropy or layered anisotropy.

Rock anisotropy refers to the directional dependence of a rock's physical properties, often caused by its mineral composition and structural arrangement. In gneissic rocks, the presence of alternating layers of flaky, elongated minerals (e.g., micas, chlorites etc.) significantly contributes to anisotropy. Mica minerals, such as muscovite and biotite, exhibit strong cleavage along specific crystallographic planes, which creates preferential weakness in the rock (Passchier & Trouw, 2005).

To verify the presence of such layering, rock samples collected from Chhotanagpur Granite Gneissic Complex (Purulia and Jasidih-Deoghar) were studied under microscope (Fig. 1.1). The observation stated that, mica and chlorite minerals are distributed in an elongated, clustered arrangement, defining a penetrative foliation within the rock fabric. In Fig. 1.1a, the foliation is thin, well-defined, and

closely spaced. In contrast, Fig. 1.1c displays a widened foliation zone characterized by elongated mica and chlorite grains that are more widely spaced. Fig. 1.1b presents an intermediate case, where the foliated layer exhibits moderate thickness and spacing, comparable to but slightly more dispersed than in Fig. 1.1a. In essence, the mechanical anisotropy in layered metamorphic rocks in CGGC is a resultant of the differential mechanical behaviour between mica-rich and quartz-feldspar-rich layers, affecting their response to stress and deformation.

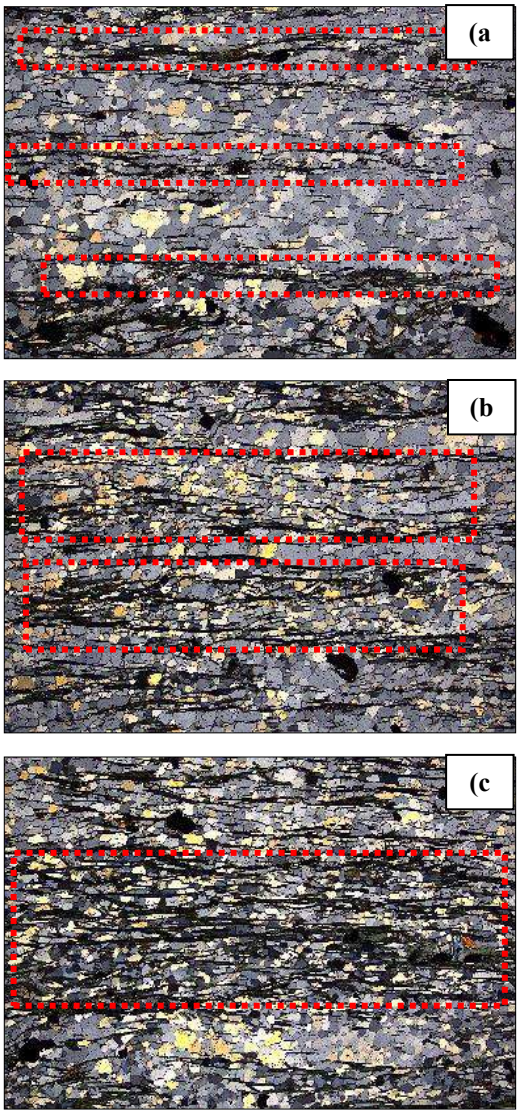

Fig. 1.1: Microstructural variations in foliation defined by mica and chlorite minerals (labelled by red coloured dashed box) collected from CGGC. (a) Thin, well-defined, and closely spaced foliation. (b) Moderately thick foliation with intermediate spacing. (c) Widened foliation zone with elongated mica and chlorite grains that are more widely spaced. The width of each photomicrograph is set as 6mm.

The thickness of mica layers plays a crucial role in controlling strain partitioning, which subsequently leads to anisotropy. These layers are distributed unevenly throughout the rock fabric, creating zones where strain is preferentially accommodated. This variability enhances the degree of anisotropy, making certain planes within the rock more susceptible to deformation or fracture. As a result, the rock exhibits directional weakness, allowing for easier movement along these planes. This process significantly influences the mechanical behaviour of the rock during deformation.

Layered anisotropy is theoretically defined by the presence of such homogenous, alternating competent and incompetent layers (Biot, 1965). This concept has been widely applied in various fields within geology, geophysics, and materials science (Bayly, 1970; Cobbold et al., 1971; Stromgard, 1973; Treagus, 1973, 1981, 1983, 1985, 1988; Cobbold, 1976; Johnson, 1977; Platt and Vissers, 1980; Cobbold and Watkinson, 1981; Casey and Huggenberger, 1985; Latham, 1985; Allegre and Turcotte, 1986; Christensen, 1987; Nicolas, 1989; Ribe, 1989; Ridley and Casey, 1989; Bose et al., 2020). However, the quantification of layered anisotropy in a viscous regime was first introduced by Weijermars (1992) in terms of the ratio of normal to shear viscosities ($\delta = \eta_N/\eta_S$), following the concept originally provided by Honda (1986) for planar anisotropy in geophysical layering.

To calculate the normal viscosity (η_N) and shear viscosity (η_S) of a layered rock body, the total thickness across the layers of the rock body under consideration is denoted as d and the individual thickness and viscosity of each layer are d_a and η_a, where both d_a and η_a vary layer to layer. Also, total number of layers is denoted as q.

According to Honda (1986) and Weijermars (1992) the normal viscosity (η_N) and shear viscosity (η_S) of that layered medium is as follows.

$$\eta_N = \sum_{a=1}^{q} \frac{(\eta_a \times d_a)}{d} \quad (1)$$

$$\eta_S = \frac{1}{\sum_{a=1}^{q} \frac{d_a}{(d \times \eta a)}} \quad (2)$$

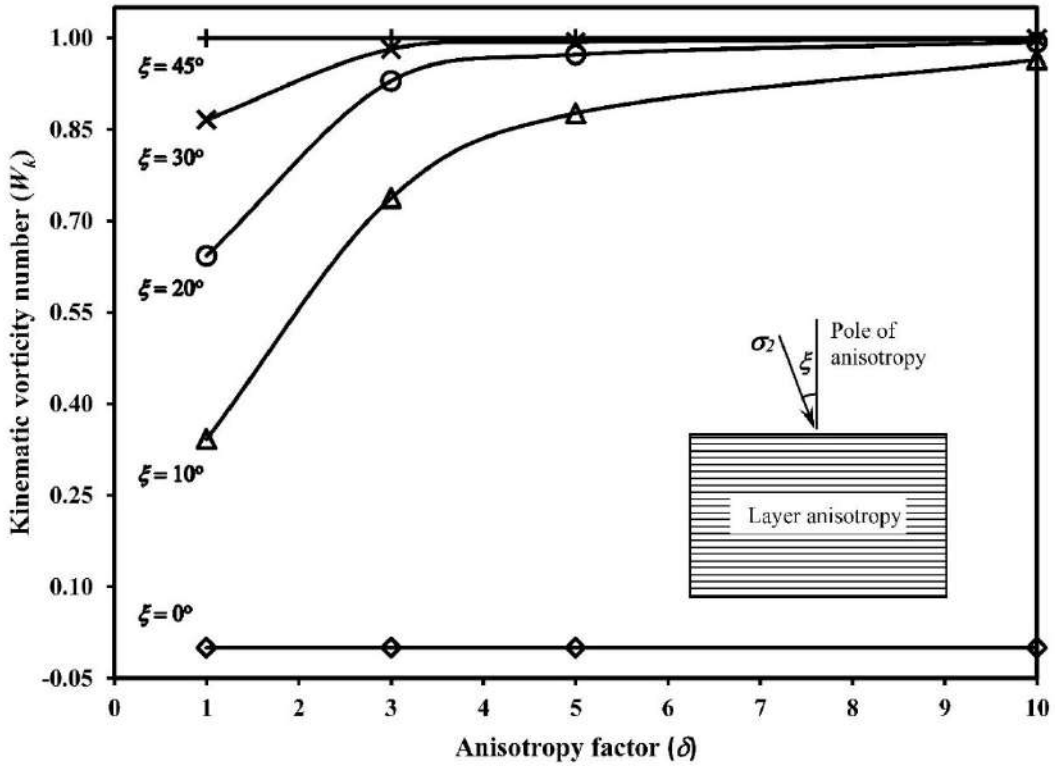

Fig. 1.2: Variation of kinematic vorticity number (W_k) with anisotropy factor (δ) for different orientation of principal stress axis (ζ) with respect to the pole of anisotropy (A_p). Note that for $\zeta = 0^o$ and 45^o, anisotropy factor does not have any influence on the flow of material.

Weijermars (1992) also established a theoretical relationship between the angle of the flow apophyses (α) (Bobyarchick, 1986) or the kinematic vorticity number (W_k) with the anisotropic factor (δ) and the orientation of the principal stress axes (ζ) with respect to the pole of anisotropy (A_p) (fig. 5, Weijermars, 1992). This relationship is expressed as

$$W_k = \cos[tan^{-1}\left\{\frac{cot2\xi}{\delta}\right\}] \quad (3)$$

It is evident from the above formulation that the magnitude of the kinematic vorticity number (W_k) can vary significantly within an anisotropic medium for a given orientation of the principal stress axes. For orientations except for ξ = 0° and 45°, the variation of W_k from an isotropic to an anisotropic rock decrease with increasing ξ (Fig. 1.2 and Table 1.1).

Table 1.1: Variation of W_k w.r.t. ζ and δ

Orientation of Principal stress axis (ζ)	Anisotropy factor (δ)	Kinematic vorticity number (W_k)
0°	1	0.00
	5	0.00
	10	0.00
10°	1	0.34
	5	0.88
	10	0.96
45°	1	1.00
	5	1.00
	10	1.00

1.1.1 Boudinage Structures

Boudinage structures are among the most visually arresting features observed in deformed, layered rocks. They form when a mechanically robust layer, embedded within a more ductile matrix, undergoes layer-parallel extension. As the competent layer fragments, the resulting boudins typically exhibit characteristic geometries—from initially rectangular shapes to more complex forms such as barrel-shaped, fish-mouth, or even bone-shaped structures (Treagus et al., 1996; Marques et al., 2012;

Abe and Urai, 2012). Early investigations by Ramberg (1955) and Wilson (1961) laid the groundwork for understanding the mechanics of boudinage, while later studies (Ramsay, 1967; Strömgård, 1973; Ghosh and Ramberg, 1976) expanded the conceptual framework to encompass both brittle and ductile processes. More recent work has highlighted the role of post-boudinage modifications—such as metamorphism, migmatization, and fluid–rock chemical reactions—in further modifying the original boudin geometries (Ray et al., 2011; Samanta and Deb, 2014).

The evolution of boudinage is not merely a record of extensional strain; it is also a sensitive indicator of the rheological properties of the involved materials. Detailed geometric analyses of boudin margins have been used to estimate relative viscosities and to infer the mechanical contrasts between the boudin, the inter-boudin infill, and the host matrix. Such studies, which combine field measurements with numerical simulations, provide a powerful means of reconstructing the deformation history of the lower crust.

1.1.2 Folds in Layered Rock

Folding is a fundamental mode of deformation in compressional regimes, where the bending of rock layers produces continuous, wave-like structures. The geometry of folds—characterized by parameters such as wavelength, amplitude, and the configuration of axial planes—has long been used as a proxy for interpreting the strain history and mechanical properties of the crust (Schmalholz and Podladchikov, 2001a; Bastida et al., 2005; Hudleston and Treagus, 2010). Early analogue models (Currie et al., 1962; Ramberg, 1963; Hudleston, 1973) and subsequent analytical techniques (Biot, 1961; Johnson and Fletcher, 1994; Hunt et al., 1996) provided

initial frameworks for understanding fold formation. With the advent of finite element modeling, researchers have been able to reproduce fold geometries under controlled conditions (Dieterich, 1970; Cobbold, 1977; Zhang et al., 1996; Mancktelow, 1999; Schmalholz et al., 2001).

In natural, multilayered rock systems, folding is inherently complex. The interaction between thin and thick layers, their spacing, and the relative viscosity contrast between the layers and the surrounding medium collectively influence the resulting fold geometry. The concept of a "dominant wavelength," introduced by Biot (1957), provides a theoretical basis for predicting fold wavelengths; however, the heterogeneous strain produced by adjacent layers often leads to deviations from the idealized dominant wavelength. As demonstrated by Ramberg (1960, 1963) and supported by our numerical studies, the "contact strain zone"—the region over which a folded layer influences its neighbours—plays a critical role in modifying fold geometry. Consequently, folds in layered rocks may evolve from harmonic to polyharmonic and eventually to disharmonic configurations as deformation progresses.

1.1.3 Flanking Structures

Flanking structures develop in response to the localized interaction between a cross-cutting element (such as a fracture or a small intrusion) and the preexisting planar fabrics within a rock. These structures record the deflection, rotation, and dragging of fabrics adjacent to the discontinuity. Early descriptions by Gayer et al. (1978) and Hudleston (1989) were later refined by Passchier (2001), who popularized the term "flanking structures" in contemporary structural geology.

Subsequent studies by Grasemann and Stüwe (2001), as well as by Exner et al. (2004, 2006) and Kocher and Mancktelow (2005), have shown that the geometry of flanking structures is highly sensitive to both the kinematic regime and the inherent anisotropy of the rock.

Numerical modelling studies have further advanced our understanding by demonstrating that the initial orientation of the cross-cutting element (CE) and its subsequent evolution under shear control the nature of the resulting fabric offsets. For instance, Basu Majumder and Samanta (2023) introduced a classification scheme that distinguishes between *Type I* (open) and *Type II* (closed) cross-cutting elements, highlighting that differences in offset (synthetic versus antithetic) and drag patterns (normal versus reverse) can be linked to variations in mechanical anisotropy. These insights are critical for reconstructing shear kinematics in tectonically deformed regions.

1.2 Objectives and Research Questions

The primary objective of this thesis is to unravel the complex deformation processes in layered rocks by integrating studies on boudinage, flanking structures, and folding. The specific research questions addressed in this work include:

1. **What are the controlling factors governing the evolution of boudinage structures in layered rocks?**

   This study investigates how parameters such as layer competence, initial aspect ratio, and post-fracture processes influence the morphology of boudins. The research also examines how subsequent deformation—through

mechanisms such as migmatization and fluid–rock interactions—modifies the initial boudin geometry (Treagus et al., 1996; Samanta and Deb, 2014).

2. **In what manner do the interactions between thin and thick layers influence fold geometry?**

   The research examines the influence of layer thickness, inter-layer spacing, and viscosity contrast on fold wavelength, amplitude, and harmonicity. The concept of the dominant wavelength is revisited, and the effects of the contact strain zone on multilayer folding are evaluated (Biot, 1957; Ramberg, 1960, 1963).

3. **Can quantitative parameters derive from numerical models be used to estimate rheological contrasts in natural rock systems?**

   The thesis introduces measures such as the wavelength factor (W-factor) as diagnostic tools for linking model predictions with field observations. These parameters serve to constrain viscosity ratios and effective strain, thereby facilitating more accurate tectonic reconstructions.

4. **How does the presence of a cross-cutting element affect the deflection of planar fabrics to form flanking structures?**

   By employing numerical modelling under both general and simple shear conditions, this thesis explores the role of initial CE orientation, mechanical anisotropy, and kinematic parameters in controlling fabric offset, drag patterns, and the rotation of the CE (Passchier, 2001; Basu Majumder and Samanta, 2023).

1.3 Methodological Approach

This thesis employs an integrated methodological framework that combines finite element modelling, analogue experiments, and extensive literature review. The numerical models are developed using advanced finite element software (ABAQUS and ANSYS) under plane strain conditions, which are well suited to simulate the ductile deformation of lower crustal rocks. Key aspects of the modelling approach include:

- **Boudinage Modelling:**

  The finite element models simulate the fragmentation of competent layers and track the evolution of boudin shapes under layer-parallel extension. By varying viscosity ratios and incorporating narrow inter-boudin separation zones, the models capture the transition from rectangular to curved geometries, thereby reflecting the effects of both initial conditions and post-fracture deformation.

- **Folding in Layered Rocks:**

  The modelling of folding involves a three-layer system comprising a central thin layer flanked by thicker layers. By imposing layer-parallel shortening and varying parameters such as layer thickness, inter-layer spacing, and viscosity ratio, the models investigate how thin-layer perturbations influence the fold geometry in adjacent thick layers. The evolution of fold wavelength and harmonicity is quantified using the *W*-factor, and the influence of the contact strain zone is thoroughly analyzed.

- **Flanking Structures Modelling:**

  Numerical simulations of flanking structures focus on the development of

fabric offsets adjacent to cross-cutting elements. By systematically varying the initial orientation of the CE, the degree of mechanical anisotropy (δ), and the imposed shear conditions (e.g., kinematic vorticity number, W_k), the models provide detailed insights into the mechanisms of fabric deflection and drag. This approach builds upon the work of Passchier (2001) and Basu Majumder and Samanta (2023), enabling the development of a refined classification scheme for flanking structures.

Each of these modelling efforts is supported by a robust review of previous studies—from early analogue models (Currie et al., 1962; Ramberg, 1963) to modern numerical simulations (Mancktelow, 1999; Schmalholz et al., 2001). The integration of these approaches provides a comprehensive picture of the deformation processes in layered rocks.

1.4 Significance of the Study

The significance of this research lies in its holistic approach to understanding the deformation of layered rocks—a subject that is fundamental to tectonic studies and has wide-ranging implications for resource exploration, geohazard assessment, and the interpretation of seismic data. Specifically:

- **Advancing Tectonic Reconstructions:**

  By providing quantitative constraints on rheological contrasts and effective strain, this work contributes to more accurate tectonic reconstructions. The ability to infer viscosity ratios and deformation histories from structural geometries is particularly valuable in regions characterized by complex fold and fault systems.

- **Improving Deformation Models:**

  The integration of boudinage, folding, and flanking structures into a single conceptual framework represents a significant advancement in deformation modelling. The study highlights the interrelated nature of these structures and underscores the importance of considering multi-scale interactions in layered rocks.

- **Practical Applications:**

  The methodologies developed in this thesis have practical applications in engineering geology and materials science. Understanding the behaviour of layered materials under stress is crucial for the design of stable infrastructures and for the management of subsurface resources.

1.5 Structure of the Thesis

This thesis is organized into six chapters. Chapter 1 introduces the overarching themes, objectives, and significance of the research. Chapter 2 describes the study area (CGGC) of this thesis with an emphasis on Purulia and Jasidih-Deoghar regions. Chapter 3 focuses on boudinage structures, examining their formation, evolution, and implications for strain analysis. Chapter 4 explores folding in layered rock, emphasizing the mutual interaction between thin and thick layers and the resulting fold geometries. Chapter 5 addresses flanking structures in layered rocks under transpressional regime, with a detailed discussion of their kinematic development and the role of mechanical anisotropy. Chapter 6 presents numerical modelling of flanking structures under simple shear conditions, highlighting how variations in anisotropy influence fabric deflection and offset. Finally, Chapter 7

provides a comprehensive discussion and conclusions, synthesizing the findings from the previous chapters and outlining prospects for future research.

1.6 Summary

In summary, the deformation of layered rocks encompasses a spectrum of complex processes—from the fragmentation of competent layers (boudinage) to the buckling of layers into folds and the deflection of fabrics adjacent to discontinuities (flanking structures). This thesis addresses these phenomena by combining numerical modelling with extensive field and analogue observations. The insights gained from this work not only enhance our understanding of crustal deformation but also offer valuable tools for quantifying rheological contrasts and reconstructing tectonic histories.

By integrating the concepts and methodologies presented in the four core chapters—covering boudinage, folding, and flanking structures (both in general and under simple shear)—this introductory chapter sets the stage for a comprehensive exploration of deformation processes in layered rocks. The research presented herein aims to bridge the gap between theoretical predictions and natural observations, providing a robust framework for interpreting the complex interplay between material properties, structural geometry, and tectonic forces.

Chapter 2

Study Area

2.1 Introduction

The study area under investigation forms part of the extensive Chhotanagpur Granite Gneissic Complex (CGGC), one of the largest and most significant gneissic terrains in eastern India (Fig. 2.1). This complex extends over a considerable area and exhibits a wide range of metamorphic and structural features. Detailed field investigations have been carried out in two distinct sectors of the complex: the Jasidih–Deoghar area (northern part) and the Purulia area (southern part). While both areas share certain regional tectonic and metamorphic characteristics inherent to the

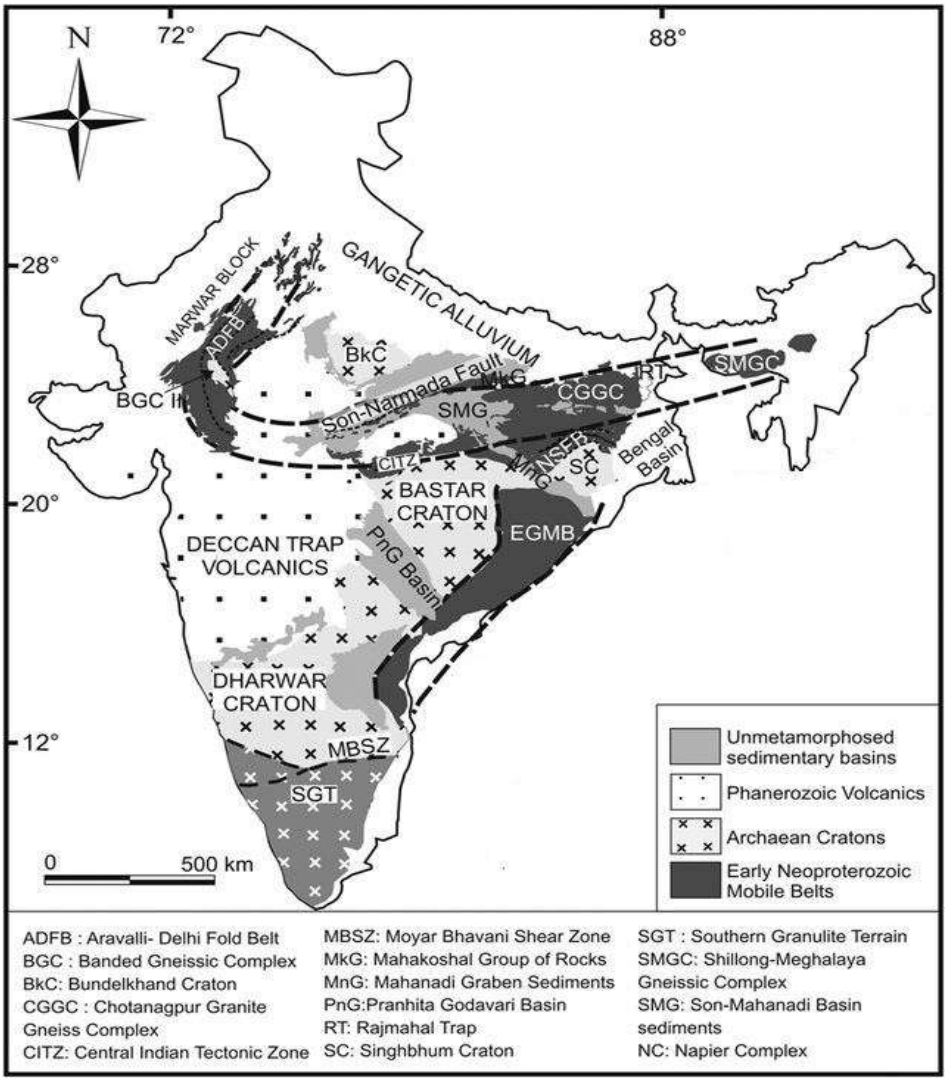

Fig. 2.1: Geological map showing Indian crystalline basements and sedimentary cover. The thick dashed line represents the Early Neoproterozoic suture (modified after Mukherjee et al., 2017).

CGGC, they also display unique lithological and structural differences. The following sections present an in-depth discussion on the overall geology of the study area, a detailed account of the rock types and structures, and a comparative analysis of the similarities and differences between the Purulia and Jasidih–Deoghar areas.

2.2 Overall Geology

The Chhotanagpur Granite Gneissic Complex (CGGC) represents a major segment of the Precambrian basement in eastern India and is renowned for its high-grade metamorphic rocks (Fig. 2.2). The region lies approximately between 22° N and 25°30′ N latitudes and 83°47′ E to 87°50′ E longitudes (Ghosh, 2004). This area, estimated to cover nearly 100,000 km², comprises a mosaic of high-grade metamorphic rocks intermingled with granitoids and localized sedimentary basins. CGGC extends over an area of approximately 105 km² and trends in an east–west direction across several states, including Chhattisgarh, Jharkhand, Odisa, and West Bengal. Its lateral extent is demarcated by contrasting geological units: to the north, the complex is bounded by the Gangetic alluvium and the subsurface extension of the Mahakoshal Basin; to the south, it is in contact with the North Singhbhum Mobile Belt (NSMB); and to the northeast, it abuts the Rajmahal basalt province. The eastern margin transitions into the sediment-rich Bengal Basin, whereas the western margin is juxtaposed against rocks of the Gondwana Supergroup. This juxtaposition of diverse geological entities makes the CGGC a critical region for understanding the evolution of the Indian continental crust.

Within the CGGC, three major subregions are recognized:

- **Jasidih–Deoghar Area:** This area is noted for its relatively well-preserved Archaean granitoids and limited later deformation. The structural record here is dominated by primary gneissic fabrics with localized ductile overprints.
- **Purulia Area:** Marked by a higher intensity of deformation, the Purulia area exhibits pronounced high-grade metamorphic overprints, ductile shear zones, and complex structural reworking. This region is characterized by a mélange of migmatites, granites, and reworked metasedimentary units.
- **Daltonganj–Hazaribagh Belt:** Although not the primary focus of this chapter, this belt features migmatitic gneisses and granulites, recording evidence for high-pressure metamorphism and isothermal decompression.

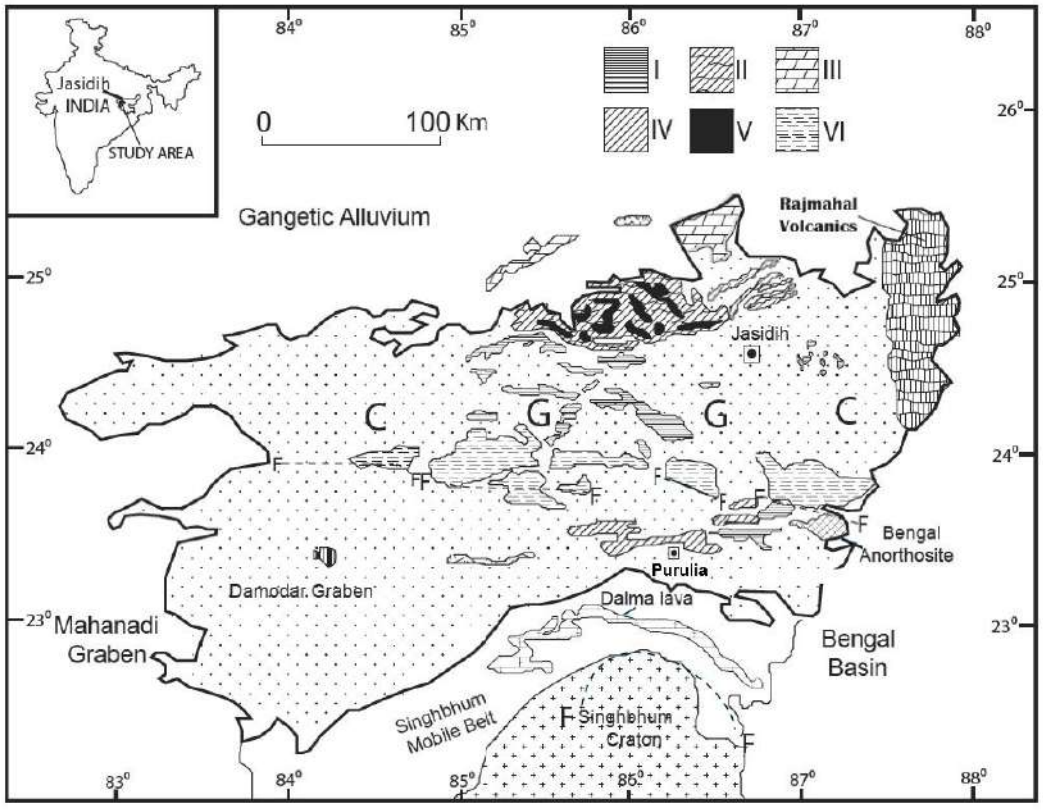

Fig. 2.2: Geological map of Chhotanagpur Granite Gneissic Complex (CGGC) showing the location of study area (Jasidih-Deoghar and Purulia) (after Samanta and Deb, 2014). I - Archean-Proterozoic metasedimentary enclaves, II- Paleo-Mesoproterozoic metasedimentary enclaves, III- Mesoproterozoic meta-sedimentary enclaves, IV- Granitic plutons of Mesoproterozoic, V- Granitic plutons of Neoproterozoic, VI- Gondwanas and younger covers. The dashed lines marked with 'F' represent faults.

The remainder of this chapter will focus on the first two subregions—Jasidih–Deoghar and Purulia—as these areas offer contrasting insights into the stratigraphic and structural evolution within the CGGC.

Both the Purulia and Jasidih–Deoghar areas have recorded a prolonged and dynamic tectonic history. The entire complex has predominantly experienced metamorphism under amphibolite facies conditions, with certain localized zones in the southeastern portions reaching granulite facies metamorphism (Mahadevan, 2002; Bhattacharya, 1976; Banerji, 1991; Sharma, 2009; Ray et al., 2011). The high-grade metamorphic imprint indicates that the rocks have been subjected to significant thermal and pressure regimes over geological time.

The CGGC embodies a record of ancient crustal evolution, with its geometry and structural fabrics reflecting multiple episodes of magmatism, deformation, and metamorphism. Its geological setting is defined by the interplay between ancient Archaean basement components and later Proterozoic overprints (Kumar et al., 2022; Mohanty, 2023).

- **Archaean Basement Components**

The earliest record in the CGGC is provided by the Archaean basement, which predominantly comprises extensively deformed Tonalite–Trondhjemite–Granodiorite (TTG) suites. These rocks, with ages estimated at approximately 3.5–3.3 Ga, delineate the early continental crust formation phase. In many parts of the CGGC, TTG complexes occur as robust, coherent bodies that have preserved primary magmatic fabrics despite later deformation events. Additionally, primary granite gneiss—with ages ranging from 3.4 to 3.1 Ga—forms another fundamental component of the basement. These plutonic rocks are characterized by their high-

grade metamorphism and are distinguished by intercalated migmatites that record early melting and deformation processes.

- **Proterozoic Overprint and Subsequent Intrusions**

Following the establishment of the Archaean nucleus, the CGGC experienced a series of Proterozoic tectono-metamorphic events that significantly altered its crustal framework. Around 1.87 Ga, ultra-high temperature (UHT) metamorphic conditions are recorded in granulite enclaves, indicating peak thermal regimes reaching beyond 900° C at pressures of 5–8 kbar. Such conditions are consistent with deep crustal burial and rapid thermal overprinting processes. Later events, spanning ages between approximately 1.55 and 1.0 Ga, include the emplacement of anorthosite and porphyritic granitoids. These younger intrusive suites are often associated with late-stage deformation and are interpreted to record processes related to the Satpura Orogeny, including significant crustal shortening and shear zone development.

Shear zones, particularly those active after 1.0 Ga, have played a crucial role in reworking the primary fabric of the CGGC. The South Purulia Shear Zone (SPSZ), for example, represents one of the major structures that has facilitated lateral displacement and ductile deformation between high-grade metamorphic units and comparatively less deformed Archaean blocks (Kumar et al., 2022).

The structural evolution of the CGGC is marked by multiple phases of deformation. Detailed field studies in both the northern (Jasidih–Deoghar) and southern (Purulia) sectors reveal that the deformation history is divided into at least four distinct phases. The earliest deformation phases (D1 and D2) are characterized by intensive, penetrative, and largely coaxial strain. These early events produced complex fold interferences that are often described as hook-shaped, reflecting the

high degree of deformation imposed on the pre-existing rock fabrics. Subsequent phases (D3 and D4) show less pervasive deformation. The D3 phase is typically associated with the development of a broad warp in the east–west axial foliation (often noted as F3), whereas the D4 phase is characterized by localized shearing and thrusting. In many parts of the CGGC, and notably in the Purulia area, high-grade metamorphic imprints correlate strongly with the early D1/D2 phases, while later retrograde metamorphic features are more evident in the overprinting of the D3/D4 phases (Sarangi & Mohanty, 1998; Goswami & Bhattachrayya, 2008; Samanta & Deb, 2014).

An important aspect of the tectono-metamorphic evolution of the CGGC is the role of fluid infiltration. Fluids have pervasively penetrated the rock sequences during various metamorphic episodes, facilitating recrystallization and contributing to the development of secondary structures. One clear manifestation of fluid involvement is the formation of migmatitic textures, where partial melting under high-temperature conditions results in the segregation of light-coloured leucosomes from dark, biotite-rich melanosomes. The pervasive gneissic foliation observed in many of the quartzofeldspathic rocks is also, in part, a secondary fabric developed during deformation under fluid-rich conditions.

In summary, the overall geology of the study area can be characterized by the following principal attributes:

- **High-Grade Metamorphism:** The region predominantly exhibits amphibolite facies metamorphism with localized granulite facies conditions (Mahadevan, 2002; Bhattacharya, 1976; Banerji, 1991; Sharma, 2009; Ray et al., 2011).

- **Multi-Phase Deformation:** Four distinct deformation phases (D1, D2, D3, and D4) have reworked the original rock fabric. Early phases produced intensive, penetrative deformation with complex fold geometries, while later phases introduced retrograde metamorphism with shearing and thrusting.
- **Fluid-Induced Alterations:** Fluid activity has been instrumental in facilitating metamorphic reactions and in developing secondary fabrics such as gneissic foliation and migmatitic structures.
- **Tectonic Positioning:** The CGGC's boundaries with the Gangetic alluvium, the Singhbhum mobile belt, and the Rajmahal basalts emphasize its transitional nature and provide context for its metamorphic and tectonic evolution.

These factors collectively form the basis for understanding the tectono-metamorphic evolution recorded in both the Purulia and Jasidih–Deoghar areas.

2.3 Rock Types and Structures

The following principal lithostratigraphic units are recognized within the CGGC:

- **Archaean TTG Suite:**

  Composed mainly of robust granitic and gneissic rocks representing the early continental crust, this unit typically exhibits coherent magmatic textures with minor alteration. Its age is constrained to approximately 3.5–3.3 Ga (Ghosh, 2004; Sanyal and Sengupta, 2012; Mukherjee et al., 2017).

- **Primary Granite Gneiss:**

  These rocks, with ages ranging from 3.4 to 3.1 Ga, display high-grade

metamorphic overprint with intercalated migmatitic bands. Their well-defined fabric preserves evidence of early magmatic processes (Goswami and Bhattacharyya, 2010; Kumar et al., 2022).

- **Younger Intrusive Suites:**

  Emplacement of porphyritic granites, nepheline syenites, and related lithologies occurred during the Proterozoic (<1.6 to about 1.0 Ga). In many regions, such as in the Purulia area, these intrusives are intimately linked with regional shear zone activity and pervasive deformation (Kumar et al., 2022; Mohanty, 2023).

- **Sedimentary and Meta-sedimentary Cover:**

  Although far less pervasive in the Jasidih–Deoghar area, some parts of the CGGC, particularly in the Purulia region, exhibit interleaved metasedimentary units, including the remnants of the Chandil Formation. These cover sequences represent later deposition events and are critical for understanding the transition from high-grade metamorphic terrains to mobile belts (Ghosh, 2004; Kumar et al., 2022).

Beside these, overall lithological assemblage of the study area is diverse, reflecting the complex interplay between sedimentation, high-grade metamorphism, and structural reworking. Both the Purulia and Jasidih–Deoghar areas display a range of rock types that are fundamental to the characterization of the CGGC. The principal rock types observed include:

- **Banded or Layered Gneisses:**

  These are the most widespread lithologies in the study area. Banded gneisses are characterized by distinct layers resulting from repeated cycles of sediment

deposition, metamorphism, and subsequent deformation. The mineralogical composition is dominated by quartz, feldspar, and amphibole, with a subordinate amount of biotite. In both regions, the banded gneisses show interlayering with amphibolite bands, suggesting variations in the original protoliths and differences in metamorphic conditions.

- **Streaky Gneisses and Augen Gneisses:**

  In addition to the banded varieties, streaky gneisses and augen gneisses are also prominent. Augen gneisses are distinguished by the presence of large, eye-shaped feldspar porphyroclasts set within a finer-grained matrix. These porphyroclasts provide evidence of intense deformation and partial melting, and their occurrence is a key indicator of high-grade metamorphism in the CGGC.

- **Migmatites:**

  Migmatites are transitional rocks that exhibit features of partial melting. They are characterized by the presence of alternating light-coloured leucosomes and dark melanosomes. The formation of migmatites in both the Purulia and Jasidih–Deoghar areas reflects the influence of high-temperature conditions and the role of fluids in facilitating partial melting and mineral segregation.

- **Pegmatitic Veins:**

  Pegmatitic veins are found within the quartzofeldspathic gneisses and are emplaced at various stages of deformation. Their coarse-grained texture is indicative of late-stage magmatic processes, and these veins serve as markers of episodic intrusions during the progressive reworking of the host rocks.

- **Intrusive Basic Rocks (Amphibolites):**

  Both study areas are intruded by mafic dykes composed predominantly of

amphibolites. These dykes are interpreted as syntectonic bodies that were emplaced during active deformation. Their mineral assemblage, mainly comprising hornblende and plagioclase (andesine), is typical of rocks metamorphosed under upper amphibolite facies conditions.

The structural architecture of the CGGC, as expressed in both the Purulia and Jasidih–Deoghar areas, reflects a long history of deformation. Key structural features common to both areas include:

- **Gneissic Foliation:**

  A well-developed gneissic foliation is observed in the quartzofeldspathic gneisses across the complex. This foliation, which is largely a secondary fabric, developed during the early phases of deformation (D1/D2) and has been overprinted by later events (D3/D4). The foliation is a critical structural element that records the directional stresses and strain patterns imposed on the rocks.

- **Interlayering of Rock Units:**

  The interlayering of quartzofeldspathic gneisses with amphibolite bands is a distinctive feature of the study area. This interlayering is a product of the original sedimentary layering, subsequently modified by high-grade metamorphism and deformation. The variable compositions of the quartzofeldspathic gneisses—from granitic and granodioritic to tonalitic types (Ghosh and Sengupta, 1999)—are preserved in both regions.

- **Syntectonic Intrusions:**

  The occurrence of syntectonic intrusions, such as the mafic dykes and pegmatitic veins, is a common structural feature in the CGGC. These

intrusions were emplaced during active deformation and are aligned with the principal foliation and fold axes. They provide valuable constraints on the timing of magmatic events in relation to the deformation history of the area.

- **Multiple Deformation Phases:**

  Both the Purulia and Jasidih–Deoghar areas have recorded four distinct deformation phases (D1, D2, D3, and D4). The early D1/D2 phases produced intensive and penetrative deformation with complex, hook-shaped folds, while the later D3/D4 phases introduced modifications through shearing, thrusting, and the development of broad warps in the axial foliation. The trends of the cross-cutting elements associated with flanking structures vary significantly (from 40° to 150°), highlighting the variability of stress regimes during the later stages of deformation.

In both the Purulia and Jasidih–Deoghar sectors, the observed rock types have been modified by a series of structural events that have left a permanent imprint on their textures and fabrics. The quartzofeldspathic gneisses, for instance, display a well-developed foliation that is continuously overprinted by younger deformation structures. This overprinting is particularly evident in regions where the interlayering with amphibolite bands is most pronounced. The presence of pegmatitic veins cutting through these gneisses also attests to the intermittent intrusion of magmatic material during active tectonism.

The basic rocks in the form of amphibolite dykes are similarly affected by the deformational history. Their alignment and orientation provide crucial insights into the regional stress fields at the time of their emplacement. In many cases, these dykes

are observed to cross-cut the dominant foliation, thereby serving as markers for relative timing between magmatic intrusion and regional deformation.

2.4 Comparative Study between the Purulia and Jasidih–Deoghar Areas

While both the Purulia and Jasidih–Deoghar areas are part of the extensive CGGC and share an overall similar high-grade metamorphic and tectonic history, there are notable similarities and differences in their lithological and structural characteristics. In this comparative study, the similarities and dissimilarities are examined to provide a nuanced understanding of the regional variability within the CGGC. The Table-1 marked the degree of coherence in between the lithostratigraphic units of the two distinct regions.

A distinctive aspect of the CGGC is the marked variation between its subregions. Studies have shown that spatial differences in lithostratigraphy, structural fabric, and metamorphic grade are vital to understanding the local evolution of tectonic regimes.

2.4.1 Jasidih–Deoghar Area

The areas in and around Jasidih-Deoghar reveal swarms of mafic (amphibolite) dykes intruding quartzofeldspathic gneisses, which include augen gneiss and migmatite with leucosomes ranging from centimeters to decimeters in thickness, alongside biotite-rich melanosomes. The banded gneisses have behaved as a complex geological multilayer that evolved through the combined effects of deformation, metamorphism, and fluid invasions.

Table 2.1: Distribution of lithostratigraphic units

Lithostratigraphic Unit	Jasidih–Deoghar Area	Purulia Area	Age (Ga)	References
Archaean TTG Suite	Exposed as coherent, less deformed granitoid gneisses exhibiting well-preserved magmatic fabrics	Present but often reworked by intense shear zone deformation along the South Purulia Shear Zone	~3.5–3.3	Sanyal and Sengupta (2012); Ghosh (2004)
Primary Granite Gneiss	Dominant exposure with uniform structures; minor migmatization evident	Often overprinted by ductile deformation and mylonitization associated with neighbouring mobile belts	~3.4–3.1	Goswami and Bhattacharyya (2010); Kumar et al. (2022)
Younger Intrusive Suite	Occurrence is localized; granitic intrusions are sharply defined and only partly disturbed	Widely distributed; intrusive bodies intercalate with metasedimentary units and are strongly reactivated	<1.6–1.0	Kumar et al. (2022); Mohanty (2023)
Sedimentary/Meta-sedimentary Unit	Generally absent or cryptic; region dominated by primary crystalline rocks	More prominent exposures showing intercalation of pelitic schists and quartzites (Chandil Formation)	<1.6	Ghosh (2004); Kumar et al. (2022)

The principal rock types in the Jasidih-Deoghar area are banded or layered gneisses, streaky gneiss, augen gneiss, and amphibolites. The quartzofeldspathic gneisses are interlayered with bands of amphibolites, and their composition varies widely—from granitic and granodioritic to tonalitic types, with granodiorite being predominant in most instances (Ghosh and Sengupta,1999). Pegmatitic veins have been emplaced within these gneisses during various stages of deformation. The dykes, originally mafic igneous rocks, have been metamorphosed under upper

amphibolite facies conditions. Their mineral assemblage is chiefly composed of hornblende and plagioclase (andesine). In some areas, a few relict grains of pyroxene occur centrally within the dykes; however, near the contacts with the country rock, pyroxene is absent and medium to coarse flakes of biotite are common (Fig. 2.3a). Biotite is more abundant in the deformed boudin blocks, concentrating mainly along drawn-out portions, in flame folds, and at the cuspate segments of the cuspate lobate folds, while remaining scarce or absent in the cores of the thicker mafic dykes. The coarse-grained leucosome in the separation zones between amphibolite boudins consists of quartz, plagioclase, and microcline. The host rock comprises solely migmatitic quartzofeldspathic gneiss (Fig. 2.3b), whose mineralogy is dominated by quartz, feldspar, amphibole, and minor biotite; it is uniformly metamorphosed and deformed, exhibiting a secondary fabric defined by foliation planes. In the augen gneiss, feldspar grains are typically ellipsoidal, though in some locations they are extremely deformed into extended thin lenses (Fig. 2.3c).

Regionally, the rocks have undergone at least three major phases of folding. Disharmonic and small parasitic folds, indicative of a buckling mechanism, are common throughout all folding events (Fig. 2.4a). The earliest exposed folds (F1) are isoclinal with axial planes striking approximately 100° and dipping north; close examination of F1 closures reveals gneissic foliations, suggesting pre-F1 deformation. The dominant F2 folds are plunging-isoclinal to very tight, with nearly vertical axial planes striking N- to NNE and fold axes plunging gently to moderately (averaging 25°) toward N- to NNE. The interference between F1 and F2, evident in both hook and mushroom-shaped outcrops, indicates a mix of coaxial and high-angle relationships (Fig. 2.4b and c). The final F3 folds are gentle to close, with sub-vertical axial surfaces striking E–W and steeply plunging fold axes. At least three

generations of boudinage—pre-F1, syn-F1, and syn-F2—are recognized, with pre-F1 boudins noted by pinch-and-swell structures and pegmatite-filled separation zones at F1 hinges (Sengupta,1983), syn-F1 boudins along F1 limbs, and the most common syn-F2 boudins formed during F2 folding, later tightened during the F3 event (Fig. 2.4d).

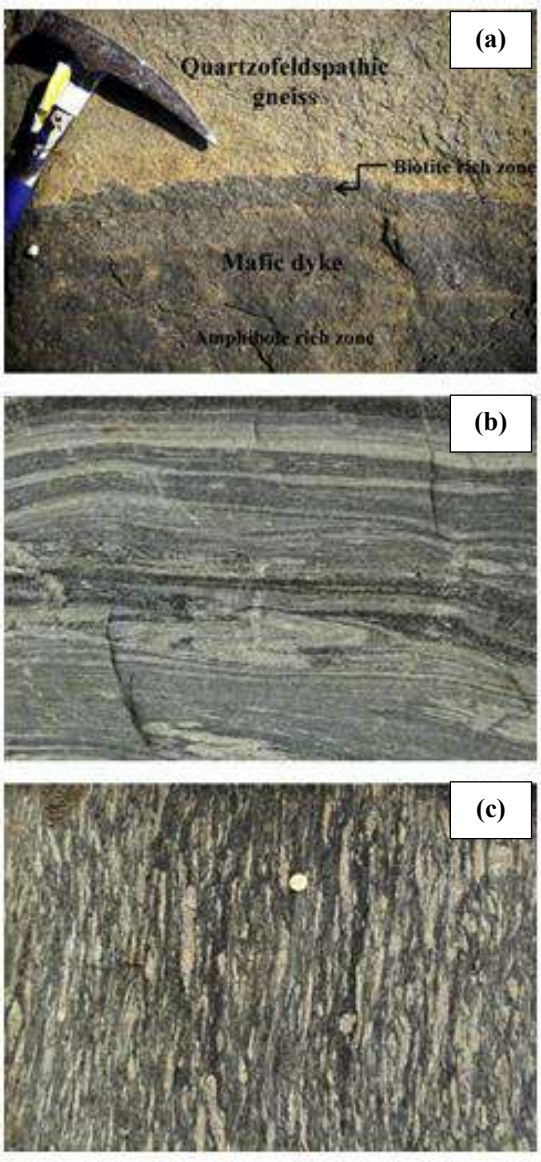

Fig. 2.3: Field photographs taken from Jasidih-Deoghar (from Samanta and Deb, 2014). (a) Mafic amphibolite dyke with the localisation of biotite at the boundary of country rock, (b) Folds in migmatitic gneiss, (c) Deformed augen gneiss. The length of photo plate for (a) and (b) is 1.2 m.

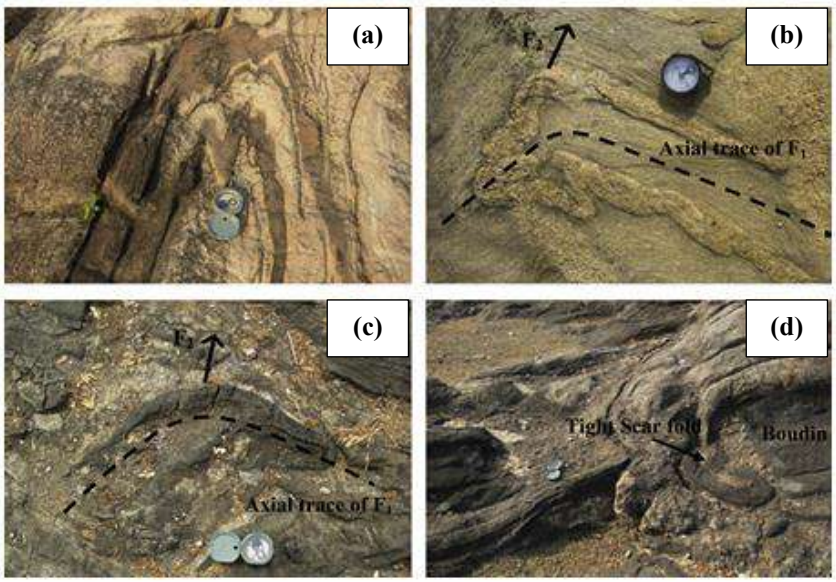

Fig. 2.4: Field photographs taken from Jasidih-Deoghar (from Samanta and Deb, 2014). (a) Mafic dyke showing M-shaped parasitic folds at the hinge of F1 fold. (b) Hook-shaped fold indicating coaxial relation between F1 and F2. (c) Crescent/Mushroom shaped fold pattern signifying high angle relation between F1 and F2. (d) Isoclinal scar fold at the separation zone within two boudin blocks.

In summary, the Jasidih–Deoghar region is often characterized by the preservation of early Archaean crustal elements with minimal Proterozoic overprinting. Key features include:

- **Lithology:** Dominance of pristine granitoid gneisses that exhibit clear magmatic fabrics and relatively low deformation. The paucity of intercalated metasedimentary units allows for clearer exposure of the original TTG suites.
- **Structural Characteristics:** The region shows relatively simple deformation structures, such as open, gentle folds and occasional brittle faults. The absence of intense mylonitization indicates that it has remained largely unaffected by the later high-strain tectonic events that dominate other parts of the CGGC.

- **Metamorphic Grade:** Typically recorded at the lower amphibolite facies (temperatures of 550–600 °C), suggesting that the rocks have not been subjected to the highest metamorphic conditions noted in the complex.
- **Tectonic Implications:** The relatively pristine nature of this region makes it ideal for studies aimed at deciphering the early magmatic and crustal formation processes in the Eastern Indian Shield.

2.4.2 Purulia Area

The rock types in the Purulia area are predominantly composed of granite gneisses, migmatites, and granites of both porphyritic and massive varieties, along with enclaves of metapelitic and metabasic granulites and a few intrusive basic rocks. In this complex geological setting, four distinct phases of deformation have been recognized.

The field photographs presented in Fig. 2.5 from Purulia provide comprehensive insights into the structural complexity of the region's metamorphic rocks. Figs. 2.5(a) and (b) depict boudinaged quartzofeldspathic layers embedded within a layered gneissic matrix, illustrating the effects of extensional forces that led to the segmentation of these rigid layers. In Figs. 2.5(c) and (d), the presence of shear bands and their associated flanking structures in a granite gneiss highlight localized zones of intense deformation, suggesting progressive strain partitioning. Furthermore, harmonic folds observed in Figs. 2.5(e) and (f) within the layered gneiss indicate regular folding patterns that likely resulted from compressive tectonic stresses. More complex fold geometries, including polyharmonic and disharmonic folds, are clearly documented in Figs. 2.5(g) and (h) within the Chhotanagpur

Gneissic Complex (CGGC), which suggest variable strain distributions and non-uniform stress fields. Fig. 2.5(i) presents a single layered fold with significant amplitudinal development, reinforcing the interpretation of heterogeneous deformation mechanisms operating within the gneissic complex. Detailed examination of these structures contributes significantly to understanding the tectonic evolution and deformation history of the studied area in the region.

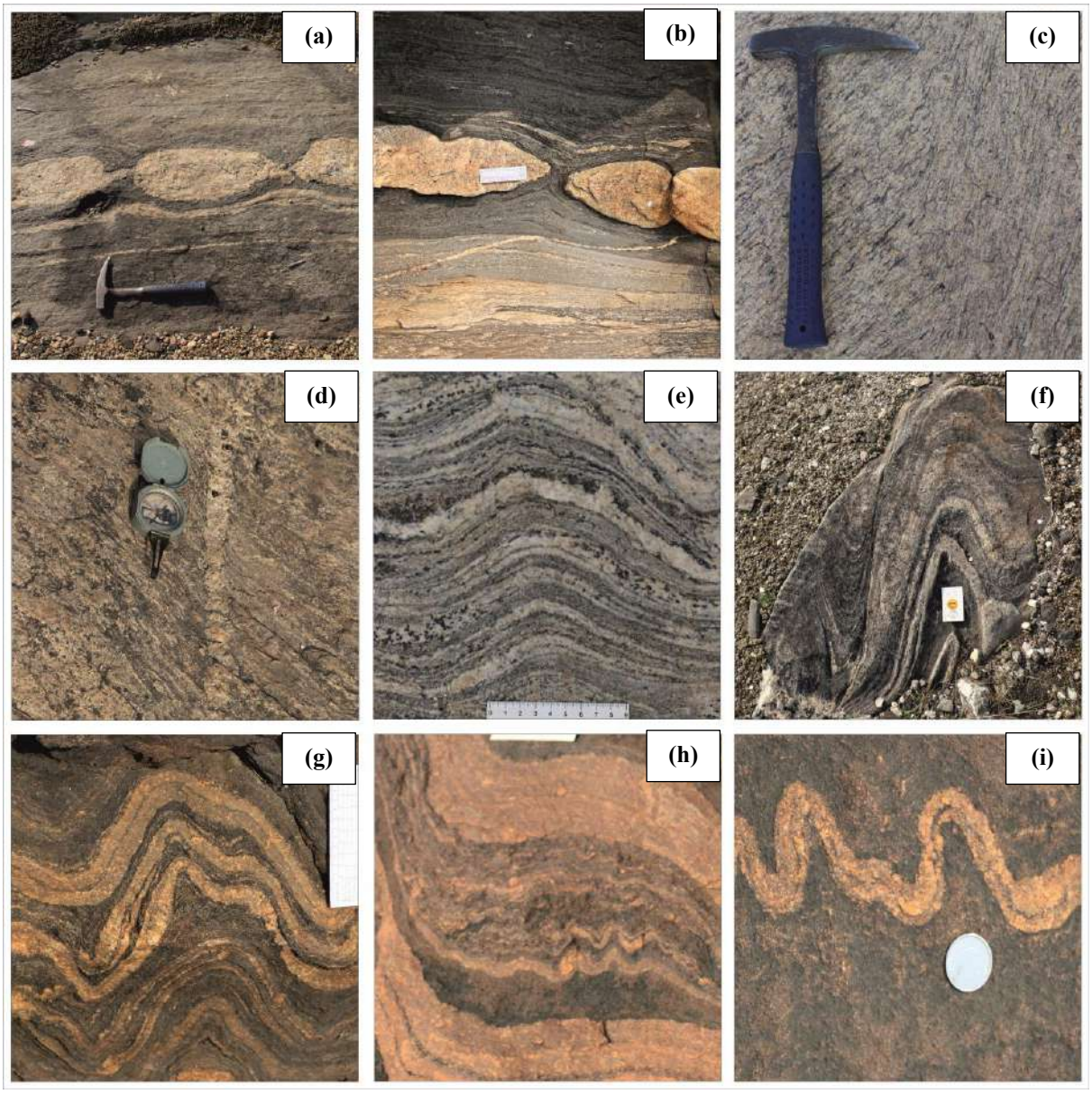

Fig. 2.5: Field photographs taken from Purulia. (a) and (b) represent boudinaged quartzofeldspathic layer within layered gneissic rock. (c) and (d) represent shear band and flanking structures respectively within granite gneiss. (e) and (f) represent harmonic folds within layered gneiss. (g) and (h) exhibit polyharmonic and disharmonic folds respectively in CGGC. (i) exhibits single layered fold with significant amplitudinal development in gneissic complex.

The first two phases, designated as D1 and D2, are characterized by intensive, penetrative deformation that is more or less coaxial in nature. This coaxial deformation has led to a complex interference of folds, often resulting in hook-shaped structures, as documented by Sarangi and Mohanty (1998), Goswami and Bhattachrayya (2008), and Samanta and Deb (2014). The later phases of deformation, referred to as D3 and D4, are observed to be less penetrative compared to the earlier D1 and D2 events. In certain portions of the Purulia area, high-grade metamorphic imprints are closely associated with the early deformation phases (D1/D2). In contrast, the later phases (D3/D4) are linked with retrograde metamorphism, indicating a reversal or overprinting of the earlier high-grade metamorphic conditions.

Within the host granite gneiss, basic rocks have been emplaced as small syntectonic bodies, signifying their intrusion concurrent with tectonic activity. Meanwhile, granitoids are found to be emplaced along the axial planes of structures that range from synformal to antiformal configurations, occurring as syn- to late-kinematic intrusions with respect to the F2 fold generation. This suggests that the granitoids were emplaced during the active phase of folding or immediately following it, thus playing an integral role in the overall tectonic evolution of the region.

The development of a broad warp, which is referred to as the F3 fold, in the northeastern part of the area is responsible for the third deformation phase (D3). This F3 fold is defined by an east-west axial foliation, which has been broadly interpreted as the result of regional tectonic forces acting in that direction. The D4 deformation phase, on the other hand, is distinctly characterized by shearing and thrusting, which further modified the pre-existing structural framework.

Regional gneissic foliations in the Purulia area generally strike in a broad east-west direction. Additionally, the trend of cross-cutting elements related to the flanking structures varies significantly, ranging from 40° to 150°. This variation in orientation is associated with the combined effects of the D3 and D4 deformation phases, which have influenced the geometry and distribution of these structural elements. Overall, the Purulia area's tectonic evolution is marked by multiple deformation events, each contributing to the present-day structural complexity and the diverse rock types observed in the region.

In summary the Purulia area presents a more complex geological record resulting from multiple episodes of deformation and metamorphism:

- **Lithology:** Here, the lithostratigraphic sequence is more diverse. In addition to the primary granitoids, the area hosts significant occurrences of migmatites, granulites, and metasedimentary units such as the Chandil Formation. This diversity is indicative of a long and complex depositional and metamorphic history.
- **Structural Fabric:** The Purulia region is dominated by ductile shear zones, most notably the South Purulia Shear Zone. The intense deformation in this area is evidenced by the widespread occurrence of mylonitic fabrics, isoclinal folding, and well-developed boudinage features (Fig. 2.5e to i). Asymmetric flanking folds and axial planar cleavage develop prominently in the metasedimentary cover, suggesting localized strain concentration.
- **Metamorphic Grade:** Metamorphic conditions in Purulia often record higher temperatures (up to 750–800 °C) associated with granulite facies

metamorphism. These elevated conditions reflect both deeper crustal burial and rapid thermal episodes likely related to tectonic compression.

- **Tectonic Implications:** The intense reworking and high-grade metamorphism indicate that the Purulia area has been significantly influenced by lateral tectonic transport and deformation events. Detailed structural analyses reveal that the intense tectonic reactivation has overprinted the primary lithofacies, leading to a complex assemblage that is instrumental in unravelling the polyphase history of the CGGC.

2.4.3 Similarities between Purulia and Jasidih–Deoghar

- **Metamorphic Grade and Deformation History:**

  Both areas have predominantly experienced amphibolite facies metamorphism with localized occurrences of granulite facies conditions. The multi-phase deformation history (D1, D2, D3, and D4) is recorded in the rock fabrics of both sectors. Intensive penetrative deformation during the early phases and retrograde overprinting during the later phases are common features. These similarities indicate that both regions have been subjected to comparable thermal and pressure regimes during their evolution (Mahadevan, 2002; Bhattacharya, 1976; Banerji, 1991; Sharma, 2009; Ray et al., 2011).

- **Presence of Gneissic Foliation:**

  A well-developed gneissic foliation is a pervasive feature in both the Purulia and Jasidih–Deoghar areas. This foliation, which results from the early intense deformation (D1/D2) and is modified by later events (D3/D4), is observed consistently throughout the CGGC. In both areas, the foliation

serves as a primary structural control on the alignment of other rock units and on the emplacement of syntectonic intrusions.

- **Interlayering and Lithological Diversity:**

  The interlayering of quartzofeldspathic gneisses with amphibolite bands is a prominent characteristic found in both study areas. This interlayering preserves the heterogeneity of the original sedimentary protoliths and records the variations in metamorphic conditions experienced across the complex. Additionally, both areas host similar rock types—including banded or layered gneisses, streaky and augen gneisses, migmatites, pegmatitic veins, and intrusive amphibolite dykes—that reflect the complex interplay of sedimentation, metamorphism, and deformation.

- **Syntectonic Intrusions:**

  In both regions, the emplacement of basic rocks (mafic dykes) and pegmatitic veins during active deformation is well documented. These syntectonic intrusions are aligned with the regional foliation and fold axes, indicating that they were emplaced contemporaneously with the ongoing deformation. Their similar petrographic and mineralogical characteristics in both areas further underscore the shared tectono-metamorphic history.

2.4.4 Dissimilarities between Purulia and Jasidih–Deoghar

- **Lithological Variations:**

  Although both areas share a similar suite of rock types, there are notable differences in their lithological compositions. In the Purulia area, the rock types are dominated by granite gneisses, migmatites, and granites—both

porphyritic and massive varieties—with enclaves of metapelitic and metabasic granulites. In contrast, the Jasidih–Deoghar area is characterized by banded or layered gneisses, streaky gneisses, augen gneisses, and migmatites that are interlayered with amphibolites. The compositional variations in the quartzofeldspathic gneisses of the Jasidih–Deoghar area, which range from granitic and granodioritic to tonalitic types (Ghosh and Sengupta, 1999), differ from the dominantly granitic nature of the Purulia area.

- **Structural Complexity and Deformation Styles:**

  The deformation styles observed in the two regions also display some dissimilarities. In the Purulia area, the structural fabric is significantly influenced by the presence of large granitoid bodies and enclaves of granulites, which add complexity to the overall deformation pattern. In contrast, the Jasidih–Deoghar area exhibits a more uniform banded structure with a pronounced interlayering of amphibolite dykes. Although both areas record four phases of deformation (D1–D4), the intensity and style of deformation—such as the development of hook-shaped folds and the orientation of cross-cutting elements (ranging from 40° to 150°)—may differ slightly, reflecting local variations in the stress field.

- **Extent of Fluid Influence:**

  While fluid infiltration has been a significant factor in both regions, its impact appears to be more pronounced in certain parts of the Jasidih–Deoghar area. This is evidenced by the well-developed migmatitic textures and the prominent presence of leucosomes and melanosomes, which indicate extensive partial melting. In the Purulia area, although migmatites are

present, the overall impact of fluid-assisted metamorphism may be less extensive compared to the Jasidih–Deoghar area.

- **Emplacement of Syntectonic Intrusions:**

  The timing and distribution of syntectonic intrusions also show variations between the two areas. In the Purulia area, granitoids are often emplaced along the axial planes of synformal to antiformal structures and are interpreted as syn-to late-kinematic intrusions with respect to the F2 phase. In the Jasidih–Deoghar area, the mafic dykes and pegmatitic veins are more uniformly distributed and are closely associated with the early phases of deformation, highlighting subtle differences in the magmatic evolution during the tectonic reworking of the region.

2.4.5 Synthesis of the Comparative Study

The comparative study between the Purulia and Jasidih–Deoghar areas illustrates that while both sectors of the CGGC share a common overall tectono-metamorphic history, they exhibit distinct lithological and structural characteristics. These differences can be attributed to variations in the original protolith compositions, local metamorphic conditions, and the intensity and style of deformation. The similarities—such as the pervasive high-grade metamorphism, well-developed gneissic foliation, and the occurrence of syntectonic intrusions—underscore the regional continuity of the CGGC's evolution. In contrast, the dissimilarities in lithological composition, structural complexity, and the extent of fluid influence highlight the localized variability that has resulted from differential tectonic reworking and metamorphic processes.

Understanding these similarities and differences is essential for constructing a comprehensive model of the CGGC's evolution. Both the Purulia and Jasidih–Deoghar areas contribute valuable information that, when integrated, provide a more complete picture of the high-grade metamorphism and multi-phase deformation that have shaped this significant Precambrian terrain.

2.5 Summary

The study area within the Chhotanagpur Granite Gneissic Complex, comprising both the Purulia and Jasidih–Deoghar regions, represents a unique and highly informative segment of eastern India's Precambrian basement. The overall geology is dominated by extensive high-grade metamorphism under amphibolite facies conditions, with localized granulite facies imprints, and has been overprinted by at least four distinct phases of deformation (D1 to D4). The pervasive gneissic foliation, the role of fluid-induced metamorphism, and the occurrence of syntectonic intrusions collectively document the dynamic tectono-metamorphic evolution of the area.

The rock types observed in both regions—banded or layered gneisses, streaky and augen gneisses, migmatites, pegmatitic veins, and intrusive basic rocks in the form of amphibolite dykes—reflect the complex interplay between sedimentation, metamorphism, and deformation. While the Purulia area is characterized by a dominantly granitic suite with associated migmatites and enclaves of granulites, the Jasidih–Deoghar area displays a more varied assemblage of quartzofeldspathic gneisses with distinct interlayering with amphibolites. The subtle differences in

structural fabric and the extent of fluid involvement between the two areas further emphasize the localized variability within a region that shares an overall similar tectonic history.

Chapter 3

Boudinage Structures in Layered Gneissic Rock[1]

[1] *This chapter is based on:* Samanta, S. K., Basu Majumder, D., & Sarkar, G. (2017). Geometry of torn boudin—An indicator of relative viscosity. *Journal of Structural Geology, 104*, 21–30.

3.1 Introduction

Boudinage structures represent a frequently encountered class of features in deformed, layered rocks. They are especially common in settings where adjacent strata display contrasting rheological behaviours and are subjected to layer-parallel extension. In many studies, these structures are exploited as natural strain markers, enabling geologists to estimate finite strain in rocks that have experienced significant deformation. The detailed geometry of an individual boudin – as defined by the configuration of its outer margins when viewed in a profile section – provides key insights not only into the modes of fracture but also into the rheological contrasts between the boudinaged layers and the surrounding host medium (Treagus et al., 1996; Marques et al., 2012; Abe and Urai, 2012).

In natural settings, a wide variety of boudin geometries can be observed. These geometric differences are primarily controlled by factors such as the competence contrast between the layered unit and its embedding host, the nature and style of the deformation, and the degree of plastic deformation that occurs from the pre- to the post-boudinage stage (Ramberg, 1955; Wilson, 1961; Ramsay, 1967; Strömgård, 1973; Ghosh and Ramberg, 1976; Lloyd and Ferguson, 1981; Treagus et al., 1996; Ghosh and Sengupta, 1999; Treagus and Lan, 2000, 2004; Passchier et al., 2005; Maeder et al., 2009; Fossen, 2010; Samanta and Deb, 2014). Moreover, the angular relationships that exist between the layering and the axes of deformation (kinematic axes) also have a pronounced effect on the observed boudin shapes (Goldstein 1988, Passchier and Druguet 2002).

Following the fragmentation of a relatively stiffer layer, the intervening zones between individual boudins—the inter-boudin zones—are typically infilled by

material from the host rock, or by siliceous or calcareous substances that behave in a softer manner than either the boudin or the surrounding matrix under the prevailing geological conditions. During subsequent stages of deformation, when the inter-boudin material is present, an originally rectangular boudin may progressively evolve into a form with curved margins. This evolution can yield boudins exhibiting concave faces along with bi-convex exterior margins. Such forms have been variously described as ‘barrel-shaped’ boudins (Lloyd and Ferguson, 1981), ‘extreme barrel-shaped’ boudins (Lloyd et al., 1982), and even as ‘fish-mouth’ or ‘false-isocline’ boudins (DePaor et al., 1991; Swanson, 1992). In other cases, the resulting geometry may lead to ‘fish-head’ boudins (Wegmann, 1932; Ghosh and Sengupta, 1999).

In these situations, changes in the composition of the boudin, the inter-boudin, and the surrounding matrix can occur as a result of metamorphism, migmatization, or fluid–rock chemical reactions (Ray et al., 2011). These processes have the potential to alter the relative viscosities of the various components. Consequently, a boudin may exhibit behaviour that is mechanically “incompetent” relative to both the matrix and the inter-boudin materials. The outcome is the development of a ‘bone-shaped’ boudin, characterized by concave exterior margins and face margins that are either straight or only weakly convex (Malavielle and Lacassin, 1988; Swanson, 1992). The impact of such rheological variations on the sequential development of boudins has been documented in natural examples (Ghosh and Sengupta, 1999; Ray et al., 2011) and has been further investigated through analogue and numerical modeling approaches (Druguet and Carreras, 2006; Samanta and Deb, 2014).

It is worth noting that similar boudin-type structures can form during subsequent phases of layer-parallel shortening or extension. In these cases, a single layer—segmented by veins that cut perpendicularly to the layer (whether these veins are generated by the boudinage process itself or through hydraulic fracturing)—may evolve into structures that have been described as shortened torn boudins. These include variants such as ‘double-sided mullions’ or those with an ‘extreme convex surface’, as well as bone-shaped structures often termed ‘dog-bones’ or ‘trapezoidal boudins’ (Kenis et al., 2002; Goscombe et al., 2004).

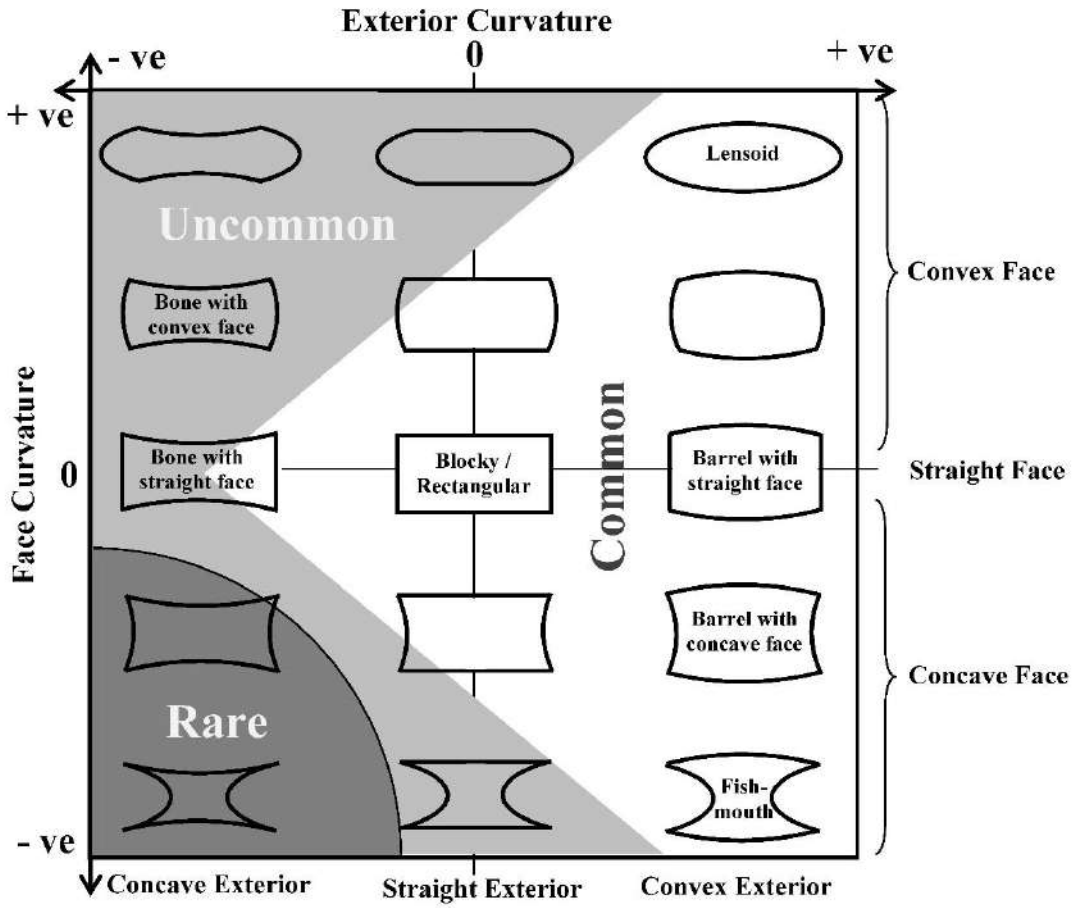

Fig. 3.1: Types of common symmetric boudins and their positions with respect to their face and exterior curvature. +ve and –ve indicate the convex and concave curvature respectively.

Torn boudins are defined as symmetric boudins that form as a result of the segmentation of a layer by high-angle, sharp, and ostensibly 'brittle' failure planes. Although the classic image of a torn boudin is that of an angular, blocky object with parallel edges, field observations indicate that these objects frequently undergo internal deformation after fragmentation. Such post-fracture modifications often lead to boudins with curved exterior or face margins (Fig. 3.1). In a comprehensive study, Goscombe et al. (2004) classified torn boudins into two primary groups: straight-face boudins and concave-face boudins. The subdivision is based on natural observations drawn from a diverse array of geological settings worldwide.

Within the straight-face category, further subdivisions have been proposed. These include blocky boudins (which maintain parallel margins), bone-type boudins (which are defined by concave exterior margins), and straight-face boudins that feature vein infill. Blocky boudins are often alternatively described as rectangular, extension fracture, or rectilinear boudins. In these cases, the boudin faces are typically arranged at a high angle and are nearly orthogonal to the original boudinaged layer (Lloyd and Ferguson, 1981; Lloyd et al., 1982; DePaor et al., 1991; Mandal et al., 2000; Zulauf et al., 2009). In contrast, concave-face boudins are further subdivided into those termed bow-tie vein boudins and barrel boudins. With increasing finite strain, barrel boudins may transform into forms that are recognized as fish-mouth, fish-head, or even lensoid-shaped boudins. This classification relies on the degree and nature of curvature of both the boudin's exterior and face margins, which can be straight, convex, or concave (Fig. 3.2). Notably, in this classification scheme the geometries of barrel and bow-tie boudins are essentially identical except for the specific configuration of the inter-boudin material. Likewise, the geometries of blocky boudins and straight-face boudins with vein infill are similar, differing

primarily in the presence or absence of inter-boudin material. Thus, in the present study, all symmetric boudins that display combinations of straight, convex, and concave margins are considered to be examples of torn boudins. While not all types of torn boudins are common, concave-face boudins are observed frequently in nature. On the other hand, torn boudins with a convex face are extremely rare (comprising less than 5% of the investigated torn boudins in Goscombe et al., 2004), and when they do occur the degree of convexity is minimal.

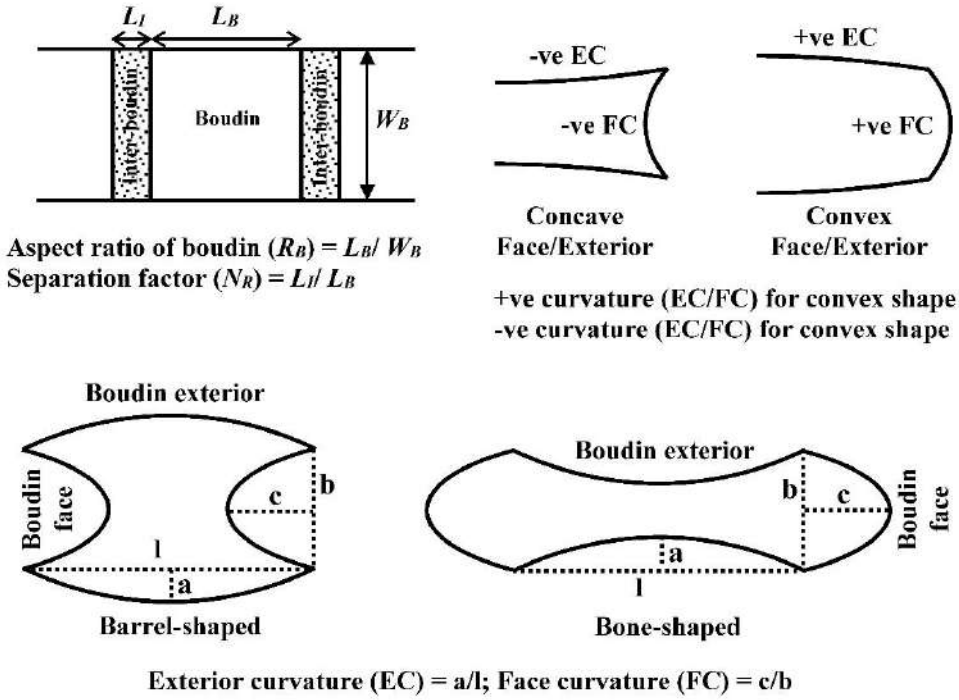

Fig. 3.2: Geometrical parameters of symmetric boudin block. L_B- length of boudin, W_B- width of boudin, L_I- length of inter-boudin, Aspect ratio of boudin (R_B) = L_B/ W_B, Separation factor (N_R) = L_I/ L_B,.

For several decades, the shapes of boudinage structures and their progressive evolution under deformation have been the subject of intensive research. Early work by Selkman (1978) involved stress and displacement analyses that sought to understand the influence of deformation on boudin shapes. Subsequent numerical experiments by Lloyd and Ferguson (1981) employed elastic-plastic rheologies to explore how material properties and deformation magnitudes affect the boudin

geometry. Later studies by Treagus et al. (1996) and Treagus and Lan (2000) examined in detail the effect of the viscosity ratio between a boudin object and its surrounding matrix under the assumption that both behave as Newtonian fluids. They demonstrated that an isolated square object would deform into a 'barrel-shape' when its viscosity exceeds that of the embedding medium, or into a 'bone-shape' when it is relatively less viscous. Further extensions of the study incorporated power-law rheology with varying power-law stress exponents (Treagus and Lan, 2004). Nevertheless, these earlier models did not perfectly capture the natural arrangement in which square or rectangular boudins occur in rows separated by inter-boudin areas of dissimilar material.

In a later study, Kenis et al. (2006) used Finite Element Method (FEM) analysis to simulate various bone- and barrel-shaped objects. Their models considered volume-constant, steady-state power-law creep rheology and varied key parameters such as the viscosity ratio between the host rock and the vein-infill material, the initial aspect ratio of the host-rock segments between veins, and the overall magnitude of finite deformation. Despite the extensive research in this field, no previous work has explicitly addressed the effect of the relative viscosity of the inter-boudin material on the shape of torn boudins. The present study is designed to fill that gap by investigating how viscosity ratios among the boudin, the matrix, and especially the inter-boudin materials affect the post-fracture evolution of a rectangular torn boudin. The ultimate aim is to use the geometry of these objects to estimate the relative viscosities among the boudin, inter-boudin, and matrix materials. By employing two-dimensional finite element modelling as well as analogue modelling under pure shear conditions, we demonstrate that a boudin object, when surrounded by a matrix and inter-boudin material of contrasting

viscosity, evolves into a variety of shapes with curved margins. This evolution is driven by the mutual interaction of material flow within the boudin, the inter-boudin, and the matrix regions.

3.2 FEM Modeling

3.2.1 Model Considerations

The progressive evolution of torn boudins is an inherently complex process that is influenced by a multitude of independent parameters. Among these are the aspect ratio of the boudin (denoted as R_B) following the fragmentation of the layer, the rheological contrast between the boudin and the matrix, the length of the inter-boudin zones, and the rheological properties of the infill material. In addition, the overall nature of the bulk deformation also plays a significant role (Passchier and Druguet, 2002; Dabrowski and Grasemann, 2014). In the present study, however, our focus is confined to exploring the effect of the viscosity ratio, which has been identified as a key control on the development of different torn boudin shapes.

Our modeling approach begins by considering the rheological state of the boudin at the moment when the competent layer has already been segmented into discrete boudin objects by the propagation of extension fractures (Ramberg, 1955; Lloyd et al., 1982). Although the fragmentation process has traditionally been studied through both theoretical and numerical analyses that assume elastic material behaviour (Hobbs, 1967; Lloyd and Ferguson, 1981; Lloyd et al., 1982; Masuda and Kuriyama, 1988; Ji et al., 1997; Ji and Saruwatari, 1998), natural observations indicate that boudin blocks continue to deform after their initial separation (Weiss,

1972; Lloyd and Ferguson, 1981; Ramsay and Huber, 1983; Hanmer and Passchier, 1991; Carreras and Druguet, 1994). This post-boudinage deformation is interpreted as a form of plastic deformation driven by strain softening, which may be induced by processes such as migmatization or fluid–rock chemical reactions during subsequent deformation (Lloyd and Ferguson, 1981; Ghosh and Sengupta, 1999; Passchier and Trouw, 2005; Ray et al., 2011). The transition from a brittle, elastic behaviour to a visco-elastic response is thus manifest in the evolving shape of the torn boudin.

An important geometric consideration in our model is that the exterior and face curvatures of the boudin are inversely proportional to the length (L_B) and width (W_B) of the boudin, respectively (see Fig. 3.2). To facilitate a direct comparison of these curvatures, we adopt an initial aspect ratio for the boudin block defined as $R_B = L_B / W_B$ (Fig. 3.2), and for many simulations, this ratio is set to 1. According to Goscombe et al. (2004), the average aspect ratio of naturally occurring torn boudins is approximately 2.9. However, this ratio is often the result of internal deformation processes. In order to verify the influence of the initial aspect ratio on the subsequently modified geometry, additional simulations were conducted with initial aspect ratios of 2 and 3 in selected cases.

The evolution of boudin shape commences immediately following the fragmentation of the layer, particularly when the resulting fractures become filled with matrix or vein materials, or when the boudin material itself undergoes rheological changes due to metamorphic reactions in the presence of an adequately infilled inter-boudin zone (Ray et al., 2011). Because it is challenging to simulate the continuous growth and filling of inter-boudin areas during progressive deformation, our models approximate the situation by simulating newly formed boudins with

small, well-defined separation zones. The dimensions of these inter-boudin zones are described by the separation factor, defined as $N_R = L_I / L_B$ (see Fig. 2.2 and Passchier and Druguet, 2002). For the majority of our models, N_R is chosen to be 0.25, meaning that the initial length of the separation zone (L_I) is one-fourth of the initial length of the boudin block. To investigate the sensitivity of our results to this parameter, additional experiments were performed with N_R values of 0.5, 0.125, and 0.0625. In line with previous numerical models, the areas of the inter-boudin zones are held constant throughout the study; that is, the inter-boudin material is assumed to be stretched in a layer-parallel fashion without any change in its overall area (Passchier and Druguet, 2002; Arslan et al., 2008; Samanta and Deb, 2014). Although this assumption does not perfectly replicate natural conditions, it does serve to highlight the significant role that the rheology of the inter-boudin material plays in the development of torn boudins with varied geometries.

3.2.2 Constitutive Equation

To elucidate the control that viscosity ratio exerts on the shape of a boudin object, we performed two-dimensional numerical modeling using the Finite Element Method (FEM) (Lloyd and Ferguson, 1981; Ramsay and Lisle, 2000; Treagus and Lan, 2004). Consistent with the approach adopted by earlier researchers, we incorporated a visco-elastic Maxwell rheology into our modeling framework (Zhang et al., 1996; Mancktelow, 1999; Passchier and Druguet, 2002; Arslan et al., 2008, 2012; Samanta and Deb, 2014). The constitutive equation for this Maxwell rheology is given by

$$\frac{d\varepsilon}{dt} = \frac{1}{\mu}\frac{d\sigma}{dt} + \frac{\sigma}{\eta}, \qquad (1)$$

where ε and σ represent the instantaneous strain and stress, respectively, and μ and η denote the Maxwell shear modulus and the viscosity, respectively. This type of rheological formulation is particularly appropriate for simulating deformation in the lower crust, where high temperatures and confining pressures result in behaviour that closely approximates that of a Maxwell visco-elastic material (Turcotte and Schubert, 1982).

For our numerical experiments, we used ANSYS (commercial FEM code, ver. 10.0) to prepare models within the structural mechanics module under a multiphysics domain. In our simulations, we selected the 'VISCO88' element, which is a quadratic (in terms of its shape functions) isoparametric element defined by eight nodes, with each node possessing two degrees of freedom (U_x and U_y). This element is widely used in two-dimensional modeling scenarios that involve Maxwell visco-elastic rheology in ANSYS, thereby providing a robust platform for our investigations.

3.2.3 Model Geometry, Meshing and Boundary Conditions

Our numerical model considers a boudinaged layer that is comprised of a series of boudin objects (designated as A1) and inter-boudin objects (designated as A3), all of which are embedded in a matrix material (labelled A2). The overall dimensions of the matrix are taken to be ten times larger than those of an individual boudin object (see Fig. 3.3a). To facilitate the analysis and measurement of

geometrical parameters, we focus our attention on the shape of a central boudin block, which is delineated by dotted lines in Fig. 3.3a.

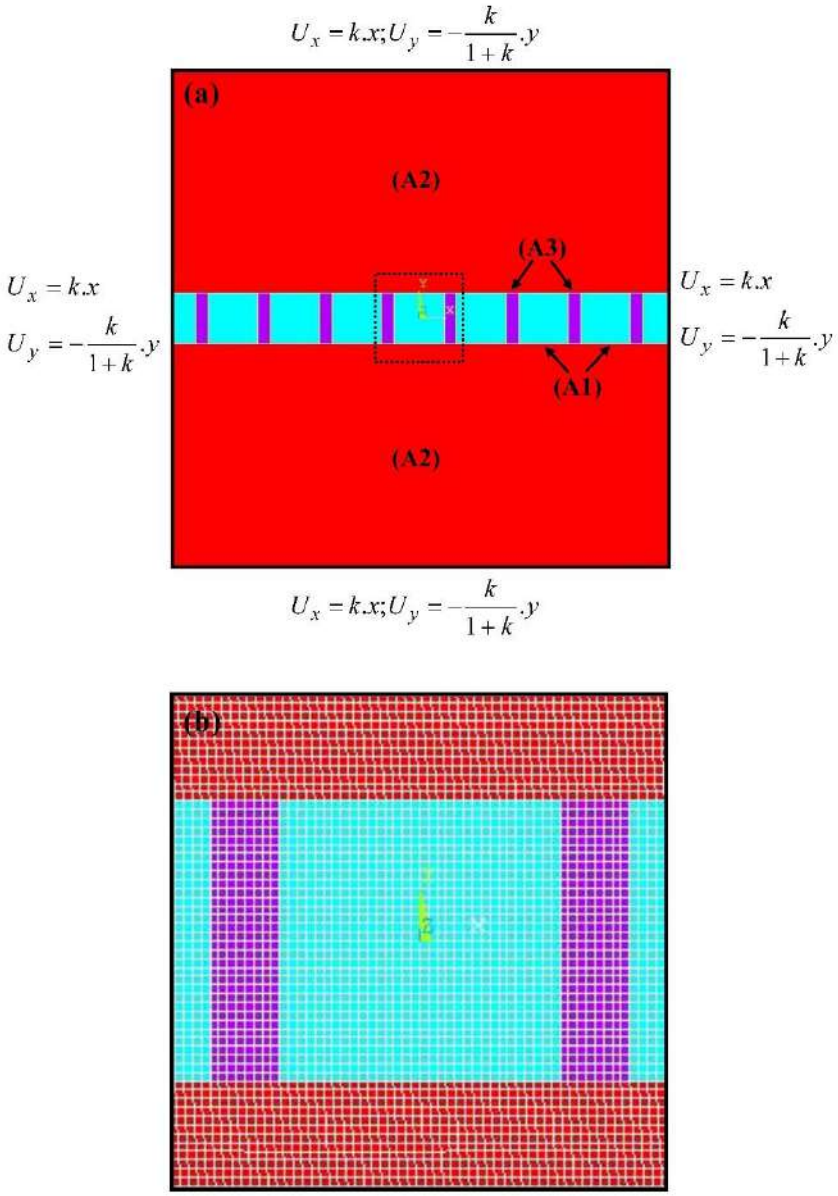

Fig. 3.3: (a) Model geometry considered in numerical simulation with separation factor (N_R) 0.25. A1- Boudin, A2- Matrix and A3- Inter-boudin. Note that pure shear flow conditions were imposed at four boundaries of the model. U_x and U_y is the displacement along X- and Y- axis respectively. k is the percentage of shortening. (b) Enlarged central square area (dotted lines of the above figure) with quadrilateral meshing.

For the purposes of modeling, we employed a free mesh technique—a method that is commonly used to discretize geometries of arbitrary shape—using a quadrilateral mesh in which the shape and size of individual elements can vary

spatially (Fig. 3.3b). In the central boudin block, the mesh consists of 3201 nodes and 1024 elements. The simulation run time was adjusted so that the strain rates achieved fell within the range of 10^{-7} s^{-1}, ensuring that the results were both convergent and representative of realistic geological deformation. The chosen mesh density and element configuration provided optimal results for the run time employed in the experiments.

The deformation in our models is imposed under pure shear conditions, which is quantified by a kinematic vorticity number, W_k, set to 0. This deformation is applied via displacement boundary conditions on all four boundaries of the model according to the following equations,

$$U_x = k.x \qquad (2)$$

$$U_y = -\frac{k}{1-k}.y \qquad (3)$$

where *k* represents the percentage of shortening in decimal. In these models, special attention is given to the deformation and resulting geometry of the central rectangular boudin block, ensuring that it is unaffected by boundary influences. Each simulation is carried out up to a maximum of 45% shortening, achieved in incremental steps of 7.5% shortening applied at the model boundaries. The coordinates of specific nodes within the central boudin block are recorded at each step, and the distances between these nodes are used to calculate both the exterior and face curvatures of the boudin.

3.2.4 Material Properties

Geological studies have shown that over geologic time scales, materials in the lower crust tend to behave similarly to a Maxwell visco-elastic substance, with viscosities ranging from 10^{17} to 10^{23} Pa s (Vergnolle et al., 2003; Copley and McKenzie, 2007; Mukherjee, 2013). Because our study is specifically aimed at determining how viscosity ratios influence boudin shapes, we have chosen seven distinct material viscosities. These viscosities were selected arbitrarily but constrained to lie within the range of values observed in natural settings (Table 3.1).

Table 3.1. Values of physical properties of Maxwell viscoelastic materials considered in the finite element modeling

Area	Viscosity (Pa s)	Viscosity ratio (η_{BM} or η_{IM})	Shear modulus (Pa)	Bulk modulus (Pa)	Relaxation time (s)	Poisson's ratio (ν)
Matrix	1×10^{19}		1.25×10^{10}	2.083×10^{10}	8×10^{8}	0.25
Boudin or Inter-boudin	1×10^{18}	0.1	1.25×10^{9}	2.083×10^{9}		
	2.5×10^{18}	0.25	3.12×10^{9}	5.208×10^{9}		
	5×10^{18}	0.5	6.25×10^{9}	1.042×10^{10}		
	1×10^{19}	1	1.25×10^{10}	2.083×10^{10}		
	2×10^{19}	2	2.50×10^{10}	4.167×10^{10}		
	5×10^{19}	5	6.25×10^{10}	1.042×10^{11}		
	1×10^{20}	10	1.25×10^{11}	2.083×10^{11}		

In our experiments, the bulk modulus and shear modulus for each material were calculated using a Poisson's ratio of 0.25. Furthermore, the Maxwell relaxation time was consistently set at 8×10^{8} s for all materials, following the precedent established by Larsen et al. (2005). The viscosity of the matrix material was fixed at 10^{19} Pa s for all experiments. A total of forty-nine experiments were performed by interchanging the material properties between the boudin and the inter-boudin zones.

In these experiments, the viscosity ratios are defined as follows: the ratio of the viscosity of the boudin to that of the matrix (denoted η_{BM}) and the ratio of the viscosity of the inter-boudin material to that of the matrix (denoted η_{IM}). Both of these ratios were varied over the following set of values: 0.1, 0.25, 0.50, 1, 2, 5, and 10.

3.2.5 Results of Numerical Simulation

The numerical simulations produced values for both the face curvature and the exterior curvature of the boudins, and these values were plotted against the inter-boudin to matrix viscosity ratio (η_{IM}) (Figs. 3.4a and 3.4b). These graphs were constructed for a range of boudin to matrix viscosity ratios (η_{BM}), demonstrating that the boudin's shape is not solely dependent on the viscosity contrast between the boudin and the matrix. Rather, the relative viscosity of the inter-boudin material plays a significant role in shaping the boudin during subsequent deformation.

When the boudin material is more competent than the inter-boudin material, the numerical results indicate that the exterior margin of the boudin adopts a convex geometry, while the face margin becomes concave (Fig. 3.5). In contrast, if the boudin material is softer than the inter-boudin, the senses of curvature are reversed. As the inter-boudin to matrix viscosity ratio is increased, the initially concave face curvatures tend to transform into convex geometries, and the exterior curvature shifts from a convex to a concave shape (for example, see the case where $\eta_{BM} = 1$ in Figs. 3.4a and 3.4b). Notably, the face curvatures exhibit their maximum variation at lower values of the inter-boudin to matrix viscosity ratio, and then tend toward a steady

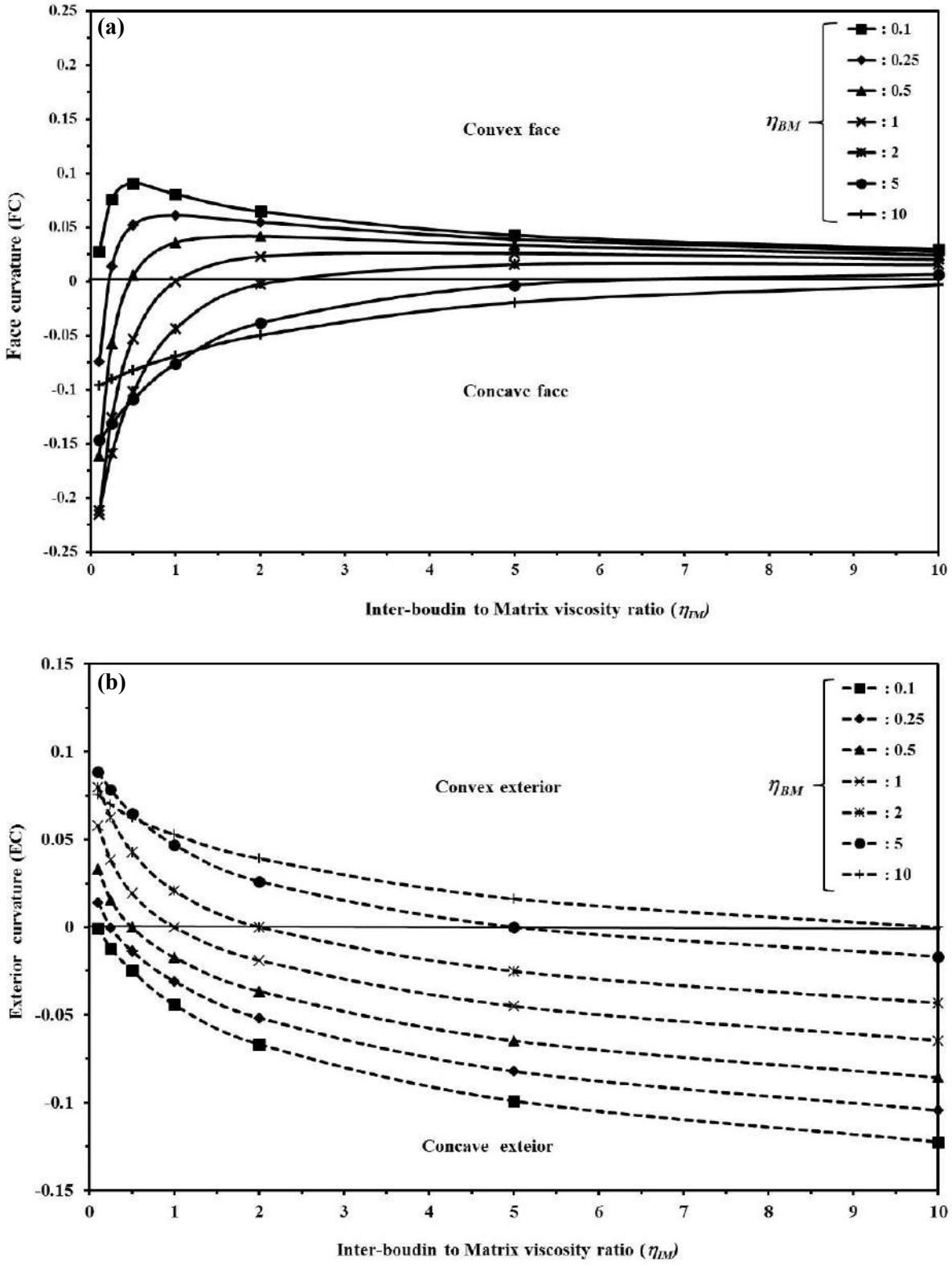

Fig. 3.4: (a) Variations of boudin face curvature (solid lines) with increasing inter-boudin to matrix viscosity ratio (η_{IM}) for different boudin – matrix viscosity ratio (η_{BM}). (b) Variations of boudin exterior curvature (dashed lines) with increasing inter-boudin to matrix viscosity ratio (η_{IM}) for different boudin – matrix viscosity ratio (η_{BM}). Shortening percentage = 45 %.

state as the ratio increases further. In all cases, the magnitude of the concave curvature is greater than that of the convex curvature. Moreover, when the viscosities of the boudin and the inter-boudin are equal, the exterior curvature nearly vanishes, regardless of the matrix viscosity (Figs. 3.4b and 3.5).

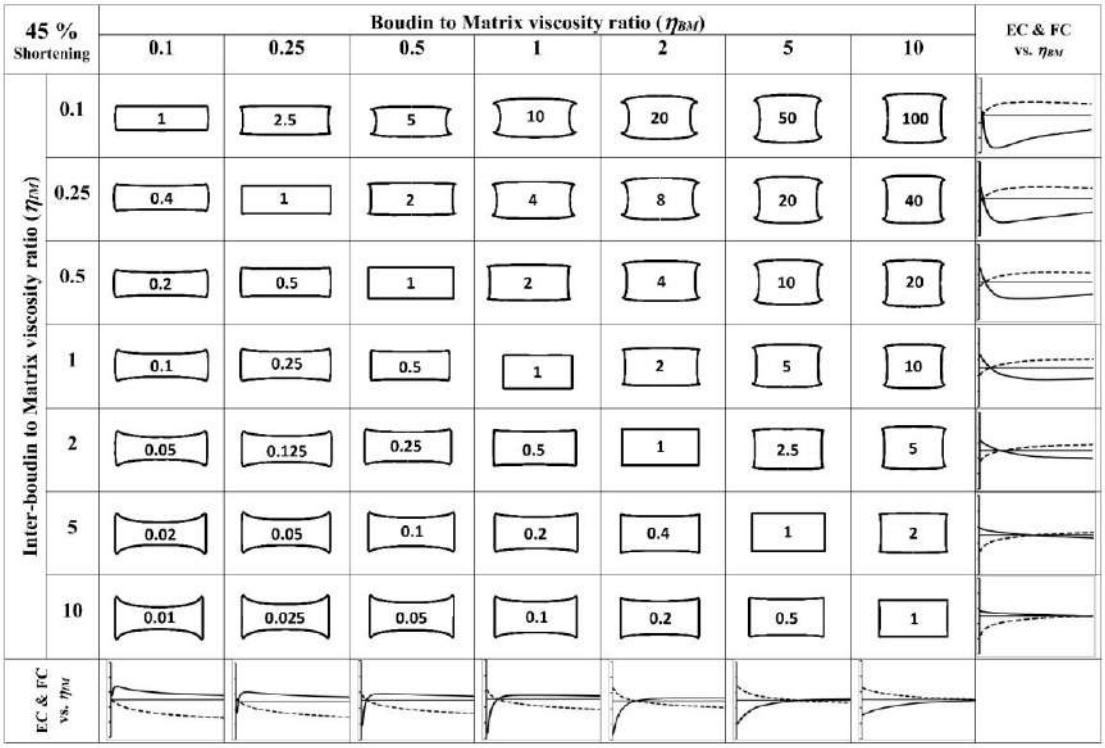

Fig. 3.5: Geometries of torn boudins obtained from FEM simulation for different viscosity ratios (η_{IM} and η_{BM}). The numerical value within the individual boudin block indicates ratio of boudin and inter-boudin viscosity (η_{BI}). The graphs at the end of row and column represent the change of exterior (dashed lines) and face curvature (solid lines) in respective row and column. Maximum and minimum values of curvature along Y-axis are 0.25 and -0.25 respectively in all graphs. Shortening percentage = 45%.

Additional numerical results indicate that significant curvature of the exterior margins only develops when there is a pronounced viscosity contrast between the boudin and the inter-boudin (Fig. 3.5). For any given matrix viscosity, boudins that develop a convex exterior margin combined with a concave face occur only when the boudin is more competent than the inter-boudin. Conversely, when the boudin material is considerably softer than the inter-boudin, the face and exterior margins

exhibit opposite curvature senses. For cases where the viscosity ratio of boudin to inter-boudin (η_{BI}) is much greater than 1, both the exterior and face margins exhibit strong curvature. However, if η_{BI} is less than 1, the exterior margins develop a pronounced concave curvature while the face curvature shows only minor convexity. With an increasing boudin to matrix viscosity ratio (η_{BM}), the geometry of the exterior margin gradually shifts from concave to convex, and the face margin correspondingly changes from convex to concave. This evolution results in a transition in boudin geometry from a bone- to a barrel-shaped form (Figs. 3.4 and 3.5). A similar change in geometry is observed if the inter-boudin to matrix viscosity ratio (η_{IM}) is progressively decreased for a fixed boudin to matrix viscosity ratio (η_{BM}). In the limiting case where there is very little or no viscosity contrast between the boudin and inter-boudin materials, the boudin retains an almost rectangular shape (Figs. 3.4a and 3.5), although the aspect ratio of the boudin increases if the viscosity of both the boudin and inter-boudin decreases relative to the matrix.

3.3 Analogue Modelling

To validate and complement the pure-shear boudinage patterns predicted by the finite-element simulations (Section 3.2), a series of analogue experiments were carried out using scaled physical models. A rigid frame constrained the model block (20 cm × 15 cm × 5 cm) to deform under homogeneous extension imposed at its lateral boundaries, thereby reproducing the displacement-controlled pure-shear conditions of the numerical models under plain strain condition. Within the model volume, a central, competent square inclusion (4 cm × 4 cm) was flanked on either

side (along the extension axis) by two less-competent rectangular inclusions (2 cm × 4 cm each), as illustrated in Fig. 3.6.

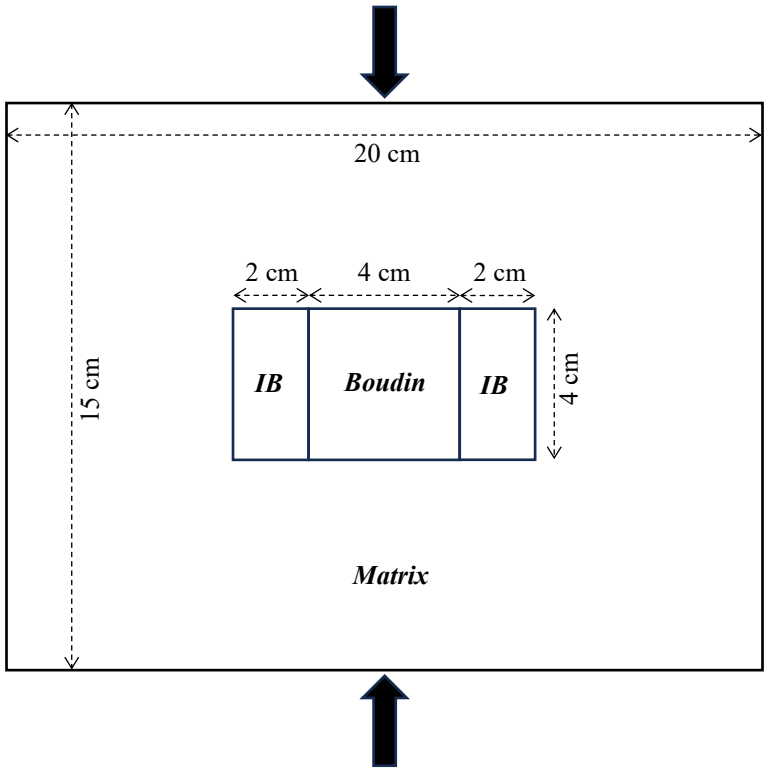

Fig. 3.6: Schematic diagram of the analogue model configuration. A 20 cm × 15 cm × 5 cm block is deformed under displacement-controlled pure-shear boundary conditions. Within the block, a central, square boudin (4 cm × 4 cm) is flanked on either side along the extension axis by two rectangular inter-boudins (2 cm × 4 cm each).

To systematically explore the effect of material rheology on boudin shape, three analogue media were selected—glass putty (GP), plasticine (P) and hand-putty (HP) —whose viscosities decrease in that order. Each experiment imposed a total bulk shortening of 30 per cent, applied at a constant rate of 1 mm min^{-1} to ensure quasi-static deformation and minimize dynamic effects. Six experiments were performed in total, combining the three rheological contrasts with two initial inclusion configurations (central boudin stiffer or softer than inter-boudins).

3.3.1 Results of Analogue Modelling

The deformation geometries and axial strain distributions recorded via time-lapse photography are compiled in Fig. 3.7 and quantified in Table 3.2. Although analogue models cannot capture the full range of subtle stress-field variations accessible to FEM, they reproduce the principal curvature trends and strain-partitioning behaviours predicted numerically.

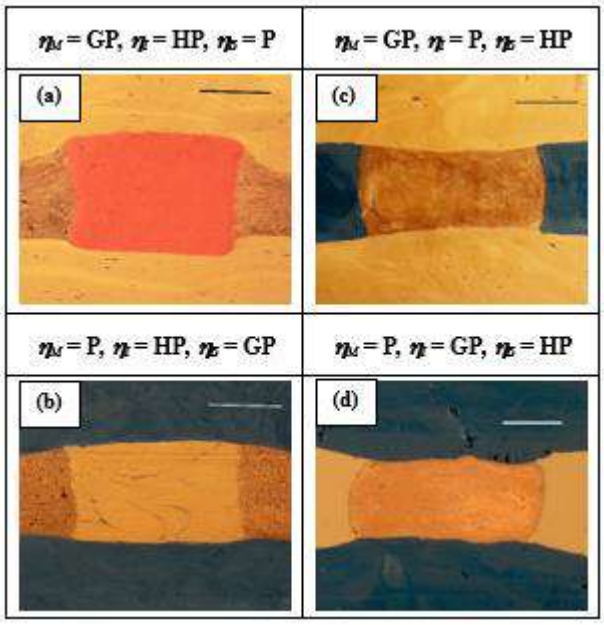

Fig. 3.7: Results of analogue experiments showing boudin geometry as a function of competence contrast after 30% bulk shortening (Scale bar: 2 cm). Panels (a, b) illustrate barrel-shaped boudins obtained when the central inclusion is more competent than the inter-boudins, with convex outer margins and concave inner margins. Panels (c, d) display bone-shaped boudins formed when the central inclusion is mechanically weaker, reversing the curvature sense. Measured curvature radii and normalized strain profiles closely match the patterns predicted by the corresponding FEM simulations.

Barrel-shaped boudins (Fig. 3.7a, b) develop when the central inclusion is more competent than its neighbouring inter-boudins. In these runs, the outer (extension-facing) margins arch outward, while the inner margins bend inward toward the weaker inter-boudins, producing the characteristic barrel profile.

Bone-shaped boudins (Fig. 3.7c, d) emerge when the central inclusion is mechanically weaker than the flanking inter-boudins. Here, the outer margins sag

inward under tension, and the inner margins bow outward, inverting the curvature sense.

Table 3.2: Analysis of geometry from analogue modelling (Fig. 3.7)	
$\eta_M > \eta_B > \eta_I$	$\eta_M > \eta_I > \eta_B$
Barrel shape	Bone shape
$\eta_B > \eta_M > \eta_I$	$\eta_I > \eta_M > \eta_B$
Barrel shape	Bone shape

In all analogue runs, strain localization initiates at inclusion interfaces and propagates symmetrically, validating the assumption of uniform stress application in the FEM framework. Minor end effects manifested as slight asymmetries near the rigid walls and did not influence the central boudin shapes. Overall, the close correspondence between physical and numerical models underscores the robustness of the pure-shear approximation in predicting boudinage style across a realistic range of competence contrasts.

3.4 Discussions

3.4.1 Role of Viscosity

The outcomes of the numerical experiments suggest that the curvatures at the interfaces—both between the boudin and the inter-boudin (face margin) and between the boudin and the matrix (exterior margin)—are not independent. Instead, they are modified by the mutual interaction of material flow in the boudin, inter-boudin, and matrix regions. The results clearly indicate that following the fragmentation of a boudinaged layer, the viscosity contrast between the boudin and the matrix is not the

sole parameter controlling the final boudin shape; the viscosity of the inter-boudin material also plays a critical role in subsequent deformation.

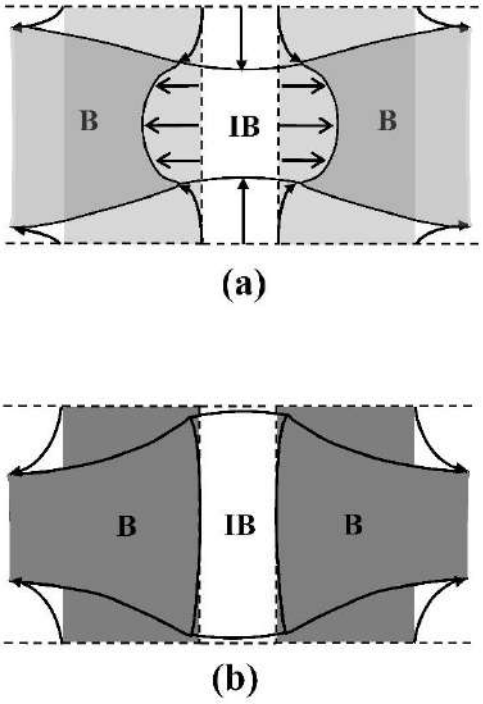

Fig. 3.8: Differential flow of boudin and inter-boudin material during deformation.
(a) Inter-boudin is softer than boudin resulting barrel- or fish-head shaped boudin and (b) Boudin is softer than inter-boudin resulting bone-shaped boudin. Arrows indicate the flow of material. Note that the boudins (shaded) shown at both sides of the inter-boudin (unshaded) are half of the length of boudin.

The curvature of the boudin face is primarily dependent on the differential lateral flow of boudin material along the face margin (Figs. 3.8a & 3.8b). This lateral flow is largely controlled by the amount of traction exerted by the surrounding matrix on the exterior surface of the boudin, in conjunction with the flow characteristics of the inter-boudin material (Mandal et al., 2000). Under conditions of layer-parallel extension, both the inter-boudin and boudin materials are mobilized laterally. In such a scenario, a more competent (harder) material tends to resist internal flow, thereby inhibiting the lateral movement of adjacent softer material. As

a result, the interface geometry between the harder and softer materials is determined by the balance between these two opposing flows. The boudin face becomes concave only if the inter-boudin material is relatively softer, allowing the boudin material to flow laterally towards the centre of the boudin (Fig. 3.5, 3.6).

In a similar vein, the geometry of the exterior margin is not governed solely by the viscosity ratio of the boudin to the matrix (η_{BM}). For instance, if the boudin is ten times softer than the matrix, the exterior margin may exhibit a range of geometries—from nearly straight to highly concave—depending on the viscosity ratio between the boudin and the inter-boudin (η_{BI}). Maximum concavity is achieved when the boudin material is significantly softer than the inter-boudin, and the curvature increases as the boudin to inter-boudin viscosity ratio (η_{BI}) decreases. Conversely, if there is no viscosity contrast between the boudin and the inter-boudin, the exterior margin remains nearly straight. However, if the inter-boudin material is softer than the boudin for any given matrix viscosity, the exterior margin adopts a convex shape.

In general, barrel- and bone-shaped boudins are believed to form when the boudin behaves in a more competent or more incompetent manner relative to the matrix, respectively (Treagus et al., 1996; Treagus and Lan, 2000, 2004). Under conditions of high finite strain, a fish-head boudin may evolve from an initially barrel-shaped boudin with a concave face, particularly when the inter-boudin material is considerably softer than the boudin. Treagus et al. (1996) noted that if there is no rheological contrast between the boudin and the matrix, both the exterior and face margins tend to remain straight. Nonetheless, under such conditions, both barrel- and bone-shaped boudins may still form in the presence of inter-boudin

materials (Fig. 3.5, column with η_{BM} = 1). Field studies have often interpreted concave-face boudins as resulting from a boudin that behaves incompetently relative to the inter-boudin (Ghosh and Sengupta, 1999). However, the present study reveals that if the boudin is softer than the inter-boudin, the face curvature will be only slightly convex while the exterior curvature becomes concave. Consequently, the development of a concave face curvature effectively inhibits the formation of a concave exterior margin. In other words, it is kinematically unfeasible to produce a boudin with both concave face and concave exterior margins simultaneously, which helps explain why such shapes are rarely observed in nature (fig. 4d of Goscombe et al., 2004). According to our analysis, bone-shaped boudins can only be produced when the inter-boudin is more competent than both the boudin and the matrix. Furthermore, the curvature of a convex face is consistently lower than that of a concave exterior margin. These findings are in agreement with the numerical modelling results presented by Maeder et al. (2009).

It should also be noted that in natural settings, boudins rarely exhibit behaviour where they are more incompetent than the inter-boudin material. Such conditions are typically associated with a rheological inversion of the boudin–matrix system (Ghosh and Sengupta, 1999) or occur in situations where stiffer veins develop within a series of perpendicular fractures in an otherwise relatively softer medium (Kenis et al., 2004; fig. 3, Kenis et al., 2006). In our numerical experiments, lensoid boudins characterized by both convex face and convex exterior margins were not directly simulated. In nature, lensoid-shaped boudins are thought to arise from the stretching of pinch-and-swell structures (referred to as ‘Tapering boudin’ in Goscombe et al., 2004; ‘lenticular’ boudins in Lloyd et al., 1982; and ‘stretched layer’ in Lacassin, 1988) or as a result of extreme modification of barrel-shaped

boudins (Wegmann, 1932). Similarly, the development of barrel-shaped boudins with straight faces is associated with pre-boudinage plastic deformation, a process that falls outside the scope of the present study.

The shape of individual boudins is frequently used in the field to qualitatively assess the viscosity contrast between the boudin and the matrix. However, before any definitive conclusions regarding the rheological contrast can be drawn, it is essential to verify whether subsequent deformation has occurred through independent field evidence. For example, rectangular boudins with straight margins are often interpreted as a consequence of an extremely high boudin-to-matrix viscosity ratio, regardless of whether subsequent deformation is present. In nature, though, both the face and exterior margins may remain straight during further deformation if the boudin-to-inter-boudin viscosity ratio is negligible, irrespective of the matrix viscosity. In such cases, while the overall aspect ratio of the boudin may remain nearly unchanged in the former scenario, it tends to increase in the latter scenario as the matrix viscosity becomes relatively higher compared to that of the boudin and the inter-boudin (compare the shape of the upper left position to the lower right position of Fig. 3.5).

3.4.2 Effect of Separation Factor and Aspect Ratio of Boudin

In the numerical models presented here, the initial length of the inter-boudin separation zone (L_I) was fixed at one fourth of the boudin length, corresponding to a separation factor of $N_R = 0.25$. To further assess the influence of the initial inter-boudin separation zone on the evolving geometry, a series of experiments were

conducted in which N_R was varied. Specifically, two sets of experiments were carried out: one with a relatively higher separation factor (N_R = 0.5) and another with lower separation factors (N_R = 0.125 and 0.0625), for various boudin-to-matrix viscosity ratios (η_{BM}). In the first series of experiments, the inter-boudin material was assumed to be softer than the matrix ($\eta_{IM} < 1$), while in the second series, the matrix was assumed to be softer than the inter-boudin ($\eta_{IM} > 1$). The numerical results clearly indicate that variations in the initial length of the inter-boudin separation zone have only a minimal effect on both the exterior and face curvatures (Figs. 3.9a and 3.9b). The variations in these curvature values remain within the range of a few hundredths. Furthermore, for cases where η_{BM} is relatively high, the influence of the inter-boudin separation length is almost negligible when the inter-boudin is softer than the matrix.

In addition to the separation factor, we also explored the impact of the initial aspect ratio of the boudin object (R_B) on its modified geometry. A series of experiments were executed for different boudin-to-matrix viscosity ratios (η_{BM}), while keeping the inter-boudin-to-matrix ratio (η_{IM}) constant at 0.5. In these models, the boudin length was incrementally increased while the boudin width was held constant. Overall, the results indicate that as the boudin length increases, the exterior curvature tends to decrease, whereas the face curvature shows an increase (Figs. 3.10a and 3.10b). The maximum variation in the face curvature was found to be approximately 0.175, whereas the exterior curvature exhibited only a negligible change. Importantly, the sense of the curvatures remains unchanged regardless of the boudin's aspect ratio.

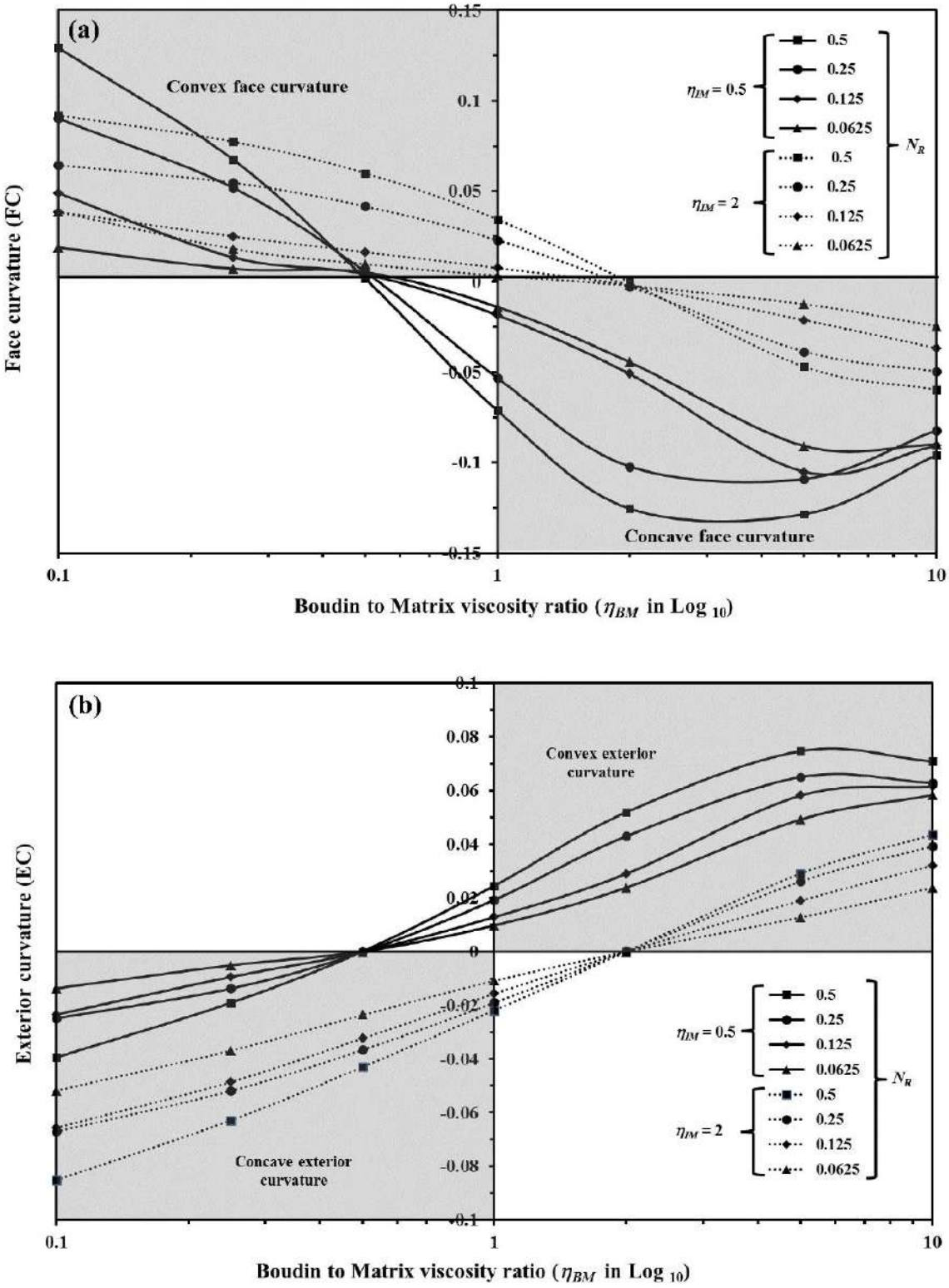

Fig. 3.9: Effect of separation factor on the shape of torn boudin. Variation of face curvature (FC) in (a) and exterior curvature (EC) in (b) with the boudin to matrix viscosity ratio (η_{BM}) for different separation factor (N_R). Solid lines represent the curvatures when inter-boudin is softer (half) than matrix, whereas dotted lines represent when inter-boudin is stiffer (double) than matrix. Note that with changing the separation factor, values of curvature vary slightly without changing the sense of curvature.

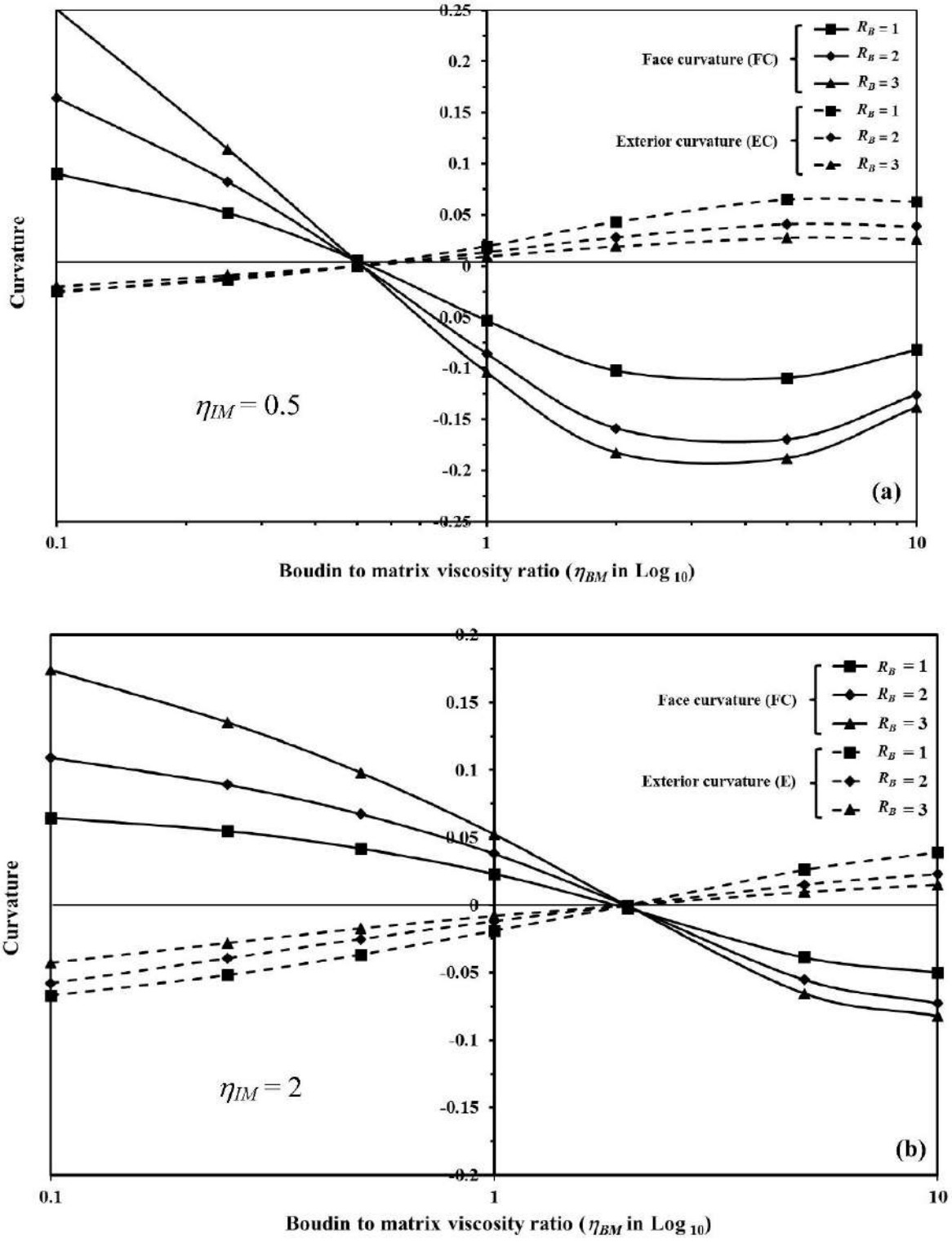

Fig. 3.10: Variation of face (solid lines) and exterior (dashed lines) curvature with the boudin to matrix viscosity ratio (η_{BM}) for different initial aspect ratio of boudin object (R_B). (a) Viscosity of inter-boudin is half of the viscosity of the matrix (η_{IM} = 0.5) and (b) viscosity of inter-boudin is double the viscosity of the matrix (η_{IM} = 2). Note that the initial aspect ratio of boudin does not have much influence on the sense of both face and exterior curvature of torn boudin.

3.5 Limitations

It is important to recognize certain limitations in the present numerical experiments. First, the interfaces between different materials are assumed to be coherent throughout the deformation process. In natural settings, however, these interfaces may not remain perfectly coherent, which could lead to slight differences in the measured face and exterior curvatures compared to our experimental results. Furthermore, the initial boudin object in our models is assumed to be square. In contrast, natural boudins often exhibit non-square shapes, which may lead to variations in the absolute values of the face and exterior curvatures. Nonetheless, the sense of the curvature (that is, whether it is convex or concave) is expected to remain consistent, and thus, the method can still be used as a qualitative tool for estimating relative viscosity.

Another limitation concerns the assumption of constant viscosity for the boudin material during deformation. In natural geological environments, the viscosity of boudin material may change during deformation—particularly in cases where post-boudinage syntectonic migmatization occurs (Samanta and Deb, 2014). While our models assume a constant viscosity for simplicity, such variations in natural systems could introduce additional complexity that is not captured in the current study.

3.6 Conclusions

The present study confirms that following the formation of a rectangular torn boudin with straight, orthogonal edges, the subsequent presence of inter-boudin

material can lead to modifications in the boudin's margins. Depending on the mutual interaction of material flow among the boudin, the inter-boudin, and the matrix, the initially straight edges may evolve into either convex or concave geometries during subsequent deformation. Our results indicate that, in addition to the boudin-to-matrix viscosity ratio, the curvature of both the face and exterior margins is strongly sensitive to the relative viscosity of the inter-boudin material during ongoing deformation.

Specifically, a bone-shaped boudin, characterized by concave exteriors and convex faces, develops when the inter-boudin material is more competent than the boudin material. This effect is particularly pronounced when the matrix is stiffer than the boudin but softer than the inter-boudin. Conversely, when the boudin behaves in a stiffer manner than the inter-boudin, barrel-shaped boudins are produced. These barrel-shaped boudins can further evolve into fish-head boudins at higher levels of finite strain. In cases where there is very little or no viscosity contrast between the boudin and the inter-boudin materials, the resulting boudin is nearly rectangular; however, its aspect ratio will vary depending on the relative viscosity of the matrix. It is noteworthy that boudins with both convex or both concave margins (in terms of face and exterior) cannot be generated under the present kinematic conditions.

Ultimately, the geometry of the boudin margins provides an important clue regarding the viscosity ratios among the boudin, inter-boudin, and matrix materials. By carefully analysing the sense and magnitude of the curvature on the exterior and face margins of a boudin object, one can qualitatively estimate the relative competency of these materials.

Chapter 4

Folds in Layered Gneissic Rock

4.1 Introduction

Folds represent one of the most ubiquitous geological structures formed in ductile compressional regimes. These wavy, continuous structures are not only visually striking but also serve as vital archives of the deformation history and rheological properties of the rocks in which they develop (Schmalholz and Podladchikov, 2001a, 2001b; Bastida et al., 2005; Schmalholz, 2006; Druguet et al., 2009; Hudleston and Treagus, 2010; Yakovlev, 2012a, 2012b; Llorens et al., 2013). Over the past several decades, extensive research efforts have been dedicated to revealing the mechanisms behind the formation of various fold geometries using a range of approaches that include analogue modeling (e.g., Currie et al., 1962; Ramberg, 1963; Hudleston, 1973; Abbassi and Mancktelow, 1992), analytical techniques (e.g., Biot, 1961; Johnson and Fletcher, 1994; Hunt et al., 1996), and numerical simulations (e.g., Dieterich, 1970; Cobbold, 1977; Zhang et al., 1996; Mancktelow, 1999; Schmalholz et al., 2001).

Folds may be broadly classified into two main categories based on the number of layers participating in the folding event. In its simplest form, a single layer fold represents the bending of one isolated layer, while multilayer folds involve the interaction of several layers. In the multilayer regime, the folding process is considerably more complex due to the additional controlling parameters inherent in a layered system. These complexities give rise to distinct fold patterns, such as chevron folds (e.g., Williams, 1980; Ramsay, 1974; Bastida et al., 2007), parallel and similar folds (e.g., Johnson and Pfaf, 1989), kink folds (e.g., Dewey, 1965), and parasitic folding (e.g., Frehner and Schmalholz, 2006; Frehner and Schmid, 2016; Liu et al., 2020).

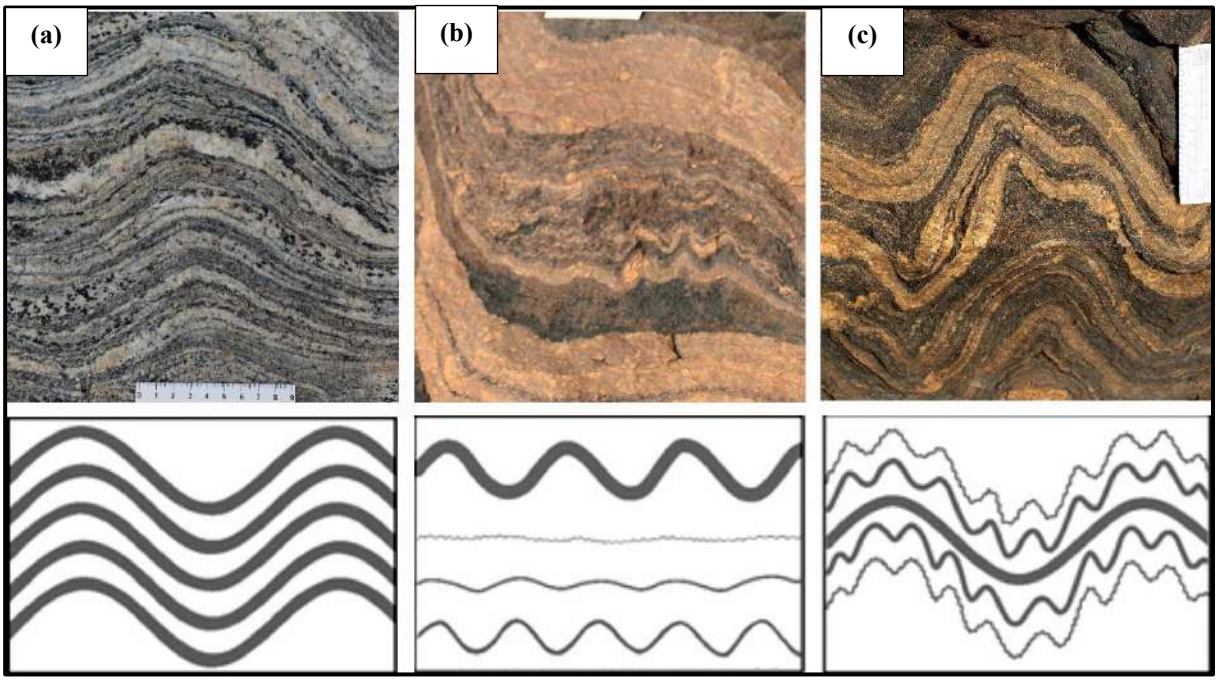

Fig 4.1: Top row consists field photographs of the different types of multilayered folds in gneissic rock based on their harmonicity. Corresponding schematic diagrams are in the bottom row. (a) Harmonic folds, (b) Disharmonic folds and (c) Polyharmonic folds. All photographs are taken from Purulia, WB

Within multilayered systems, folds with different wavelengths may be generated depending on factors such as the individual layer thicknesses, the spacing between layers, and the viscosity contrast between the layers and the surrounding medium. These factors combine to produce what are commonly termed harmonic, polyharmonic, and disharmonic folds. Fig. 4.1 illustrates a detailed examination of multilayered folds in gneissic rock, classified according to their harmonicity. The top row displays field photographs that capture the distinct structural configurations of harmonic, disharmonic, and polyharmonic folds, while the bottom row presents corresponding schematic diagrams that distinct and emphasize the key geometric features of each fold type. Harmonic folds are typically formed when the layers participating in the folding event are of nearly equal thickness and are positioned very close together (Fig. 4.1a). In contrast, if the thicknesses of the layers vary and

the spacing between them is too large for the layers to behave as a single, coherent unit within an infinitely extended medium, the folds tend to be disharmonic in nature (Fig. 4.1b). When the layer thicknesses are different but the spacing is intermediate between the two extremes, the resulting folds usually display a polyharmonic geometry (Fig. 4.1c). In the field, the harmonicity of folds is commonly identified by measuring the deviation of the traces of the axial planes of the adjacent folded layers. In an ideal harmonic fold (Fig. 4.1a), higher order folds are completely absent and the traces of the axial planes are perfectly aligned. Polyharmonic folds, on the other hand, are characterized by the presence of multiple orders of folding but with minimal deviation of the axial plane traces (Fig. 4.1c). Disharmonic folds, however, typically exhibit a significant deviation in these traces (Fig. 4.1b).

Previous studies have demonstrated that, in a layer system with similar rheological contrasts, the thinner layer is generally the first to be folded during deformation, and the thicker unit plays a decisive role in determining the geometry of the large-scale fold (Fig. 4.1). As deformation progresses, thin folded layers with shorter wavelengths (representing higher order folds) may come to mimic the larger, lower-order folds of the thicker layer through a process known as secondary folding. In nature, the concept of ideal single layer folding is rarely observed because it presupposes an infinitely extending medium that is not influenced by the presence of adjacent layers. Biot (1957) introduced the concept of a dominant wavelength for a folded structure, which depends on both the viscosity contrast and the thickness of the layer embedded in a more compliant medium. However, natural folds often deviate from this idealized conception because the deformation of any given layer may be modified by the heterogeneous strain produced by the interaction with adjacent layers.

In metasedimentary terrains, it is common to find alternate layers of varying competence and thickness. When layers of identical rheology but different thicknesses are deformed, the thinner layer is typically perturbed first during the early stages of deformation (Ramberg, 1962). Ramberg (1960) pointed out that the influence of a folded layer on the strain field in the direction perpendicular to the layer can persist only up to a distance equal to its initial wavelength on either side. Beyond this distance, the influence decreases exponentially and becomes negligible if the spacing exceeds twice the initial wavelength (the so-called "contact strain zone," Ramberg, 1963). For a constant viscosity contrast, the thinnest unit is perturbed first and is assumed to fold with its dominant wavelength. During progressive deformation, the folding of the thin layer influences the instability pattern and the folding behaviour of the adjacent thick layers within its contact strain zone. In the present study, finite element modeling (FEM) is used to investigate the development of folds in a layered system by focusing on the mutual interaction among layers. In particular, the study explores the deviation of the fold wavelength from the dominant wavelength as defined by Biot (1957).

4.2 Numerical Modelling

4.2.1 Model Consideration

4.2.1.1 Material

To elucidate the effect of mutual interaction on fold geometry, we consider a simplified layer system composed of three layers with similar rheology, all embedded within a relatively softer medium. Numerical simulations were performed

using the commercial finite element modeling software ABAQUS (ver. 2023). The simulations were carried out in two dimensions under plane strain conditions, following the approaches of Ramsay and Lisle (2000); Arslan et al. (2008); Samanta and Deb (2014); Samanta et al. (2017); and Basu Majumder and Samanta (2023).

Both the layers and the surrounding medium were modelled using Maxwell viscoelastic rheology (cf. Zhang et al., 1996; Mancktelow, 1999; Passchier and Druguet, 2002; Samanta and Deb, 2014; Basu Majumder and Samanta, 2023) to simulate the high pressure–temperature (P–T) conditions typical of lower crustal deformation (Turcotte and Schubert, 1982). For all materials, a constant Poisson's ratio of 0.25 and a relaxation time of 8×10^8 s (Larsen et al., 2005; Samanta et al., 2017; Basu Majumder and Samanta, 2023) were adopted. The constitutive equation governing the viscoelastic behaviour is given by

$$\frac{d\varepsilon}{dt} = \frac{1}{G}\frac{d\sigma}{dt} + \frac{\sigma}{\eta} \tag{1}$$

where ε represents the instantaneous strain (finite in the case of steady-state deformation), σ is the instantaneous stress, t denotes time, and G and η are the Maxwell shear modulus and viscosity, respectively.

4.2.1.2 Model Specification

To obtain optimal results within the computational limits of our available resources and in a reasonable simulation time, we adopted a rectangular block with dimensions of 5000 × 3000 units (as per Passchier et al., 2005; Eckert et al., 2014; Liu et al., 2016, 2020; Damasceno et al., 2017) as shown in Fig. 4.2. A central thin

layer with an initial thickness (t_h) of 5 units was inserted in the middle of the block. On both sides of this central thin layer, two thicker layers were positioned. The thick layers were assigned identical thicknesses, which were varied in our models to be $2t_h$ (10 units), $4t_h$ (20 units), or $6t_h$ (30 units). The spacing (s) between two adjacent layers were systematically varied to assess its influence on the folding process.

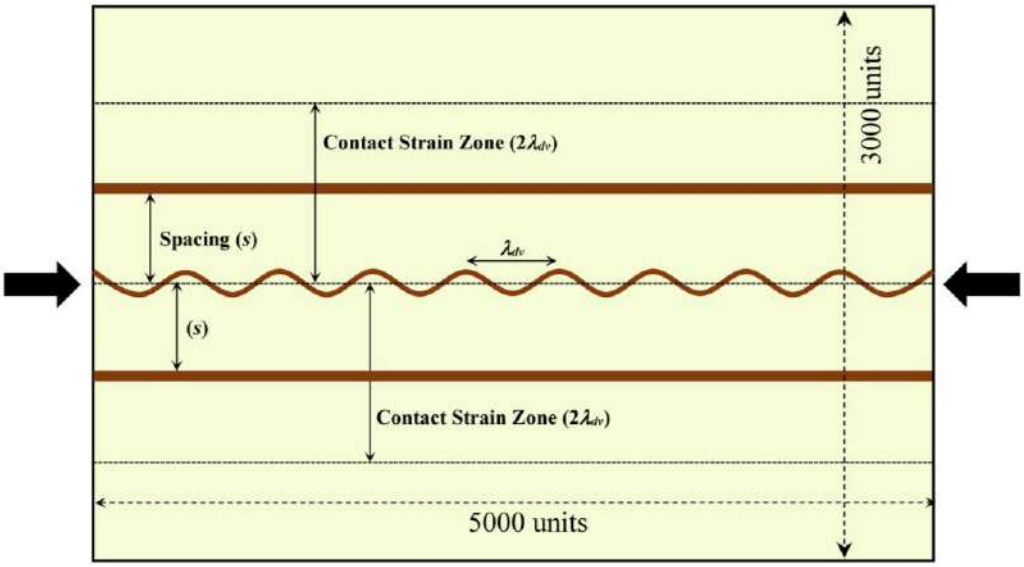

Fig 4.2: Schematic diagram of model. The thickness of the central thin (dark) layer is 5 units (t_h) and the thicknesses of adjacent thick (dark) layers are 10 units ($2t_h$) which varied in different model. The initial spacing (s) between two adjacent layers is defined by a spacing factor, n ($s = n\lambda_{dv}$, where spacing factor, $n = 0.5$, 1.0, 1.5 and 2.0) and wavelength (λ_{dv}) of initial sinusoidal perturbation of the central thin layer.

A bulk layer-parallel shortening of 30% was applied throughout the simulation, following the precedent set by earlier studies (e.g., Biot, 1957; Ramberg, 1964). All simulations were conducted using the "VISCO" step in ABAQUS, which incorporates a full Newtonian solution technique and a direct equation solver method. The entire model was discretized using a structured quadrilateral meshing scheme with a global mesh size of 2.5 units, employing the Abaqus Standard element CPE4 (a 4-node bilinear plane strain quadrilateral). The final mesh comprised

approximately 2,400,000 elements. Simulations were performed at a constant natural strain rate of 10^{-13} s^{-1} (e.g., Jeng et al., 2002; Barraud et al., 2004; Hobbs et al., 2008; Ord and Hobbs, 2013) under steady-state conditions to achieve optimal convergence.

According to Ramberg (1964), the buckling of a layer embedded in an infinite medium can only occur if certain flaws or heterogeneities are present. In our models, the thin layer is assumed to possess a minute initial perturbation, while the adjacent thick layers are assumed to be perfectly homogeneous and remain straight if oriented parallel to the shortening direction. The primary objective of this study is to isolate the effect of mutual interaction on fold development in a layered system. To this end, the thick layers located within the contact strain zone of the thin layer were deliberately oriented parallel to the shortening direction (Fig. 4.2). Consequently, sinusoidal perturbations were imposed only on the central thin layer, following the approaches described by Biot (1957, 1959a, 1959b); Schmid and Podladchikov (2006); and Frehner and Schmid (2016).

The nature of the initial perturbation of the thin layer is governed by the *R* factor, which determines whether the layer behaves in a viscous ($R < 1$) or elastic ($R > 1$) manner during folding (Schmalholz and Podladchikov, 1999; Schmalholz et al., 2001). The *R* factor is defined as the ratio between the viscous dominant wavelength (λ_{dv}) and the elastic dominant wavelength (λ_{de}) of the layer. For a single-layer fold model, the *R* factor is given by

$$R = \frac{\lambda_{dv}}{\lambda_{de}} = \sqrt[3]{\frac{1}{6}\frac{\eta_M}{\eta_L}}\sqrt{\frac{P_0}{G}} = \sqrt[3]{\frac{1}{6}\eta_R}\sqrt{\frac{1}{G}4\eta_M\dot{\varepsilon}} \qquad (2)$$

where $\eta_R = \eta_L/\eta_M$ is the viscosity ratio between the competent layer (η_L) and the soft embedded medium (η_M), *G* is the shear modulus, and P_0 is the initial layer-

parallel stress. For a constant viscosity ratio, the value of *R* in Eqn. (2) mainly depends on the viscosity of the embedded medium (η_M) and the strain rate (fixed at 10^{-13} s^{-1}). The material properties used in these simulations, along with the corresponding *R* values, are summarized in Table 4.1.

Table 4.1: Material properties used in numerical modelling

Competent layer							
Competency contrast (η_R)	Viscosity (Pa. s)	Elastic modulus (Pa)	Shear modulus (Pa)	Bulk Modulus (Pa)	Poisson's Ratio	Relaxation time (s)	R-value
1	1×10^{20}	3.13×10^{11}	1.25×10^{11}	2.08×10^{11}	0.25	8×10^{8}	0.01
Incompetent medium							
100	1×10^{18}	3.13×10^{9}	1.25×10^{9}	2.08×10^{9}	0.25	8×10^{8}	0.04
500	2×10^{17}	6.25×10^{8}	2.5×10^{8}	4.17×10^{8}			0.08
1000	1×10^{17}	3.13×10^{8}	1.25×10^{8}	2.08×10^{8}			0.10

In our simulations, the *R* value ranged between 0.01 and 0.10, indicating that the deformation occurred in the viscous regime (Table 4.1). Consequently, the sinusoidal perturbation applied to the central thin layer was set to have a minute amplitude of $0.005\lambda_{dv}$ (i.e., 0.5% of the dominant wavelength λ_{dv} of the layer). The equation of dominant wavelength for viscous material (Biot, 1957) is as follows.

$$\lambda_{dv} = 2t_h\pi\sqrt[3]{\frac{1}{6}\,\eta_R} \qquad (3)$$

where $\eta_R = \eta_L/\eta_M$ and t_h is the initial thickness of the thin competent layer. No perturbation was imposed on the thick layers, which were straight and essentially placed parallel to the shortening direction.

In contrast, no perturbation was imposed on the thick layers, which were maintained as straight and aligned parallel to the shortening direction. The thickness of the central thin layer was fixed at 5 units, while the thick layers were modelled with thicknesses of 10 ($2t_h$), 20 ($4t_h$) and 30 ($6t_h$) units in three separate model

configurations (Fig. 4.2). The spacing between the layers was varied according to the relation

$$s = n\lambda_{dv} = 2\pi n t_h \sqrt[3]{\frac{1}{6}\eta_R} \quad (4)$$

where the spacing factor, *n*, was set to values of 0.5, 1.0, 1.5, and 2.0. Throughout all simulations, the viscosity of both the thin and thick layers was held constant, while the viscosity ratio (η_R) between the layers and the embedded medium was varied across different models. The details of initial perturbation on central thin layer and corresponding spacing in between thin and thick layer are mentioned in Table 4.2.

Table 4.2: Initial perturbation of the thin layer and spacing between thin and thick layer (up to two decimal places and all are in SI unit)

Competency contrast (η_R)	Dominant wavelength (λ_{dv})	Amplitude ($0.005\lambda_{dv}$)	Spacing (s) = $n\lambda_{dv}$			
			$0.5\lambda_{dv}$	λ_{dv}	$1.5\lambda_{dv}$	$2.0\lambda_{dv}$
100	80.25	0.40	40.12	80.25	120.37	160.50
500	137.22	0.69	68.61	137.22	205.83	274.44
1000	172.89	0.86	86.44	172.89	259.33	345.78

4.2.1.3 Boundary Conditions

The entire model was subjected to layer-parallel shortening under pure shear conditions. The bulk shortening was fixed at 30% for all simulations to ensure that the overall thickness of each layer remained constant throughout the deformation process. The shortening was applied via displacement boundary conditions on all four boundaries of the model, using the following equations:

$$U_x = -k.x \quad (5)$$

$$U_y = \frac{k}{1-k}.y \quad (6)$$

In our simulations, *k* was fixed at 0.3, corresponding to a 30% bulk shortening.

4.2.2 Model Results

A total of 36 numerical simulations were performed in which three fundamental parameters governing buckle fold development were varied: (a) the viscosity ratio ($\eta_R = \eta_L/\eta_M$) between the competent layer and the embedded medium, (b) the thickness ratio of the thick to the thin layers, and (c) the spacing between two adjacent layers (*s*). The primary aim of this study was to investigate how layers of similar competency, but with differing thicknesses and mutual spacing, influence the final fold geometry. To quantify the deviation of the fold geometry from the idealized dominant wavelength predicted by Biot (1957), we introduce the *W*-factor, defined as

$$W = \lambda_{ob} / \lambda_f \quad (7)$$

where λ_{ob} is the wavelength obtained from the numerical simulation and λ_f is the expected wavelength after 30% shortening, defined as $\lambda_f = 0.7\lambda_{dv}$ (with λ_{dv} being the dominant wavelength of the respective layer). A *W*-factor of 1 indicates that the dominant wavelength is preserved after deformation, whereas $W > 1$ signifies a deviation from the dominant wavelength.

4.2.2.1 Progressive Development of Fold Geometry

The primary focus of our study is to understand how minute instabilities in a thinner layer can perturb the deformation of adjacent thicker layers embedded within a homogeneous medium. It is well known that buckling of a homogeneous layer embedded in an infinite, uniformly distributed medium is not feasible if the layer is oriented parallel to the shortening direction—even if the viscosity contrast with the surrounding medium exceeds the threshold required for buckling (Ramberg, 1962; 1964). Therefore, in our model, we positioned the thick layers on both sides of a minutely perturbed thin layer (as described in Section 5.2.1.2) such that all layers shared similar rheological properties. The objective was to observe how the thin layer influences the folding of the thick layers during progressive layer-parallel shortening.

In the first experimental setup, the layer–medium viscosity ratio (η_R) was set to 100, and the thickness of the thick layers was chosen to be 20 units, with the spacing between adjacent layers set to $1.5\lambda_{dv}$ (where λ_{dv} is the initial dominant wavelength calculated from Eqn. (3)). At an early stage of deformation, corresponding to 5% shortening, there was no visible instability in the thick layers (Fig. 4.3a). However, at 10% shortening, the amplitude of the fold in the thin layer increased, and mild instabilities began to develop in the adjacent thick layers (Fig. 4.3b). By 15% shortening, clear folded geometries were observed in the thick layers (Fig. 4.3c), and the thin folded layer started to mimic the large-scale folds, forming a polyharmonic pattern. As shortening progressed further (Figs. 4.3d to 4.3f), the amplitude of the folds in the thick layer became more accentuated, while the folding in the thin layer was only slightly modified. The overall homogeneous thickening in

the hinge region of the thick layer was measured to be only 0.95% after 30% shortening; furthermore, this thickening decreased with increasing viscosity contrast. In a similar model where the viscosity ratio (η_R) was increased to 1000 while keeping all other conditions constant, the thick layer exhibited only 0.3% thickening—a nominal change that was considered negligible in the context of our study.

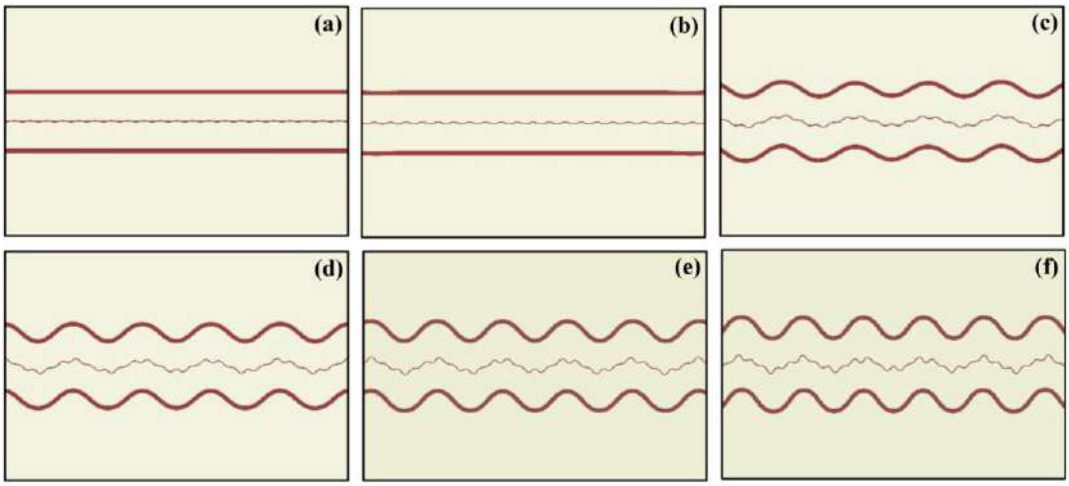

Fig. 4.3: Progressive development of folds. Viscosity contrast (η_R) is 100. Thicknesses of the thin and thick layer are 5 and 20 units respectively. The spacing between adjacent thick and thin layers is *1.5* λ_{dv}. The percentage of shortening of the models (a to f) ranges from 5% to 30% with an interval of 5%. Note that initial sinusoidal perturbation with wavelength λ_{dv} and amplitude $0.005\lambda_{dv}$ (Eqn. 3) was imposed only on the central thin layer. Adjacent thick layers were initially straight and folded later by the heterogeneous strain produced by the central thin layer and the fold geometry gradually transforms from disharmonic to poly-harmonic in progressive deformation.

These results demonstrate that even a minimal perturbation in the central thin layer can trigger and control the instability in the adjacent thick layers during the early stages of deformation. Subsequent sections elaborate on the influence of the thin layer and other controlling parameters on the initiation of fold geometry in the thick layers.

4.2.2.2 Effect of Viscosity Ratio

Previous studies (e.g., Biot, 1957; Ramberg, 1964) have shown that the viscosity ratio between the competent layer and the embedded, more compliant medium plays a critical role in determining fold geometry. In our numerical simulations, both the thin and thick layers were assigned the same viscosity, and the viscosity ratio ($\eta_R = \eta_L/\eta_M$) of the layer to the surrounding medium was varied while keeping all other parameters constant (see Fig. 4.4). Our observations reveal that as the viscosity contrast increases, the tendency for the preservation of higher order folds in the central thin layer diminishes; these higher order folds are maintained primarily in the hinge zones of the folds.

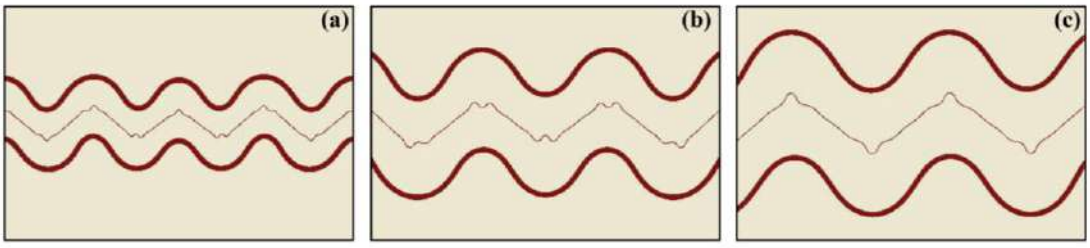

Fig. 4.4: Patterns of poly-harmonic folds generated by varying viscosity contrast. (a) $\eta_R = 100$, (b) $\eta_R = 500$ and (c) $\eta_R = 1000$. Thicknesses of the thin and thick layer are 5 and 30 units respectively. Spacing ($1.5\lambda_{dv}$) between layers increases with increasing viscosity contrast (η_R) following Eqn. 4. Finite shortening is 30%.

Although the visual effect of the viscosity ratio on the overall fold geometry may appear subtle, careful analysis of the graphical data (Fig. 4.5) shows that the *W*-factor decreases with increasing spacing factor (*n*) irrespective of the viscosity ratio. However, at lower values of *n*, the *W*-factor increases significantly with an increase in the viscosity ratio. It is also noteworthy that, when comparing the thin layer to the thick layer, the *W*-factor for the thin layer does not exhibit significant variation. This observation indicates that the preservation of the higher order folds in the thin layer

can serve as a precise indicator of the rheological contrast between the layer and the medium.

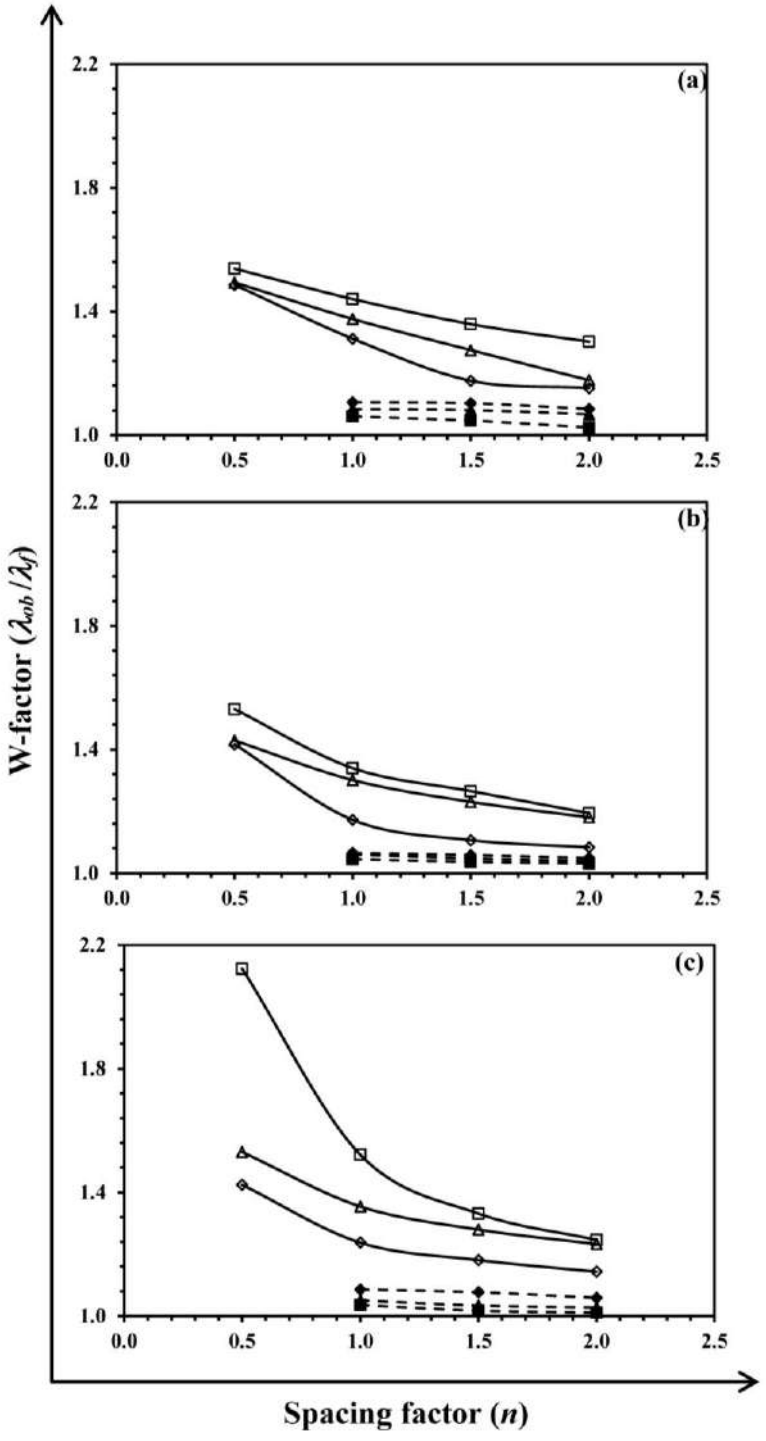

Fig. 4.5: Graphical comparison of fold geometry of thick (solid line with open marker) and thin (dashed line with solid marker) layers for different layer thickness (t_h). (a) η_R = 100, (b) η_R = 500 and (c) η_R = 1000. Hollow diamond, triangle and square markers represent 10-, 20- and 30-units thickness of the adjacent thick layer respectively. Similarly, solid markers represent thin layers under the influence of corresponding thick layers. Finite shortening is 30%. Note that deviation from deformed dominant wavelength (λ_f) is more for thicker layer and it increases with the decreasing spacing.

4.2.2.3 Effect of Layer Thickness

To assess the influence of layer thickness on fold geometry, the thickness of the thin layer was fixed at 5 units, while the thicknesses of the adjacent thick layers were varied to 10, 20, and 30 units. With increasing thickness of the thick layers, the overall fold geometry gradually transitions from disharmonic to polyharmonic folds, and the number of small-scale folds decreases (Fig. 4.6). Unlike the influence of the viscosity ratio discussed in Section 5.2.2.2, the changes in fold harmonicity associated with varying layer thicknesses are more pronounced. Analysis of the graph plotting the *W*-factor versus the spacing factor (*n*) reveals a pattern analogous to that observed with changing viscosity ratio (Fig. 4.7). These results highlight the critical role of layer thickness in controlling the harmonicity of the folds, with thicker layers tending to dominate the large-scale geometry of the fold system.

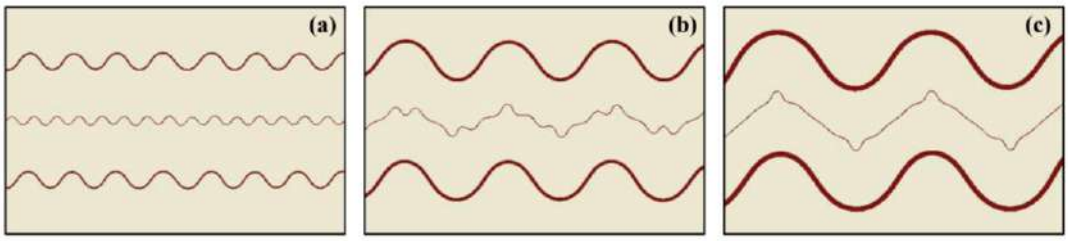

Fig. 4.6: Fold patterns generated by varying thickness of the adjacent thick layers. (a) 10 units, (b) 20 units and (c) 30 units. t_h = 5 units, η_R = 1000, $n = 1.5$. Finite shortening is 30%.

4.2.2.4 Effect of Spacing

In our model, the spacing between consecutive layers is defined by the product of a spacing factor (n) and the imposed initial dominant wavelength (λ_{dv}) of the central thin layer, such that $s = n\lambda_{dv}$. Here, λ_{dv} is determined by Eqn. (3) as described by Biot (1957). According to Ramberg (1964), under plane strain

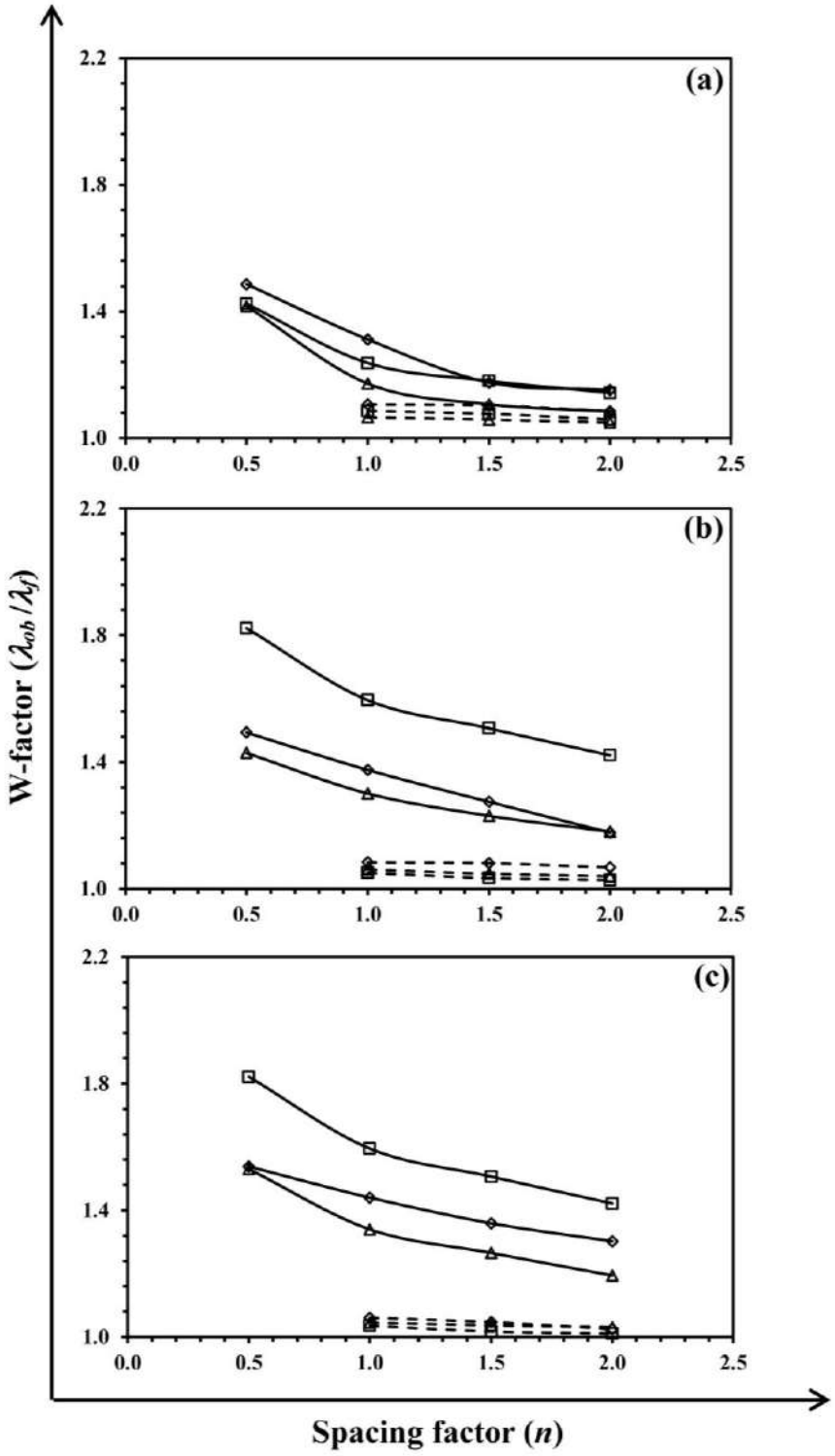

Fig. 4.7: Graphical comparison of fold geometry of thick (solid line with open marker) and thin (dashed line with solid marker) layers for different viscosity contrast (η_R). (a) $2t_h$, (b) $4t_h$ and (c) $6t_h$. Hollow diamond, triangle and square markers represents thick layers with viscosity contrast (η_R) of 100, 500 and 1000 respectively. Similarly, solid markers represent thin layers under the influence of corresponding thick layers. Finite shortening is 30%. Note that deviation from deformed dominant wavelength (λ_f) increases with the decreasing spacing.

conditions the influence of a folded layer on the adjacent material—referred to as the layer-perpendicular mutual effect—remains significant only up to a distance equal to the initial wavelength on both sides of the folded layer. Beyond this distance, the mutual influence decreases exponentially and becomes negligible when the spacing exceeds twice the initial wavelength (often termed the "contact strain zone," Ramberg, 1963).

Our numerical results indicate that as the spacing between layers increases, the fold geometry in the thin layer changes from harmonic to polyharmonic and finally to disharmonic (Fig. 4.8). A detailed analysis shows that with increasing spacing, the degree of harmonicity decreases and the number of small-scale folds in the thin layer increases. Furthermore, the graph of the W-factor versus layer thickness demonstrates that an increase in spacing results in a reduction of the W-factor, suggesting that the influence of the contact strain zone is progressively diminished with increased separation between layers (Fig. 4.9).

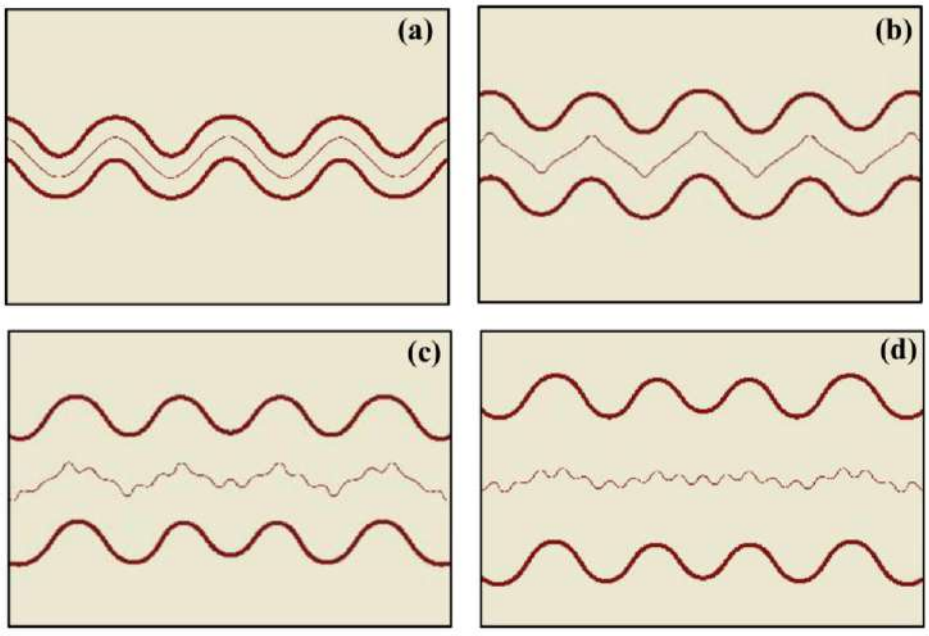

Fig. 4.8: Fold patterns generated by varying spacing ($n\lambda_{dv}$) in between adjacent thin and thick layers. (a) n = 0.5, (b) n = 1, (c) n = 1.5 and (d) n = 2. Viscosity contrast (η_R) is set as 500 and thickness of thin and thick layers are 5 and 20 units. Finite shortening is 30%.

Overall, the numerical results presented in Figs. 4.4 through 4.9 are in strong agreement with Ramberg's (1960) theory of folding within the contact strain zone.

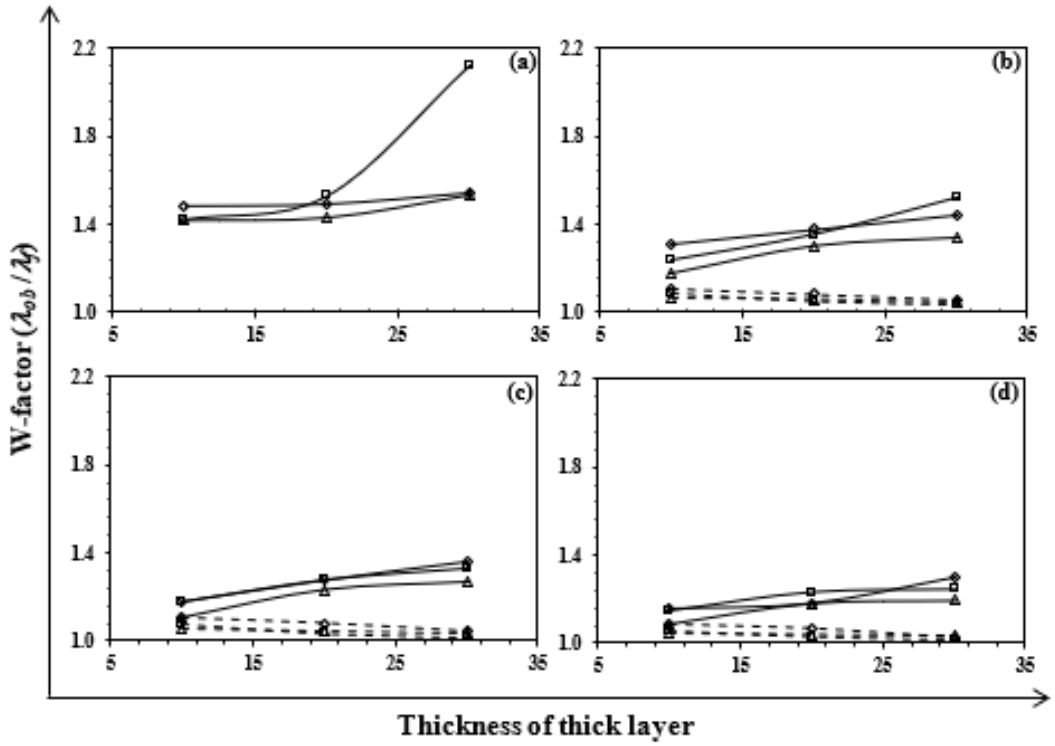

Fig. 4.9: Graphical comparison of fold patterns of thick (solid lines open marker) and thin (dashed lines with solid marker) layer for different spacing ($n\lambda_{dv}$) in between two adjacent thick and thin layers. (a) n = 0.5, (b) n = 1, (c) n = 1.5 and (d) n = 2. Hollow diamond, triangle and square markers represent thick layers with viscosity contrast (η_R) of 100, 500 and 1000 respectively. Similarly, solid markers represent thin layers under the influence of corresponding thick layers. Finite shortening is 30%. Note that deviation from deformed dominant wavelength (λ_f) increases with the thickness of the adjacent layer.

4.3. Discussions

4.3.1 Influence of Contact Strain Zone on the Harmonicity of Thin-Layered Folds

The results from our numerical simulations clearly illustrate the significant role of the "contact strain zone" (Ramberg, 1960) in dictating the harmonicity of the fold geometry in a layered system. It is a well-established fact that, in a multilayer system, the thin, competent layer is the first to be perturbed during the onset of

deformation. One of the most critical findings of this study is that even slight instabilities in the thin competent layer can propagate and induce perturbations in the adjacent thick layers—even when those thick layers are positioned at distances up to twice the initial wavelength of the thin layer. This observation not only supports the theories and analogue models developed by Ramberg (1960, 1962, 1963, and 1964) but also serves to firmly establish the pivotal role of the contact strain zone in influencing the overall fold geometry.

In our discussion, we have examined the effects of various parameters on the harmonicity of folds in both thin and thick layers. A consistent trend is observed: the thinner layer tends to develop higher order folds initially, and these folds can exert a controlling influence on the deformation pattern of the adjacent thicker layers. This mutual interaction within the contact strain zone results in the evolution of a diverse array of fold geometries ranging from harmonic to polyharmonic and finally to disharmonic folds, depending on the spacing and other controlling parameters.

An interesting observation is that the overall fold pattern becomes disharmonic when the small-scale folds in the thin layer are preserved. These small-scale folds, which are the primary folds of the thin layer, are generally suppressed when the thick layers are located in close proximity to the thin layer. The obliteration of these small-scale folds is most pronounced when the spacing factor (n) is as low as 0.5, a phenomenon that is in good agreement with the descriptions provided by Ramberg (1964). When the spacing is minimal, the discrete layers almost lose their individual identities and behave collectively as a single unit. As the spacing increases, the individual character of each layer is gradually restored, allowing the mutual interaction to produce more complex fold geometries. In essence, the

interplay between adjacent layers within the contact strain zone is the dominant control on the final fold geometry, and the extent of this influence is directly related to the initial dominant wavelength of the perturbation.

4.3.2 Estimation of Viscosity Ratio

Another important aspect addressed in our study is the estimation of the layer–medium viscosity ratio (η_R), which is defined as the ratio of the viscosity of the competent layer (η_L) to that of the surrounding, more compliant medium (η_M). In many previous studies, it has been assumed that the dominant wavelength of a folded structure is preserved in the thickest layer of the system. However, our numerical results suggest that this assumption may lead to erroneous estimates of the finite shortening and, consequently, to an inaccurate determination of the viscosity contrast.

From our analyses (see Figs. 4.5, 4.7, and 4.9), it is evident that the *W*-factor, which represents the ratio of the observed wavelength after deformation to the expected dominant wavelength after shortening, is highly sensitive to both the thickness of the layers and the spacing between them for a fixed rheological contrast. In particular, the dominant wavelength of the thin layer is more accurately preserved in the higher order folds that develop at the hinge of the secondary fold. This observation implies that the small-scale folding in the thin layer can provide a more precise measurement of the rheological contrast between the layer and the medium than the folds in the thick layer.

Field observations in the gneissic rocks of Purulia, India, support this conclusion. In these rocks, quartzo-feldspathic layers of varying thicknesses are folded within a biotite-rich matrix, and the spacing between these layers varies systematically (Figs. 4.10 and 4.11). Measurements taken from the large wavelength folds in the thicker layers, as well as from the residual small-scale folds in the thinner layers (which are concentrated in the hinge region of the secondary fold), exhibit trends that are consistent with our numerical predictions (see Table 4.3). In particular, the ratio of the observed wavelength to the layer thickness decreases as the thickness of the layer decreases and as the spacing between layers increases. By plotting the wavelength-to-thickness ratio against the spacing between layers for a known amount of bulk shortening, it is possible to estimate the viscosity ratio between the layer and the medium (Fig. 4.12). Our findings indicate that the higher order folds in the thin layer serve as a more reliable proxy for the rheological contrast than the folds in the thick layer.

Fig. 4.10: Example of natural folding in gneissic rock, generated by the mutual interaction among the layers. Photographed from Purulia, India. (23.16ºE, 86.28ºN). Scale bar is 4 cm. Details of measurement are mentioned in Table-2.

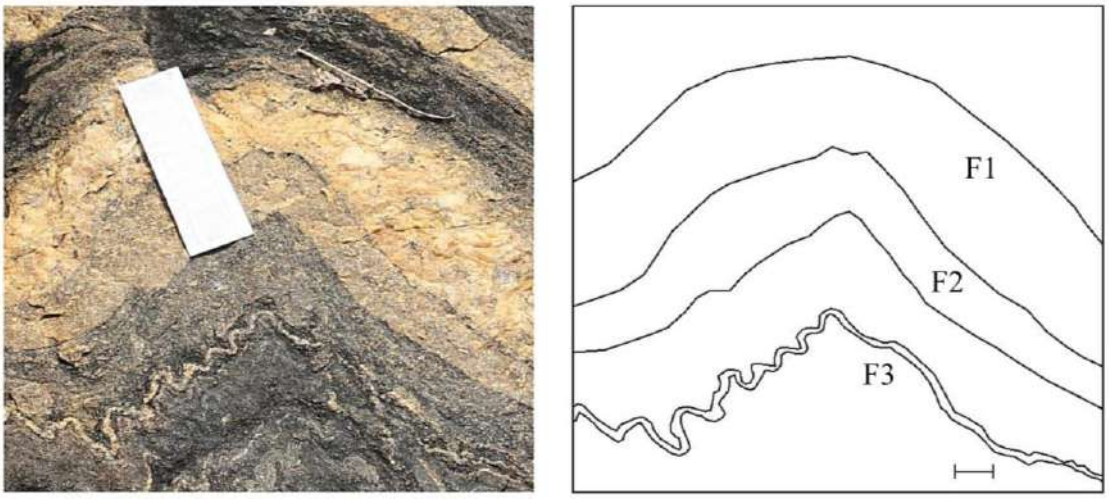

Fig. 4.11: Example of natural folding in gneissic rock, generated by the mutual interaction among the layers. Photographed from Purulia, India. (23.16°E, 86.28°N) Scale bar is 4 cm. Details of measurement are mentioned in Table-2

Table 4.3: Measurements from natural folds

For Fig. 5.10			
Fold name	Wavelength (λ_{ob}) (in cm)	Thickness (t_h) (in cm)	Wavelength-thickness ratio (λ_{ob}/t_h)
F1	122.3	18.1	6.76
F2	13.1	2.9	4.52
F3	2.4	0.7	3.43
For Fig. 5.11			
F1	88.23	10.56	8.36
F2	55.76	7.77	7.18
F3	3.13	0.8	3.91

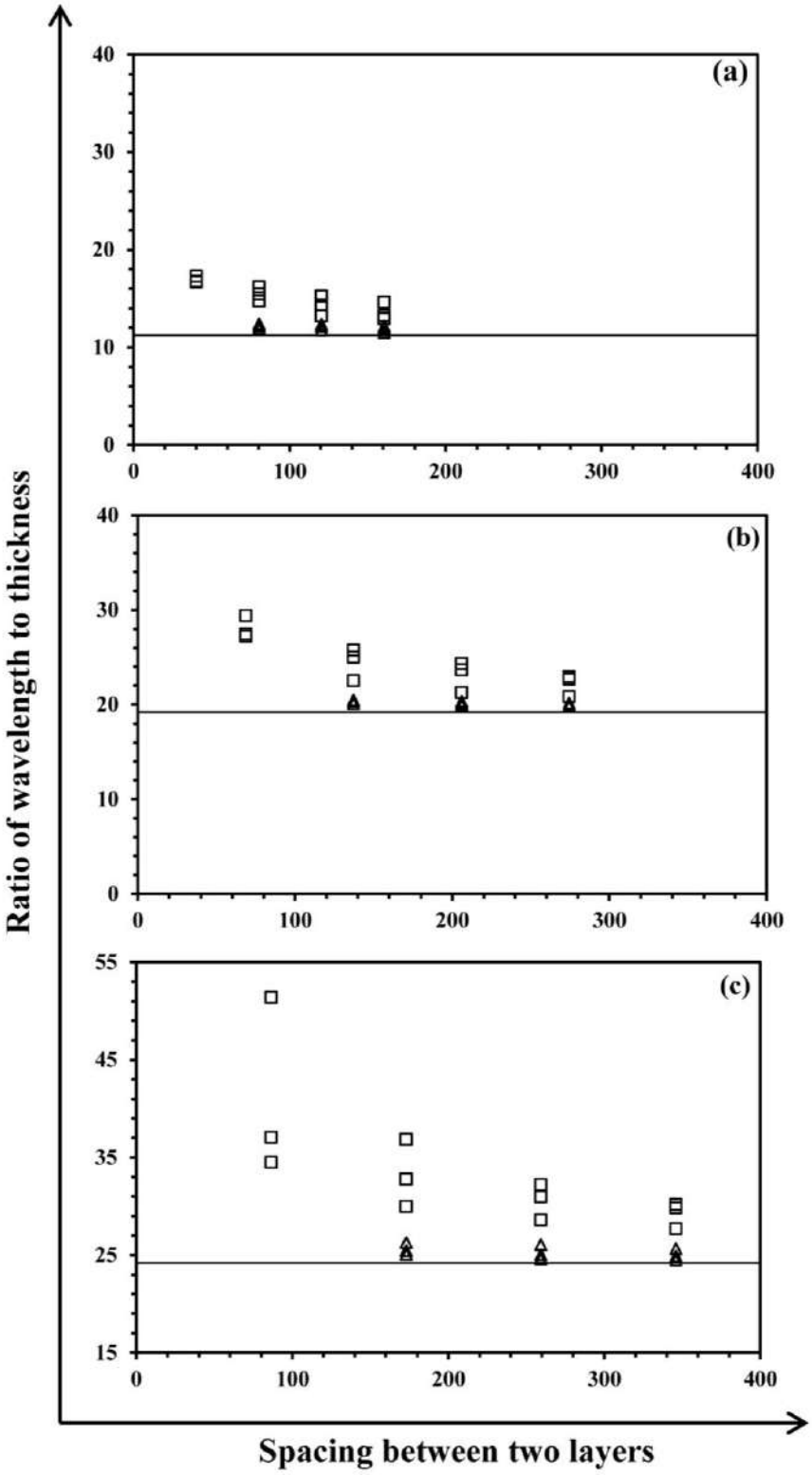

Fig. 4.12: Estimation of viscosity contrast from folded layers of different thicknesses. Horizontal line represents an ideal single layer. Square and triangular markers denote thick and thin layers respectively. (a) $\eta_R = 100$, (b) $\eta_R = 500$ and (c) $\eta_R = 1000$. Finite shortening is 30%. Note that the competency contrast can be estimated more precisely from the folds of thinner unit.

4.4 Limitations

While our study provides important insights into the geometry of folds in layered rock systems, several limitations must be acknowledged. First, our models assume homogeneous material properties for both the layers and the surrounding medium, as well as a three-layer system with two different thicknesses that share the same competency contrast relative to the embedded medium. In natural settings, however, layers may exhibit a range of thicknesses, spacing, and viscosities, which can lead to more complex fold geometries than those produced in our simplified models.

Another limitation is related to the imposed boundary conditions and the simplifications inherent in the numerical model. Our simulations assume a constant bulk shortening of 30% and a uniform strain rate, conditions that may not fully capture the variability of deformation in natural tectonic settings. Furthermore, the initial perturbation imposed on the thin layer is represented by a small-amplitude sinusoidal wave, an idealization that may differ from the more complex heterogeneities present in natural rock layers. Despite these limitations, our study is focused on isolating the effect of mutual interaction among layers on fold geometry, and we believe that the results provide valuable insights into the fundamental mechanisms governing folding in a layered system.

4.5 Conclusions

The following conclusions can be drawn from our observations and numerical experiments:

1. **Control by the Thin Layer:**

   In a layered rock system, the overall fold geometry is predominantly governed by the folding pattern of the thinnest layer. This thin layer initiates a perturbation in the strain field that subsequently influences the folding of the adjacent thicker layers. In effect, the small-scale folds that develop in the thin layer are critical in controlling the overall fold geometry.

2. **Progressive Deformation and Fold Harmonicity:**

   As deformation progresses, the thicker layers exert an increasing influence on the thin layer, leading to the evolution of folds from harmonic to polyharmonic and eventually to disharmonic geometries. In a progressive deformation scenario, the thin layer initially folds with a higher order (shorter wavelength) that eventually mimics the larger-scale (lower order) folds of the thicker layers.

3. **Significance of the Contact Strain Zone:**

   The “contact strain zone” plays a significant role in the development of fold geometry in a layered system. The interaction between the thin and thick layers within this zone is critical in determining the final fold geometry. The extent of this interaction is controlled by the initial dominant wavelength of the thin layer and the spacing between the layers.

4. **Influence of Viscosity Ratio, Layer Thickness, and Spacing:**

   In addition to the effects of the contact strain zone, the viscosity ratio ($\eta_R = \eta_L/\eta_M$), the relative thicknesses of the layers, and the spacing between adjacent layers are the primary parameters that control the final fold geometry. Our numerical experiments demonstrate that the higher order folds

in the thin layer are the most reliable indicators for estimating the relative viscosity between the layer and the embedded medium.

5. **Practical Implications for Field Studies:**

   In natural settings, such as the metasedimentary terrains of Purulia, India, the geometry of folded quartzo-feldspathic layers within a biotite-rich matrix can be quantitatively analysed using the relationships established in our study. The wavelength-to-thickness ratio, when plotted against the spacing between layers and compared to numerical predictions, provides a means to estimate the viscosity ratio between the layers and the surrounding medium.

Chapter 5

Flanking Structures in Layered Gneissic Rock[1]

[1] *This chapter is based on:* Basu Majumder, D., & Samanta, S. K. (2023). Development of flanking structures in layered gneissic rock: Insights from numerical modelling. *Journal of Structural Geology, 174*, 104935.

5.1 Introduction

Flanking structures are widely recognized features in deformed rocks. They are most commonly defined as the deflection or bending of linear and planar fabrics that occur adjacent to any cross-cutting fracture or object. These structures are frequently observed in both layered and/or foliated metamorphic rocks at scales ranging from microscopic to mesoscopic. Although the term "flanking structures" was formally introduced by Passchier (2001), the phenomenon was originally described by Gayer et al. (1978) and Hudleston (1989). Since their early identification, these structures have been interpreted under various names, including roll-over anticlines (Barnett et al., 1987; Reches and Eidelman, 1995; Grasemann et al., 2005), fringe folds (Grasemann et al., 1999), and flanking folds (Druguet et al., 1997; Grasemann et al., 1999; Grasemann and Stüwe, 2001).

The classification of flanking structures is typically based on several criteria. First, the classification considers the instantaneous orientation of the cross-cutting element (CE). Second, it distinguishes between the geometries of the dragged linear and planar fabrics in the immediate vicinity of the CE (referred to as the internal host element) versus those farther away (the external host element) (Passchier, 2001; Coelho et al., 2005; Passchier and Trouw, 2005). Finally, the relative sense of offset of the external host element across the CE is taken into account (Grasemann et al., 2003; Coelho et al., 2005; review in Mukherjee, 2014). Over the past several decades, numerous researchers have worked to understand the evolution of these structures, as they provide critical insights into the kinematic conditions of deformation (including shear sense, among other factors; see review in Dutta and Mukherjee, 2019).

Both analogue and numerical models have been extensively used to study the evolution of flanking structures. These models have been implemented under simple shear and general shear deformation regimes, often by treating the rock as an isotropic, homogeneous medium (Grasemann and Stüwe, 2001; Grasemann et al., 2003; Exner et al., 2004, 2006; Kocher and Mancktelow, 2005; Wiesmayr and Grasemann, 2005; Grasemann et al., 2005; Mulchrone, 2007a; Grasemann et al., 2019; Mayrhofer et al., 2022). In many of these investigations, the initial cross-cutting element is considered to be a slip line or plane along which the external fabrics offset with minimal modification of their shape.

A notable study by Mulchrone (2007a) simulated flanking structures within a homogeneous viscous matrix using a deformable elliptical inclusion. In that work, the focus was on two principal parameters: the viscosity ratio (comparing the cross-cutting element to the host element) and the degree of simple shear. This study was able to elucidate the drag geometry produced in the passive layers that surround the deformable elliptical body. Similarly, Exner and Dabrowski (2010) extended these ideas by numerically investigating the three-dimensional development of flanking structures. In their work, they replaced the conventional cylindrical crack (which is perpendicular to the marker plane) with an ellipsoidal crack having an elliptical face. In all these studies, the host element was typically modelled as a homogeneous isotropic elastic or viscous medium that contained a passive marker line to track deformation.

In natural settings, flanking structures can be observed in two main contexts. In one scenario, they occur in rocks that are homogeneously deformed and where the linear fabrics are passive. In another scenario, they are observed in foliated

metamorphic rocks where the planar fabrics are actively deformed (Passchier, 2001; Grasemann and Stüwe, 2001; Grasemann et al., 2003, 2005; Passchier et al., 2008). In addition, flanking structures are present even at the micro-scale, where processes such as mineral growth and shear within one mineral phase can deflect the cleavage planes of another (Mukherjee and Koyi, 2009). In high-grade gneissic rocks, these structures are often associated with thin shear fractures or small elliptical pegmatitic bodies. In such rocks, alternating layers of mafic (melanosome) and felsic (leucosome) minerals create a mechanical anisotropy as a result of heterogeneous slip along their interfaces (Carreras et al., 2013; Goswami and Baruah, 2016). This anisotropy is further enhanced in the presence of biotite (Samanta and Deb, 2014). In schistose rocks, the presence of flaky minerals produces mechanical anisotropy that effectively defines slip surfaces (Cosgrove, 1976; Price and Cosgrove, 1990; Saroglou and Tsiambaos, 2007). Thus, it becomes essential to determine whether the observed geometry of flanking structures is predominantly controlled by the anisotropic behaviour of gneissic layers associated with a cross-cutting fracture element or with a small lensoid pegmatitic body.

Analytical and numerical techniques have been applied to these problems. For instance, Kocher and Mancktelow (2006) demonstrated that strong anisotropy in the host medium promotes the formation of reverse shear bands and reverse *a*–type structures. In contrast, normal or reverse *s*–type flanking structures tend to be diminished under such conditions. However, their model focused on instantaneous flanking structures by representing the sense of offset through the vertical component of velocity. This approach, while informative, makes the overall geometry of the flanking structure challenging to visualize. In reality, the initial geometry of a flanking structure is strongly influenced by the instantaneous flow field but evolves

progressively during continued deformation. In the present study, two-dimensional numerical modeling is used to investigate the progressive development of flanking structures in anisotropic layered rocks. Key parameters considered include the initial orientation of the cross–cutting element (θ), the degree of mechanical anisotropy of the medium (δ), and the orientation of the principal stress axis (ξ). This approach enables detailed visualization of the precise geometries of flanking structures and how these geometries evolve as finite strain accumulates.

5.2 Flanking Structures in Gneissic Rock

Within the Chhotanagpur Granite Gneissic Complex (CGGC), a variety of flanking structures, ranging in length from centimeters to meters, have been documented. These structures, which developed primarily during the last phase of deformation (D4), are related to isolated cross-cutting elements of short length. In the present study, our focus is on those flanking structures that are associated with either a small elliptical quartzo-feldspathic pegmatitic body or with shear fractures that occur without the presence of pegmatite.

We broadly classify these flanking structures into two types (Figs. 5.1a and 5.2):

- ***Type I*: Open-fracture flanking structures**
- ***Type II*: Close-fracture flanking structures**

It is important to note that this classification differs from that described by Mukherjee and Koyi (2009). The geometry of the *Type I* and *Type II* varieties shows a close resemblance to the symmetric (orthorhombic symmetry) and asymmetric

(monoclinic symmetry) internal boudinage or foliation boudinage structures, respectively (Cobbold et al., 1971; Hambrey and Milnes, 1975; Goscombe et al., 2004; Arslan et al., 2008, 2012).

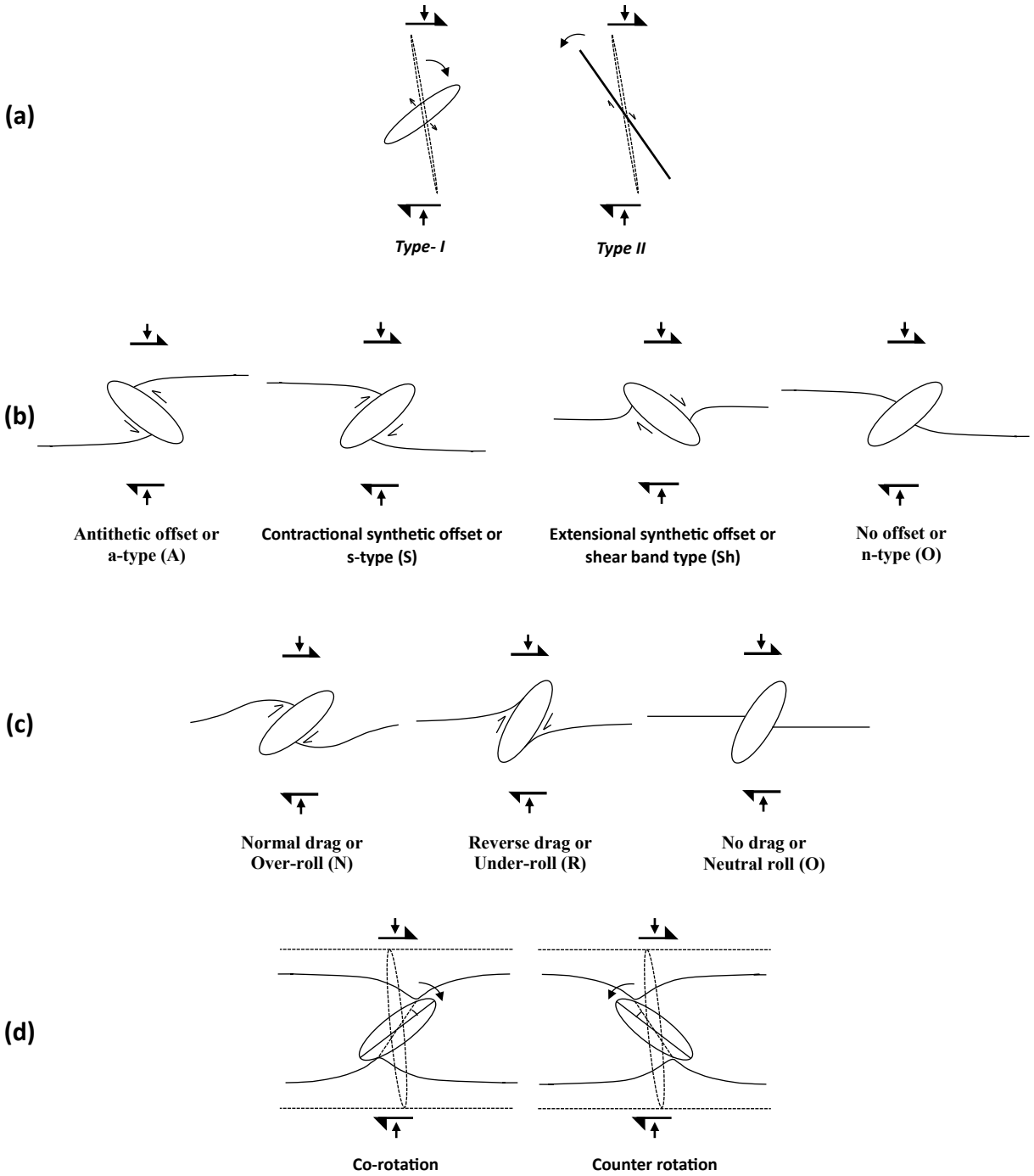

Fig. 5.1: Schematic diagram showing different parameters used for nomenclature of flanking structures. (a) *Types* (*I* or *II*) of flanking structure.; (b) Nature of fabric offset, (c) Fabric drag pattern, (d) Angular shift (β) of tip points with respect to the shear direction; Dashed and solid lines represent initial and final positions respectively.

In many natural instances, flanking structures may be associated with either a single cross-cutting element or with multiple such elements that are aligned in a particular trend and separated by inter-boudin objects. In the present paper, we have chosen to investigate the structures that are associated with a single cross-cutting element/object. Although *Type II* flanking structures are more commonly reported by many researchers (Passchier, 2001; Grasemann et al., 2003; Exner et al., 2004; Grasemann et al., 2019), the *Type I* structure—characterized by the conspicuous dragging of foliations alongside a cross-cutting element—has received comparatively little attention. This is particularly true when the long axis of the cross-cutting element is oriented at a high angle relative to the foliation. Under these circumstances, strong dragging is observed near the closure points of the cross-cutting element, while the central portion exhibits almost no drag (*O*), similar to the neutral (*0*) roll described by others (Mulchrone, 2007a; Coelho et al., 2005).

The nature of the offset in these structures can be further categorized. The offset may be synthetic (characterized by contractional, *S* type, or extensional shear-band, *Sh* type movement) or antithetic (*A*) with respect to the bulk shear direction, or it may display no offset at all (*O*, equivalent to *n*-type) (Figs. 5.1b and 5.2). In addition, the convex or concave geometries of the drag relative to the sense of offset are designated as normal (*N*) or reverse (*R*), respectively (Fig. 5.1c). In the present study, the nomenclature for both natural examples and numerical results is established by the sequential arrangement of these three key features—Shape, Nature of offset, and Pattern of drag. For instance, a flanking structure associated with a small elliptical pegmatitic body that exhibits antithetic offset with normal drag is denoted as *I*-*A*-*N* geometry.

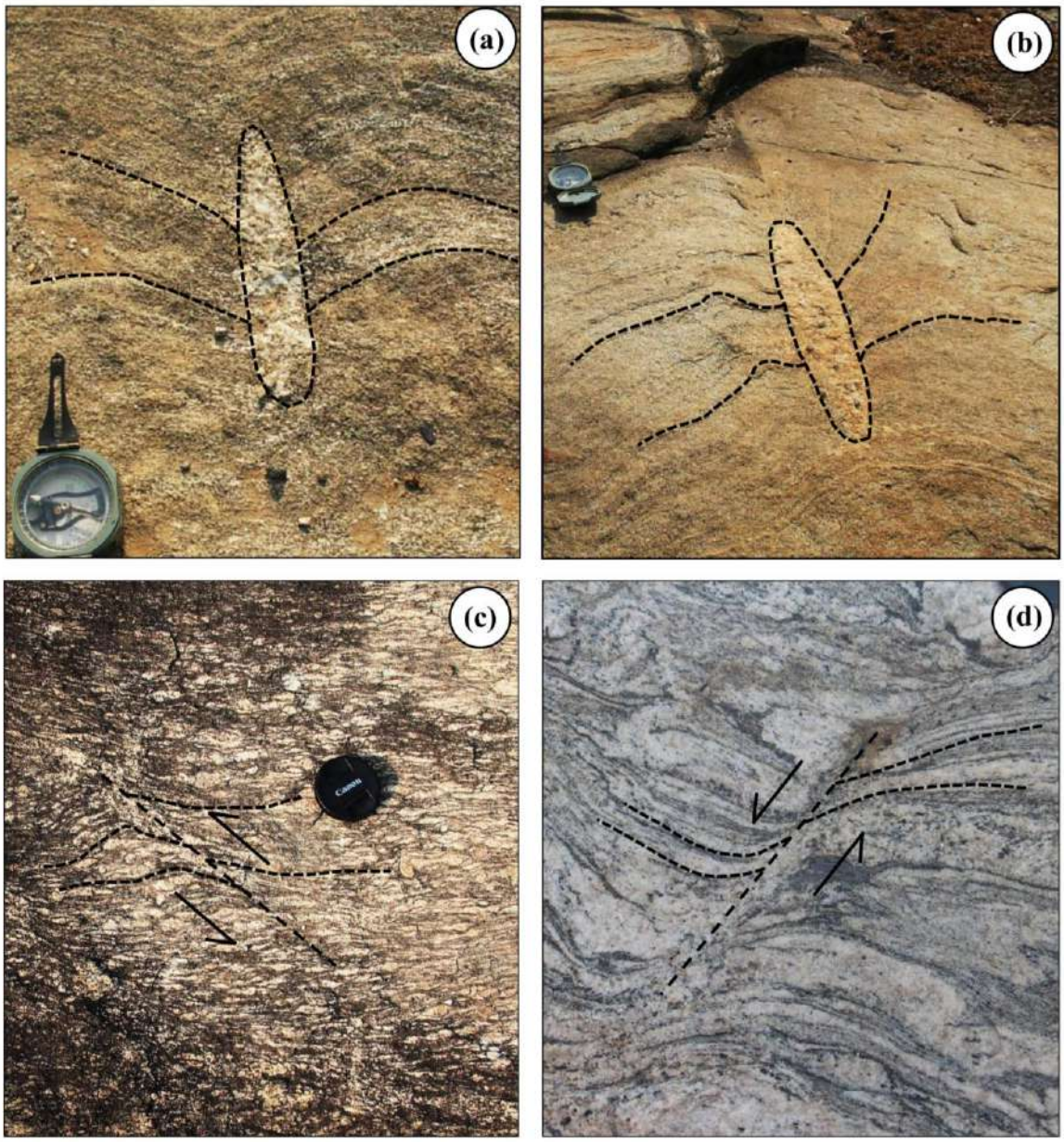

Fig. 5.2: *Type I* and *Type II* flanking structures in gneissic rock. a) *I-O-O* (*Type I* with no offset and no drag) (Loc.- 24°30.600' N 86°40.524' E), b) *I-A-N* (*Type I* with antithetic normal drag) (Loc.- 24°30.722' N 86°40.578' E), c) *II-A-R* (*Type II* with antithetic reverse drag) (Loc.- 24°30.722' N 86°40.578' E), d) *II-A-N* (*Type II* with antithetic normal drag) (Loc.- 23°16.157' N 86°22.020' E). Bulk shear sense is dextral. Diameters of brunton compass and the lens cover are ~ 6.6 and 6.8 cm. respectively and width of photo-plate (d) is ~35 cm.

Spectacular examples of flanking structures from gneissic rocks are discussed in detail below. *Type I* flanking structures are readily identifiable in association with small elliptical pegmatitic bodies (Figs. 5.2a, b and 5.3). It has also been observed that *Type I* flanking structures with a lower aspect ratio tend to occur in biotite-rich

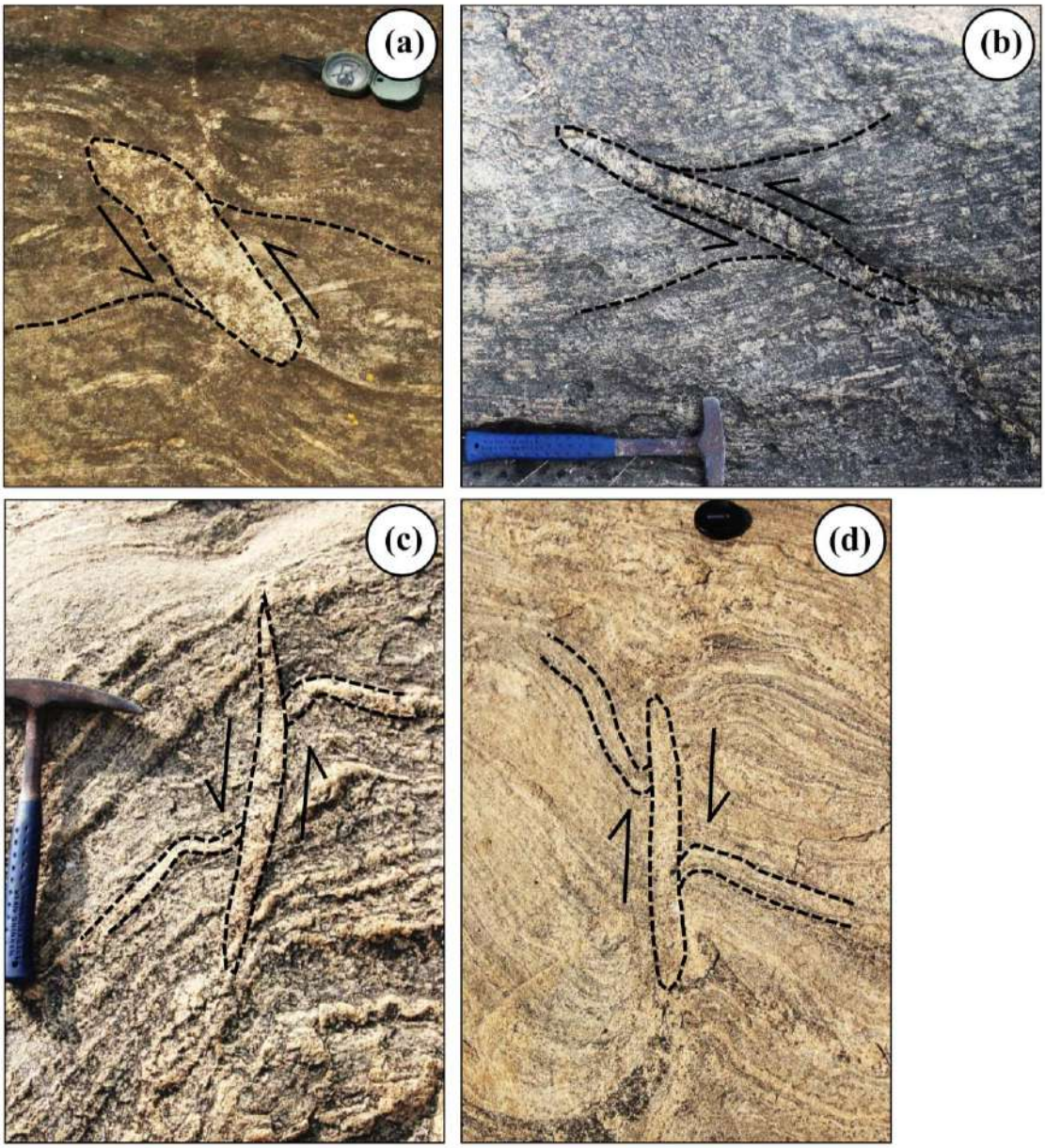

Fig. 5.3: *Type I* flanking structures in gneissic rock. a) *I-A-R* (*Type I* with antithetic reverse drag) (Loc.- 24°30.393' N 86°40.766' E), b) *I-A-R (Type I* with antithetic reverse drag) (Loc.- 24°30.923' N 86°39.375' E), c) *I-A-N* (*Type I* with Antithetic normal drag) (Loc.- 24°30.874' N 86°39.344' E), d) *I-Sh-R* (*Type I* with Shear-band type with reverse drag) (Loc.- 24°30.524' N 86°40.795' E). Bulk shear sense is dextral. Diameters of Brunton compass and the lens cover are ~ 6.6 and 6.8 cm. respectively. The length of geological hammer is ~ 33 cm.

rocks, which likely result in higher mechanical anisotropy. Conversely, *Type II* flanking structures are commonly described as thin shear bands associated with planar fracture discontinuities that occur in the absence of any pegmatitic body (Figs.

5.2c and d). In nature, flanking structures can be either symmetric or asymmetric, and they may occur with or without an offset along the cross-cutting element (Figs. 5.2 and 5.3).

5.3 Numerical Modelling

To gain a deeper understanding of the kinematics and progressive evolution of flanking structures in layered, anisotropic rocks, we have employed two-dimensional numerical modeling using the Finite Element Method (FEM). The following sections provide an in-depth discussion of the model considerations, including the material properties, the treatment of layered anisotropy, the simulation of the cross-cutting element (fracture/object), the model specifications, and the boundary conditions.

5.3.1 Model Consideration

5.3.1.1 Material

In order to investigate the influence of layered anisotropy on the development of flanking structures, two-dimensional numerical modeling was performed under plane strain conditions using the Finite Element Method (FEM) (Ramsay and Lisle, 2000; Arslan et al., 2008; Samanta and Deb, 2014; Samanta et al., 2017). It is acknowledged that the geometry and the values of the physical parameters used in the numerical model are not an exact replication of natural conditions. Consequently, while the results obtained from these simulations do not reproduce the precise

geometries observed in the field, they provide invaluable insights into the kinematics of flanking structures in layered gneissic rocks.

The rheological behaviour of the materials in the model is described by a visco-elastic Maxwell rheology (cf. Zhang et al., 1996; Mancktelow, 1999; Passchier and Druguet, 2002; Samanta and Deb, 2014). This choice is justified because the Maxwell rheology is well suited for simulating deformation in the lower crust, where temperature and confining pressure are high (Turcotte and Schubert, 1982). The constitutive equation for the Maxwell rheology used in our simulations is given by

$$\frac{d\varepsilon}{dt} = \frac{1}{G}\frac{d\sigma}{dt} + \frac{\sigma}{\eta} \qquad (1)$$

where ε and σ represent the instantaneous strain (finite in the case of steady state deformation) and stress, respectively, and G and η denote the Maxwell shear modulus and viscosity, respectively.

5.3.1.2 Layered Anisotropy

In the present study, two-dimensional mechanical anisotropy is modelled as orthotropic (Jaeger and Cook, 1979) or "transversely isotropic" (Banik, 1987) behaviour, meaning that the viscosities differ in two mutually perpendicular directions. The layers in the model are oriented parallel to the x-axis, and the pole of anisotropy (A_p) is aligned parallel to the y-axis. To simulate layered anisotropy in the numerical modeling, we use alternate thin competent and incompetent layers (η_C and η_I for viscosities of competent and incompetent layer respectively) that have equal thickness and are present in equal numbers, with coherent interfaces between them.

Hence the equation 1 and 2 of section 1.1 (Chapter 1: Introduction) are reduced as follows.

$$\eta_N = \frac{\eta_C + \eta_I}{2} \tag{2}$$

$$\eta_S = \frac{2 \times \eta_C \times \eta_I}{\eta_C + \eta_I} \tag{3}$$

Therefore, for this study anisotropic factor (δ) is equated as

$$\delta = \frac{\eta_N}{\eta_S} = \frac{(\eta_C + \eta_I)^2}{4\eta_C \eta_I} \tag{4}$$

Given that the deformation is assumed to be in a steady state and that the two types of layers share the same Poisson's ratio and Maxwell relaxation time, the degree of anisotropy is defined by the anisotropic factor (δ) as follows (Biot, 1957; Weijermars, 1992):

$$\delta = \frac{(\eta_C + \eta_I)^2}{4\eta_C \eta_I} = \frac{(G_C + G_I)^2}{4G_C G_I} = \frac{(E_C + E_I)^2}{4E_C E_I}, \tag{7}$$

where η, G, and E are the viscosity, shear modulus, and elastic modulus, respectively. The subscripts C and I denote competent and incompetent layers, respectively.

5.3.1.3 Cross-Cutting Element/Fracture/Object

In our numerical modeling, the initial cross-cutting element is represented by an elliptical cut with a high aspect ratio. This elliptical cut is oriented such that its long axis forms various angles with the layers of the host element (Grasemann and Stuwe, 2001; Exner et al., 2004; Kocher and Mancktelow, 2006; Exner and

Dabrowski, 2010). During deformation, the two walls of the elliptical cut either slide past or move away from each other, resulting in an observable offset in the layers that cross the cut. To economize on simulation time while remaining consistent with natural conditions, the elliptical cut is maintained as a vacant zone. This approach is justified by assuming that the cut is filled with a highly incompetent viscous material—such as residual metamorphic melt with a viscosity on the order of ~10^5 Pa.s. (Holtz et al., 2001)—embedded within the surrounding quartzo-feldspathic gneissic material (viscosity ~10^{22} Pa.s., Shi and Cao, 2008). Approximately fifty key simulations were run using an elliptical cut filled with low viscous material, and the results were found to be nearly identical.

The geometry of the flanking structures in our models is characterized by several factors: the deformed shape of the cross-cutting element, the sense and magnitude of the offset or slip along the element, and the curvature of the drag pattern relative to the slip sense. In our analyses, five different initial orientations (θ) of the cut are considered (Fig. 5.4). These orientations are 150°, 120°, 90°, 60°, and 30° with respect to the layers, measured anticlockwise. Additional simulations were also performed for other initial orientations to fully explore the parameter space.

5.3.1.4 Model Specifications

Numerical modeling was performed using ABAQUS (ver. 2020), a commercial FEM software package. Following the procedures outlined by Passchier et al. (2005), we verified our numerical results using different model dimensions. To obtain optimal results within a reasonable simulation time, a rectangular block with

dimensions of 200 x 200 units was used. This block consisted of 200 alternating thin competent and incompetent layers, each 1 unit thick. An elliptical opening with an aspect ratio of 200 (with dimensions 40 / 0.2 unit) was inserted at the centre of the model. The long axis of this elliptical opening was oriented at different angles (θ) relative to the layers (Fig. 5.4). A thin layer immediately below the central line of the model was designated as a marker for measuring offset.

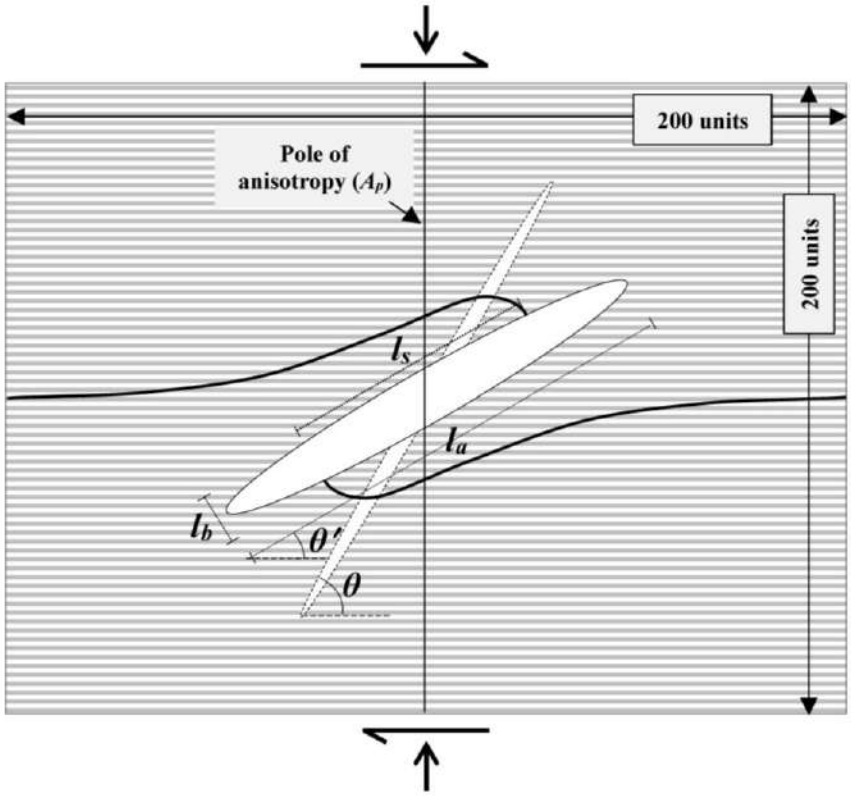

Fig. 5.4: Geometrical parameters (schematic diagram, not in scale) of flanking structure in layered anisotropic medium. l_a and l_b are the length of major and minor axis of elliptical cut after deformation. l_s is the offset length of marker/layers across the element/fracture/object. θ and θ' are the initial (dashed line) and final (solid line) orientations of the major axis of the cross-cutting element respectively. Width of individual layer is 1 unit. Length and width of the initial elliptical cut element was 40 and 0.2 units respectively.

For the simulation, a designated formulation for the viscoelastic material "VISCO" step was adopted, utilizing a full Newtonian solution technique and a direct equation solver method. The total deformation time was set to 1×10^{10} s, which is significantly longer than the Maxwell relaxation time (8×10^{8} s) assumed for the

materials (Larsen et al., 2005; Samanta et al., 2017). The entire model was meshed using quad-dominated free meshing based on an advancing front technique, with an approximate global element size of 0.5 units. This mesh size provided optimal results within the confines of the simulation time. The ABAQUS Standard element CPE4 (a 4-node bilinear plane strain quadrilateral) was used throughout the modeling, with a total of approximately 80,000 elements in the model.

In keeping with natural conditions of deformation in gneissic rocks, the viscosity of the materials was set in the range of 10^{17}–10^{23} Pa. s (Vergnolle et al., 2003; Copley and McKenzie, 2007; Mukherjee, 2013). In the present study, we have chosen four arbitrary materials while ensuring that their properties remain within these natural bounds. The values of the bulk relaxation modulus, shear relaxation modulus, and elastic relaxation modulus were calculated using a constant Poisson's ratio of 0.25. The Maxwell relaxation time was uniformly set at 8×10^{8} s for all materials (Larsen et al., 2005; Samanta et al., 2017). The anisotropy factor (δ) was allowed to vary up to 10, which is consistent with conditions observed in natural settings (Kocher and Mancktelow, 2006), beyond which the influence of the pure shear component becomes negligible. Table 5.1 presents the material properties used in the experiments.

Table 5.1: Material properties used in numerical modelling

Incompetent layer						
Anisotropic Factor (δ)	Viscosity (Pa.s)	Elastic modulus (Pa)	Shear modulus (Pa)	Bulk Modulus (Pa)	Poisson's Ratio	Relaxation time (s)
1	1×10^{20}	3.13×10^{11}	1.25×10^{11}	2.08×10^{11}	0.25	8×10^{8}
3	1.01×10^{19}	3.16×10^{10}	1.26×10^{10}	2.10×10^{10}		
5	5.57×10^{18}	1.74×10^{10}	6.97×10^{9}	1.16×10^{10}		
10	2.63×10^{18}	8.23×10^{9}	3.29×10^{9}	5.49×10^{9}		
Competent layer						
1	1×10^{20}	3.13×10^{11}	1.25×10^{11}	2.08×10^{11}	0.25	8×10^{8}

5.3.1.5 Boundary Conditions

One of the crucial parameters in the present study is the orientation of the principal stress axes. However, numerically applying stress from various directions to simulate progressive deformation is technically challenging. To address this, the numerical simulations were conducted by applying displacement boundary conditions at the model boundaries. These displacements were applied for different anisotropy factors and kinematic vorticity numbers (W_k) as a substitute for varying the orientation of the principal stress axes. Following the relation between the kinematic vorticity number (W_k) and the angle between two flow apophyses (α), where $W_k = \cos \alpha$ (Bobyarchick, 1986), the models were deformed under conditions of pure shear and sub-simple shear (dextral) for W_k values of 0, 0.26, 0.5, 0.71, 0.87, and 0.97. These correspond to α values of 90°, 75°, 60°, 45°, 30°, and 15°, respectively. Displacements were applied at all four boundaries of the model using the following equations:

$$U_x = k.x + \gamma.y \quad (4)$$

$$U_y = -\frac{k}{(1+k)}.y \quad (5)$$

Where $\gamma = \tan \varphi \,.\frac{k-\frac{1}{k}}{2.\ln(k)}$, the effective shear strain and φ is the degree of simple shear and k is the percentage of shortening in decimal (Merle, 1986; Tikoff and Fossen, 1993). The area of the entire model remained constant throughout the simulation. For all experiments, finite shortening was set up to maximum 30% and degree of simple shear was calculated by using the equation $W_k = \cos\left\{\tan^{-1}\frac{2k}{\tan\varphi}\right\}$

(Tikoff and Fossen, 1993). Table 5.2 lists the values of k and γ for different W_k at 10% and 30% shortening.

Table 5.2: Amount of pure and simple shear for different W_k

Kinematic vorticity number (W_k)	Pure shear shortening (k in %)	Simple shear (φ in degree)	Effective Finite shear strain (γ)
0.97	10	35.43	0.71
	30	62.95	1.96
0.87	10	18.27	0.33
	30	42.27	0.91
0.71	10	10.79	0.19
	30	27.69	0.52
0.5	10	6.28	0.11
	30	16.85	0.30
0.26	10	2.92	0.05
	30	8	0.14
0	10	0	0
	30	0	0

5.3.2 Model Results

A total of 360 numerical experiments were performed, varying parameters such as the initial orientation of the cross-cutting element (θ), the anisotropy factor (δ), and the kinematic vorticity number (W_k). The final geometries of the flanking structures obtained from these simulations are classified according to three key features, as proposed in the nomenclature process (Table 5.3). The geometry is quantified by several parameters:

1. The shape of the cross-cutting element, defined by the normalized aspect ratio of the cut after deformation, R_N ($= \frac{l_a/l_b}{200}$).
2. The offset of the marker layer normalized to the final object length, L_N ($= l_s/l_a$). The sense of offset is indicated by synthetic (positive, *S* or *Sh*) or antithetic (negative, *A*) movement relative to the bulk shear direction.
3. The curvature of the drag of the external fabric (Fig. 5.4).

Table 5.3: Geometry of flanking structures obtained from numerical modelling

W_k		0		0.26		0.5		0.71		0.87		0.97	
θ	δ	10%	30%	10%	30%	10%	30%	10%	30%	10%	30%	10%	30%
30°	1	II-A-N	II-A-N	II-A-N	II-A-N	II-A-N	II-A-N	II-A-N	II-A-N	II-S-N	II-S-N	II-S-N	II-S-N
	3	I-A-N	I-A-R	II-A-N	I-A-R	II-A-N	I-A-R	II-A-N	II-A-N	II-A-N	II-A-N	II-A-N	II-A-N
	5	I-A-N	I-A-R	I-A-N	I-A-R	I-A-N	I-A-R	II-A-N	II-A-R	II-A-N	II-A-N	II-A-N	II-A-N
	10	I-A-N	I-A-R	I-A-N	I-A-R	I-A-N	I-A-R	I-A-N	I-A-R	II-A-N	II-A-R	II-A-N	II-A-N
60°	1	I-A-R	I-A-R	I-A-R	I-A-R	II-A-R	II-A-R	II-A-R	II-A-R	II-A-R	II-A-R	II-A-R	II-A-R
	3	I-A-R	I-A-R	I-A-R	I-A-R	I-A-R	I-A-R	I-A-R	I-A-R	I-A-R	II-A-R	II-A-R	II-A-R
	5	I-A-R	I-A-R	I-A-R	I-A-R	I-A-R	I-A-R	I-A-R	I-A-R	I-A-R	II-A-R	II-A-R	II-A-R
	10	I-A-R	I-A-R	I-A-R	I-A-R	I-A-R	I-A-R	I-A-R	I-A-R	I-A-R	I-A-R	II-A-R	II-A-R
90°	1	I-O-O	I-O-O	I-A-R	I-A-R	I-A-R	I-A-R	I-A-R	I-A-R	I-A-R	II-A-R	II-A-R	II-A-R
	3	I-O-O	I-O-O	I-A-R	I-A-R	I-A-R	I-A-R	I-A-R	I-A-R	I-A-R	I-A-R	II-A-R	II-A-R
	5	I-O-O	I-O-O	I-A-R	I-A-R	I-A-R	I-A-R	I-A-R	I-A-R	I-A-R	I-A-R	I-A-R	II-A-R
	10	I-O-O	I-O-O	I-A-R	I-A-R	I-A-R	I-A-R	I-A-R	I-A-R	I-A-R	I-A-R	I-A-R	II-A-R
120°	1	I-Sh-R	I-Sh-R	I-Sh-R	I-Sh-R	I-Sh-R	I-Sh-R	I-Sh-R	I-Sh-R	I-A-N	I-A-N	I-A-N	II-A-N
	3	I-Sh-R	I-Sh-R	I-Sh-R	I-Sh-R	I-Sh-R	I-Sh-R	I-Sh-R	I-Sh-R	I-Sh-R	I-A-N	I-A-N	I-A-N
	5	I-Sh-R	I-Sh-R	I-Sh-R	I-Sh-R	I-Sh-R	I-Sh-R	I-Sh-R	I-Sh-R	I-Sh-R	I-A-N	I-A-N	I-A-N
	10	I-Sh-R	I-Sh-R	I-Sh-R	I-Sh-R	I-Sh-R	I-Sh-R	I-Sh-R	I-Sh-R	I-Sh-R	I-A-N	I-A-N	I-A-N
150°	1	II-Sh-N	II-Sh-N	II-Sh-N	II-Sh-N	II-Sh-N	II-Sh-N	I-Sh-N	I-Sh-N	I-Sh-N	I-Sh-R	I-Sh-R	I-Sh-R
	3	I-Sh-N	I-Sh-R	I-Sh-N	I-Sh-R	I-Sh-N	I-Sh-R	I-Sh-N	I-Sh-R	I-Sh-N	I-Sh-R	I-Sh-R	I-Sh-R
	5	I-Sh-N	I-Sh-R	I-Sh-N	I-Sh-R	I-Sh-N	I-Sh-R	I-Sh-N	I-Sh-R	I-Sh-N	I-Sh-R	I-Sh-R	I-Sh-R
	10	I-Sh-N	I-Sh-R	I-Sh-N	I-Sh-R	I-Sh-N	I-Sh-R	I-Sh-N	I-Sh-R	I-Sh-R	I-Sh-R	I-Sh-R	I-Sh-R

In progressive deformation, shape of the cross-cutting element may apparently change by shifting their original tip points and developing a new position of long axis of the cross-cutting element. The original tip points can easily be recognized by the maximum bending of external fabric element near the closures of the elliptical object. Shifting of tip points depends on the degree of anisotropy which may be towards (co-rotation) or opposite (counter-rotation) to bulk shear direction (Fig. 5.1d). In presence of high degree of anisotropy, the shape of cross-cutting element may even transform to rhombic geometry. Thus, the shape of cross-cutting element, amount of offset and the shifting of tip points (measured by angle between old and new long axis) are considered to be important parameters for determining anisotropic factor.

Progressive development of flanking structure in numerical modelling is described separately for different zones categorizing by the initial orientation of cross-cutting element. Three broad zones are identified, separated by the maximum and minimum principal stress axes (σ_1 and σ_2) based on sense of slip (Fig. 5.5). Zone 1 and 2 are further subdivided in two subzones separated by the compressional flow apophyse (a_2) and pole of anisotropy (A_p) respectively on the basis of slip and drag pattern. Another two small zones showing normal drag were described by the approximately 30^o both clockwise and anticlockwise from the extensional flow apophyse (a_1) (Grasemann et al., 2005; Kocher and Mancktelow, 2006). However, the above zonation was established based on instantaneous flanking structure. So, the final geometry of structures depends on the initial orientation of the cut element, kinematic vorticity number (W_k), the anisotropy factor (δ) and the final orientation of the CE (θ') (indirectly amount of finite strain). For a specific orientation of principal stress axis, the compressional flow apophyse (a_2) deviates away from the pole of anisotropy with increasing anisotropy factor (δ). When the principal stress (ξ) is

oriented at high angle with the pole of anisotropy (A_p), there is little or no differences in geometries in both isotropic and anisotropic medium (Fig. 1.1, Chapter 1). However, the difference becomes significant in case of lower orientation of principal stress (ξ), specially at higher finite strain when the cut element crosses pole of anisotropy. When the initial cut does not cross the pole of anisotropy, the drag pattern remains relatively simpler in geometry. To represent natural situation, the final geometries of flanking structures obtained from the numerical modelling for 10% and 30% of shortening are presented in Table 5.3.

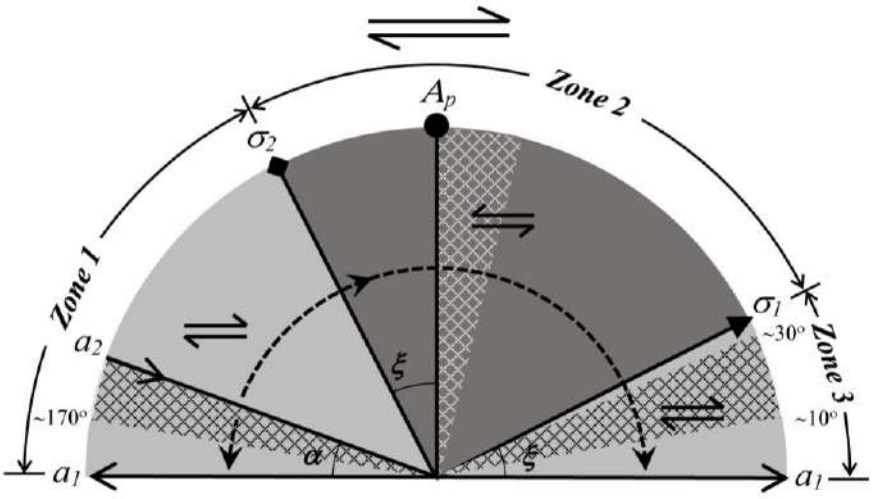

Fig. 5.5: Zones of synthetic (Zones 1 and 3) and antithetic (Zone 2) offset with respect to the flow apophyses (a_1 and a_2), principal stress axes (σ_1 and σ_2) and pole of anisotropy (A_p). a_1 and a_2 - Extensional and compressional flow apophyses; α- Acute angle between two flow apophyses; ξ – Orientation of principal stress axes. Note that the position of a_2 (α) depends on ξ. Curved dashed lines with arrow indicate the sense of rotation (co-rotation and counter-rotation). Light and dark grey zones indicate zones of synthetic and antithetic offset respectively. Crosshatch fields indicate zones of normal drag.

5.3.2.1 Shape of Cross-Cutting Element

One of the most critical criteria for classifying flanking structures in a layered anisotropic medium is the shape of the cross-cutting element. This is quantified by

the normalized aspect ratio (R_N). As deformation progresses, the originally slender elliptical cut may change its apparent shape, including an apparent rotation of its long axis. The deformed shape can be broadly categorized into two geometries. In some cases, the cross-cutting element remains nearly closed without any significant opening, a situation that is termed as a *Type II* structure ($R_N \approx 1$). In contrast, in other cases, the cross-cutting element opens up, transforming into an elliptical or even circular shape, which is termed as a *Type I* structure ($R_N < 1$). *Type I* structures tend to form when the cut element is initially oriented at a relatively low angle with respect to the compressional flow apophyse (a_2), the orientation of which itself varies with the anisotropy factor for a given stress axis orientation. With increasing anisotropy, the direction of the compressional flow apophyse (a_2) makes a larger angle with the minimum principal stress direction (σ_2). Thus, flanking structures with complex drag patterns are relatively rare, while *Type I* flanking structures are generally more common in rocks with higher anisotropy. At higher W_k values, *Type II* structures are observed when the initial orientation of the cut element is less than 90° (i.e., near the pole of anisotropy). In a deformation regime dominated by pure shear ($W_k < 0.8$), the R_N value consistently tends to decrease with increasing anisotropy for all initial orientations (Fig. 5.6). In Table 5.3, structures are classified as *Type I* when the R_N value is lower than 1. In highly anisotropic layers, the cross-cutting element may even evolve into a parallelogram shape, reminiscent of the "mica-fish" structure observed at higher finite strain (Fig. 5.7).

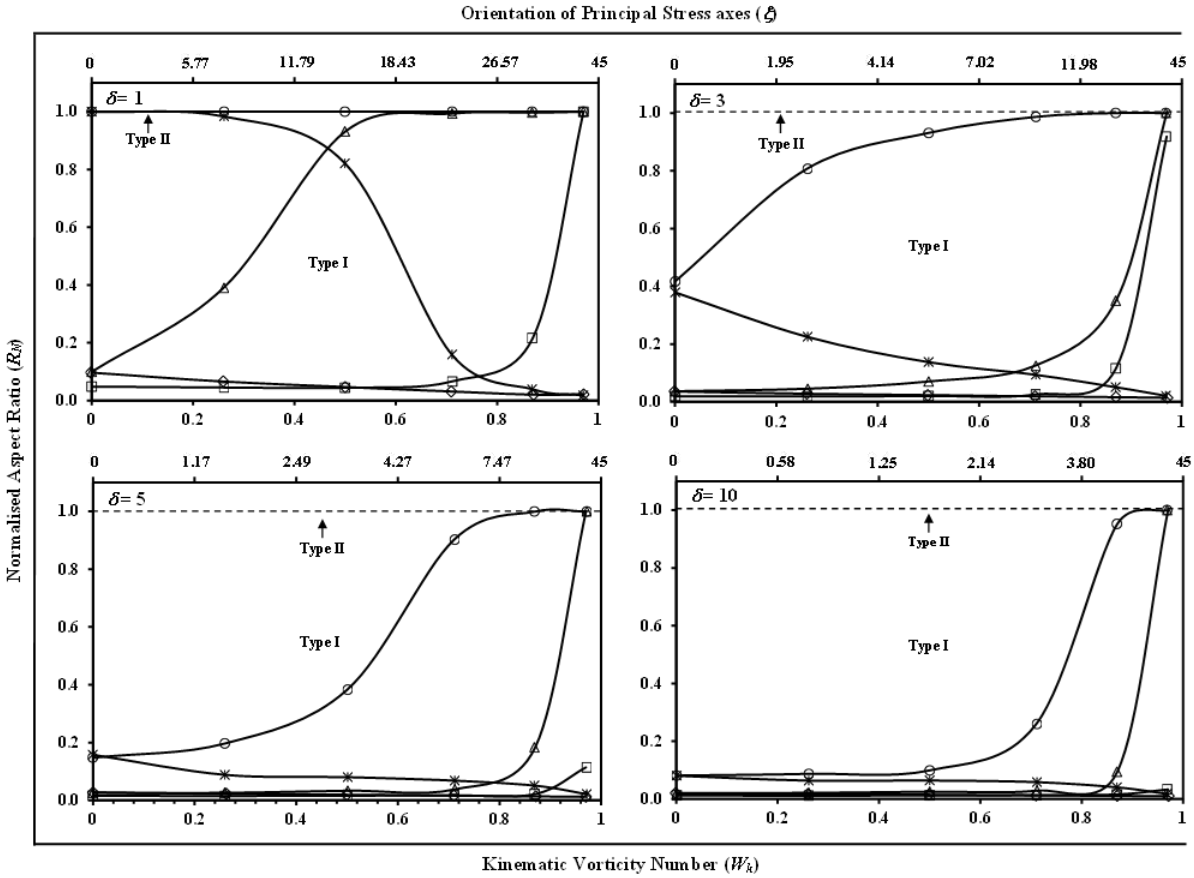

Fig. 5.6: Variation of normalised aspect ratio (R_N) with kinematic vorticity number (W_k) for different initial orientation of cross-cutting element (θ). Note for *Type I*, $R_N < 1$ and for *Type II*, $R_N \approx 1$. o : $\theta = 30^o$, Δ : $\theta = 60^o$, □: $\theta = 90^o$, ◊: $\theta = 120^o$ and x: $\theta = 150^o$. Finite shortening is 10%.

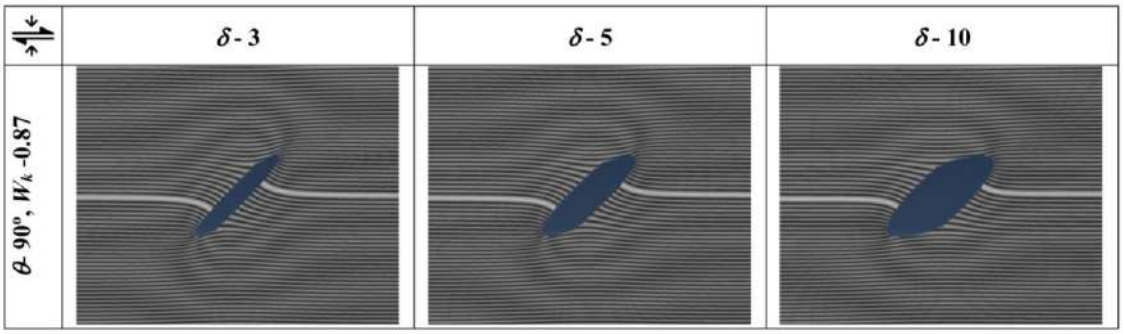

Fig. 5.7: Development of mica-fish like geometry of cross-cutting element with increasing anisotropy. Finite shortening is 20%.

5.3.2.2 Amount and Sense of Offset of Planar Fabric

The offset of the planar fabric is quantified by the parameter normalized offset length (L_N), which is measured from the slip indicated by the marker line along the long axis of the cross-cutting element. The sense of the offset is defined by its relation to the bulk shear direction: if the offset results from synthetic movement, it is recorded as a positive offset (*S* or *Sh*), whereas if the offset is antithetic, it is recorded as a negative offset (*A*). The amount and sense of offset are strongly dependent on the progressive rotation of the cross-cutting element from its initial to its final position relative to the principal stress axes and the pole of anisotropy. For example, if the cross-cutting element initially lies within Zone 2, an antithetic offset develops; however, if it is initially oriented at an angle greater than that of the minimum principal stress (σ_2) (Zone 1) or less than that of the maximum principal stress (σ_1) (Zone 3), the offset will display a synthetic sense (Figs. 5.5 and 5.8).

5.3.2.3 Drag Pattern of Planar Fabric

The drag pattern of the external planar fabrics adjacent to the cross-cutting element is described in terms of whether the curvature is normal or reverse. The criterion is based on whether the convexity of the drag is directed towards or opposite to the sense of offset. Published literature does not provide a direct one-to-one relationship between the geometry of flanking structures and the orientation of flow apophyses, the principal stress axes, or the pole of anisotropy. For instantaneous deformation, fields of normal drag have been demarcated at approximately 30° clockwise and anticlockwise relative to the extensional flow apophyse, with the

remainder of the field showing reverse drag (Grasemann et al., 2005; Kocher and Mancktelow, 2006). However, this demarcation is valid only at very low finite strains in an isotropic medium. In an anisotropic medium, the fields of normal drag depend on the degree of anisotropy, the position of the compressional flow apophyse, and the amount of finite strain achieved during deformation.

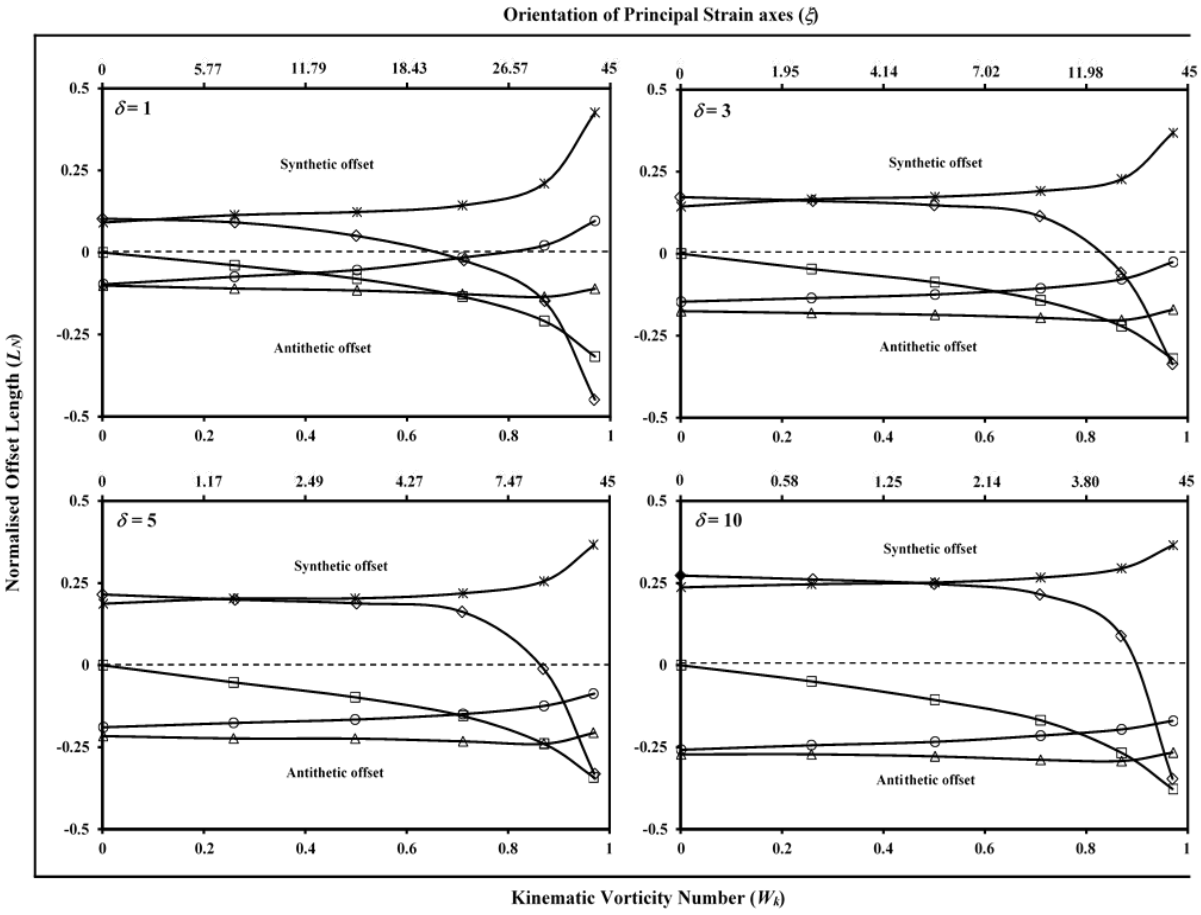

Fig. 5.8: Variation of normalised offset (L_N) of external fabric with kinematic vorticity number (W_k) for different initial orientation of cross-cutting element (θ). o : $\theta = 30^o$, Δ : $\theta = 60^o$, □: $\theta = 90^o$, ◊: $\theta = 120^o$ and x: $\theta = 150^o$. Finite shortening is 10%.

In the regime of co-rotation (when $\theta < a_2$ or $\theta < 180°\text{-}\alpha$), two distinct fields of normal drag are observed: one field extends from the pole of anisotropy (A_p) toward the shear direction, and a second field is observed between approximately 30°

and 10°. In contrast, in the regime of counter-rotation (when $\theta > a_2$ or $\theta > 180°-\alpha$), the lower limit of the normal drag field is fixed at approximately 170°, while the upper limit is defined by the position of the compressional flow apophyse (a_2), with a maximum limit of about 150° (Fig. 5.5). If the cross-cutting element remains entirely within the ranges from a_2 to A_p or from A_p to 30° during progressive deformation, the drag pattern remains unchanged. However, the drag geometry can become complex if the element crosses these demarcated boundaries. It has been observed that reverse drag patterns may transform into normal drag, resulting in fold-like complex structures when the cross-cutting element crosses the pole of anisotropy (A_p) during deformation (Figs. 5.2d, 5.3c, and 5.5). In these cases, the complexity of the drag pattern increases with an increasing anisotropy factor. Interestingly, under progressive deformation, a normal drag pattern can also transform back into a reverse drag pattern if the cross-cutting element moves from a field of normal drag to one of reverse drag. In general, higher anisotropy tends to favour the development of reverse drag (Kocher and Mancktelow, 2006).

5.3.2.4 Shifting of Tip Points of Cross-Cutting Element

The numerical results clearly reveal that Type I flanking structures are particularly common in strongly anisotropic layered rocks (see Table 5.3). During progressive deformation, in the case of *Type I* flanking structures, the cross-cutting element undergoes a slight rotation and gradually changes its shape. This change is characterized by the migration or shifting of the original tip points, resulting in the development of a new long axis. The initial tip points can be readily identified by the sharp bending observed in the external fabrics near the boundaries of the cross-

cutting element (Fig. 5.1d). The amount of shifting depends on the initial position of the cross-cutting element relative to the pole of anisotropy, the orientation of the principal stress axes, and the positions of the flow apophyses during deformation. At lower finite strain, if the initial orientation of the long axis of the cross-cutting element is ≤ 90° (or is aligned with A_p), the long axis shifts towards the bulk shear direction (co-rotation). Conversely, if the initial orientation is more than 90° (with respect to A_p), the shifting is in the opposite sense (counter-rotation) (Fig. 5.9). Under conditions of simple shear-dominated deformation, if the cross-cutting element crosses the pole of anisotropy during deformation, the sense of rotation may even reverse. Due to this shifting of tip points from their original positions, the cross-cutting element appears to have rotated either synthetically (co-rotation) or antithetically (counter-rotation) relative to the bulk shear rotation (Figs. 5.1d, 5.9 and 5.10). Notably, this rotation of the long axis is particularly prominent in *Type I* flanking structures. The phenomenon is similar to the deformation observed in low-viscosity inclusions (Grasemann and Stüwe, 2001; Mancktelow, 2011; Grujic and Mancktelow, 2022) and to the rotation of rigid objects under slip-interface conditions (Mancktelow et al., 2002; Samanta and Bhattacharyya, 2003; Mulchrone, 2007b; Johnson et al., 2009; Mancktelow, 2013; Jiang, 2016), where the estimated mean kinematic vorticity number (W_m) is typically found to be lower than the actual value.

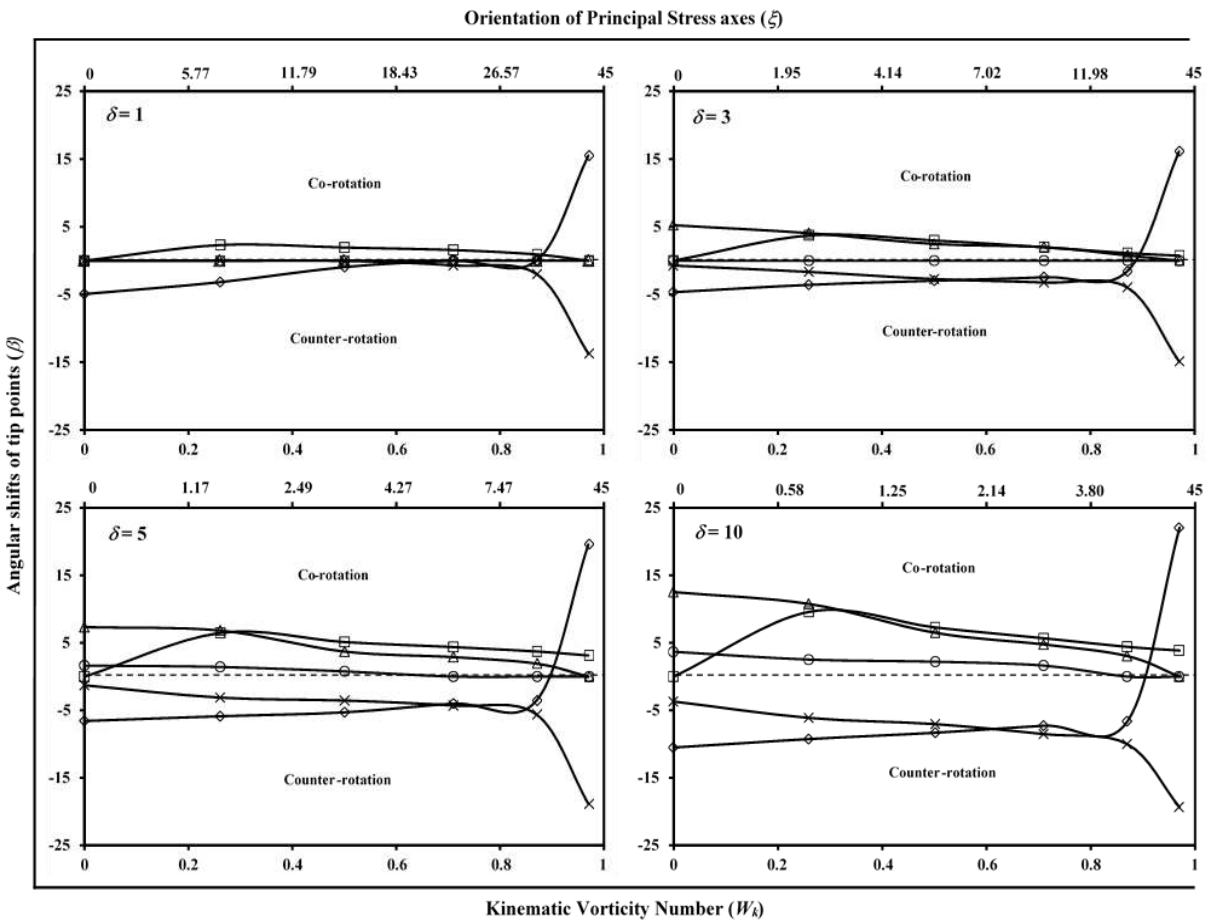

Fig. 5.9: Variation of angular shift of tip points (β) of cross cutting-object with kinematic vorticity number (W_k) for different initial orientation of cross-cutting element (θ). o : $\theta = 30^o$, Δ : $\theta = 60^o$, □: $\theta = 90^o$, ◊: $\theta = 120^o$ and x: $\theta = 150^o$. Finite shortening is 10%.

5.4 Discussions

5.4.1 Progressive Development of Flanking Structures

To approximate natural conditions, our numerical simulations were run to a maximum of 30% shortening for various values of W_k. The results obtained at 30% shortening for different anisotropy factors are compared in Fig. 5.11. It is evident from these results that the final geometry of a flanking structure is dependent on the progressive change in the position of the long axis of the cross-cutting element

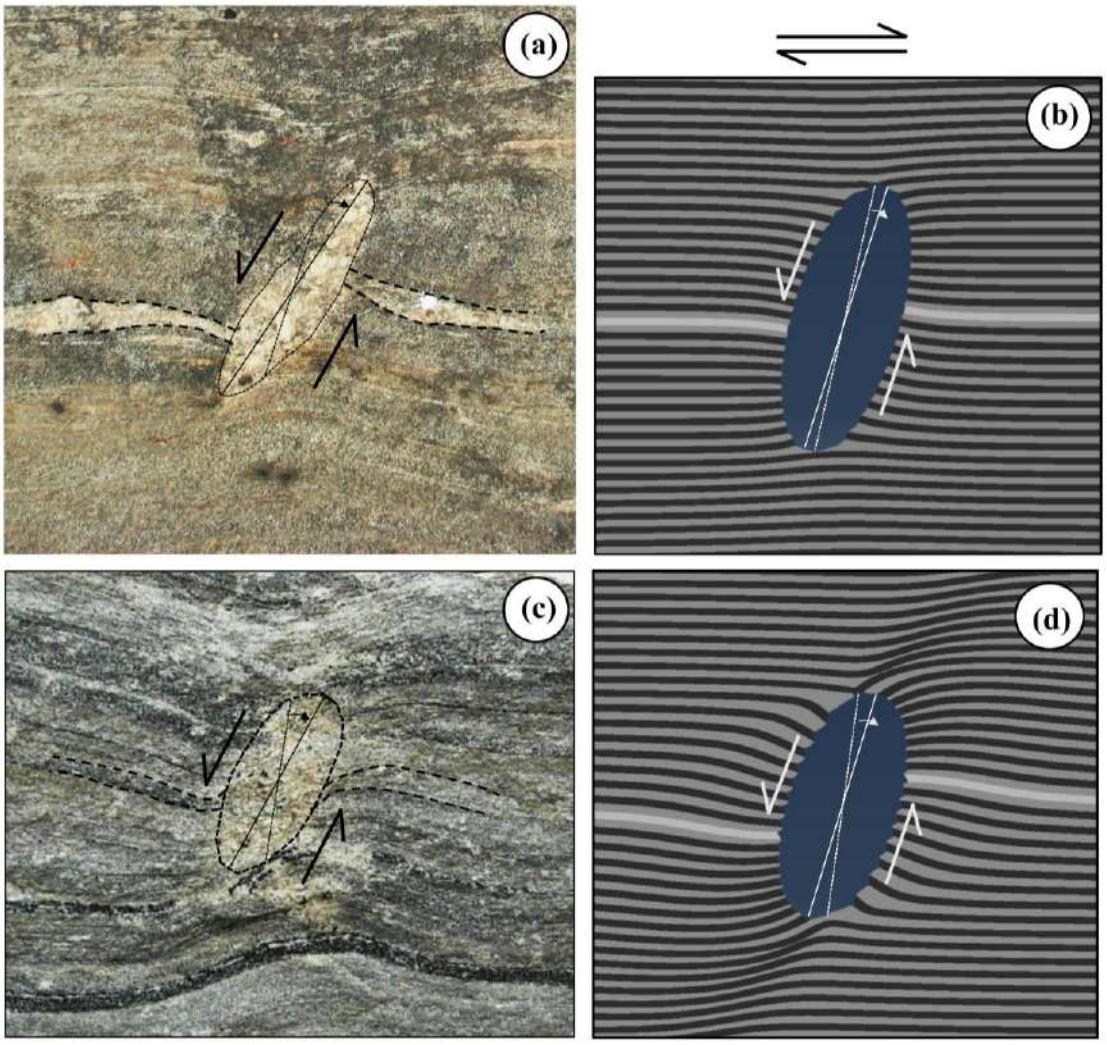

Fig. 5.10: Comparison of *Type I* flanking structures from gneissic rock in Jasidih area and results obtained from numerical modelling. (a) *I-A-R* flanking structure with shifting of tip point (Loc.- 24°30.232' N 86°40.659' E), (b) Numerical results representing (a) at $\theta = 90^{o}$, $W_k = 0.71$, $\delta = 10$; (c) *I-A-N* flanking structure without shifting of tip point (Loc.- 24°30.197' N 86°40.557' E). (d) Numerical results representing (c) at $\theta = 120^{o}$, $W_k = 0.97$, $\delta = 10$. Note that they have developed in layered medium with higher mechanical anisotropy. The shifting of tip points in all cases is clockwise i.e. co-rotation. Dashed and solid lines indicate initial and final axis of the cross-cutting element. Finite shortening of the numerical results are 10%.

relative to the flow apophyses, the principal stress axes, and the pole of anisotropy. With increasing finite strain, the geometry of the flanking structures becomes more complex, reflecting systematic changes in specific parameters as the cross-cutting element migrates from one field to another. At higher finite strains, *Type II* flanking structures become predominant as the cross-cutting element rotates from the pole of

anisotropy (A_p) toward the extensional flow apophyse. In rocks with higher anisotropy, particularly under simple shear-dominated deformation, high strain zones tend to localize in the vicinity of the cross-cutting element, originating from its initial tip points (Fig. 5.11).

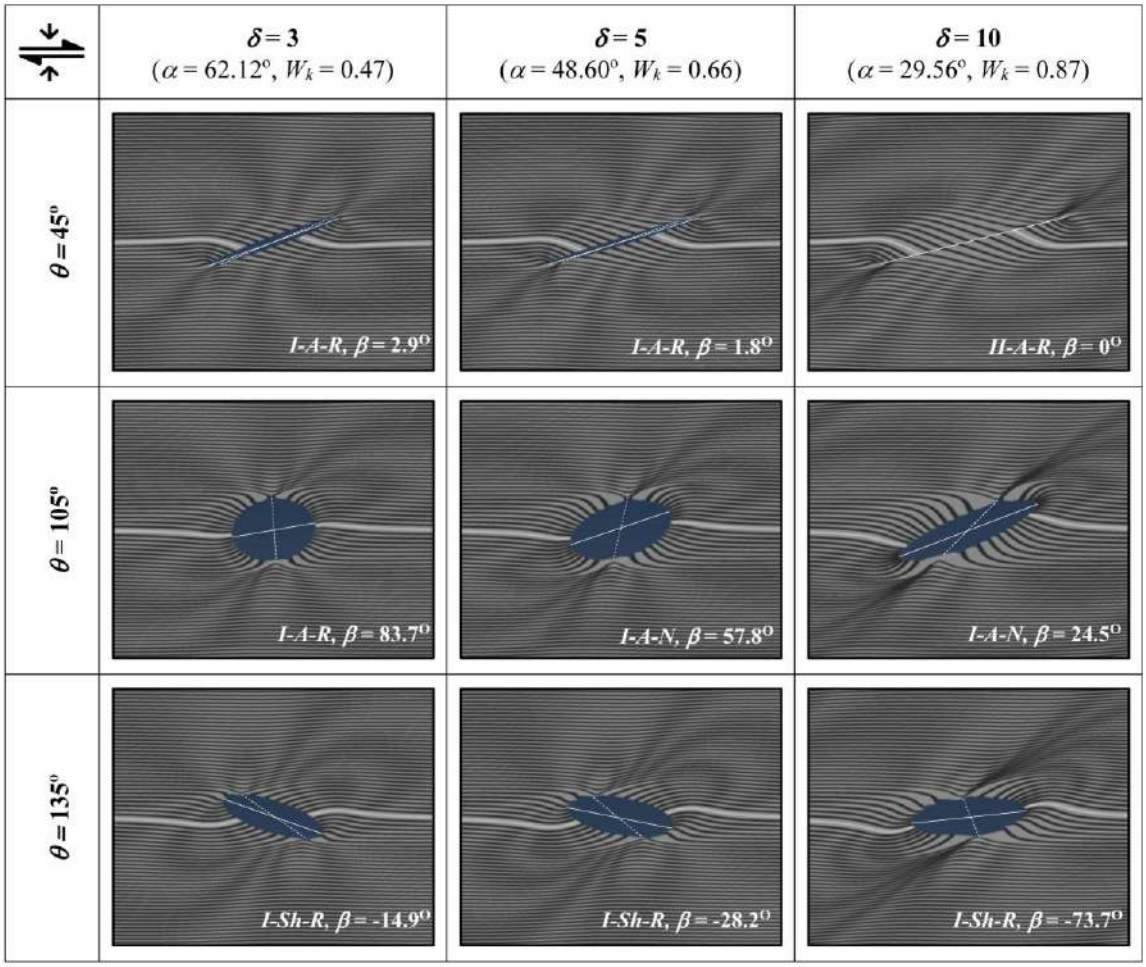

Fig. 5.11: Flanking structures showing the shape of cross-cutting element, nature of offset, drag pattern and angular shifting of axis (β, acute angle between dashed and solid white lines) with increasing anisotropy factor (δ) and W_k for $\boldsymbol{\xi = 5^o}$**.** Central part (cropped image) of the model is shown. Finite shortening is 30%.

In layered anisotropic rocks, cross-cutting elements are initially formed in two distinct orientations, designated as C1 and C2, at a low angle relative to the minimum principal stress axis (Fig. 5.12) (Platt and Vissers, 1980; Gomez-Rivas et

al., 2015). As deformation progresses, Type I structures evolve through the opening of these fractures, with subsequent filling by fluid under favourable conditions. Due to their positions relative to the flow apophyses, both types of fracture-filled objects tend to rotate toward the shear direction, and their shapes change temporarily depending on the degree of anisotropy and the overall bulk deformation. Flanking structures associated with C1 fractures initially exhibit a synthetic offset with reverse drag, but as deformation progresses and the fracture crosses the minimum principal stress axis, the offset gradually transforms into an antithetic offset. In contrast, flanking structures associated with C2 fractures consistently show an antithetic offset. Additionally, the drag pattern may transform from reverse to normal at higher finite strains when the cross-cutting element crosses the pole of anisotropy. Therefore, *Type I* flanking structures (such as *I-A-R* and *I-A-N*) are very common in the gneissic terrain under study. In some cases, a *Type I* flanking structure may develop without any offset if the long axis of the fracture is initially oriented almost parallel to the minimum principal stress axis and at a low angle to the pole of anisotropy (A_p). However, when the principal stress axis forms a high angle with the pole of anisotropy, offset accompanied by the dragging of external planar fabrics becomes more pronounced.

5.4.2 Estimation of Mechanical Anisotropy

The Chhotanagpur Gneissic Complex is characterized by rocks that commonly contain mafic dykes embedded within gneissic units composed of alternating layers of mafic (e.g., pyroxene, amphibole, biotite) and felsic (e.g., quartz, feldspar) minerals. The process of H_2O infiltration through granitic intrusions

has led to the transformation of pyroxene into amphibole during progressive deformation. At later stages, amphibole is further converted into biotite as a result of potassium (K^+)-metasomatism (Ray et al., 2011). Consequently, biotitization is often more pronounced near the margins of the pegmatitic bodies. As discussed in Sections 4.3.2.1 and 4.4.1, *Type I* flanking structures are especially common in the vicinity of larger pegmatitic bodies, where the effects of biotitization are most prominent (Fig. 5.10c).

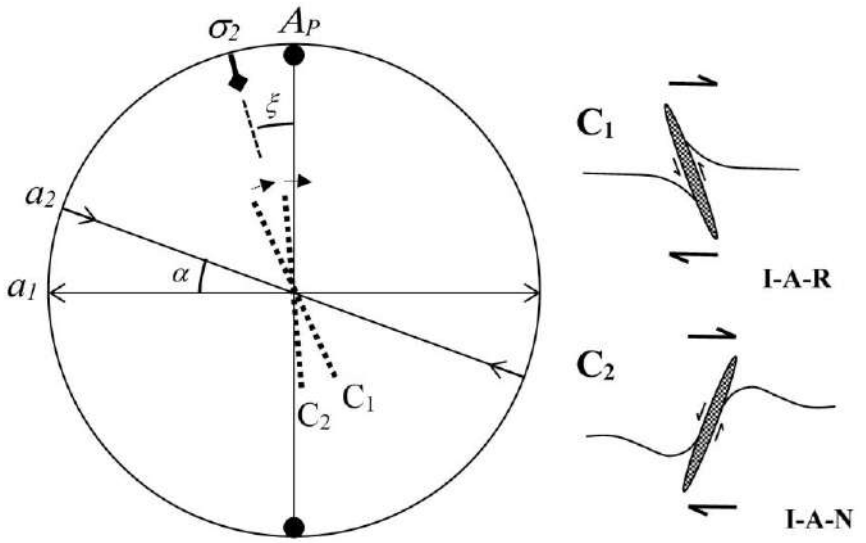

Fig. 5.12: Progressive development of flanking structures associated with cut elements (shear fractures) of different orientations with respect to minimum principal stress axis (σ_2). Note that $\alpha \approx 19^o$ for $\xi \approx 15^o$ and $\delta \approx 5$. Two sets of fractures (C_1 and C_2) do not necessarily form at same location. See the Fig. 5.5 for the fields of offset and drag pattern.

In deformed geological terrains, the orientation of the tectonic stress or principal stress axis tends to remain spatially constant for layers with a similar strike. Therefore, in natural settings, layered rocks with the same strike may exhibit different kinematic vorticity numbers (W_k) if the degree of mechanical anisotropy varies (Weijermars, 1992; Kocher and Mancktelow, 2006). Layered rocks with

higher anisotropy are more likely to be deformed predominantly under simple shear flow. After a thorough analysis of our numerical results and the controlling parameters, it is apparent that the geometry of flanking structures can serve as an important qualitative tool for estimating the degree of mechanical anisotropy in layered rock systems. The propensity for developing a *Type I* flanking structure increases with the anisotropy factor (Table 5.3). In natural conditions, the effect of layer anisotropy is likely to be more prominently preserved in deformed terrains where the paleo-stress direction (ζ) is relatively low (Fig. 1.1, Chapter 1).

Three key parameters—R_N (normalized aspect ratio of the cross-cutting element), L_N (normalized offset length), and β (the shifting of tip points)—can be employed to estimate the degree of anisotropy, depending on the final orientation (θ') of the cross-cutting element relative to the foliation plane. If the final orientation (θ') is less than 90°, then R_N increases and β decreases with increasing anisotropy. Conversely, if the orientation (θ) is greater than 90°, the relationships are reversed. In all cases, L_N increases with increasing anisotropy (Fig. 5.11).

5.5 Limitations

Despite the detailed nature of the numerical model, several limitations must be acknowledged. In migmatitic gneiss, cross-cutting elements may undergo dynamic growth and changes in geometry depending on the degree of partial melting. Such dynamic modifications can have a significant impact on the deformation behaviour of an anisotropic layer, especially at higher finite strains (Druguet and Carreras, 2006; Arslan et al., 2008). To simplify the numerical model, we have

assumed that the cross-cutting fracture remains stationary in terms of its geometry during deformation—that is, we have considered only the changes in the shape of the cross-cutting fracture, without any additional growth, analogous to a stationary fracture (Arslan et al., 2008). In natural systems, however, the geometry of flanking structures may be modified by later stages of deformation, and these additional effects should be considered when comparing numerical results with natural examples.

5.6. Conclusions

The integrated study of flanking structures as documented from layered gneissic rocks, combined with our comprehensive numerical modeling, leads to the following conclusions:

i. Mechanical anisotropy exerts a strong influence on the geometry of flanking structures in layered gneissic rocks.

ii. The geometry of flanking structures in layered anisotropic rocks depends on both the initial orientation (θ) and the final orientation (θ') of the cross-cutting element relative to the principal stress axes and the pole of anisotropy as deformation progresses.

iii. The shape of the cross-cutting element (R_N), the shifting of its tip points (β), and the amount of layer offset (L_N) are the most critical parameters for estimating the anisotropy factor.

iv. The normalized offset length (L_N) consistently increases with increasing anisotropy factor. When $\theta' < 90°$, the normalized aspect ratio (R_N) increases and the tip point shift (β) decreases with increasing anisotropy; the relationships are reversed when $\theta' > 90°$.

Chapter 6

Flanking Structures in Simple Shear Regime

6.1 Introduction

Flanking structures develop as a result of the dragging and deflection of planar fabrics within a rock body, particularly in regions where a marked rheological contrast exists (Passchier, 2001; Grasemann and Stüwe, 2001). These structures are of significant importance because they help to unravel the kinematic conditions—such as shear sense and magnitude—imprinted on a deformed rock mass (Wiesmayr and Grasemann, 2005; Kocher and Mancktelow, 2005). Essentially, the formation of flanking structures occurs when planar fabrics are deflected or "dragged" in the vicinity of a cross-cutting element (CE), a process that can occur under a variety of kinematic regimes including pure shear, simple shear, and general shear environments.

A number of numerical and analogue modeling studies have attempted to decipher the formation and pattern of these instantaneous flanking structures, often assuming a homogeneous isotropic matrix (Grasemann and Stüwe, 2001; Grasemann et al., 2003; Exner et al., 2004, 2006; Kocher and Mancktelow, 2005; Wiesmayr and Grasemann, 2005; Grasemann et al., 2005; Mulchrone, 2007a, b; Grasemann et al., 2019; Mayrhofer et al., 2022). In these studies, the initial cross-cutting element is typically modelled as a planar discontinuity, along which the surrounding fabric experiences minimal alteration in shape. Kocher and Mancktelow (2006) were among the first to introduce the effect of layered anisotropy into the modeling of instantaneous flanking structures. More recently, Basu Majumder and Samanta (2023) employed numerical modeling under general shear conditions—by varying both the kinematic vorticity number and the anisotropy factor—to document the progressive development of flanking structures.

Previous studies, such as those by Grasemann and Stüwe (2001) and Exner et al. (2004), have primarily focused on the formation of flanking structures under the sole influence of simple shear, using a limited set of initial orientations for the cross-cutting element. Consequently, the full spectrum of flanking structures that can develop under simple shear conditions has not been entirely captured. Moreover, many earlier works concentrated exclusively on the instantaneous orientation of the long axis of the deformed CE for structural analyses. In contrast, Basu Majumder and Samanta (2023) demonstrated that the initial orientation of the CE is equally critical in determining its final geometry. They also introduced a classification scheme that differentiates between *Type I* (open) and *Type II* (closed) cross-cutting elements, thereby broadening the perspective on the role of anisotropy.

Although both Kocher and Mancktelow (2006) and Basu Majumder and Samanta (2023) have explored the influence of anisotropy on flanking structure formation, none of these studies have isolated the effect of simple shear on the development of flanking structures within an anisotropic regime. According to Weijermars (1992), who introduced the anisotropy factor (δ) in geology, achieving pure simple shear conditions (with a kinematic vorticity number, $W_k = 1$) requires that the angular relation (ξ) between the pole of anisotropy and the principal stress axis be 135° (measured counter-clockwise with respect to the shear plane), irrespective of δ. Similarly, for a pure shear condition ($W_k = 0$), ξ must be 0°. However, Basu Majumder and Samanta (2023) noted that even when kinematic conditions remain constant (for $W_k = 0$), structural variations can occur at both finer and more significant scales. These variations likely result from heterogeneities induced by the alternating layering of competent and incompetent materials, which is representative of natural settings.

In this chapter, we utilize numerical modeling to investigate the effect of anisotropy on flanking structure development under simple shear conditions. By maintaining the same material properties and model configuration as used by Basu Majumder and Samanta (2023) but altering the boundary conditions from general shear to simple shear, our study focuses on isolating the impact of anisotropy. We aim to examine the progressive development of flanking structures in a simple shear regime and to propose a nomenclature for probable structures observed at different deformation intervals.

6.2 Numerical Modelling

6.2.1 Model Consideration

To explore the geometric patterns of flanking structures under progressive simple shear, we have adopted the identical model setup and material properties as described by Basu Majumder and Samanta (2023). However, we have modified the boundary conditions from general shear (where the kinematic vorticity number, W_k, is less than 1) to a simple shear condition ($W_k = 1$), applied in a dextral sense.

The boundary conditions for the simple shear case are prescribed as follows:

$$U_x = x.\gamma \tag{1}$$

$$U_y = 0 \tag{2}$$

where $\gamma = \tan(\psi)$ represents the strain induced by simple shearing, and ψ is the degree of simple shear. The numerical modelling was performed using ABAQUS (ver. 2024). In our model, the initial orientation (θ) of the preexisting cross-cutting element (CE) is measured counter-clockwise with respect to the shear plane. Because

previous studies have demonstrated that the final geometry of a flanking structure is strongly influenced by the initial orientation of the CE's long axis, we consider a range of θ from 150° to 165° at regular 15° intervals. To focus primarily on the initiation of flanking structures—with progressive deformation being a secondary consideration—we also fix the degree of simple shear ψ to vary from 10° to 40° at 15° intervals.

The effect of layered anisotropy is incorporated using the anisotropy factor (δ) as prescribed by Weijermars (1992). To capture the geometrical diversity of flanking structures, we consider both an isotropic homogeneous matrix ($\delta = 1$) and anisotropic homogeneous matrices with $\delta = 3$, 5, and 10 (Kocher and Mancktelow, 2006; Basu Majumder and Samanta, 2023).

6.2.2 Model Results

A total of 176 numerical simulations were performed. The outcomes of these simulations are described by the final geometry of the flanking structures, following the definitions provided by Basu Majumder and Samanta (2023). In addition, a new orientation factor (ω) has been introduced to quantify the rotation of the CE's initial orientation (α) as ψ and δ increase. The ω factor, discussed in detail in later sections, offers insights into the degree and direction of rotation of the CE. It is important to note that the shifting of tip points is essentially excluded in these simulations because that feature is only significant when pure shear is a part of the deformation process.

6.2.2.1 Shape of the Cross-Cutting Element

Basu Majumder and Samanta (2023) defined the shape of the CE in terms of a normalized aspect ratio (R_N). This R_N is the ratio of the deformed aspect ratio (measured as the ratio of the major to the minor axis of the deformed elliptical CE) to its initial aspect ratio (assumed to be 200). The CE's deformed shape can either remain closed—referred to as a *Type II* CE, where $R_N \approx 1$—or open, corresponding to a *Type I* CE (where $R_N < 1$).

Our simulations reveal that when $\theta \leq 90°$—meaning that the CE's long axis is initially inclined below the pole of anisotropy and oriented toward the bulk shear direction—a *Type II* CE is produced. This result is in good agreement with analogue experiments conducted by Exner et al. (2004). It has also been shown that increasing the amount of simple shear (i.e., by increasing the effective shear strain, which in turn increases W_k) tends to favour the development of *Type II* CEs over *Type I*. Conversely, when $\theta > 90°$, the majority of cases exhibit a *Type I* CE, implying that both the initial and the final orientations of the CE's long axis are crucial in these scenarios. For $\theta \leq 90°$, the normalized aspect ratio (R_N) appears to be independent of the anisotropy factor δ. However, for $\theta > 90°$, within the regime where a *Type I* CE is observed, R_N increases with increasing δ—an observation that contrasts with findings under general shear conditions (Basu Majumder and Samanta, 2023). Consequently, at higher levels of shear, the probability of obtaining a *Type II* CE increases (see Fig. 6.1).

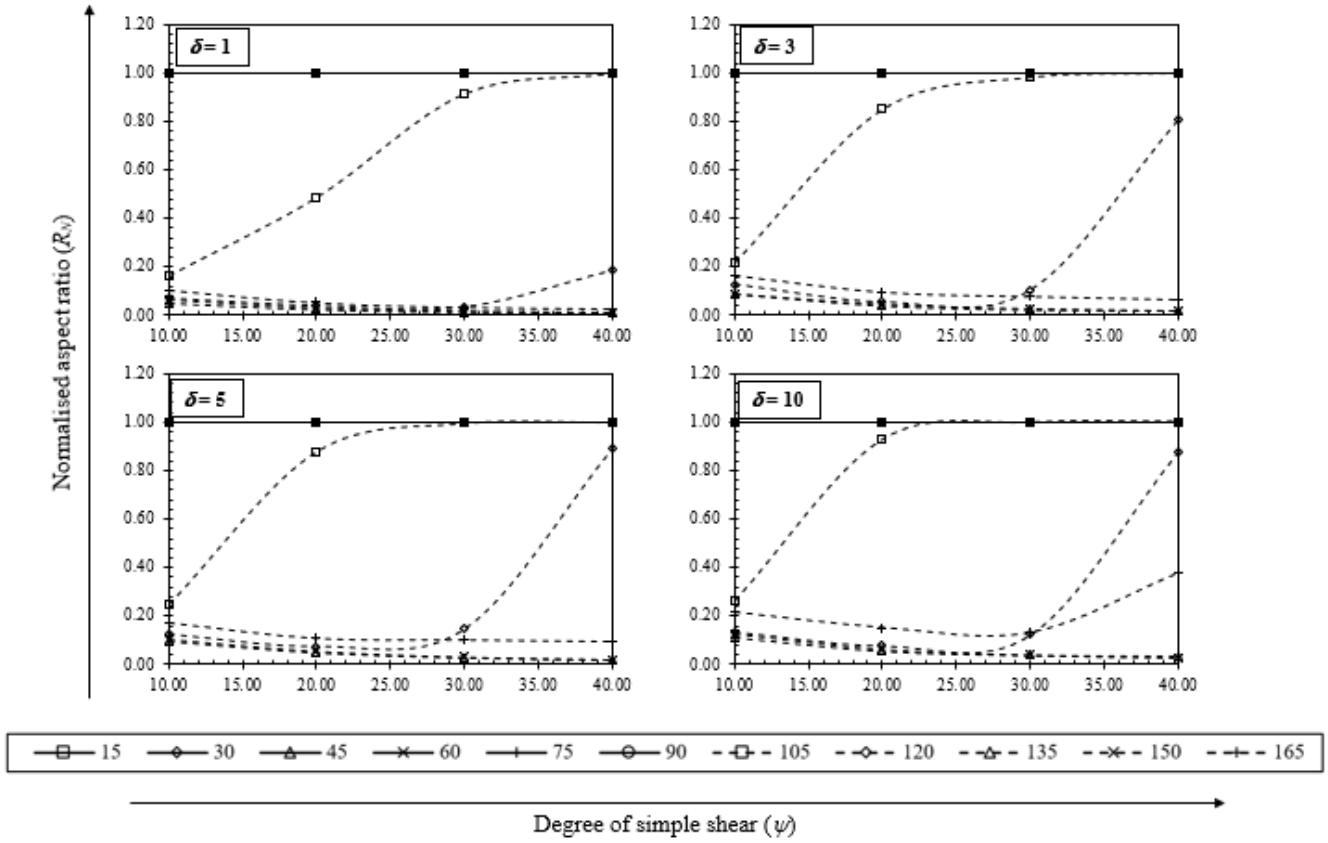

Fig. 6.1: Variation of normalised aspect ratio (R_N) with degree of simple shear (ψ) for different initial orientation of cross-cutting element (θ).

6.2.2.2 Amount and Sense of Offset of Planar Fabric

The normalized offset length (L_N) is defined as the ratio of the offset length—generated by the displacement of the central marker line—to the final length of the deformed CE (Basu Majumder and Samanta, 2023). The sense of the offset is determined by comparing the relative displacement along the CE's long axis with the bulk shear direction. When the offset is in the same direction as the bulk shear, it is termed synthetic (*s*-type or *sh*-type, indicated by a positive sign). Conversely, when the offset is opposite to the bulk shear direction, it is classified as antithetic (*a*-type, indicated by a negative sign).

Analysis of the simulation results (see Table 6.1) indicates that synthetic offsets are common when $\theta \leq (180° - \xi)$, i.e., for $\theta \leq 45°$. For initial orientations greater than this threshold, up to 150°, antithetic offsets tend to develop. At an initial orientation of $\theta = 165°$, synthetic (*sh*-type) offsets are again observed due to counter-rotation of the CE's long axis relative to the shear direction. For synthetic offsets, the absolute value of L_N decreases as θ increases. The behaviour is reversed for antithetic offsets up to $\theta \leq 90°$, although for initial orientations just above the pole of anisotropy, the offset behaviour becomes more complex. In general, for antithetic offsets with $\theta > 90°$, the absolute value of L_N behaves similarly to synthetic offsets. Additionally, when all other parameters are held constant, increasing the anisotropy factor δ leads to a decrease in L_N. In particular, within the transition zone between normal s-type and reverse *a*-type offsets—recognized for initial orientations between 45° and 60°— L_N is nearly negligible, indicating an absence of offset and a condition of neutral dragging (Exner et al., 2004). This observation further implies that with higher δ values, the range of L_N is constricted, thereby reducing the impact of the initial orientation (α) in a strongly anisotropic regime (see Fig. 6.2).

6.2.2.3 Drag Pattern of Planar Fabric

The drag pattern of the surrounding planar fabric is characterized as "normal" when the fabric exhibits a convex curvature oriented toward the direction of slip along the CE, and "reverse" when the curvature is concave relative to the slip direction. Our simulations show that for initial orientations $\theta \leq (180° - \xi)$, normal drag is predominant. For values of θ within the range $(180° - \xi) < \theta < \xi$, reverse drag appears, whereas for $\theta \geq \xi$, normal drag prevails again. Notably, at higher strains—

Table 6.1
Geometry of flanking structures obtained from numerical modelling

δ		**1**		**3**		**5**		**10**	
ψ		10^0	40^0	10^0	40^0	10^0	40^0	10^0	40^0
θ	15^0	*II-S-N*	*II-S-N*	*II-S-N*	*II-S-N*	*II-S-N*	*II-S-N*	*II-S-N*	*II-S-N*
	30^0	*II-S-N*	*II-S-N*	*II-S-N*	*II-S-N*	*II-S-N*	*II-S-N*	*II-S-N*	*II-S-N*
	45^0	*II-S-N*	*II-S-N*	*II-A-R*	*II-S-N*	*II-A-R*	*II-S-N*	*II-A-R*	*II-S-N*
	60^0	*II-A-R*	*II-A-R*	*II-A-R*	*II-A-R*	*II-A-R*	*II-A-R*	*II-A-R*	*II-A-R*
	75^0	*II-A-R*	*II-A-R*	*II-A-R*	*II-A-R*	*II-A-R*	*II-A-N*	*II-A-R*	*II-A-N*
	90^0	*II-A-R*	*II-A-R*	*II-A-R*	*II-A-R*	*II-A-R*	*II-A-R*	*II-A-R*	*II-A-R*
	105^0	*I-A-R*	*II-A-R*	*I-A-R*	*II-A-R*	*I-A-R*	*II-A-R*	*I-A-R*	*II-A-R*
	120^0	*I-A-R*	*I-A-R*	*I-A-R*	*I-A-R*	*I-A-R*	*I-A-R*	*I-A-R*	*I-A-N*
	135^0	*I-A-N*	*I-A-N*	*I-A-N*	*I-A-N*	*I-A-N*	*I-A-N*	*I-A-N*	*I-A-N*
	150^0	*I-A-N*	*I-A-N*	*I-A-N*	*I-A-N*	*I-A-N*	*I-A-N*	*I-A-N*	*I-A-N*
	165^0	*I-Sh-R*	*I-Sh-N*	*I-Sh-N*	*I-Sh-N*	*I-Sh-N*	*I-Sh-N*	*I-Sh-N*	*I-Sh-N*

specifically for initial orientations of 75° and 165° in cases with high anisotropy (δ)—the drag pattern transitions from reverse to normal. The phenomenon of reverse-to-normal drag transition in an isotropic medium at higher strains, as well as the development of normal *s*-type flanking folds from reverse a-type structures under conditions where $\theta \leq (180° - \xi)$, has been previously documented by Exner et al. (2004). In anisotropic media, however, the transition to normal drag occurs at lower strain levels compared to the isotropic case. Furthermore, in contrast to general shear regimes—where higher anisotropy typically promotes reverse drag (Kocher and Mancktelow, 2006)—in a simple shear regime, higher anisotropy appears to favour normal drag. At the transitional interval between normal and reverse drag (specifically for initial orientations between 45° and 60°), the drag effect becomes

minimal, effectively resulting in a neutral drag appearance. Careful interpretation is required in these cases due to the subtle nature of the observed changes.

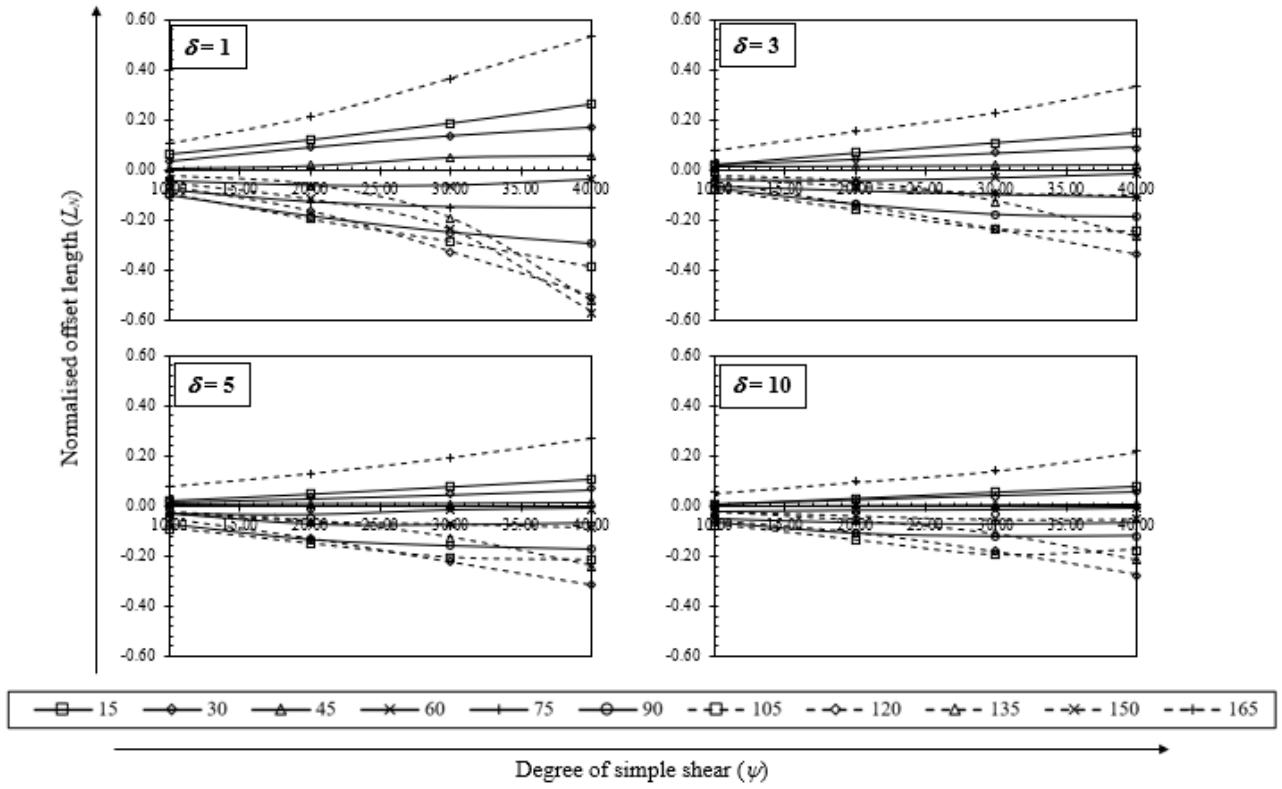

Fig. 6.2: Variation of normalised offset (L_N) of external fabric with degree of simple shear (ψ) for different initial orientation of cross-cutting element (θ).

6.2.2.4 Orientation of the Long Axis of the CE

Under the influence of simple shear, the long axis of the cross-cutting element (CE) rotates during deformation. However, the rate and direction of this rotation—whether co-rotational (aligned with the bulk shear direction) or counter-rotational—are not uniform. To quantify this behaviour, we introduce an orientation factor (ω), defined as the ratio of the current orientation of the CE's long axis to its initial orientation (θ). Values of ω less than 1 indicate co-rotation, ω equal to 1 signifies no rotation, and ω greater than 1 implies counter-rotation with respect to the bulk shear sense.

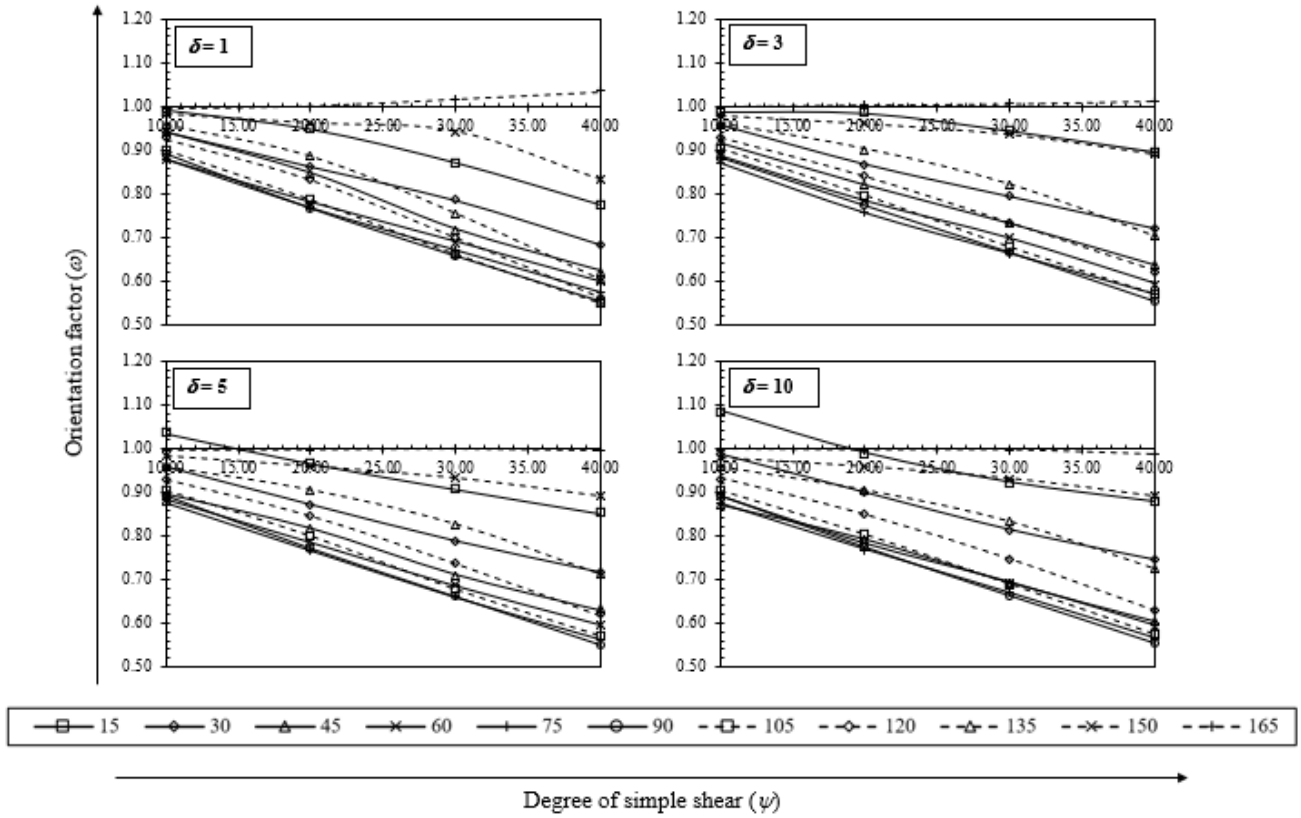

Fig. 6.3: Variation of orientation factor (ω) of external fabric with degree of simple shear (ψ) for different initial orientation of cross-cutting element (θ).

For initial orientations below the pole of anisotropy ($\theta \leq 90°$), our simulations show that ω gradually decreases with increasing θ, indicating that flanking structures with their CE initially oriented more toward the shear direction exhibit a higher rate of co-rotation. In contrast, for $\theta > 90°$, ω increases with θ, indicating a sluggish co-rotation or even counter-rotation of the CE's long axis. Even in lower anisotropy or isotropic conditions, an initial orientation of $\theta = 165°$ results in counter-rotation. In general, a higher anisotropy factor favours a greater rate of co-rotation (or reduced counter-rotation) for $\theta \leq 90°$, whereas for $\theta > 90°$ the trend is reversed (see Fig. 6.3).

6.3 Discussion

Flanking structures are ubiquitous features within shear zones, as documented by numerous studies (e.g., Grasemann and Stüwe, 2001; Grasemann et al., 2003; Exner et al., 2004; Wiesmayr and Grasemann, 2005). Despite their prevalence, the specific effect of a layered anisotropic medium on the formation of flanking structures under a pure simple shear regime had not been fully explored until recently. In this study, we have concentrated on the initial stages of deformation by applying up to 40° of simple shear parallel to the layers. As observed in previous general shear approaches, our results indicate that higher finite strains tend to favour the formation of *Type II* flanking structures. For initial orientations where $\theta \leq 90°$ (i.e., below the pole of anisotropy), only *Type II* CEs are observed, independent of the anisotropy factor δ. However, for initial orientations greater than 90°, *Type I* structures dominate at least during the early phases of deformation.

An interesting observation in our simulations is that, under general shear conditions, counter-rotation of the CE's long axis is typically restricted to orientations lying between the acute angles generated by the compressional and extensional flow apophyses (Basu Majumder and Samanta, 2023). In the simple shear regime, however, where the flow apophyses tend to coalesce and eventually align with the shear direction, counter-rotation is observed even at an initial orientation of $\theta = 165°$. This observation aligns with the understanding that in simple shear, the relative positioning of the principal stress axis—assumed here to be at 135° counter-clockwise—plays a critical role in the initiation of mode I fractures within the range of 120° to 150°. Additionally, shear fractures may form below the pole of anisotropy, ensuring that both *Type I* and *Type II* structures are common in flanking structures associated with simple shear deformation (see Fig. 6.4).

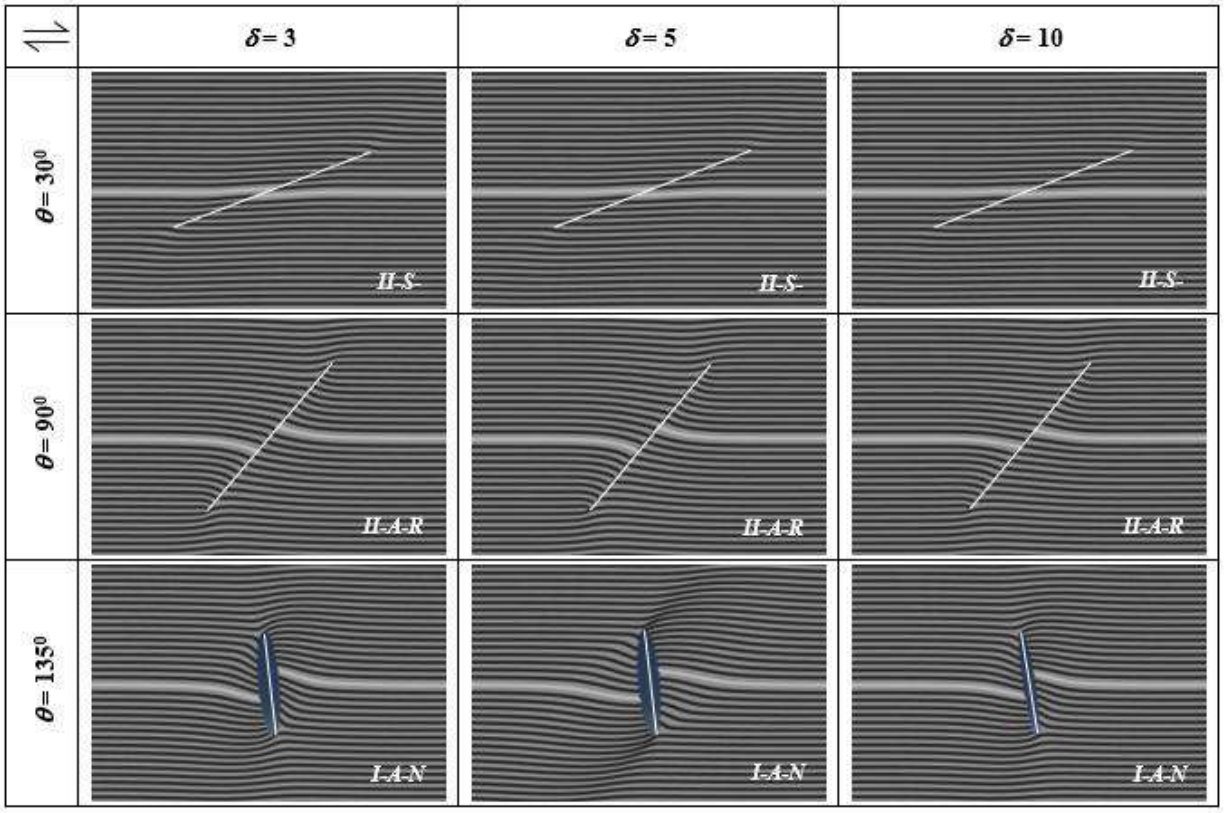

Fig. 6.4: Flanking structures showing the shape of cross-cutting element, nature of offset, drag pattern and angular shifting of axis (β, acute angle between dashed and solid white lines) with increasing anisotropy factor (δ). Finite shear strain (γ) is 0.84.

Given that our primary focus is on the final geometry of flanking structures at the time of their formation, our study does not extensively address the quantification of the anisotropy factor under conditions of very high finite strain. Nevertheless, for rocks experiencing low to medium grades of deformation ($\gamma \leq 1$), our results suggest that the normalized offset length (L_N) is the most sensitive parameter for estimating δ qualitatively. In general, an increase in δ leads to a decrease in the absolute value of L_N and a gradual increase in the normalized aspect ratio (R_N) for *Type I* structures (which are typically observed for $\theta > 90°$). Furthermore, a conversion from reverse to normal drag is observed under high anisotropy conditions when all other parameters are held constant. These findings imply that, although the effects of

anisotropy in simple shear are less pronounced than those under general shear, it is still possible to infer the degree of anisotropy from the geometrical characteristics of flanking structures.

6.4 Limitations

The primary objective of this research is to determine the geometry of flanking structures under simple shear in the initial stages of deformation. To maintain focus on this objective, the maximum degree of simple shear applied in our simulations was fixed at 40°. It is important to note that in natural environments, higher degrees of simple shear are possible, and deformation is often accompanied by an additional pure shear component. Moreover, during natural deformation processes, partial melting of layers may occur, particularly in gneissic terrains, where the cross-cutting element (CE) may grow and change its geometry dynamically. Such effects, which can significantly influence the behaviour of an anisotropic layer at high finite strains (Druguet and Carreras, 2006; Arslan et al., 2008), have been deliberately omitted from our current model. Instead, we have adopted a modelling approach similar to that of Basu Majumder and Samanta (2023) and Arslan et al. (2008), in which the CE is allowed to change shape (e.g., open versus closed) but is not permitted to grow during deformation. It should be acknowledged that subsequent deformation processes, which might further modify the flanking structures, need to be considered when comparing numerical results with natural examples.

6.5 Conclusions

Based on the numerical modelling and analysis presented in this chapter, the following conclusions can be drawn regarding flanking structures generated under the influence of simple shear:

1. **Relative Influence of Layered Anisotropy:**

   In the simple shear regime, layered anisotropy does not exert as strong an effect on the formation of flanking structures as it does under general shear conditions. Although anisotropy remains an important factor, its influence is comparatively more subdued when simple shear is the dominant kinematic regime.

2. **Importance of Initial and Final Orientation:**

   Similar to findings in general shear deformation, both the initial and the final orientations of the CE's long axis (with respect to the pole of anisotropy and the principal stress axes) are equally critical in determining the final geometry of the flanking structure. The evolution of these orientations controls the transition between *Type I* (open) and *Type II* (closed) cross-cutting elements.

3. **Stagnation Zone in Offset Behaviour:**

   For initial orientations in the range of 45° to 65°, the long axis of the CE and the principal stress axis are nearly concurrent in their extensional component, leading to minimal displacement (L_N tends to zero). This transition—from normal s-type to reverse a-type offset—results in a drag pattern that appears neutral. This range, which we refer to as a point of stagnation, requires careful structural analysis.

4. **Normalized Offset Length (L_N) as a Key Parameter:**

   Among the various geometric parameters, the normalized offset length (L_N), defined as the ratio of the offset length to the final length of the CE, is the most sensitive indicator for estimating the anisotropy factor (δ). As δ increases, the absolute value of L_N decreases.

5. **Shape of the Cross-Cutting Element (R_N):**

   The openness of the CE, quantified by the normalized aspect ratio (R_N), is particularly relevant for *Type I* flanking structures. R_N not only reflects the degree of opening but also provides insights into the probable initial orientation of the CE relative to the pole of anisotropy. In our simple shear simulations, R_N increases with increasing δ for initial orientations greater than 90°.

6. **Drag Pattern Transition:**

   In contrast with general shear conditions—where higher anisotropy typically leads to a preference for reverse drag—in the simple shear regime, a higher anisotropy factor favours the development of normal drag. At transitional orientations ($45° \leq \theta \leq 60°$), the drag may become nearly neutral, indicating a delicate balance in the deformation process.

In summary, our study demonstrates that under simple shear conditions, the final geometry of flanking structures is a function of the initial orientation of the cross-cutting element, the degree of layered anisotropy, and the imposed shear strain. The geometric parameters R_N, L_N, and the newly introduced orientation factor ω collectively provide a robust framework for estimating the anisotropy factor and understanding the kinematic evolution of flanking structures.

Chapter 7

Discussions and Conclusions

7.1 Introduction

This final chapter synthesizes the extensive experimental, numerical, and theoretical work presented in Chapters 3 through 6, thereby forming the culminating discussion of this thesis. It aims to provide a comprehensive analysis of deformation processes in layered rocks as investigated through studies of torn boudinage, folds in layered rock and flanking structures under both transpressional and simple shear regimes. The chapter elaborates on the problem identification, assumptions, methodologies, results, and comparative evaluations inherent in each of these studies. In doing so, it places the findings within the context of established theoretical frameworks and field observations, and it discusses their broader implications for structural geology and tectonics. The discussion is organized into several major sections that cover an overview of the thesis contributions, detailed analyses of each deformation process, a critical evaluation of the experimental and numerical methods employed, an integration with existing theoretical models, broader implications for geosciences, directions for future research, and final concluding remarks. This chapter is intended to serve not only as a synthesis of the research but also as a self-contained narrative that documents the fundamentals and technical details in a collaborative and cohesive manner.

7.2 Overview of Thesis Contributions

The research presented in this thesis addresses the intricate interplay between mechanical heterogeneity, strain localization, and interlayer interactions in deformed layered rocks. Each chapter has focused on a different structural phenomenon, and together they contribute a comprehensive understanding of the deformation

processes. In Chapter 3, the focus was on torn boudins that develop during layer-parallel extension. The research in this chapter investigated how an initially continuous, competent layer can become segmented into discrete blocks or boudins as a result of localized variations in thickness and rheological properties with the help of numerical modelling by ANSYS. It was assumed that the competent layer, before fragmentation, had an almost rectangular geometry and that small differences in material properties provided the stress concentrations necessary to trigger brittle failure along high-angle fracture planes. Experimental observations, supported by high-resolution numerical simulations using Maxwell viscoelastic rheology, demonstrated that these variations could cause an evolution from simple rectangular forms into more complex geometries such as barrel-shaped, bone-shaped, or fish-head boudins. The geometric transformations were closely correlated with the viscosity contrasts between the boudin, the softer inter-boudin zones, and the surrounding matrix. These observations reinforced the utility of boudin geometry as a natural strain marker and were in good agreement with earlier theoretical models proposed by Treagus et al. (1996) and Lloyd & Ferguson (1981).

In Chapter 4, the attention turned to multilayer folding under layer-parallel compression. This chapter addressed the complexity that arises when several layers interact during deformation. The research problem was centered on understanding how the thickness, spacing, and viscosity contrasts among layers contribute to the formation of fold geometries that range from harmonic to disharmonic. It was assumed that while the layers shared similar rheological properties, they varied in thickness and were embedded within a more compliant matrix. Finite element modeling under plane strain conditions was employed to simulate the folding process, and the simulations revealed that thinner layers are generally perturbed first

and can drive secondary folding in thicker layers. The concept of a "contact strain zone" was used to explain the spatial extent over which the influence of a folded layer persists. The numerical results, which included detailed measurements of fold wavelengths, amplitudes, and secondary folds, provided a robust quantitative framework that integrated well with theoretical predictions by Biot (1957) and Ramberg (1963).

Chapter 5 extended the investigation to flanking structures under transpressional regimes. In this study, the interaction between compression and shear was examined in the context of how cross-cutting elements (CEs) deflect adjacent planar and linear fabrics. The problem was framed by recognizing that the development of flanking structures in an anisotropic host rock provides key insights into local kinematics and the mechanisms that govern the dragging of fabrics. The study assumed that the host rock was anisotropic, following established parameters from Weijermars (1992), and that the initial geometry of the cross-cutting element was well defined. A set of numerical models allowed for the systematic variation of the CE orientation and the anisotropy factor (δ), leading to a detailed mapping of the resulting fabric deflections. The results highlighted that even subtle variations in the orientation of the CE could generate significant asymmetries in offset and curvature, thereby underlining the importance of both the imposed kinematics and the intrinsic anisotropy in controlling the evolution of these structures.

Finally, Chapter 6 presented an in-depth investigation on the formation of flanking structures under simple shear regimes. In contrast to the transpressional environment, simple shear was used to isolate the effect of shear on the deflection of preexisting fabrics. The central assumption was that, under pure simple shear conditions (where the kinematic vorticity number W_k equals to 1), the deformation

would be dominated by shear-induced drag, and any variability in the final geometry would primarily result from the initial orientation of the cross-cutting element and the degree of anisotropy in the host rock. Numerical models were developed using modified boundary conditions in ABAQUS, and a range of shear angles and anisotropy factors were systematically applied. The results showed that the fabric drag under simple shear was more uniform compared to transpressional conditions, yet even minor variations in the initial conditions produced discernible differences in the geometry of the flanking structures. A classification system was proposed to distinguish between open (*Type I*) and closed (*Type II*) flanking structures, further refining our understanding of how shear influences the morphology of deformed fabrics.

7.3 Deformation Processes of Different Structures in Layered Rock

In this section, each deformation process is discussed in depth with a focus on the underlying problems, the assumptions made, the methodologies employed, and the resulting observations. Comparisons among the different processes are also presented to highlight commonalities and differences.

7.3.1 Boudinage Structures

The study of boudinage structures, as presented in Chapter 3, addresses the critical problem of how a competent layer becomes segmented under layer-parallel extension. In many deformed terranes, the geometry of boudins serves as an essential record of the strain history. The initial assumption in this study was that the competent block, prior to any fragmentation, exhibits an almost rectangular geometry

and that small-scale heterogeneities—whether in thickness, composition, or pre-existing microstructural weaknesses—can serve as the sites for stress concentration. These localized stresses are then sufficient to induce brittle failure along high-angle planes, leading to the formation of boudins.

In our study, we observed that the fragmentation of a competent layer into discrete boudins is controlled by several parameters, including the initial aspect ratio of the layer, the viscosity contrast between the boudin and its host, and the degree of post-fracture deformation. Early works (Ramberg, 1955; Wilson, 1961) provided the conceptual framework for boudinage formation, while subsequent research (Ramsay, 1967; Strömgård, 1973; Ghosh and Ramberg, 1976) expanded the discussion to incorporate both brittle and ductile mechanisms.

The methodology involved a set of finite element numerical simulations. Numerical simulations in ANSYS were used to replicate these conditions using Maxwell viscoelastic rheology, which is particularly suited for modeling the lower crust where high temperature and pressure conditions prevail. The numerical models employed fine-scale meshes to capture the localized strain, and the deformation of an individual boudin block was tracked quantitatively. Figures 3.1 and 3.2 display the progression from an initial rectangular geometry to various curved forms, while Fig. 3.5 provides the final geometry obtained from numerical simulations.

Our numerical models illustrate that when a competent layer is segmented by extensional fractures, the geometry of individual boudins is initially rectangular. However, as deformation proceeds, internal flow within the boudin and interaction with the softer inter-boudin material led to the development of curved margins. The observed evolution—from blocky to barrel-shaped or even bone-shaped boudins—is

a direct function of the relative viscosities (η_{BM} and η_{IM}) and the strain history (Treagus et al., 1996; Lloyd and Ferguson, 1981; Treagus and Lan, 2000, 2004). In particular, our simulations confirm that when the boudin material is significantly more competent than the inter-boudin, the exterior margin tends to develop a convex curvature, whereas a softer boudin relative to the inter-boudin results in a concave face (see also Ghosh and Sengupta, 1999).

Furthermore, the discussion emphasizes that the evolution of boudin geometry is not a static process. Post-fracture deformation, in which the boudins undergo internal modification due to continued shear, further refines their shape. Field studies (such as those reported by Goscombe et al., 2004) have documented similar transformations in natural settings, thereby reinforcing the significance of the experimental findings. Such modifications include internal deformation, curvature of margins, and even transformation into secondary structures (e.g., “torn” boudins) that record complex strain histories. These findings highlight the importance of considering post-boudinage processes (Ray et al., 2011; Samanta and Deb, 2014) when interpreting field observations of boudinage. The output from numerical methods not only corroborates these observations but also provides a quantitative framework that can be used to estimate strain from boudin geometry in various tectonic environments.

7.3.2 Folds

The deformation of multilayered systems, discussed in Chapter 4, presents a complex problem due to the interactions among multiple layers of varying thicknesses and spacing. The primary challenge is to understand how these

interactions modify fold geometry and influence strain partitioning. The study assumes that while the individual layers have similar rheological properties, they differ in thickness and are embedded in a more compliant matrix. Deformation is imposed under layer-parallel compression, a condition that is common in ductile tectonic regimes.

The methodology employs finite element modeling (FEM) using ABAQUS under plane strain conditions. Systematic variations in layer thickness and interlayer spacing allow the simulation of a range of fold geometries, from ideal harmonic folds—where layers of equal thickness fold coherently—to disharmonic folds, where significant variations in layer thickness and spacing produce complex, multi-order folding. The concept of the "contact strain zone," as discussed by Ramberg (1960, 1963), is used to explain the spatial extent of influence that a folded layer has on its neighbours, which leads to an overall evolution from harmonic to polyharmonic and ultimately to disharmonic fold geometries. The numerical results, including detailed measurements of fold wavelength, amplitude, and secondary folding features (illustrated in Fig. 4.1), reveal that thin layers are generally the first to be folded and that their deformation strongly influences adjacent thicker layers.

The spacing between layers also emerges as a critical parameter. According to Ramberg (1963), the influence of a folded layer on its neighbours—the contact strain zone—decays exponentially beyond a distance equal to approximately one initial dominant wavelength. Our simulations confirm that when the spacing is small (i.e., the layers are closely packed), the mutual interaction is strong, and the fold geometry tends to be disharmonic. Conversely, when the spacing increases, the interaction diminishes, allowing each layer to develop folds closer to its dominant wavelength, thereby producing a more harmonic pattern. These observations have important

implications for field studies, as the measured wavelength-to-thickness ratios in natural folds can provide insights into both the initial layer geometry and the degree of interaction among layers (Bastida et al., 2007; Hudleston and Treagus, 2010).

The viscosity contrast between the competent layers and the softer surrounding medium is another pivotal factor influencing fold geometry. Our models demonstrate that a higher viscosity ratio tends to preserve the dominant wavelength in the thin layer, particularly in the hinge zones of thicker layers. In contrast, lower viscosity contrasts allow for greater perturbation and the development of higher-order folds that deviate from the ideal dominant wavelength. This behaviour underscores the complexity inherent in natural systems, where heterogeneous rheological properties can lead to a broad spectrum of fold geometries, ranging from nearly harmonic to strongly disharmonic (Biot, 1957; Ramberg, 1964).

The *W*-factor, defined as the ratio of the observed fold wavelength to the expected wavelength after shortening, serves as an effective quantitative measure of this deviation. Our analysis shows that the *W*-factor is highly sensitive to both the spacing between layers and the viscosity contrast. In field settings, accurate measurements of fold wavelength and layer thickness, when combined with the *W*-factor, can be used to estimate the relative viscosity of rock layers, providing a crucial link between fold geometry and the underlying rheological properties (Llorens et al., 2013; Yakovlev, 2012a, 2012b).

These observations are significant because they challenge the simplified view of folding as an isolated process. Instead, they underscore that the evolution of multilayer folds is a dynamic, interactive process where secondary folding plays a crucial role in determining the overall fold geometry. The deviations observed in fold

wavelengths from the theoretical dominant wavelength predicted by Biot (1957) highlight the importance of interlayer interactions. The comprehensive analysis of multilayer folding provides a quantitative framework that integrates with and extends existing theoretical models, offering deeper insights into the strain partitioning processes that shape fold-thrust belts in natural settings.

7.3.3 Flanking Structures

Flanking structures are explored in Chapters 5 and 6, which examine their development under transpressional and simple shear regimes, respectively. Both studies address the fundamental problem of how linear and planar fabrics are deflected in the vicinity of cross-cutting elements (CEs) and how these deflections can be used to interpret the kinematic history of deformation.

Under transpressional conditions, as discussed in Chapter 5, the deformation environment is characterized by a combination of compressional and shear forces. The problem here is to understand how the interplay between these forces leads to the bending and deflection of fabrics adjacent to a CE. The study assumes that the host rock is anisotropic and that the CE is a planar feature with a well-defined initial orientation. The methodology combines field study and numerical simulations, with systematic variations in the orientation of the CE and the anisotropy factor (δ). The resulting flanking structures are analysed in terms of their offset patterns and curvature, as shown in Figures 5.1 and 5.2.

The findings reveal that the geometry of flanking structures is highly sensitive to the initial orientation of the CE. When the CE is oriented at a high angle relative to the primary foliation, strong asymmetry is observed in the fabric

deflection. The offset of the external host element is significantly different from that of the internal element, with synthetic (contractional) or antithetic (extensional) offsets developing according to the local kinematics. For example, when the CE's long axis is initially oriented below the pole of anisotropy, the structure tends to develop as a closed (*Type II*) form, exhibiting minimal offset and nearly neutral drag (Exner et al., 2004). In contrast, when the initial orientation exceeds this critical angle, the structure evolves into an open (*Type I*) geometry, with more pronounced offsets and a more complex drag pattern (Basu Majumder and Samanta, 2023). These observations are consistent with theoretical predictions by Grasemann et al. (2003) and are further supported by the numerical simulations, which capture the nuanced interplay between boundary conditions and intrinsic anisotropy.

In the simple shear regime, as investigated in Chapter 6, the problem is refined to isolate the effects of shear without the complicating influence of significant compressional forces. Here, the assumption is that the deformation is dominated solely by simple shear (with a kinematic vorticity number, W_k, equal to 1), and the host rock is modelled with varying degrees of anisotropy. The numerical simulations employ boundary conditions tailored for simple shear, and the initial orientation of the CE is varied to observe its effect on the final geometry. In an isotropic medium ($\delta = 1$), the offset and drag are relatively symmetric and predictable. However, as δ increases, the magnitude of the offset (quantified by the normalized offset length, L_N) decreases, and the drag pattern shifts from reverse to normal. This transition implies that higher anisotropy restricts the range of fabric displacement, leading to a more constrained deformation field (Kocher and Mancktelow, 2006). The results, depicted in various figures and supported by simulation data, indicate that simple shear induces a more uniform fabric drag

compared to transpressional conditions. However, even slight differences in the CE's initial orientation result in measurable variations in curvature. The study proposes a classification system that distinguishes between open (*Type I*) and closed (*Type II*) flanking structures based on the degree of offset and curvature, thereby providing a refined framework for interpreting fabric deflection in shear-dominated environments.

The introduction of the orientation factor (ω) in our models allows us to quantify the rotation of the CE's long axis during deformation. Our results indicate that for initial orientations below 90°, ω decreases, reflecting a pronounced co-rotation with the bulk shear. Conversely, for orientations above 90°, ω increases, indicating a tendency toward counter-rotation. These findings underscore the fact that both the initial and final orientations of the CE are critical for understanding the evolution of flanking structures, particularly in anisotropic rocks where the layering exerts a strong control on deformation (Passchier, 2001; Grasemann and Stüwe, 2001).

The geometry of flanking structures provides valuable constraints on the shear sense and magnitude of deformation. By carefully analysing the offset (L_N) and drag patterns, it is possible to infer the direction of shear and even estimate the effective strain experienced by the rock. In our study, the transition between synthetic and antithetic offsets—with some cases exhibiting a neutral drag state—highlights the complex interplay between the imposed shear and the inherent anisotropy of the rock. Such detailed geometrical analyses are crucial for reconstructing the kinematic history of shear zones and for distinguishing between different deformation regimes (Wiesmayr and Grasemann, 2005; Mukherjee, 2014).

Collectively, the investigations into flanking structures demonstrate that the evolution of these features is controlled by both the imposed kinematics and the inherent anisotropy of the rock. They provide a detailed record of the local shear history and contribute significantly to our understanding of strain partitioning in deformed terranes.

7.4 Critical Evaluation of Analogue and Numerical Methods

A critical evaluation of the methods used throughout this thesis reveals both strengths and limitations that bear on the interpretation of the results. The analogue and numerical approaches were designed to control as many variables as possible, but some inherent limitations remain.

In terms of methodological rigor, the experiments were conducted under highly controlled conditions, with careful attention paid to boundary conditions and material properties. The use of high-resolution finite element meshes in ANSYS and ABAQUS ensured that the numerical simulations captured fine-scale features of deformation, such as localized strain concentrations and curvature variations. The integration of analogue experiments with numerical simulations provided a robust means of validating the observed deformation mechanisms, as consistency was observed between laboratory results and simulation outputs. Furthermore, the use of established rheological models, particularly Maxwell viscoelastic rheology, allowed the simulations to approximate the behaviour of rocks under lower crustal conditions. These approaches have yielded quantitative data that align well with existing theoretical models and field observations.

However, there are limitations that must be acknowledged. The analogue materials used in the experiments, while effective in mimicking key aspects of rock behaviour, do not capture the full spectrum of heterogeneity and anisotropy inherent in natural rock formations. Natural rocks often exhibit complex mineralogical and microstructural variability that can influence deformation in ways not fully replicated by simplified laboratory analogues. In addition, the scale of the experiments and numerical models is inherently limited; while laboratory experiments and numerical simulations can capture processes at small scales, extrapolation to geological scales requires caution. Processes such as long-term creep, stress relaxation, and fluid-rock interactions, which occur over millions of years in the Earth's crust, may not be fully represented in the current models.

Boundary conditions and initial geometries are also sources of uncertainty. The experiments often assume idealized conditions such as pure shear or perfectly rectangular initial geometries. While these assumptions are necessary to isolate specific mechanisms, they may limit the direct applicability of the results to more complex natural settings where stress fields and initial geometries are highly variable. Computational limitations also play a role; despite the use of high-resolution meshes, some fine-scale features of strain localization may remain unresolved. Future improvements in computational methods and increased computational resources may help to overcome these challenges.

Finally, the rheological models used—primarily Maxwell viscoelastic rheology—are well suited for simulating ductile deformation in the lower crust but do not account for non-Newtonian behaviours or brittle failure mechanisms that are also important in certain tectonic regimes. While the present models provide a robust framework for understanding deformation processes, further refinements to

incorporate additional rheological complexities would enhance the predictive power of the models.

7.5 Integration with Existing Theoretical Frameworks

The collective findings from the studies of boudinage, flanking structures, and folding in layered rocks provide a comprehensive picture of deformation in heterogeneous crustal systems. Although these processes occur at different scales and under varying kinematic conditions, they are fundamentally linked by the interplay between material properties (such as viscosity and competence) and the geometry of the layers.

A recurring theme throughout this thesis is the sensitivity of structural geometry to the relative rheological contrasts and the spatial configuration of layers. In both boudinage and folding, the initial geometry of a competent layer—whether it be the aspect ratio of a boudin or the thickness of a folded unit—plays a crucial role in determining the final structural pattern. Similarly, in flanking structures, the initial orientation of a cross-cutting element and its subsequent rotation under shear control the development of offsets and drag patterns.

Another key aspect is the concept of a “contact strain zone,” which is critical for understanding the mutual interaction among layers. In both folding and flanking structure formation, the deformation of one layer can significantly influence adjacent layers if they lie within a certain distance—typically on the order of the initial dominant wavelength. This interaction not only modifies the idealized deformation behaviour (as predicted by classical theories such as Biot’s) but also results in a spectrum of observed geometries, ranging from nearly harmonic to disharmonic.

The findings of this thesis integrate well with, and in many cases extend, existing theoretical frameworks in structural geology and tectonics. The experimental observations regarding torn boudinage provide empirical support for classical models, such as those proposed by Lloyd and Ferguson (1981) and Treagus et al. (1996), which link boudin geometry to viscosity contrasts between the competent layer and its host. The detailed measurements of curvature and aspect ratios presented in this thesis serve to refine these models by quantifying the effects of inter-boudin material properties on boudin evolution.

The multilayer folding studies offer further integration with established theories, particularly the concepts of dominant folding wavelength and contact strain zones as described by Biot (1957) and Ramberg (1963). The experimental data indicate that interlayer interactions significantly influence fold geometry, leading to deviations from the idealized dominant wavelength. This insight enhances our understanding of secondary folding processes and provides a quantitative framework for analysing fold-thrust belts in metasedimentary terrains.

Similarly, the work on flanking structures, both under transpressional and simple shear regimes, builds on the theoretical foundations laid by Passchier (2001) and Grasemann and Stüwe (2001). By systematically varying the orientation of the cross-cutting element and the anisotropy factor, the numerical simulations provide a more nuanced understanding of fabric drag and offset patterns. These results highlight the sensitivity of flanking structure geometry to initial conditions and the inherent anisotropy of the host rock, thereby offering refinements to existing kinematic models and contributing to a more detailed interpretation of shear-related deformation.

The integrated understanding of these deformation processes has significant implications for geological interpretations. First, by analysing the geometry of boudinage and folds, geologists can infer the relative viscosities and mechanical properties of rock units. For instance, the preservation of a dominant wavelength in a folded thin layer may indicate a high viscosity contrast with the surrounding medium, whereas the presence of higher-order folds may suggest a lower viscosity contrast or stronger mutual interaction among layers.

Second, the study of flanking structures provides a powerful tool for unravelling the kinematics of shear zones. Detailed measurements of offset lengths, drag patterns, and the rotation of cross-cutting elements enable the reconstruction of strain fields and shear senses in deformed rocks. Such reconstructions are critical for tectonic reconstructions and for understanding the evolution of major shear zones in the crust.

Finally, the integration of numerical modelling with field observations—as exemplified in this thesis—demonstrates the utility of quantitative approaches in structural geology. By comparing model predictions (e.g., the W-factor, orientation factor ω) with measured fold wavelengths and offsets in natural terrains, it is possible to refine estimates of key parameters such as the viscosity ratio and the effective strain. This integrated approach helps bridge the gap between theoretical models and real-world geological systems.

7.6 Broader Implications for Structural Geology and Tectonics

The implications of the research presented in this thesis extend beyond the confines of the laboratory and numerical models. The insights gained have

significant ramifications for our understanding of tectonic processes, seismic hazard assessment, and resource exploration.

The detailed investigation of torn boudinage provides geologists with a valuable natural strain marker that can be applied to quantify deformation in a wide range of tectonic settings. The ability to estimate finite strain from boudin geometry, particularly when refined by the consideration of inter-boudin properties, enhances our capacity to interpret the tectonic history of deformed terranes. This, in turn, has practical applications in the assessment of seismic hazards, as regions with pronounced boudinage may indicate zones of significant strain localization that are prone to brittle failure.

The multilayer folding investigations have direct applications in subsurface modeling and resource exploration. Understanding how layers interact during folding provides valuable information for characterizing hydrocarbon and geothermal reservoirs. The geometric parameters derived from the FEM simulations, such as fold wavelength and amplitude, can be used to infer the mechanical properties of reservoir rocks and to predict fluid flow patterns within folded structures.

Similarly, the studies on flanking structures offer important insights into shear kinematics and the role of anisotropy in deformation. The refined classification of flanking structures and the demonstration of their sensitivity to initial conditions can inform more accurate models of shear zone evolution. Such models are critical for understanding the processes that control the initiation and propagation of faults, thereby contributing to improved seismic hazard assessments.

Furthermore, the methodological advancements presented in this thesis—particularly the integration of analogue experiments with high-resolution numerical

simulations—set new standards for future research in structural geology. The techniques developed herein can be adapted to simulate more complex, coupled deformation processes that include thermal and fluid interactions, thereby advancing our understanding of the dynamic behaviour of the Earth's crust.

7.7 Future Research Directions

Despite the significant advances achieved in this work, several challenges remain that pave the way for future investigations. One important avenue for further research is the incorporation of a broader range of analogue materials and natural rock samples to better capture the inherent heterogeneity and anisotropy of the Earth's crust. Future studies should aim to systematically examine the effects of mineralogical variations, grain size, and pre-existing microstructural features on deformation behaviour.

Another key area is the development of coupled process models that integrate thermal, fluid, and chemical effects with mechanical deformation. While the current study focuses primarily on mechanical processes using Maxwell viscoelastic rheology, natural tectonic environments are influenced by a range of coupled phenomena that can significantly alter deformation behaviour over geological timescales. Longer-duration experiments and advanced numerical simulations that account for these additional factors would provide a more comprehensive picture of crustal deformation.

Multi-scale modeling represents another critical direction for future research. Bridging the gap between laboratory-scale observations and geological-scale processes remains a significant challenge. Advances in computational resources and

the development of high-resolution models that integrate field data will be essential for creating predictive models that accurately reflect natural deformation processes. In particular, integrating detailed numerical simulations with seismic, geochronological, and outcrop studies could yield powerful insights into the scaling behaviour of deformation features.

Further refinement of boundary conditions and initial geometries in numerical models is also needed. While the present study employs idealized conditions to isolate specific deformation mechanisms, future research should explore more realistic boundary conditions that mimic the complex stress fields present in natural tectonic settings. Incorporating dynamic boundary conditions and variable stress fields may help to better simulate the evolution of deformation over time.

Finally, continued field validation and model calibration are imperative. Detailed field studies that document the geometry, strain, and structural history of deformed terranes are essential for validating the models developed in this thesis. Collaborative efforts between experimentalists, numerical modelers, and field geologists will be crucial for ensuring that theoretical models accurately reflect natural phenomena and can be reliably used in seismic hazard assessment and resource exploration.

7.8 Final Conclusions and Synthesis

The research presented in this thesis has advanced our understanding of deformation in layered rock systems through a rigorous, integrated approach that combines experimental investigations, numerical simulations, and theoretical modeling. The study of torn boudinage has shown that small-scale heterogeneities

and viscosity contrasts are critical in driving the segmentation of competent layers, resulting in a diverse range of boudin geometries that serve as natural markers of finite strain.

The multilayer folding experiments have highlighted the complexities that arise when multiple layers interact during deformation. The observations indicate that thin layers are perturbed first and that their deformation can significantly influence the folding behaviour of adjacent thicker layers. The concept of secondary folding and the deviation of fold wavelengths from the ideal dominant wavelength underscore the importance of interlayer interactions in shaping fold geometry.

The investigations into flanking structures, conducted under both transpressional and simple shear regimes, have elucidated how the deflection of fabrics adjacent to cross-cutting elements is controlled by the initial orientation of these elements and the inherent anisotropy of the host rock. These studies contribute to a more refined understanding of shear kinematics and the mechanisms of strain partitioning in tectonically active regions.

Collectively, the findings of this thesis not only validate existing theoretical frameworks—such as those developed by Biot, Ramberg, Lloyd and Ferguson, and Treagus et al.—but also extend them by incorporating detailed experimental and numerical data. The integrated approach adopted herein demonstrates that the evolution of deformation in layered rocks is governed by a dynamic interplay between mechanical heterogeneity, strain localization, and interlayer interactions. These processes operate across a range of scales and are fundamental to understanding the formation of structures observed in fold-thrust belts, metamorphic terranes, and other tectonically deformed regions.

The broader implications of this work are significant. By improving our understanding of the fundamental mechanisms of deformation, this research contributes to the development of more accurate tectonic models, enhances seismic hazard assessments, and informs subsurface resource exploration. The methodological advancements and experimental techniques introduced in this thesis set the stage for future investigations that will further elucidate the complex, coupled processes that govern crustal deformation.

7.9 Final Remarks

In summary, this thesis represents a substantial contribution to the field of structural geology and tectonics. Through the detailed study of torn boudins, multilayer folds, and flanking structures, the research provides a unified framework for understanding the deformation of layered rock systems. The work emphasizes that even minor variations in material properties and initial geometries can lead to significant differences in deformation behaviour, thereby underscoring the importance of considering heterogeneity and interlayer interactions in both experimental and numerical studies.

The integrated, multidisciplinary approach employed in this research—combining high-resolution laboratory experiments, rigorous finite element modeling, and theoretical analysis—has yielded a robust set of results that not only support existing models but also offer new insights into the mechanisms that control tectonic deformation. While challenges remain, particularly in replicating the full complexity of natural systems and scaling laboratory observations to geological dimensions, the

methodologies developed in this thesis provide a strong foundation for future research.

Acknowledgement

I am deeply grateful to my PhD supervisor and guide, Prof. Susanta Kumar Samanta, whose mentorship and wisdom have been the cornerstone of my academic journey.

The Research Advisory Committee (RAC) members, Prof. Supriya Mondal and Dr. Tridib Kumar Mondal, are also acknowledged for their valuable suggestions.

I extend heartfelt thanks to my lab mates cum field mates, Subhabrata Das and Masud Rana, for their invaluable collaboration, insightful discussions, and constant support throughout our shared endeavours.

A special note of thanks goes to Imtiaz da, whose dedication as the Purulia field driver ensured the success of our fieldworks.

My sincere appreciation also goes to the Department of Geological Sciences, Jadavpur University for providing infrastructural facilities, computational support, and a conducive lab environment that have been instrumental in my research.

Finally, I am forever indebted to my family, whose unwavering moral support and love have continuously inspired and uplifted me.

References

1. Abbassi, M. R., & Mancktelow, N. S. (1992). Single layer buckle folding in non-linear materials: I. Experimental study of fold development from an isolated initial perturbation. *Journal of Structural Geology, 14*(1), 85–104.
2. Abe, S., & Urai, J. L. (2012). Discrete element modeling of boudinage: Insights on rock rheology, matrix flow, and evolution of geometry. *Journal of Geophysical Research, 117*, B01407.
3. Allegre, J. C., & Turcotte, D. L. (1986). Implications of a two-component marble-cake mantle. *Nature, 323*, 123–127.
4. Arslan, A., Koehn, D., Passchier, C. W., & Sachau, T. (2012). The transition from single layer to foliation boudinage—A dynamic modelling approach. *Journal of Structural Geology, 42*, 118–142.
5. Arslan, A., Passchier, C. W., & Koehn, D. (2008). Foliation boudinage. *Journal of Structural Geology, 30*, 291–309.
6. Banerji, A. K. (1991). Presidential address. Geology of the Chotanagpur region. *Indian Journal of Geology, 63*, 275–282.
7. Banik, N. C. (1987). An effective anisotropy parameter in transversely isotropic media. *Geophysics, 52*, 1654–1664.
8. Barnett, J. A. M., Mortimer, J., Rippon, J. H., Walsh, J. J., & Watterson, J. (1987). Displacement geometry in the volume containing a single normal fault. *AAPG Bulletin, 71*, 925–937.

9. Barraud, J., Gardien, V., Allemand, P., & Grandjean, P. (2004). Analogue models of melt-flow networks in folding migmatites. *Journal of Structural Geology, 26*, 307–324.

10. Bastida, F., Aller, J., Bobillo-Ares, N. C., & Toimil, N. C. (2005). Fold geometry: A basis for their kinematical analysis. *Earth-Science Reviews, 70*, 129–164.

11. Bastida, F., Aller, J., Toimil, N. C., Lisle, R. J., & Bobillo-Ares, N. C. (2007). Some considerations on the kinematics of chevron folds. *Journal of Structural Geology, 29*, 1185–1200.

12. Basu Majumder, D., & Samanta, S. K. (2023). Development of flanking structures in layered gneissic rock: Insights from numerical modelling. *Journal of Structural Geology, 174*, 104935.

13. Bayly, M. B. (1970). Viscosity and anisotropy estimate from measurements on chevron folds. *Tectonophysics, 9*, 459–474.

14. Bhattacharya, B. P. (1976). Metamorphism of the Precambrian rocks of the central part of Santhal Parganas district, Bihar. *Quaternary Journal of the Geology, Mining and Metallurgical Society of India, 48*, 183–196.

15. Biot, M. A. (1957). Folding instability of a layered viscoelastic medium under compression. *Proceedings of the Royal Society of London. Series A, Mathematical and Physical Sciences, 242*, 444–454.

16. Biot, M. A. (1959a). Folding of a layered viscoelastic medium derived from an exact stability theory of a continuum under initial stress. *Quarterly of Applied Mathematics, 17*, 185–204.

17. Biot, M. A. (1959b). On the instability and folding deformation of a layered viscoelastic medium in compression. *Journal of Applied Mechanics, 26*, 393–400.

18. Biot, M. A. (1961). Theory of folding of stratified viscoelastic media and its implications in tectonics and orogenesis. *Geological Society of America Bulletin, 72*, 1595–1620

19. Biot, M. A. (1965). *Mechanics of incremental deformations*. Wiley.

20. Bobyarchick, A. R. (1986). The eigenvalues of steady flow in Mohr space. *Tectonophysics, 122*, 35–51.

21. Bose, N., Dutta, D., & Mukherjee, S. (2020). Refraction of micro-fractures due to shear-induced mechanical stratigraphy in a low-grade meta-sedimentary rock. *Journal of Structural Geology, 133*, 103995.

22. Carreras, J., & Druguet, E. (1994). Structural zonation as a result of inhomogeneous non-coaxial deformation and its control on syntectonic intrusions: An example from the Cap de Creus area, Eastern-Pyrenees. *Journal of Structural Geology, 16*, 1525–1534.

23. Carreras, J., Cosgrove, J. W., & Druguet, E. (2013). Strain partitioning in banded and/or anisotropic rocks: Implications for inferring tectonic regimes. *Journal of Structural Geology, 50*, 7–21.

24. Casey, M., & Huggenberger, P. (1985). Numerical modelling of finite-amplitude similar folds developing under general deformation histories. *Journal of Structural Geology, 7*, 103–114.

25. Christensen, U. (1987). Some geodynamical effects of anisotropic viscosity. *Geophysical Journal International, 91*, 711–736.

26. Cobbold, P. R. (1976). Mechanical effects of anisotropy during large finite deformations. *Bulletin de la Société Géologique de France, 18*, 1497–1510.

27. Cobbold, P. R. (1977). Finite-element analysis of fold propagation: A problematic application? *Tectonophysics, 38*, 339–358.

28. Cobbold, P. R., & Watkinson, A. J. (1981). Bending anisotropy: A mechanical constraint on the orientation of fold axes in an anisotropic medium. *Tectonophysics, 72*, T1–T10.

29. Cobbold, P. R., Cosgrove, J. W., & Summers, J. M. (1971). Development of internal structures in deformed anisotropic rocks. *Tectonophysics, 12*, 23–53.

30. Coelho, S., Passchier, C. W., & Grasemann, B. (2005). Geometric description of flanking structures. *Journal of Structural Geology, 27*, 597–606.

31. Copley, A., & McKenzie, D. (2007). Models of crustal flow in the India–Asia collision zone. *Geophysical Journal International, 169*, 683–698.

32. Cosgrove, J. W. (1976). The formation of crenulation cleavage. *Journal of the Geological Society, London, 132*, 155–178.

33. Currie, I. B., Patnode, H. W., & Trump, R. P. (1962). Development of folds in sedimentary strata. *Geological Society of America Bulletin, 73*, 655–674.

34. Dabrowski, M., & Grasemann, B. (2014). Domino boudinage under layer-parallel simple shear. *Journal of Structural Geology, 68*, 58–65.

35. Damasceno, D. R., Eckert, A., & Liu, X. (2017). Flexural-slip during visco-elastic buckle folding. *Journal of Structural Geology, 100*, 62–76.

36. DePaor, D. G., Simpson, C., Bailey, C. M., McCaffrey, K. J. W., Bean, E., Gower, R. J. W., & Aziz, G. (1991). The role of solution in the formation of boudinage and transverse veins in carbonate rocks at Rheems, Pennsylvania. *Geological Society of America Bulletin, 103*, 1552–1563.

37. Dewey, J. F. (1965). Nature and origin of kink-bands. *Tectonophysics, 1*, 459–494.

38. Dieterich, J. H. (1970). Computer experiments on mechanics of finite amplitude folds. *Canadian Journal of Earth Sciences, 7*, 467–476.

39. Druguet, E., & Carreras, J. (2006). Analogue modelling of syntectonic leucosomes in migmatitic schists. *Journal of Structural Geology, 28*, 1734–1747.

40. Druguet, E., Alsop, G. I., & Carreras, I. (2009). Coeval brittle and ductile structures associated with extreme deformation partitioning in a multilayer sequence. *Journal of Structural Geology, 31*, 498–511.

41. Druguet, E., Passchier, C. W., Carreras, J., Victor, P., & Den Brock, S. (1997). Analysis of a complex high-strain zone at Cap de Creus, Spain. *Tectonophysics, 280*, 31–45.

42. Dutta, D., & Mukherjee, S. (2019). Opposite shear senses: Genesis, global occurrences, numerical simulations and a case study from the Indian Western Himalaya. *Journal of Structural Geology, 126*, 357–392.

43. Eckert, A., Connolly, P., & Liu, X. (2014). Large-scale mechanical buckle fold development and the initiation of tensile fractures. *Geochemistry, Geophysics, Geosystems, 15*, 4570–4587.

44. Exner, U., & Dabrowski, M. (2010). Monoclinic and triclinic 3D flanking structures around elliptical cracks. *Journal of Structural Geology, 32*, 2009–2021.

45. Exner, U., Grasemann, B., & Mancktelow, N. S. (2006). Multiple faults in ductile simple shear: Analogue models of flanking structure systems. *Geological Society Special Publications, 253*, 381–395.

46. Exner, U., Mancktelow, N. S., & Grasemann, B. (2004). Progressive development of s-type flanking folds in simple shear. *Journal of Structural Geology, 26*, 2191–2201.

47. Fossen, H. (2010). *Structural geology*. Cambridge University Press.

48. Frehner, M., & Schmalholz, S. M. (2006). Numerical simulations of parasitic folding in multilayers. *Journal of Structural Geology, 28*, 1647–1657.

49. Frehner, M., & Schmid, T. (2016). Parasitic folds with wrong vergence: How pre-existing geometrical asymmetries can be inherited during multilayer buckle folding. *Journal of Structural Geology, 87*, 19–29.

50. Gayer, R. A., Powell, D. B., & Rhodes, S. (1978). Deformation against metadolerite dykes in the Caledonides of Finnmark, Norway. *Tectonophysics, 46*, 99–115.

51. Ghosh, A. (2004). Prehistory of the Chotanagpur Region, India: A Stratigraphic Overview. *Geological Survey of India Bulletin*, 12, 45–68.

52. Ghosh, S. K., & Ramberg, H. (1976). Reorientation of inclusions by combination of pure and simple shear. *Tectonophysics, 34*, 1–70.

53. Ghosh, S. K., & Sengupta, S. (1999). Boudinage and composite boudinage in superposed deformations and syntectonic migmatisation. *Journal of Structural Geology, 21*, 97–110.

54. Goldstein, A. G. (1988). Factors affecting the kinematic interpretation of asymmetric boudinage in shear zones. *Journal of Structural Geology, 10*, 707–715.

55. Gomez-Rivas, E., Griera, A., & Llorens, M. G. (2015). Fracturing of ductile anisotropic multilayers: Influence of material strength. *Solid Earth, 6*, 497–509.

56. Goscombe, B. D., Passchier, C. W., & Hand, M. (2004). Boudinage classification: End-member boudin types and modified boudin structures. *Journal of Structural Geology, 26*, 739–763.

57. Goswami, B., & Bhattacharyya, C. (2010). Tectonothermal Evolution of the Chotanagpur Granite Gneiss Complex: A Case Study from the Purulia District, Eastern India. *Indian Journal of Geology*, 80, 41–54.

58. Goswami, B., & Bhattachrayya, C. (2008). Tectonothermal evolution of Chhotanagpur Granite Gneiss Complex from northeastern part of Puruliya district, West Bengal, eastern India. *Indian Journal of Geology, 80*, 41–54.

59. Goswami, T., & Baruah, S. (2016). Flanking structures as shear sense indicators in the Higher Himalayan gneisses near Tato, West Siang District, Arunachal Pradesh, India. In S. Mukherjee & K. F. Mulchrone (Eds.), *Ductile shear zones: From micro- to macro-scales* (pp. 293–317). John Wiley & Sons.

60. Grasemann, B., & Stuwe, K. (2001). The development of flanking folds during simple shear and their use as kinematic indicators. *Journal of Structural Geology, 23*, 715–724.

61. Grasemann, B., Dabrowski, M., & Schöpfer, M. P. J. (2019). Sense and non-sense of shear reloaded. *Journal of Structural Geology, 125*, 20–28.

62. Grasemann, B., Fritz, H., & Vannay, J.-C. (1999). Quantitative kinematic flow analysis from the Main Central Thrust Zone (NW-Himalaya, India): Implications for a decelerating strain path and the extrusion of orogenic wedges. *Journal of Structural Geology, 21*, 837–853.

63. Grasemann, B., Martel, S., & Passchier, C. W. (2005). Reverse and normal drag along a fault. *Journal of Structural Geology, 27*, 999–1010.

64. Grasemann, B., Stuwe, K., & Vannay, J. C. (2003). Sense and non-sense of shear in flanking structures. *Journal of Structural Geology, 25*, 19–34.

65. Grujic, D., & Mancktelow, N. (2022). Strain-rate- and capillary-number-dependent deformation of weak viscous particles. *Journal of Structural Geology, 162*, 104673.

66. Hambrey, M. J., & Milnes, A. G. (1975). Boudinage in glacier ice: Some examples. *Journal of Glaciology, 14*, 383–393.

67. Hanmer, S., & Passchier, C. W. (1991). Shear-sense indicators: A review. *Geological Survey of Canada*, 72 pp.

68. Hobbs, B., Regenauer-Lieb, K., & Ord, A. (2008). Folding with thermal–mechanical feedback. *Journal of Structural Geology, 30*, 1572–1592.

69. Hobbs, D. W. (1967). The formation of tension joints in sedimentary rocks: An explanation. *Geological Magazine, 104*, 550–556.

70. Holtz, F., Johannes, W., Tamic, N., & Behrens, H. (2001). Maximum and minimum water contents of granitic melts generated in the crust: A reevaluation and implications. *Lithos, 56*, 1–14.

71. Honda, S. (1986). Strong anisotropic flow in a finely layered asthenosphere. *Geophysical Research Letters, 13*, 1454–1457.

72. Hudleston, P. J. (1973). An analysis of "single-layer" folds developed experimentally in viscous media. *Tectonophysics, 16*, 189–214.

73. Hudleston, P. J. (1989). The association of folds and veins in shear zones. *Journal of Structural Geology, 11*, 949–957.

74. Hudleston, P. J., & Treagus, S. H. (2010). Information from folds: A review. *Journal of Structural Geology, 32*, 2042–2071.

75. Hunt, G., Muhlhaus, H., Hobbs, B., & Ord, A. (1996). Localized folding of viscoelastic layers. *Geologische Rundschau, 85*, 58–64.

76. Jaeger, J. C., & Cook, N. G. W. (1979). *Fundamentals of Rock Mechanics* (3rd ed.). Chapman & Hall.

77. Jeng, F. S., Lai, Y. C., & Teng, M. H. (2002). Influence of strain rate on buckle folding of an elasto-viscous single layer. *Journal of Structural Geology, 24*, 501–516.

78. Ji, S., & Saruwatari, K. (1998). A revised model for the relationship between joint spacing and layer thickness. *Journal of Structural Geology, 20*, 1495–1508.

79. Ji, S., Zhao, P., & Saruwatari, K. (1997). Fracturing of garnet crystals in anisotropic rocks during uplift. *Journal of Structural Geology, 19*, 603–620.

80. Jiang, D. (2016). Viscous inclusions in anisotropic materials: Theoretical development and perspective applications. *Tectonophysics, 693*, 116–142.

81. Johnson, A. M. (1977). *Styles of folding*. Elsevier.

82. Johnson, A. M., & Fletcher, R. C. (1994). *Folding of viscous layers*. Columbia University Press.

83. Johnson, A. M., & Pfaff, V. J. (1989). Parallel, similar and constrained folds. *Engineering Geology, 27*, 115–180.

84. Johnson, S. E., Lenferink, H. J., Price, N. A., Marsh, J. H., Koons, P. O., West Jr, D. P., & Beane, R. (2009). Clast-based kinematic vorticity gauges: The effects of slip at matrix/clast interfaces. *Journal of Structural Geology, 31*, 1322–1339.

85. Kenis, I., Sintubin, M., Muchez, P., & Burke, E. A. J. (2002). The 'boudinage' question in the High-Ardenne Slate Belt (Belgium): A combined structural and fluid-inclusion approach. *Tectonophysics, 348*, 93–110.

86. Kenis, I., Urai, J. L., Sintubin, M. (2006). The development of bone-shaped structures in initially segmented layers during layer-parallel extension: Numerical modelling and parameter sensitivity analysis. *Journal of Structural Geology, 28*, 1183–1192.

87. Kenis, I., Urai, J. L., van der Zee, W., & Sintubin, M. (2004). Mullions in the High-Ardenne Slate Belt (Belgium): Numerical model and parameter sensitivity analysis. *Journal of Structural Geology, 26*, 1677–1692.

88. Kocher, T., & Mancktelow, N. S. (2005). Dynamic reverse modelling of flanking structures: A source of quantitative kinematic information. *Journal of Structural Geology, 27*, 1346–1354.

89. Kocher, T., & Mancktelow, N. S. (2006). Flanking structure development in anisotropic viscous rock. *Journal of Structural Geology, 28*, 1139–1145.

90. Kumar, R.R., Dwivedi, S.B., & Pathak, P. (2022). Phase Equilibria Modelling and Geochemistry of High-Grade Gneiss from Daltonganj of the Chotanagpur Granite Gneiss Complex, Eastern India: Implications for Tectono-Metamorphic Evolution. *Geosystems and Geoenvironment*, 2, 100082.

91. Lacassin, R. (1988). Large-scale foliation boudinage in gneisses. *Journal of Structural Geology, 10*, 643–647.

92. Larsen, C. F., Motyka, R. J., Freymueller, J. T., Echelmeyer, K. A., & Ivins, E. R. (2005). Rapid viscoelastic uplift in southeast Alaska caused by post-Little Ice Age glacial retreat. *Earth and Planetary Science Letters, 237*, 548–560.

93. Latham, J. P. (1985). The influence of nonlinear material properties and resistance to bending on the development of internal structures. *Journal of Structural Geology, 7*, 225–236.

94. Liu, X., Eckert, A., & Connolly, P. (2016). Stress evolution during 3D single-layer visco-elastic buckle folding: Implications for the initiation of fractures. *Tectonophysics, 679*, 140–155.

95. Liu, X., Eckert, A., Connolly, P., & Thornton, D. (2020). Visco-elastic parasitic folding: Influences on the resulting porosity distribution. *Journal of Structural Geology, 130*, 103892.

96. Llorens, M. G., Bons, P. D., Griera, A., Gomez-Rivas, E., & Evans, L. A. (2013). Single layer folding in simple shear. *Journal of Structural Geology, 50*, 209–220.

97. Lloyd, G. E., & Ferguson, C. C. (1981). Boudinage structure: Some new interpretations based on elastic-plastic finite element simulations. *Journal of Structural Geology, 3*, 117–128.

98. Lloyd, G. E., Ferguson, C. C., & Reading, K. (1982). A stress transfer model for the development of extension fracture boudinage. *Journal of Structural Geology, 4*, 355–372.

99. Maeder, X., Passchier, C. W., & Koehn, D. (2009). Modelling of segment structures: Boudins, bone-boudins, mullions and related single- and multiphase deformation features. *Journal of Structural Geology, 31*, 817–830.

100. Mahadevan, T. M. (2002). *Geology of Bihar & Jharkhand* (Text Book Series, 114). Journal of Geological Society of India, Bangalore.

101. Malavielle, J., & Lacassin, R. (1988). "Bone-shaped" boudins in progressive shearing. *Journal of Structural Geology, 10*, 335–345.

102. Mancktelow, N. S. (1999). Finite-element modelling of single-layer folding in elasto-viscous materials: The effect of initial perturbation geometry. *Journal of Structural Geology, 21*, 161–177.

103. Mancktelow, N. S. (2011). Deformation of an elliptical inclusion in two-dimensional incompressible power-law viscous flow. *Journal of Structural Geology, 33*, 1378–1393.

104. Mancktelow, N. S. (2013). Behaviour of an isolated rimmed elliptical inclusion in 2D slow incompressible viscous flow. *Journal of Structural Geology, 46*, 235–254.

105. Mancktelow, N. S., Arbaret, L., & Pennacchioni, G. (2002). Experimental observations on the effect of interface slip on rotation and stabilisation of rigid particles in simple shear and a comparison with natural mylonites. *Journal of Structural Geology, 24*, 567–585.

106. Mandal, N., Chakraborty, C., & Samanta, S. K. (2000). Boudinage in multilayered rocks under layer-normal compression: A theoretical analysis. *Journal of Structural Geology, 22*, 373–382.

107. Marques, F. O., Fonseca, P. D., Lechmann, S., Burg, J. P., Marques, A. S., Andrade, A. J. M., & Alves, C. (2012). Boudinage in nature and experiment. *Tectonophysics, 526–529*, 88–96.

108. Masuda, T., & Kuriyama, M. (1988). Successive "mid-point" fracturing during microboudinage: An estimate of the stress–strain relation during a natural deformation. *Tectonophysics, 147*, 171–177.

109. Mayrhofer, F., Schöpfer, M. P. J., Adamuszek, M., Dabrowski, M., & Grasemann, B. (2022). Transtensional flanking structures. *Journal of Structural Geology, 161*, 104659.

110. Merle, O. (1986). Patterns of stretch trajectories and strain rates within spreading-gliding nappes. *Tectonophysics, 124*, 211–222.

111. Mohanty, S.P. (2023). Structural and Tectonic Analyses of the Chotanagpur Granite Gneiss Complex: Implications for a Global Model. *Geosystems and Geoenvironment*, 2, 100202.

112. Mukherjee, S. (2013). Channel flow extrusion model to constrain dynamic viscosity and Prandtl number of the Higher Himalayan Shear Zone. *International Journal of Earth Sciences, 102*, 1811–1835.

113. Mukherjee, S. (2014). Review of flanking structures in meso- and micro-scales. *Geological Magazine, 151*, 957–974.

114. Mukherjee, S., & Koyi, H. A. (2009). Flanking microstructures. *Geological Magazine, 146*, 517–526.

115. Mukherjee, Subham & Dey, Anindita & Sanyal, Sanjoy & Ibañez-Mejia, Mauricio & Dutta, Upama & Sengupta, Pulak. (2017). Petrology and U-Pb geochronology of zircon in a suite of charnockitic gneisses from parts of the Chotanagpur Granite Gneiss Complex (CGGC): Evidence for the reworking of a Mesoproterozoic basement during the formation of the Rodinia supercontinent. *Geological Society London Special Publications, 457*, 197–231

116. Mulchrone, K. F. (2007a). Modelling flanking structures using deformable high axial ratio ellipses: Insights into finite geometries. *Journal of Structural Geology, 29*, 1216–1228.

117. Mulchrone, K. F. (2007b). An analytical solution in 2D for the motion of rigid elliptical particles with a slipping interface under a general deformation. *Journal of Structural Geology, 29*, 950–960.

118. Nicolas, A. (1989). *Structures of Ophiolites and Dynamics of Oceanic Lithosphere*. Kluwer Academic Publishers.

119. Ord, A., & Hobbs, B. (2013). Localised folding in general deformations. *Tectonophysics, 587*, 30–45.

120. Passchier, C. W. (2001). Flanking structures. *Journal of Structural Geology, 23*, 951–962.

121. Passchier, C. W., & Druguet, E. (2002). Numerical modelling of asymmetric boudinage. *Journal of Structural Geology, 24*, 1789–1803.

122. Passchier, C. W., & Trouw, R. A. J. (2005). *Microtectonics*. Springer-Verlag.

123. Passchier, C. W., Mancktelow, N. S., & Grasemann, B. (2005). Flow perturbations: A tool to study and characterize heterogeneous deformation. *Journal of Structural Geology, 27*, 1011–1026.

124. Passchier, C., Heesakkers, V., & Coelho, S. (2008). Two mechanisms for forming flanking folds. In D. De Paor (Ed.), *Journal of the Virtual Explorer, 30*.

125. Platt, J. P., & Vissers, R. L. M. (1980). Extensional structures in anisotropic rocks. *Journal of Structural Geology, 2*, 397–410.

126. Price, N. J., & Cosgrove, J. W. (1990). *Analysis of Geological Structures*. Cambridge University Press.

127. Ramberg, H. (1955). Natural and experimental boudinage and pinch-and-swell structures. *The Journal of Geology, 63*, 512–526.

128. Ramberg, H. (1960). Relationships between length of arc and thickness of ptygmatically folded veins. *American Journal of Science, 258*, 36–46.

129. Ramberg, H. (1962). Contact strain and folding instability of a multilayered body under compression. *Geologische Rundschau, 51*, 405–439.

130. Ramberg, H. (1963). Fluid dynamics of viscous buckling applicable to folding of layered rocks. *Bulletin of the American Association of Petroleum Geologists, 47*, 484–505.

131. Ramberg, H. (1964). Selective buckling of composite layers with contrasted rheological properties, a theory for simultaneous formation of several orders of folds. *Tectonophysics, 1*, 307–341.

132. Ramsay, J. G. (1967). *Folding and Fracturing of Rocks*. McGraw-Hill.

133. Ramsay, J. G. (1974). Development of chevron folds. *Geological Society of America Bulletin, 85*, 1741–1754.

134. Ramsay, J. G., & Huber, M. I. (1983). *The techniques of modern structural geology: Volume 1: Strain analysis*. Academic Press.

135. Ramsay, J. G., & Lisle, R. J. (2000). *Applications of Continuum Mechanics in Structural Geology* (Vol. 3). Academic Press.

136. Ramsay, J. G., & Lisle, R. J. (2000). *The techniques of modern structural geology: Volume 3: Applications of continuum mechanics in structural geology* (pp. 702–1061). Academic Press.

137. Ray, S., Sanyal, S., & Sengupta, P. (2011). Mineralogical control on rheological inversion of a suite of deformed mafic dykes from parts of the Chottanagpur Granite Gneiss Complex of Eastern India. In R. K. Srivastava (Ed.), *Dyke swarms: Keys for geodynamic interpretation*.

138. Reches, Z., & Eidelman, A. (1995). Drag along faults. *Tectonophysics, 247*, 145–156.

139. Ribe, N. M. (1989). Seismic anisotropy and mantle flow. *Journal of Geophysical Research, 94*, 4213–4223.

140. Ridley, J., & Casey, M. (1989). Numerical modeling of folding in rotational strain histories: Strain regimes expected in thrust belts and shear zones. *Geology, 17*, 875–878.

141. Samanta, S. K., & Bhattacharyya, G. (2003). Modes of detachment at the inclusion–matrix interface. *Journal of Structural Geology, 25*, 1107–1120.

142. Samanta, S. K., & Deb, I. (2014). Development of concave-face boudin in Chhotanagpur Granite Gneiss Complex of Jasidih-Deoghar area, eastern India: Insight from finite element modeling. *Journal of Structural Geology, 62*, 38–51.

143. Samanta, S. K., Basu Majumder, D., & Sarkar, G. (2017). Geometry of torn boudin—An indicator of relative viscosity. *Journal of Structural Geology, 104*, 21–30.

144. Sanyal, S., & Sengupta, P. (2012). Metamorphic Evolution of the Chotanagpur Granite Gneiss Complex of the East Indian Shield: Current Status. *Geological Society, Special Publications*, 365, 117–145.

145. Sarangi, S., & Mohanty, S. (1998). Structural studies in the Chhotanagpur gneissic complex near Gomoh, Dhanbad district, Bihar. *Indian Journal of Geology, 70*, 73–80.

146. Saroglou, H., & Tsiambaos, G. (2007). Classification of anisotropic rocks. In *Proceedings of the 11th ISRM Congress* (pp. 9–13). Lisbon, Portugal.

147. Schmalholz, S. M. (2006). Scaled amplification equation: A key to the folding history of buckled viscous single-layers. *Tectonophysics, 419*, 41–53.

148. Schmalholz, S. M., & Podladchikov, Y. Y. (1999). Buckling versus folding: Importance of viscoelasticity. *Geophysical Research Letters, 26*, 2641–2644.

149. Schmalholz, S. M., & Podladchikov, Y. Y. (2001a). Strain and competence contrast estimation from fold shape. *Tectonophysics, 340*, 195–213.

150. Schmalholz, S. M., & Podladchikov, Y. Y. (2001b). Viscoelastic folding: Maxwell versus Kelvin Rheology. *Geophysical Research Letters, 28(9), 1835–1838.*

151. Schmalholz, S. M., Podladchikov, Y. Y., & Schmid, D. W. (2001). A spectral/finite-difference method for simulating large deformations of heterogeneous, viscoelastic materials. *Geophysical Journal International, 145*, 199–208.

152. Schmid, D. W., & Podladchikov, Y. Y. (2006). Fold amplification rates and dominant wavelength selection in multilayer stacks. *Philosophical Magazine, 86*, 3409–3423.

153. Selkman, S. (1978). Stress and displacement analysis of boudinages by the finite-element method. *Tectonophysics, 44*, 115–139.

154. Sengupta, S. (1983). Folding of boudinaged layers. *Journal of Structural Geology, 5*, 197–210.

155. Sharma, R. S. (2009). *Cratons and fold belts of India* (Lecture Notes in Earth Sciences). Springer-Verlag.

156. Shi, Y. L., & Cao, J. L. (2008). Effective viscosity of the China continental lithosphere. *Earth Science Frontiers, 15*, 82–95.

157. Stromgard, K. E. (1973). Stress distribution during formation of boudinage and pressure shadows. *Tectonophysics, 16*, 215–248.

158. Swanson, M. T. (1992). Late Acadian-Alleghenian transpressional deformation: Evidence from asymmetric boudinage in the Casco Bay area, coastal Maine. *Journal of Structural Geology, 14*, 323–341.

159. Tikoff, B., & Fossen, H. (1993). Simultaneous pure and simple shear: The unified deformation matrix. *Tectonophysics, 217*, 267–283.

160. Treagus, S. H. (1973). Buckling stability of a viscous single-layer system, oblique to the principal compression. *Tectonophysics, 19*, 271–289.

161. Treagus, S. H. (1981). A theory of stress and strain variations in viscous layers, and its geological implications. *Tectonophysics, 72*, 75–103.

162. Treagus, S. H. (1983). A theory of finite strain variation through contrasting layers, and its bearing on cleavage refraction. *Journal of Structural Geology, 5*, 351–368.

163. Treagus, S. H. (1985). The relationship between foliation and strain: An experimental investigation: Discussion. *Journal of Structural Geology, 7*, 119–121.

164. Treagus, S. H. (1988). Strain refraction in layered systems. *Journal of Structural Geology, 10*, 517–527.

165. Treagus, S. H., & Lan, L. (2000). Pure shear deformation of square objects, and applications to geological strain analysis. *Journal of Structural Geology, 22*, 105–122.

166. Treagus, S. H., & Lan, L. (2004). Deformation of square objects and boudins. *Journal of Structural Geology, 26*, 1361–1376.

167. Treagus, S. H., Hudleston, P. J., & Lan, L. (1996). Non-ellipsoidal inclusions as geological strain markers and competence indicators. *Journal of Structural Geology, 18*, 1167–1172.

168. Turcotte, D. L., & Schubert, G. (1982). *Geodynamics: Applications of continuum physics to geological problems*. Wiley.

169. Vergnolle, M., Pollitz, F., & Calais, E. (2003). Constraints on the viscosity of the continental crust and mantle from GPS measurements and postseismic deformation models in western Mongolia. *Journal of Geophysical Research, 108*, 2502.

170. Wegmann, C. E. (1932). Note sur le boudinage. *Bulletin de la Société Géologique Française, 5(ii)*, 477–489.

171. Weijermars, R. (1992). Progressive deformation in anisotropic rocks. *Journal of Structural Geology, 14*, 723–742.

172. Weiss, L. E. (1972). *The minor structures of deformed rocks*. Springer-Verlag.

173. Wiesmayr, G., & Grasemann, B. (2005). Sense and non-sense of shear in flanking structures with layer-parallel shortening: Implications for fault-related folds. *Journal of Structural Geology, 27*, 249–264.

174. Williams, J. R. (1980). Similar and chevron folds in multilayers using finite-element and geometric models. *Tectonophysics, 65*, 323–338.

175. Wilson, G. (1961). Tectonic significance of small scale structures and their importance to geologists in the field. *Annales, Société Géologique de Belgique, 84*, 423–549.

176. Yakovlev, F. L. (2012a). Methods for detecting formation mechanisms and determining a final strain value for different scales of folded structures. *Comptes Rendus Geosci, 344*, 125–137.

177. Yakovlev, F. L. (2012b). Identification of geodynamic setting and of folding formation mechanisms using the strain ellipsoid concept for multi-scale structures of Greater Caucasus. *Tectonophysics, 581*, 93–113.

178. Zhang, Y., Hobbs, B. E., Ord, A., & Muhlhaus, H. B. (1996). Computer simulation of single layer buckling. *Journal of Structural Geology, 18*, 643–655.

179. Zulauf, G., Zulauf, J., Bornemann, O., Kihm, N., Peinl, M., & Zanella, F. (2009). Experimental deformation of a single-layer anhydrite in halite matrix under bulk constriction. Part 1: Geometric and kinematic aspects. *Journal of Structural Geology, 31*, 460–474.

APPENDICES

A.1 Marksheet of Coursework

JADAVPUR UNIVERSITY

KOLKATA-700 032

MARK SHEET

NO.: CW/19052/ 0200

(For Ph.D/M. Phil. Course Work)

Results of the PH.D. COURSE WORK EXAMINATION, 2021

In SCIENCE

Name DEBOJYOTI BASU MAJUMDER Class Roll No. 202020403007

Examination Roll No. PHDGEOL21207 Registration No. _ of

held in JULY, 2021

Subject Code / Name	Credit Hr.(c_i)	Marks
COMPULSORY UNITS:: EX/GELS/PHD/A & B RESEARCH METHODOLOGY & REVIEW OF RESEARCH WORK	4	89
ELECTIVE UNITS ::	4	93
EX/GELS/PHD/13 :: BASIC TECHNIQUES OF NUMERICAL MODELING STRUCTURAL GELOGY & T EX/GELS/PHD/14 :: USE OF MESO & MICRO-SCALE STRUCTURES IN STRUCTURAL ANALYSIS		

Total Marks : 182 (out of 200) **Remarks:** P

Prepared by : Checked by :

Date of issue : 04-10-2021

Controller of Examinations

APPENDICES

A.2 Published Research Articles

Journal of Structural Geology 104 (2017) 21–30

Contents lists available at ScienceDirect

Journal of Structural Geology

journal homepage: www.elsevier.com/locate/jsg

Geometry of torn boudin–An indicator of relative viscosity

Susanta Kumar Samanta*, Debojyoti Basu Majumder, Goutam Sarkar

Department of Geological Sciences, Jadavpur University, Kolkata, 700032, India

ARTICLE INFO

Keywords:
Boudin geometry
Boudin exterior and face
FEM
Visco-elastic
Viscosity ratio

ABSTRACT

The present study determines the role of viscosity on the development of rectangular torn boudin and its various types, defined by the curvature of their exterior and face margins. Numerical modeling was performed with the help of Finite Element Method considering Maxwell visco-elastic materials in commercial code ANSYS. Seven different viscosities were used and interchanged among the boudin, inter-boudin and matrix materials to understand the effect of viscosity ratios, specifically of relative viscosity of inter-boudin material. Results show that the viscosity of inter-boudin material has significant control on the shape of torn boudins apart from the viscosity ratio of boudin to matrix material. Bone-shaped boudin develops only when the inter-boudin is more competent than boudin and it becomes more prominent when matrix is also competent than boudin, but incompetent than inter-boudin. When boudins are stiffer than inter-boudin, barrel-shaped and fish-head boudins with concave faces develop. Exterior or face margins remain almost straight when boudin is relatively rigid compared to its surrounding matrix materials, or when there is no or very little viscosity contrast between boudin and inter-boudin material even in case of large boudin-matrix viscosity contrast. Therefore, the relative viscosity among the boudin, inter-boudin and matrix materials can be estimated qualitatively by studying the shape of boudin in the field.

1. Introduction

Boudinage structures are common features in deformed layered rocks, especially with contrasting rheologies, forming under layer parallel extension. These structures are often used to estimate finite strain in deformed rocks. The shape of an individual boudin object, defined by the geometry of outer margins in profile section, is also very useful for determining the modes of fracture and the rheological contrast of the boudinaged layers with respect to the embedding medium (Treagus et al., 1996; Marques et al., 2012; Abe and Urai, 2012). In nature, varieties of boudin geometries are observed which are controlled by the competence contrast between layer and the embedding host materials, the type of deformation, pre-to post-boudinage plastic deformation (Ramberg, 1955; Wilson, 1961; Ramsay, 1967; Strömgård, 1973; Ghosh and Ramberg, 1976; Lloyd and Ferguson, 1981; Treagus et al., 1996; Ghosh and Sengupta, 1999; Treagus and Lan, 2000, 2004; Passchier et al., 2005; Maeder et al., 2009; Fossen, 2010; Samanta and Deb, 2014) and also by the angular relationships between the layer and the deformation (kinematic) axes (Goldstein, 1988; Passchier and Druguet, 2002).

In nature, after fragmentation of stiffer layer, the inter-boudin zones are commonly filled either by host material or by siliceous or calcareous material which behave softer than boudin or/and matrix in geological condition. During subsequent deformation in presence of inter-boudin material, the rectangular boudin may gradually change resulting in boudins with concave faces, and bi-convex exteriors, forming 'barrel-shaped' boudins (Lloyd and Ferguson, 1981), 'extreme barrel-shaped' boudins (Lloyd et al., 1982), 'fish-mouth' or 'false-isocline' boudins (DePaor et al., 1991; Swanson, 1992), 'fish-head' boudins (Wegmann, 1932; Ghosh and Sengupta, 1999). In such situation, the compositions of boudin, inter-boudin and matrix may also change due to metamorphism, migmatization or fluid-rock chemical reactions (Ray et al., 2011), which lead to a change in their relative viscosities. As a result of that boudin may even behave incompetently with respect to both matrix and inter-boudin materials resulting in 'bone-shaped' boudin with concave exterior margins and straight or little convex face margins (Malavielle and Lacassin, 1988; Swanson, 1992). The effects of such rheological changes on the development of sequential boudins are reported from nature (Ghosh and Sengupta, 1999; Ray et al., 2011) and are also simulated in analogue and numerical modeling (Druguet and Carreras, 2006; Samanta and Deb, 2014). However, similar kinds of structures may also form in nature during subsequent layer-parallel shortening or extension of single layer that is segmented by layer perpendicular veins (whether formed by the process of boudinage or by the process of hydraulic fracturing) stiffer than host rock. They are described as shortened torn boudins ('double-sided mullions' or 'extreme

* Corresponding author.
E-mail address: susanta_ju@hotmail.com (S.K. Samanta).

http://dx.doi.org/10.1016/j.jsg.2017.10.003
Received 2 June 2017; Received in revised form 20 September 2017; Accepted 1 October 2017
Available online 03 October 2017

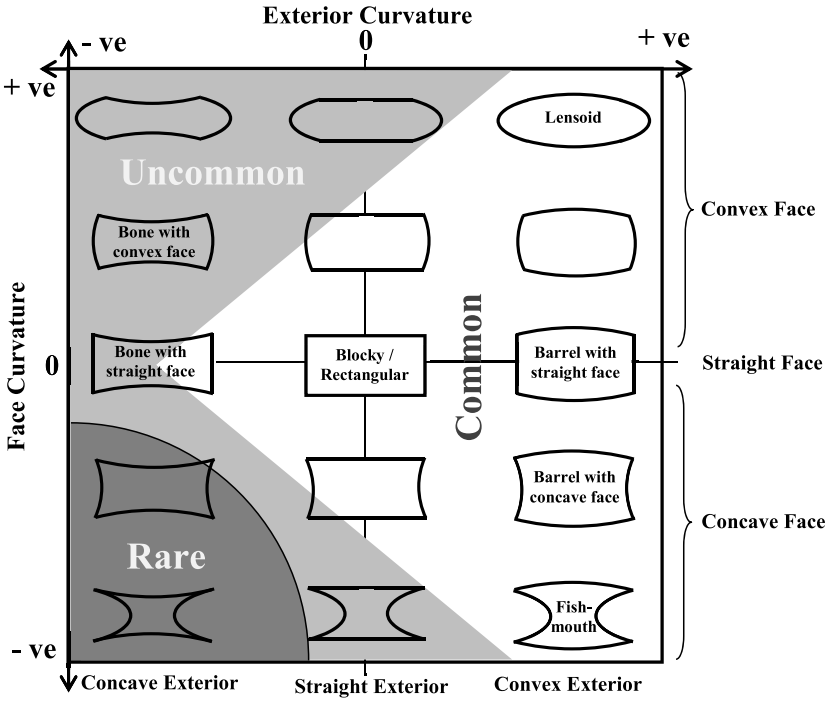

Fig. 1. Types of torn boudin and their positions with respect to their face and exterior curvature (redrawn from Goscombe et al., 2004). +ve and –ve indicate the convex and concave curvature respectively.

convex surface') and bone-shaped structures ('dog-bones' or 'trapezoidal boudins') (Kenis et al., 2002; Goscombe et al., 2004).

Torn boudin is described as symmetric boudin formed due to segmentation of layer by high angle, sharp, apparently 'brittle' planes of failure. Although, classical torn boudin is angular- and blocky-shaped with parallel edges, they often deform internally after fragmentation resulting in objects with curved exterior or face margins (Fig. 1). Goscombe et al. (2004) divided the torn boudins into straight-face and concave-face boudins as per the natural evidences from a wide variety of geological contexts worldwide. Straight-face boudins are sub-divided into blocky boudins (parallel margins), bone-type boudins (concave exterior margins) and straight-face with vein infill boudins. Blocky boudins are also described as rectangular or extension fracture or rectilinear boudins where the faces are aligned at a high angle and typically orthogonal to the boudinaged layer (Lloyd and Ferguson, 1981; Lloyd et al., 1982; DePaor et al., 1991; Mandal et al., 2000; Zulauf et al., 2009). Concave face boudins are sub-divided into bow-tie vein boudins and barrel boudins, where latter transforms to fish-mouth or fish-head or lensoid-shaped boudins with increasing finite strain. This classification is presented on the basis of the sense and amount of curvature of boudin's exterior and face margins, which may be straight, convex or concave in shape (Fig. 2). In this classification, shape of barrel and bow-tie boudin is same except the geometry of the inter-boudin, whereas geometries of blocky and straight-face with vein infill boudins are also identical except the absence and presence of inter-boudin respectively. Therefore, all symmetric boudins with combinations of straight, convex and concave margins are considered as torn boudins in the present study. Although all types of torn boudins are not very common, the concave-face boudins are observed frequently in nature. The torn boudin with convex face is rarely found in nature (less than 5% of investigated torn boudins of Goscombe et al., 2004). In such case, the amount of convexity is very less.

Shapes of boudinage structures and their progressive development have been subject of research over the last few decades. Stress and displacement analysis of boudinage and their influence on the shapes of boudins was first investigated by Selkman (1978). Lloyd and Ferguson (1981) performed series of numerical experiments considering elastic-plastic rheology to reveal the effects of material properties and amount of deformation on boudin shape. Treagus et al. (1996) and Treagus and Lan (2000) thoroughly investigated the effect of viscosity ratio of object to matrix considering both as Newtonian fluids. They showed that an isolated square object deforms to a 'barrel-shape' and 'bone-shape' if its viscosity is greater and lesser than the viscosity of the embedding medium respectively. The study was also extended to objects of power-law rheology with different values of power-law stress exponent (Treagus and Lan, 2004). However, their models do not exactly replicate natural situation where square or rectangular objects (boudins) are arranged in a row separated by inter-boudin areas of different material. Later, Kenis et al. (2006) simulated various bone- and barrel-shaped objects in Finite Element Method (FEM) analysis considering volume-constant steady-state power-law creep rheology by changing viscosity ratio between host and vein-infill material, initial aspect ratio of host-rock segments between two veins and the amount of finite deformation. In spite of quite a lot of studies on this subject, there is no such work considering the effect of relative viscosity of inter-boudin on the shape of torn boudin. The present work is intended to reveal the role of viscosity ratios among boudin, matrix and specially the inter-boudin materials on the post-fracture evolution of rectangular torn boudin, aiming to utilize their geometry for estimating the relative viscosities among boudin, inter-boudin and matrix. With the help of 2-D finite element modeling, we demonstrate that a boudin object, surrounded by a matrix and inter-boudin material of contrasting viscosity, is modified to objects of various shapes with curved margins under pure shear condition resulting from the mutual interaction of material flow within boudin, inter-boudin and matrix regions.

2. FEM modeling

2.1. Model considerations

Progressive development of torn boudin is a very complex process which is influenced by several independent parameters like aspect ratio

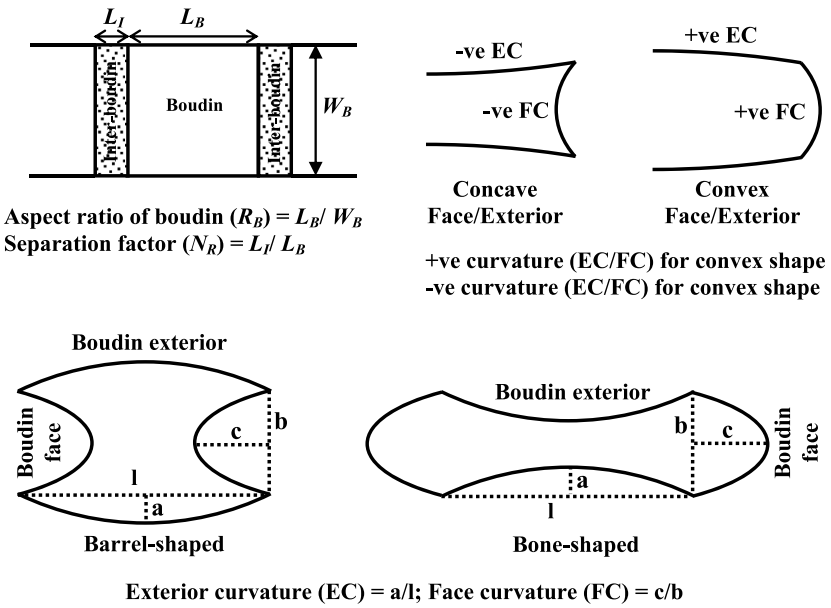

Fig. 2. Geometrical parameters of symmetric boudin block. L_B- length of boudin, W_B- width of boudin, L_I- length of inter-boudin, Aspect ratio of boudin (R_B) = L_B/W_B, Separation factor (N_R) = L_I/L_B, (after Passchier and Druguet, 2002).

of boudin (R_B) after layer fragmentation, rheological contrast between boudin and matrix, length of inter-boudin zones and rheology of infill material, nature of bulk deformation (Passchier and Druguet, 2002; Dabrowski and Grasemann, 2014). Here, we emphasize only the effect of viscosity ratio, which plays a significant role on the development of different shapes of torn boudins.

We considered the boudin rheology at the stage, when the competent layer has been segmented into boudin objects by extension fractures (Ramberg, 1955; Lloyd et al., 1982). Fragmentation of layer is often investigated theoretically and numerically considering elastic materials (Hobbs, 1967; Lloyd and Ferguson, 1981; Lloyd et al., 1982; Masuda and Kuriyama, 1988; Ji et al., 1997; Ji and Saruwatari, 1998). However, in nature, there are evidences of continuous deformation of the boudin blocks after their separation (Weiss, 1972; Lloyd and Ferguson, 1981; Ramsay and Huber, 1983; Hanmer and Passchier, 1991; Carreras and Druguet, 1994). It may be interpreted as post boudinage plastic deformation due to strain softening, induced by migmatization or fluid rock chemical reactions in subsequent deformation (Lloyd and Ferguson, 1981; Ghosh and Sengupta, 1999; Passchier and Trouw, 2005; Ray et al., 2011). This transformation from brittle elastic to visco-elastic nature is well reflected in the shape of torn boudin. The boudinage structures are modified either by a second phase of deformation (compression/extension) separated from the first by a significant period of time (reworked), or continued extension similar to the condition that caused the boudinage under the effect of strain softening (sequential) (Goscombe et al., 2004).

Since exterior and face curvatures are inversely proportional to the length (L_B) and width (W_B) of the boudin respectively (Fig. 2), in our model the initial aspect ratio of boudin block ($R_B = L_B/W_B$, Fig. 2) was taken as 1 so that both curvatures can be compared. According to Goscombe et al. (2004), the mean aspect ratio of torn boudin was found as 2.9 in natural rock, but this ratio may be achieved after internal deformation. However, to verify the effect of initial aspect ratio of boudin on its modified geometry, simulations were also done for initial aspect ratios of 2 and 3 in specific cases.

The modification of boudin shape starts after layer fragmentation when the fractures are filled with matrix or vein materials, or when rheological changes of boudin material take place due to metamorphic reaction in presence of adequate infilled material within the inter-boudin zones (Ray et al., 2011). Since it is difficult to simulate growing and filling of inter-boudin areas in progressive deformation, our models simulate newly developed boudins with small areas of separation zones. The dimension of the inter-boudin zone is defined by the separation factor ($N_R = L_I/L_B$) (Fig. 2, Passchier and Druguet, 2002). We choose this factor (N_R) as 0.25 where the initial length of separation zone (L_I) was one fourth of the initial length of boudin block. However, the effect of dimension of separation zone was also investigated considering N_R value 0.5, 0.125 and 0.0625. Like previous numerical models, the areas of inter-boudin zones are kept constant in our study and the inter-boudin material get stretched parallel to the layer without change in their areas (Passchier and Druguet, 2002; Arslan et al., 2008; Samanta and Deb, 2014). Although this condition does not exactly simulate the natural situation, the present study enlightens the significance of inter-boudin rheology on development of torn boudins of different geometries.

2.2. Constitutive equation

In order to understand the control of viscosity ratio on the shape of boudin object, two dimensional numerical modeling was performed using Finite Element Method (FEM) (Lloyd and Ferguson, 1981; Ramsay and Lisle, 2000; Treagus and Lan, 2004). Like earlier workers, we also considered Maxwell visco-elastic rheology in the modeling (Zhang et al., 1996; Mancktelow, 1999; Passchier and Druguet, 2002; Arslan et al., 2008, 2012; Samanta and Deb, 2014). The constitutive equation of this rheology is the following,

$$\frac{d\varepsilon}{dt} = \frac{1}{\mu}\frac{d\sigma}{dt} + \frac{\sigma}{\eta}, \quad (1)$$

Where, ε and σ are the instantaneous strain and stress respectively, and μ and η are the Maxwell shear modulus and viscosity respectively. This type of rheology is considered in modeling the lower crustal deformation where temperature and confining pressure is high (Turcotte and Schubert, 1982). With the help of ANSYS (commercial FEM code, ver. 10.0), models were prepared in structural mechanics under multiphysics domain. The 'VISCO88', a quadratic (shape functions) isoparametric element defined by eight nodes having two degrees of freedom at each node (U_x and U_y), was chosen in the model. This element is commonly used for two dimensional modeling with Maxwell visco-elastic rheology in ANSYS.

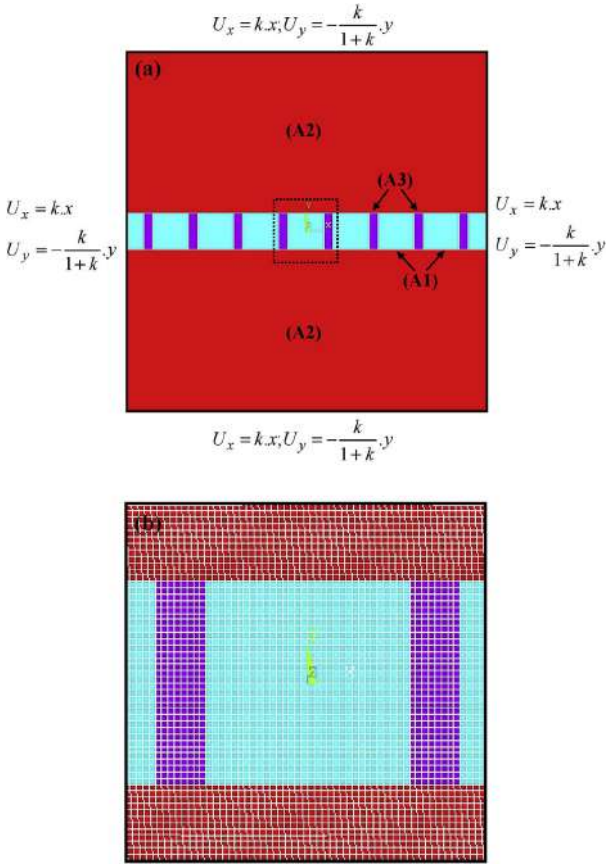

Fig. 3. (a) Model geometry considered in numerical simulation with separation factor (N_R) 0.25. A1- Boudin, A2- Matrix and A3- Inter-boudin. Note that pure shear flow conditions were imposed at four boundaries of the model. U_x and U_y are the displacement along X- and Y- axis respectively. k is the percentage of shortening. (b) Enlarged central square area (dotted lines of the above figure) with quadrilateral meshing.

2.3. Model geometry, meshing and boundary conditions

In our numerical model, we considered a boudinaged layer consisting series of boudin (A1) and inter-boudin (A3) objects embedded in a matrix material (A2) of dimension ten times larger than boudin object (Fig. 3a). To compare and measure the geometrical parameters of boudin, the shape of central boudin block was considered (area with dotted lines in Fig. 3a).

For modeling purpose we took up the free mesh technique (commonly used for any geometry) with quadrilateral mesh where shape and size of individual element varies from place to place (Fig. 3b). Number of nodes and elements in central boudin block were 3201 and 1024 respectively. The run time was set in such a way that the strain rates were achieved in the range of $10^{-7}s^{-1}$ and also the convergent results were obtained. The nature and number of meshing used in the model provided best possible results at particular run time.

Models were deformed in pure shear conditions (kinematic vorticity number, $W_k = 0$) employing displacements at the four boundaries of models with the following equations,

$$U_x = k \cdot x$$
$$U_y = -\frac{k}{1+k} \cdot y \quad (2)$$

Where, k is the percentage of shortening. In the present model, we considered the deformation and geometry of central rectangular block on which there was no influence of the boundaries. Each model was deformed up to 45% of shortening which was achieved in successive steps with a constant percentage (7.5%) of shortening at the model boundaries. The coordinates of specific nodes of middle boudin block were noted and the distances among those nodes were calculated to obtain the exterior- and face-curvature.

2.4. Material properties

Geological evidence suggests that, over a long period of time the lower crustal materials behave closely like a Maxwell visco-elastic substance with the viscosity in the order of 10^{17}–10^{23} Pa s (Vergnolle et al., 2003; Copley and McKenzie, 2007; Mukherjee, 2013). Since the present study is aimed at determining the role of viscosity ratios on the shapes of boudins, we choose seven material viscosities arbitrarily but within the range of natural values (Table 1). The values of bulk modulus, shear modulus were calculated utilizing the Poisson's ratio of 0.25. The Maxwell relaxation time was taken as 8×10^8 s for all materials (Larsen et al., 2005). The viscosity of matrix (10^{19} Pa s) was also kept constant for all experiments. We performed forty-nine experiments by interchanging the aforesaid materials between boudin and inter-boudin. In our experiments, both the viscosity ratios of boudin to matrix (here denoted by, η_{BM}) and inter-boudin to matrix (here denoted by, η_{IM}) were taken 0.1, 0.25, 0.50, 1, 2, 5 and 10.

2.5. Results of numerical simulation

The values of face and exterior curvatures obtained from the numerical simulations were plotted against the inter-boudin to matrix viscosity ratio (η_{IM}) (Fig. 4a and b). Such graphs were prepared for different boudin to matrix viscosity ratios. Results show that the shape of boudin not only depends on the viscosity ratio of the boudin and matrix material but also on the relative viscosity of the inter-boudin material. When boudin is more competent than inter-boudin, the exterior curvature is convex shaped and the face curvature is concave shaped (Fig. 5). The senses of curvatures are just opposite when the boudin material is softer than inter-boudin. With increasing the inter-boudin to matrix viscosity ratio, the concave face curvatures transform to convex geometry and the exterior curvature changes from convex to concave geometry (e.g. $\eta_{BM} = 1$ in Fig. 4 a & b). The face curvatures

Table 1
Values of physical properties of Maxwell viscoelastic materials considered in the finite element modeling.

Area	Viscosity (η, in Pa s)	Viscosity ratio (η_{BM} or η_{IM})	Shear modulus (μ, in Pa)	Bulk modulus (K, in Pa)	Relaxation time (in s)	Poisson's ratio (ν)
Matrix	1×10^{19}		1.25×10^{10}	2.083×10^{10}	8×10^8	0.25
Boudin or Inter-boudin	1×10^{18}	0.1	1.25×10^9	2.083×10^9		
	2.5×10^{18}	0.25	3.12×10^9	5.208×10^9		
	5×10^{18}	0.5	6.25×10^9	1.042×10^{10}		
	1×10^{19}	1	1.25×10^{10}	2.083×10^{10}		
	2×10^{19}	2	2.50×10^{10}	4.167×10^{10}		
	5×10^{19}	5	6.25×10^{10}	1.042×10^{11}		
	1×10^{20}	10	1.25×10^{11}	2.083×10^{11}		

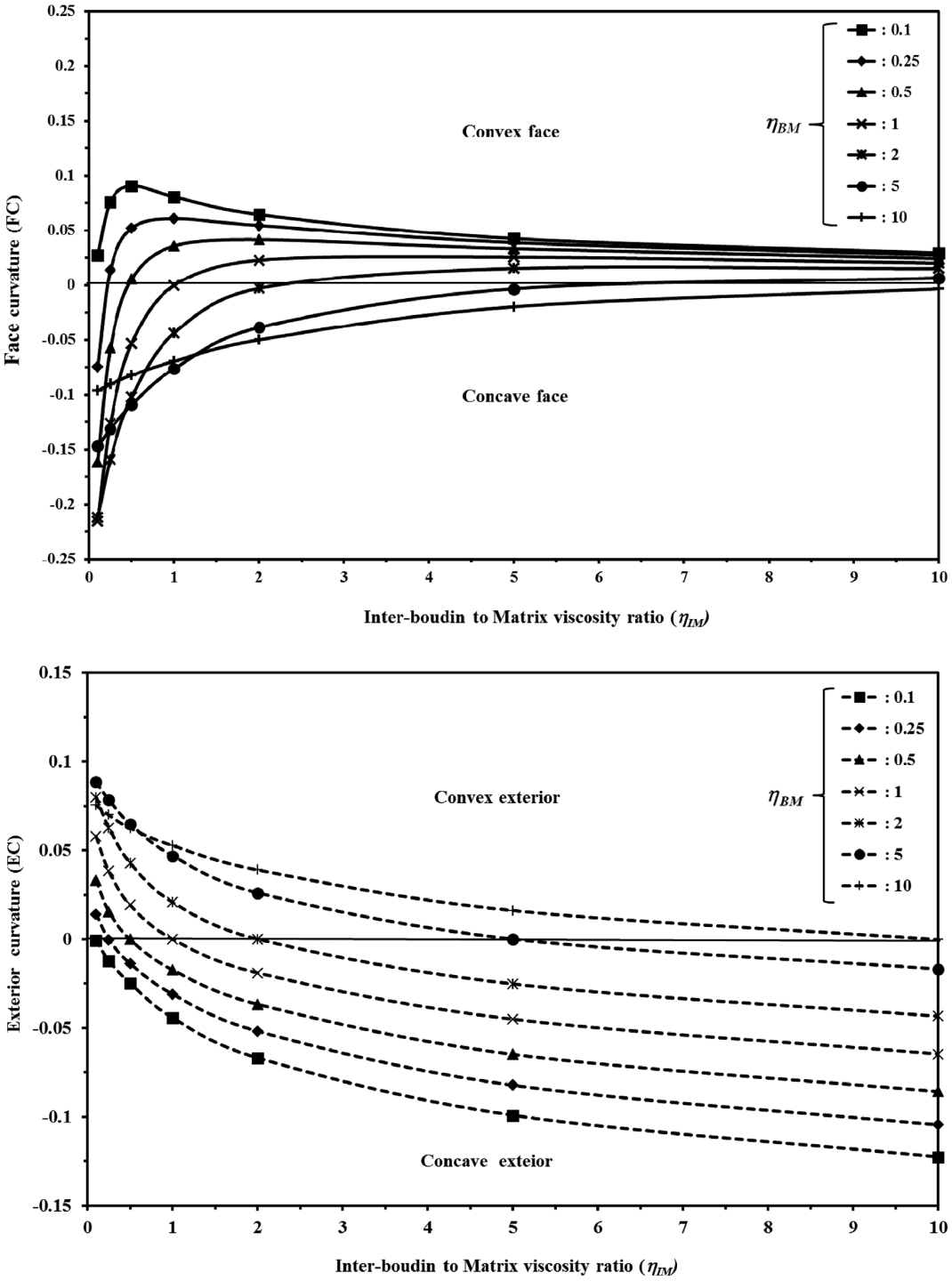

Fig. 4. (a) Variations of boudin face curvatures (solid lines) with increasing inter-boudin to matrix viscosity ratio (η_{IM}) for different boudin – matrix viscosity ratio (η_{BM}). (b) Variations of boudin exterior curvature (dashed lines) with increasing inter-boudin to matrix viscosity ratio (η_{IM}) for different boudin – matrix viscosity ratio (η_{BM}). Shortening percentage = 45%.

vary maximum at lower value of inter-boudin to matrix viscosity ratio and reaches almost a steady value when the viscosity ratio is much higher. The curvature of concave geometry is always more than that of the convex geometry. The exterior curvature becomes almost zero when the viscosity of boudin and inter-boudin is same for any viscosity of the matrix (Figs. 4b and 5).

Numerical results also reveal that exterior margins show strong curvatures only when there is a large viscosity contrast between boudin and inter-boudin (Fig. 5). For a specific matrix viscosity, boudins with convex exterior and concave face develop only when boudin is more

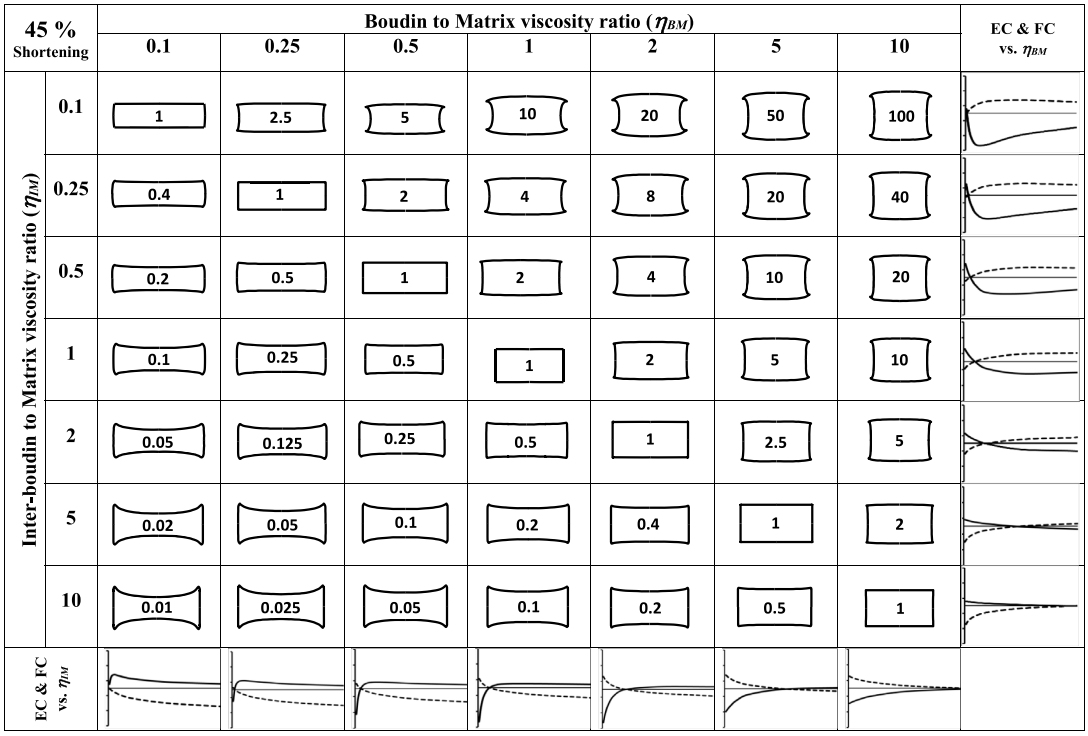

Fig. 5. Geometries of torn boudins obtained from FEM simulation for different viscosity ratios (η_{IM} and η_{BM}). The numerical value within the individual boudin block indicates ratio of boudin and inter-boudin viscosity (η_{BI}). The graphs at the end of row and column represent the change of exterior (dashed lines) and face curvature (solid lines) in respective row and column. Maximum and minimum values of curvature along Y-axis are 0.25 and −0.25 respectively in all graphs. Shortening percentage = 45%.

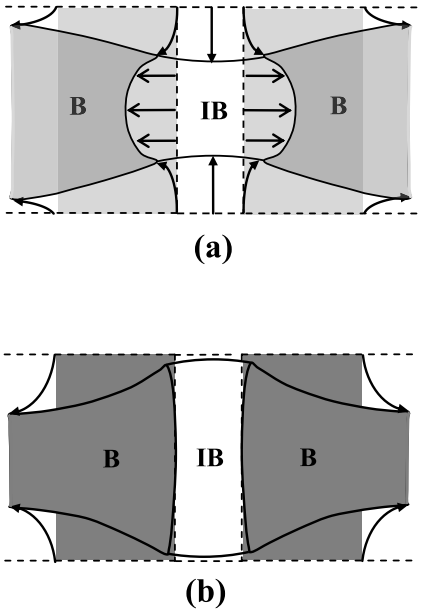

Fig. 6. Differential flow of boudin and inter-boudin material during deformation. (a) Inter-boudin is softer than boudin resulting barrel- or fish-head shaped boudin and (b) boudin is softer than inter-boudin resulting bone-shaped boudin. Arrows indicate the flow of material. Note that the boudins (shaded) shown at both sides of the inter-boudin (unshaded) are half of the length of boudin.

competent than inter-boudin. The curvature of face and exterior margin will be just opposite when the boudin is much softer than the inter-boudin. For higher viscosity ratio of boudin to inter-boudin ($\eta_{BI} \gg 1$) both the exterior and face shows strong curvature. But, the exterior curvatures show strong concavity with very little convexity in face curvature when the boudin to inter-boudin ratio is lesser then 1 ($\eta_{BI} < 1$). With increasing the boudin to matrix viscosity ratio (η_{BM}) the geometry of exterior margins gradually shift from concave to convex shape, whereas, the face curvatures changes from convex to concave shape resulting the change of boudin geometry from bone-to barrel-shaped (Figs. 4 and 5). Similar changes of boudin geometries also take place if the inter-boudin to matrix viscosity ratio (η_{IM}) is gradually decreased for a specific boudin to matrix viscosity ratio (η_{BM}). When there is very little or no viscosity contrast between the boudin and inter-boudin materials, the boudin shape becomes almost rectangular (Figs. 4a and 5) (Treagus and Lan, 2000). However, their aspect ratios increase with decreasing viscosity of boudin and inter-boudin with respect to matrix.

3. Discussions

3.1. Role of viscosity

Results obtained from numerical experiments suggest that the changes of curvatures of boudin and inter-boudin interfaces (face margin) and boudin and matrix interfaces (exterior margin) are not independent. They are modified by the mutual interaction of material flow among boudin, inter-boudin and matrix regions. It is revealed that after the fragmentation of boudinaged layer, in addition to the viscosity contrast between boudin and matrix, the viscosity of inter-boudin material has significant role on the shape of boudin in subsequent deformation. Face curvature depends on the differential lateral flow (from

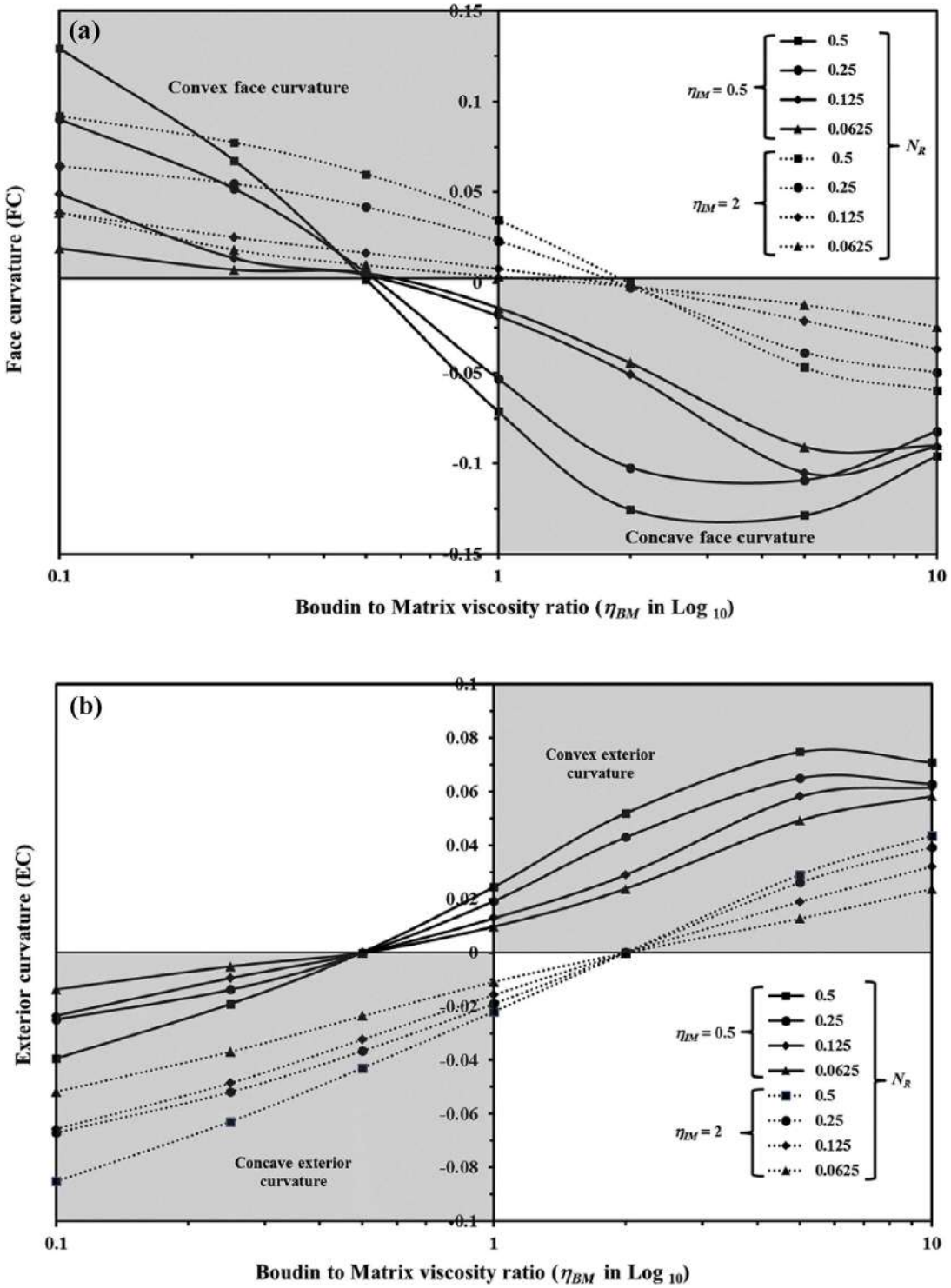

Fig. 7. Effect of separation factor on the shape of torn boudin. Variation of face curvature (FC) in (a) and exterior curvature (EC) in (b) with the boudin to matrix viscosity ratio (η_{BM}) for different separation factor (N_R). Solid lines represent the curvatures when inter-boudin is softer (half) than matrix, whereas dotted lines represent when inter-boudin is stiffer (double) than matrix. Note that with changing the separation factor, values of curvature vary slightly without changing the sense of curvature.

margin to inner portion along the boudin face) of boudin material (Fig. 6 a & b), which is largely controlled by the amount of traction exerted by the matrix on the boudin exterior surface and the flow of inter-boudin material (Mandal et al., 2000). Under layer parallel extension, both inter-boudin and boudin materials flow laterally. Harder material resists flow within it, and hence, impedes the flow of adjacent softer material. The geometry of interface between harder and softer materials is governed by the resultant of these two flows. When the boudin material tries to flow sidewise, it is hindered or facilitated by the inter-boudin material. So, the boudin face becomes concave shaped only when the inter-boudin material is relatively softer and it allows to flow boudin material laterally towards the boudin's center (Fig. 5). Similarly, shape of exterior margin is not merely depended on the boudin to matrix viscosity ratio (η_{BM}). For example, if the boudin is ten times softer than the matrix, exterior margins may vary from straight to highly concave in geometry (Fig. 5, first column) depending on the viscosity ratio of boudin to inter-boudin material (η_{BI}). Maximum concavity develops when the boudin material is much softer than inter-boudin material and its curvature increases with decreasing the boudin to inter-boudin viscosity ratio (η_{BI}). Exterior margins remain almost straight if there is no viscosity contrast between boudin and inter-boudin, whereas, it becomes convex shape if the inter-boudin is softer than boudin for any matrix viscosity.

Generally, barrel- and bone-shaped boudins form when they behave more competently and incompetently with respect to matrix respectively (Treagus et al., 1996; Treagus and Lan, 2000, 2004). Fish-head boudin may develop from barrel-shaped boudin with concave face at higher finite strain specially when inter-boudin is much softer than boudin. According to Treagus et al. (1996), the exterior and face margins remain straight when there is no rheological contrast between boudin and matrix. Under such condition, however, both barrel- and bone-shaped boudins can be produced in presence of inter-boudin materials (Fig. 5, column with $\eta_{BM} = 1$). From the field study, it is assumed that concave-face boudin are produced when boudin behaves incompetently with respect to the inter-boudin (Ghosh and Sengupta, 1999). But, the present study reveals that the face curvature will be slightly convex and the exterior curvature will be concave shaped if the boudin is softer than inter-boudin. So, conditions for the development of concave face curvature inhibit the exterior margin to become a concave shape. It is kinematically not possible to produce a boudin with both concave face and concave exterior margins together. As a result of that such kind of boudin shape is rarely found in nature (Fig. 4d of Goscombe et al., 2004). According to the present analysis, bone-shaped boudins can be produced only when inter-boudin is more competent than boudin and matrix. But the curvature of convex face is always lower than the curvature of concave exterior margin. These results conform to the results of numerical modeling by Maeder et al. (2009). However, in nature, boudins are rarely incompetent than the inter-boudin materials except the rheological inversion of boudin-matrix system (Ghosh and Sengupta, 1999) or the situation where stiffer veins occur within the series of perpendicular fractures in relatively softer medium (Kenis et al., 2004, 2006, Fig. 3). In our numerical experiment, lensoid boudin with both convex shaped face and exterior margins cannot be simulated directly. In nature, lensoid-shaped boudins are produced due to stretching of pinch-and-swell structures ('Tapering boudin' in Goscombe et al., 2004; 'lenticular' boudins in Lloyd et al., 1982 and 'stretched layer' in Lacassin, 1988) or by extreme modification of barrel-shaped boudin (Wegmann, 1932). Similarly, barrel-shaped boudins with straight faces develop due to pre-boudinaged plastic deformation which is outside the scope of this study.

Shapes of individual boudins are often used to determine the viscosity contrast between boudin and matrix qualitatively. But, before taking any firm conclusion about the rheological contrast one has to ascertain the presence or absence of any subsequent deformation from other field evidences. For example, rectangular boudins with straight margins are commonly interpreted as a result of extremely high boudin to matrix viscosity ratio with or without subsequent deformation. But, in nature both face and exterior margins remain even straight during subsequent deformation when boudin to inter-boudin viscosity ratio is almost negligible irrespective of the matrix viscosity. Only the aspect ratio of boudin remains almost unaltered in former case, whereas in the latter case it increases with increasing matrix viscosity with respect to the boudin and inter-boudin (compare shape of upper left position to the lower right position of Fig. 5).

3.2. Effect of separation factor (N_R) and aspect ratio of boudin (R_B)

In the present numerical models, the initial length of inter-boudin separation zone (L_I) was kept as one fourth of the length of boudin with a separation factor (N_R) 0.25. However, the effect of initial length of the inter-boudin separation zone was also investigated. Two series of experiments were conducted with one relatively higher separation factor ($N_R = 0.5$) and two relatively lower separation factors ($N_R = 0.125$ and 0.0625) for different boudin to matrix viscosity ratio (η_{BM}). In the first series, the inter-boudin was softer than matrix ($\eta_{IM} < 1$) and in the second series, matrix was softer than inter-boudin ($\eta_{IM} > 1$). It is evident from the numerical results that the change of initial length of inter-boudin does not influence much on both exterior and face curvature (Fig. 7 a and b). Their variations are within the range of second decimal. Moreover, in case of higher η_{BM} ratio, this variation is almost negligible when inter-boudin is softer than matrix.

Numerical models were also run to investigate the effect of aspect ratio of initial boudin object (R_B). We ran series of experiments for different boudin to matrix viscosity ratio (η_{BM}) keeping the inter-boudin to matrix ratio (η_{IM}) constant (0.5). In our model we increased the boudin length keeping the boudin width constant. In overall, the exterior curvature drops, whereas the face curvature increases (Fig. 8 a and b). The maximum variation of face curvature is found 0.175 whereas the exterior curvature varies negligibly. However, the senses of curvatures remain same irrespective of the aspect ratio of boudin.

3.3. Limitations

In numerical experiments, the interfaces are assumed to be coherent which may not be perfectly maintained in natural examples. The initial boudin object was taken as square in numerical experiments. But, in nature non-square shapes are common which may lead to slightly different values of face and exterior curvature from our experimental results. But, the sense of curvature will not change, thus, it can be used for measuring relative viscosity. The viscosity of boudin material was also kept constant during deformation which may not prevail in some natural situations where, for instance, post-boudinage syntectonic migmatizations occurs (Samanta and Deb, 2014).

4. Conclusions

The present study confirms that, after the formation of rectangular torn boudin with straight and orthogonal edges, in presence of inter-boudin material, the edges may remain straight or modify to convex or concave geometries due to mutual interaction of flow among boudin, inter-boudin and matrix material in subsequent deformation. It is revealed that in addition to the boudin to matrix viscosity ratio, the curvature of both face and exterior margins of boudins are strongly sensitive to the relative viscosity of the inter-boudin material in subsequent deformation.

Bone-shaped boudin with concave exteriors and convex faces develops when inter-boudin material is more competent than boudin material. It becomes more prominent when matrix is stiffer than boudin, but softer than inter-boudin. When boudin behaves stiffer than inter-boudin, barrel-shaped boudins develop, which become more prominent when boudin is also stiffer than matrix. Barrel-shaped boudins transform to fish-head boudins at higher finite strain. In case of

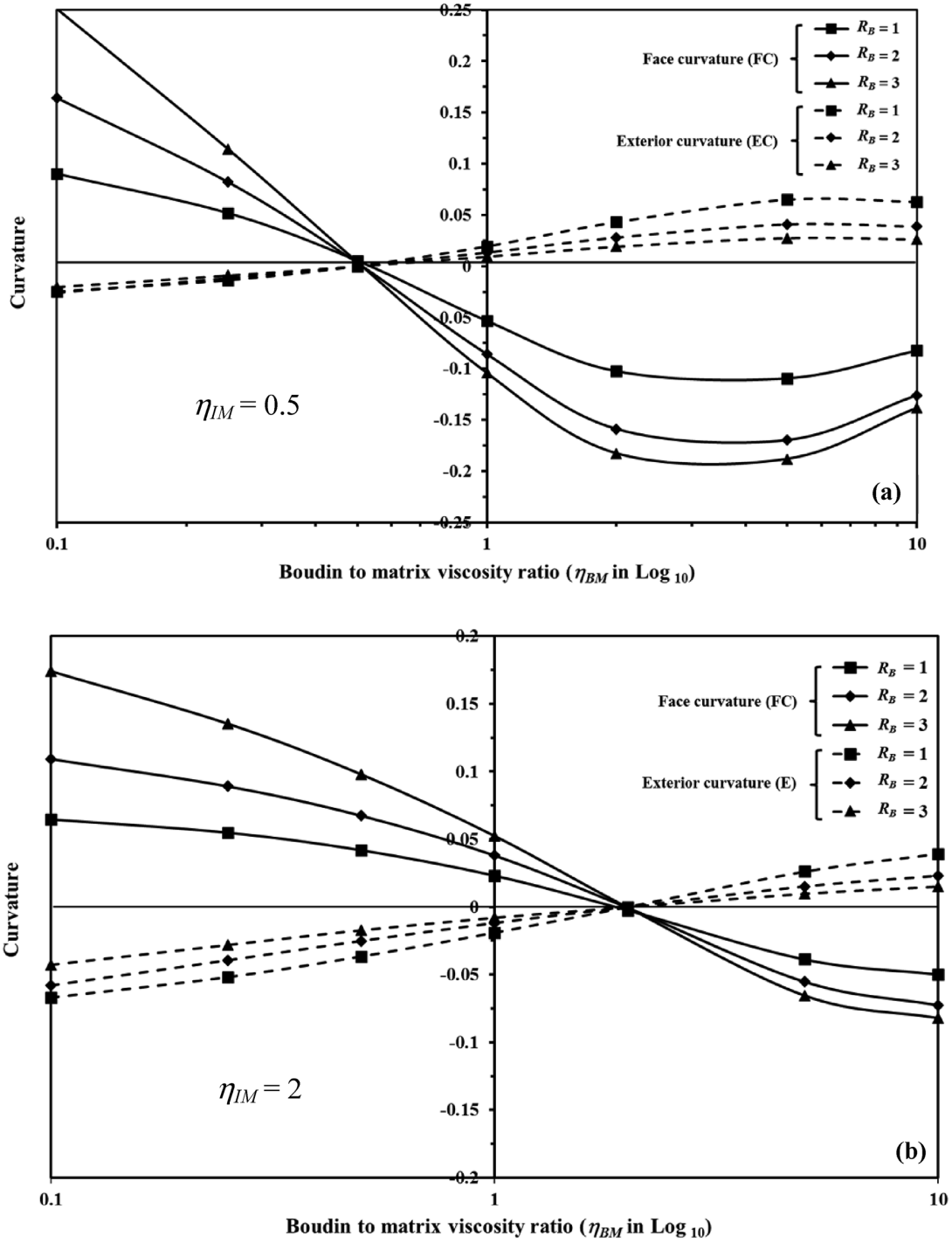

Fig. 8. Variation of face (solid lines) and exterior (dashed lines) curvature with the boudin to matrix viscosity ratio (η_{BM}) for different initial aspect ratio of boudin object (R_B). (a) Viscosity of inter-boudin is half of the viscosity of the matrix ($\eta_{IM} = 0.5$) and (b) viscosity of inter-boudin is double the viscosity of the matrix ($\eta_{IM} = 2$). Note that the initial aspect ratio of boudin does not have much influence on the sense of both face and exterior curvature of torn boudin.

very little or no viscosity contrast between the boudin and inter-boudin materials, rectangular boudin is produced. However, their aspect ratios vary with relative viscosity of the matrix. Boudin with either both convex or both concave margins (face and exterior) cannot be produced in present kinematic conditions.

The geometry of boudin margin can give us important clue about the viscosity ratio among the boudin, inter-boudin and matrix material. So, their relative competency can be estimated qualitatively from the sense of curvature of exterior and face margin of boudin object.

Acknowledgements

We are grateful to Drs. E. Druguet, and A. Arslan for their detailed review comments that has improved the manuscript significantly. We are also thankful to Profs. R.J. Lisle, S.H. Treagus for their insightful comments on the manuscript. Constructive suggestions from Prof. J. Hippertt are also sincerely acknowledged. The work was supported by DST, India through PURSE Program, Phase-II sanctioned to SKS. The infrastructural facilities were provided by the Center of Advanced Study (Phase VI), Department of Geological Sciences, Jadavpur University. Indrasish Deb is acknowledged for helping in some of the numerical modeling at the initial stage of the work.

References

Abe, S., Urai, J.L., 2012. Discrete element modeling of boudinage: insights on rock rheology, matrix flow, and evolution of geometry. J. Geophys. Res. 117, B01407.
Arslan, A., Passchier, C.W., Koehn, D., 2008. Foliation boudinage. J. Struct. Geol. 30, 291–309.
Arslan, A., Koehn, D., Passchier, C.W., Sachau, T., 2012. The transition from single layer to foliation boudinage: a dynamic modelling approach. J. Struct. Geol. 42, 118–126.
Carreras, J., Druguet, E., 1994. Structural zonation as a result of inhomogeneous non-coaxial deformation and its control on syntectonic intrusions: an example from the Cap de Creus area, Eastern-Pyrenees. J. Struct. Geol. 16, 1525–1534.
Copley, A., McKenzie, D., 2007. Models of crustal flow in the India–Asia collision zone. Geophys. J. Int. 169, 683–698.
Dabrowski, M., Grasemann, B., 2014. Domino boudinage under layer-parallel simple shear. J. Struct. Geol. 68, 58–65.
DePaor, D.G., Simpson, C., Bailey, C.M., McCaffrey, K.J.W., Bean, E., Gower, R.J.W., Aziz, G., 1991. The role of solution in the formation of boudinage and transverse veins in carbonate rocks at Rheems, Pennsylvania. Geol. Soc. Am. Bull. 103, 1552–1563.
Druguet, E., Carreras, J., 2006. Analogue modelling of syntectonic leucosomes in migmatitic schists. J. Struct. Geol. 28, 1734–1747.
Fossen, H., 2010. Structural Geology. Cambridge University Press 463 pp.
Ghosh, S.K., Ramberg, H., 1976. Reorientation of inclusions by combination of pure and simple shear. Tectonophysics 34, l–70.
Ghosh, S.K., Sengupta, S., 1999. Boudinage and composite boudinage in superposed deformations and syntectonic migmatisation. J. Struct. Geol. 21, 97–110.
Goldstein, A.G., 1988. Factors affecting the kinematic interpretation of asymmetric boudinage in shear zones. J. Struct. Geol. 10, 707–715.
Goscombe, B.D., Passchier, C.W., Hand, M., 2004. Boudinage classification: end-member boudin types and modified boudin structures. J. Struct. Geol. 26, 739–763.
Hanmer and Passchier, 1991. Shear-sense Indicators: a Review. Geological Survey of Canada 72 pp.
Hobbs, D.W., 1967. The formation of tension joints in sedimentary rocks: an explanation. Geol. Mag. 104, 550–556.
Ji, S., Saruwatari, K., 1998. A revised model for the relationship between joint spacing and layer thickness. J. Struct. Geol. 20, 1495–1508.
Ji, S., Zhao, P., Saruwatari, K., 1997. Fracturing of garnet crystals in anisotropic rocks during uplift. J. Struct. Geol. 19, 603–620.
Kenis, I., Sintubin, M., Muchez, Ph, Burke, E.A.J., 2002. The 'boudinage' question in the High-Ardenne Slate Belt (Belgium): a combined structural and fluid-inclusion approach. Tectonophysics 348, 93–110.
Kenis, I., Urai, J.L., van der Zee, W., Sintubin, M., 2004. Mullions in the High-Ardenne Slate Belt (Belgium). Numerical model and parameter sensitivity analysis. J. Struct. Geol. 26, 1677–1692.
Kenis, I., Urai, J.L., Sintubin, M., 2006. The development of bone-shaped structures in initially segmented layers during layer-parallel extension: numerical modelling and parameter sensitivity analysis. J. Struct. Geol. 28, 1183–1192.
Lacassin, R., 1988. Large-scale foliation boudinage in gneisses. J. Struct. Geol. 10, 643–647.
Larsen, C.F., Motyka, R.J., Freymueller, J.T., Echelmeyer, K.A., Ivins, E.R., 2005. Rapid viscoelastic uplift in southeast Alaska caused by post-Little Ice Age glacial retreat. Earth Planet. Sci. Lett. 237, 548–560.
Lloyd, G.E., Ferguson, C.C., 1981. Boudinage structure: some new interpretations based on elastic-plastic finite element simulations. J. Struct. Geol. 3, 117–128.
Lloyd, G.E., Ferguson, C.C., Reading, K., 1982. A stress transfer model for the development of extension fracture boudinage. J. Struct. Geol. 4, 355–372.
Maeder, X., Passchier, C.W., Koehn, D., 2009. Modelling of segment structures: boudins, bone-boudins, mullions and related single- and multiphase deformation features. J. Struct. Geol. 31, 817–830.
Malavielle, J., Lacassin, R., 1988. "Bone-shaped" boudins in progressive shearing. J. Struct. Geol. 10, 335–345.
Mancktelow, N.S., 1999. Finite-element modeling of single layer folding in elasto-viscous materials: the effect of the initial perturbation geometry. J. Struct. Geol. 21, 161–177.
Mandal, N., Chakraborty, C., Samanta, S.K., 2000. Boudinage in multilayered rocks under layer-normal compression: a theoretical analysis. J. Struct. Geol. 22, 373–382.
Marques, F.O., Fonseca, P.D., Lechmann, S., Burg, J.P., Marques, A.S., Andrade, A.J.M., Alves, C., 2012. Boudinage in nature and experiment. Tectonophysics 526–529, 88–96.
Masuda, T., Kuriyama, M., 1988. Successive "mid-point" fracturing during micro-boudinage: an estimate of the stress – strain relation during a natural deformation. Tectonophysics 147, 171–177.
Mukherjee, S., 2013. Channel flow extrusion model to constrain dynamic viscosity and Prandtl number of the Higher Himalayan Shear Zone. Int. J. Earth Sci. 102, 1811–1835.
Passchier, C.W., Druguet, E., 2002. Numerical modelling of asymmetric boudinage. J. Struct. Geol. 24, 1789–1803.
Passchier, C.W., Trouw, R.A.J., 2005. Microtectonics, second ed. Springer-Verlag, Berlin 366 pp.
Passchier, C.W., Mancktelow, N.S., Grasemann, B., 2005. Flow perturbations: a tool to study and characterize heterogeneous deformation. J. Struct. Geol. 27, 1011–1026.
Ramberg, H., 1955. Natural and experimental boudinage and pinch-and-swell structures. J. Geol. 63, 512–526.
Ramsay, J.G., 1967. Folding and Fracturing of Rocks. McGraw Hill, New York.
Ramsay, J.G., Huber, M.I., 1983. The Techniques of Modern Structural Geology. Strain Analysis, vol. 1 Academic Press, London 1–308.
Ramsay, J.G., Lisle, R.J., 2000. The Techniques of Modern Structural Geology. Applications of Continuum Mechanics in Structural Geology, vol. 3 Academic Press, London 702–1061.
Ray, S., Sanyal, S., Sengupta, P., 2011. Mineralogical control on rheological inversion of a suite of deformed mafic dykes from parts of the chottanagpur granite gneiss complex of eastern India. In: Srivastava, R.K. (Ed.), Dyke Swarms: Keys for Geodynamic Interpretation.
Samanta, S.K., Deb, I., 2014. Development of concave-face boudin in Chhotanagpur Granite Gneiss Complex of Jasidih-Deoghar area, eastern India: insight from finite element modeling. J. Struct. Geol. 62, 38–51.
Selkman, S., 1978. Stress and displacement analysis of boudinages by the finite-element method. Tectonophysics 44, 115–139.
Strömgård, K.E., 1973. Stress distribution during formation of boudinage and pressure shadows. Tectonophysics 16, 215–248.
Swanson, M.T., 1992. Late Acadian-Alleghenian transpressional deformation: evidence from asymmetric boudinage in the Casco Bay area, coastal Maine. J. Struct. Geol. 14, 323–341.
Treagus, S.H., Lan, L., 2000. Pure shear deformation of square objects, and applications to geological strain analysis. J. Struct. Geol. 22, 105–122.
Treagus, S.H., Lan, L., 2004. Deformation of square objects and boudins. J. Struct. Geol. 26, 1361–1376.
Treagus, S.H., Hudleston, P.J., Lan, L., 1996. Non-ellipsoidal inclusions as geological strain markers and competence indicators. J. Struct. Geol. 18, 1167–1172.
Turcotte, D.L., Schubert, G., 1982. Geodynamics: Applications of Continuum Physics to Geological Problems. Wiley, New York.
Vergnolle, M., Pollitz, F., Calais, E., 2003. Constraints on the viscosity of the continental crust and mantle from GPS measurements and postseismic deformation models in western Mongolia. J. Geophys. Res. 108, 2502.
Wegmann, C.E., 1932. Note sur le boudinage. Bull. la Soc. Geol. Francaise Ser 5 (ii), 477–489.
Weiss, L.E., 1972. The Minor Structures of Deformed Rocks. Springer-Verlag, Berlin 431 pp.
Wilson, G., 1961. Tectonic significance of small scale structures and their importance to geologists in the field. Ann. Société Géologique Belg. 84 423–549.
Zhang, Y., Hobbs, B.E., Ord, A., Muhlhaus, H.B., 1996. Computer simulation of single-layer buckling. J. Struct. Geol. 18, 643–655.
Zulauf, G., Zulauf, J., Bornemann, O., Kihm, N., Peinl, M., Zanella, F., 2009. Experimental deformation of a single-layer anhydrite in halite matrix under bulk constriction. Part 1: geometric and kinematic aspects. J. Struct. Geol. 31, 460–474.

Journal of Structural Geology 174 (2023) 104935

Contents lists available at ScienceDirect

Journal of Structural Geology

journal homepage: www.elsevier.com/locate/jsg

Development of flanking structures in layered gneissic rock: Insights from numerical modelling

Debojyoti Basu Majumder, Susanta Kumar Samanta *

Department of Geological Sciences, Jadavpur University, Kolkata, 700032, India

ARTICLE INFO

Keywords:
Layered rock
Anisotropy factor
General deformation
Foliation drag
FEM model

ABSTRACT

Flanking structures defined by dragged planar fabrics alongside of quartzo-feldspathic veins in gneissic rocks are very common. Varieties of mesoscale flanking structures were observed in parts of the Chhotonagpur Granite Gneissic Complex (CGGC), Eastern India. Alternate thin layering of quartzo-feldspathic and mafic minerals in gneissic rock causes mechanical anisotropy in rock during deformation. This study aims to explore specially the influence of mechanical anisotropy on the development of flanking structures. With the help of two –dimensional Finite Element modelling, we attempt to understand the effect of initial orientation of cross-cutting element (θ), kinematic vorticity number (W_k) and the anisotropy factor (δ) on the development of flanking structures. Deformed shape of cross-cutting element (R_N), amount (L_N) and nature (antithetic or synthetic) of offset of layers and pattern of drag (reverse or normal) are considered as important parameters for their nomenclature. As the final geometry of flanking structure does not only depend on the instantaneous deformational condition, we analyze the progressive development of flanking structures by varying the above parameters. Study reveals that mechanical anisotropy has strong influence on the geometry of flanking structures in layered gneissic rock, which depends on the initial orientation of long axis of cross-cutting element and its final position with respect to the orientation of principal stress axes and pole of anisotropy. The study also reveals that the flanking structures can be used as important tool for estimating the mechanical anisotropy in layered rock. Shape of cross-cutting element, amount of offset and the shifting of the object-tip points are the most important parameters for determining the anisotropy factor.

1. Introduction

Flanking structures, generally defined as deflection of linear and planar fabrics alongside of any cross-cutting fracture/object, are commonly found in layered and/or foliated metamorphic rock in micro- and meso-scale. Although the term was first introduced by Passchier (2001), the structures were first described by Gayer et al. (1978) and Hudleston (1989) which were, later, described as roll-over anticlines (Barnett et al., 1987; Reches and Eidelman, 1995; Grasemann et al., 2005), fringe folds (Grasemann et al., 1999) and flanking folds (Druguet et al., 1997; Grasemann et al., 1999; Grasemann and Stuwe, 2001). Such structures are broadly classified based on instantaneous orientations of cross-cutting element (CE), geometry of dragging of linear and planar fabrics in neighborhood (internal host element) and far away (external host element) (Passchier, 2001; Coelho et al., 2005; Passchier and Trouw, 2005), and the relative sense of offset of external host element across the cross-cutting element (Grasemann et al., 2003; Coelho et al., 2005; review in Mukherjee, 2014). In last few decades, many researchers tried to understand the evolution of these structures as they are one of the most important features for determining kinematic conditions (shear sense etc., review in Dutta and Mukherjee, 2019). Both analogue and numerical modelling were attempted under simple shear and general shear deformational conditions considering the rock as isotropic homogeneous medium (Grasemann and Stuwe, 2001; Grasemann et al., 2003; Exner et al., 2004, 2006; Kocher and Mancktelow, 2005; Wiesmayr and Grasemann, 2005; Grasemann et al., 2005; Mulchrone, 2007a; Grasemann et al., 2019; Mayrhofer et al., 2022). In their model, they considered the initial cross-cutting element mostly as slip line/plane where the external fabrics offset along the cut without much change of its shape. In particular, Mulchrone (2007a) simulated the flanking structure in homogeneous viscous matrix by using a deformable elliptical inclusion. He primarily considered two parameters, the viscosity ratio (cross-cutting element to host element) and degree of simple shear, and explained the drag geometry of passive layers around

* Corresponding author.
E-mail address: susantak.samanta@jadavpuruniversity.in (S.K. Samanta).

https://doi.org/10.1016/j.jsg.2023.104935
Received 17 March 2023; Received in revised form 26 July 2023; Accepted 8 August 2023
Available online 10 August 2023

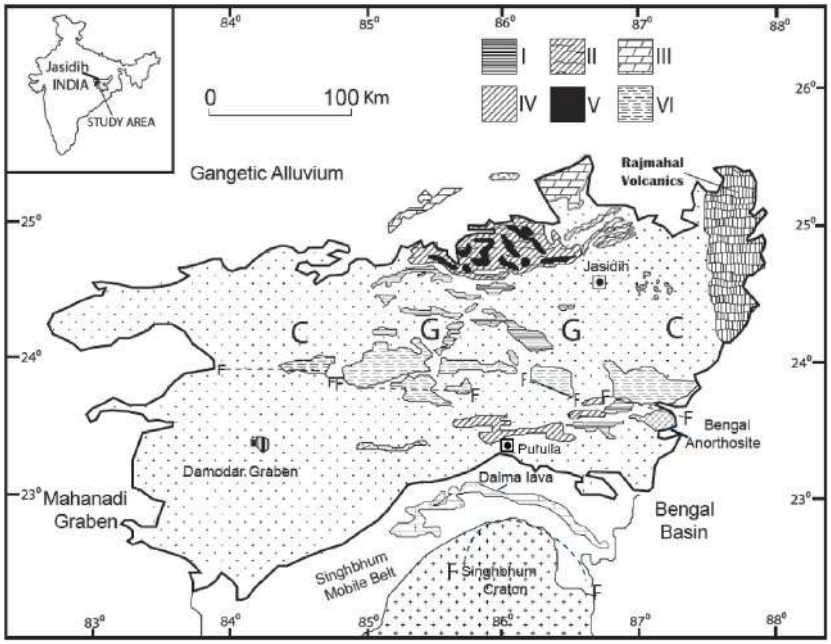

Fig. 1. Geological map of Chhotanagpur Granite Gneissic Complex (CGGC) showing the location of study area (Jasidih-Deoghar and Purulia) (after Samanta and Deb, 2014). I - Archean-Proterozoic metasedimentary enclaves, II- Paleo-Mesoproterozoic metasedimentary enclaves, III- Mesoproterozoic meta-sedimentary enclaves, IV- Granitic plutons of Mesoproterozoic, V- Granitic plutons of Neoproterozoic, VI- Gondwanas and younger covers. The dashed lines marked with 'F' represent faults.

deformable elliptical object. Exner and Dabrowski (2010) investigated numerically the development of flanking structures in three dimensions considering ellipsoidal crack instead of cylindrical crack (perpendicular to marker plane) with elliptical face. In all the previous research works, flanking structures were modelled by considering the host element consisting of passive marker line within homogenous isotropic elastic or viscous material.

In nature, flanking structures are found either in homogeneous deformed rocks with passive linear fabrics or in foliated metamorphic rocks where the planar fabrics deform actively (Passchier, 2001; Grasemann and Stuwe, 2001; Grasemann et al., 2003, 2005; Passchier et al., 2008). They can also be found in micro-scale where growth and shear of minerals inside another can deflect the cleavage planes of the later (Mukherjee and Koyi, 2009). In high-grade gneissic rock, they are mostly associated with thin shear fractures or small elliptical pegmatitic bodies where the alternative layers of mafic (melanosome) and felsic (leucosome) minerals create mechanical anisotropy due to heterogeneous slip at their interfaces (Carreras et al., 2013; Goswami and Baruah, 2016). Mechanical anisotropy may be more prominent in presence of biotite in gneissic rock (Samanta and Deb, 2014). In schistose rocks, the effect of mechanical anisotropy is brought by flaky minerals, which defines the slip surfaces (Cosgrove, 1976; Price and Cosgrove, 1990; Saroglou and Tsiambaos, 2007). Thus, it is very much important to understand that whether geometry of flanking structures is influenced by the anisotropic behaviour of gneissic layers associated with cross-cutting fracture element or small lensoid pegmatitic body. With the help of analytical and numerical techniques, Kocher and Mancktelow (2006) concluded that strong anisotropy favours the development of reverse shear bands and reverse a-type structures, whereas normal or reverse s-type flanking structures almost disappear. However, in their model they investigated instantaneous flanking structures and presented sense of offset in the form of vertical component of velocity, where the geometry of flanking structure is also difficult to visualize. In reality, the geometry of flanking structure initiates by the influence of instantaneous flow field, but gradually modify during progressive deformation. Using two –dimensional numerical modelling, the present study primarily investigates the progressive development of flanking structures in anisotropic layered rock depending on the initial orientation of cross-cutting element (θ), degree of mechanical anisotropy of the medium (δ) and the orientation of the principal stress axis (ξ). The exact geometries of flanking structures and their progressive changes can be visualized at any finite strain.

2. Flanking structures in gneissic rock

2.1. Study area and rock types

Natural examples of flanking structure were documented from the Chhotanagpur Granite Gneissic Complex (CGGC), largest gneissic complex of eastern India, covering an area $\sim 10^5$ km^2, which extends in the E-W across the states of Chhattisgarh, Jharkhand, Odisa and West Bengal of eastern India (Fig. 1). The rocks of the CGGC have undergone predominantly amphibolite facies metamorphism reaching up to granulite facies in few places (south-eastern part of CGGC; Mahadevan, 2002; Bhattacharya, 1976; Banerji, 1991; Sharma, 2009; Ray et al., 2011). Field works were carried out in the northern (Jasidih-Deoghar, Bihar) and southern part (Purulia, West Bengal) of the complex. The major rock types in the Jasidih–Deoghar area are banded or layered gneisses, streaky gneisses, augen gneisses and migmatites with centimeter to decimeter thick leucosomes and biotite rich melanosomes. The mineralogy of this unit is dominated by quartz, feldspar, amphibole and minor biotite. The quartzo-feldspathic gneisses are interlayered with bands of amphibolites. The composition of the quartzo-feldspathic gneisses varied widely, from granitic, granodioritic to tonalitic types with granodiorite in most places (Ghosh and Sengupta, 1999). Pegmatitic veins are emplaced within the quartzo-feldspathic gneisses at different stages of deformation. This unit is invariably metamorphosed and deformed, and thus has secondary fabric (gneissic foliations). The rock type of Purulia area consists dominantly of granite gneisses, migmatites and granites (porphyritic and massive variety) with enclaves of

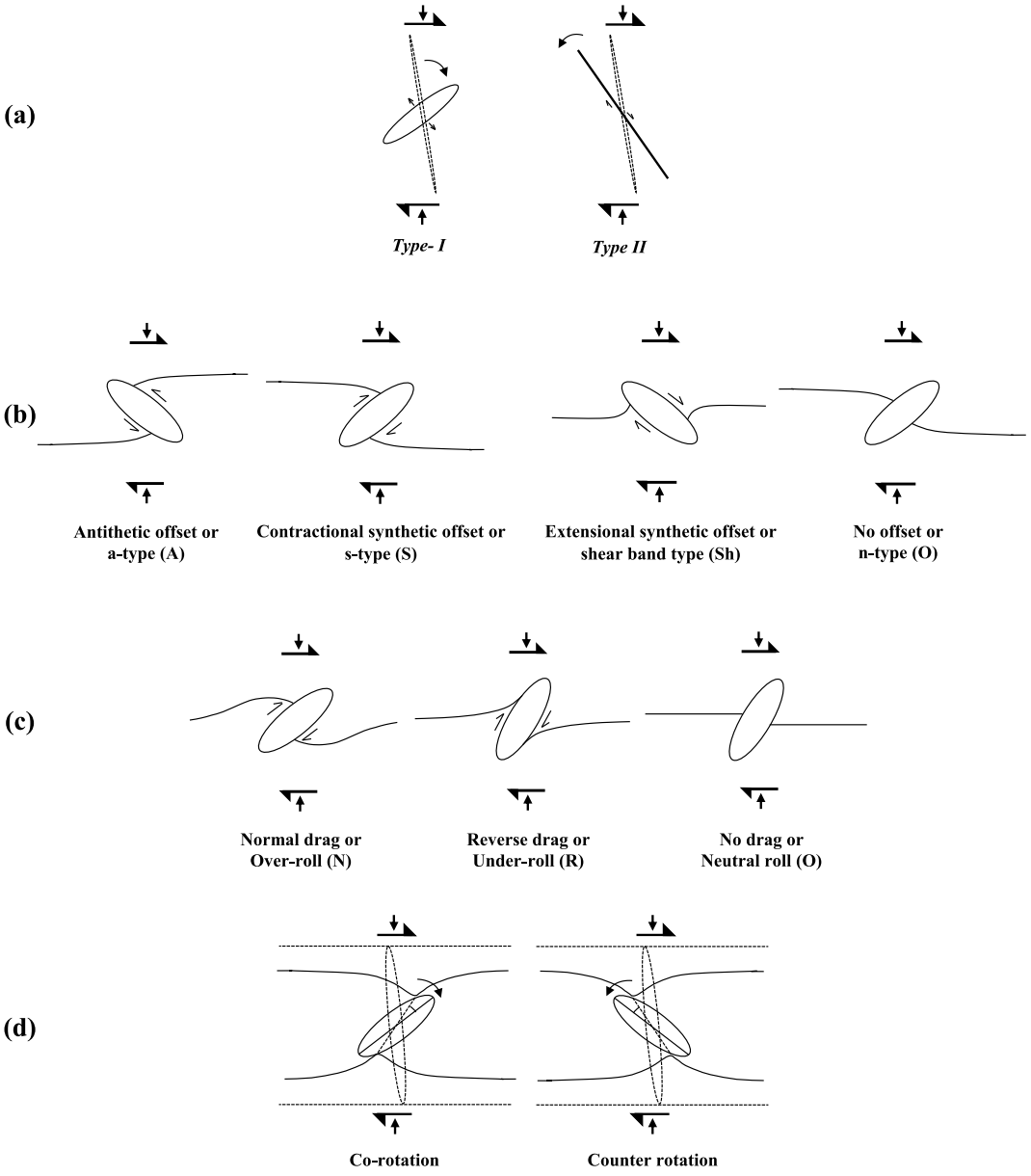

Fig. 2. Schematic diagram showing different parameters used for nomenclature of flanking structures. (a) *Types* (*I* or *II*) of flanking structure.; (b) Nature of fabric offset, (c) Fabric drag pattern, (d) Angular shift (β) of tip points with respect to the shear direction; Dashed and solid lines represent initial and final positions respectively.

metapelitic and metabasic granulites and some intrusive basic rocks.

In this complex terrain, four phases of deformation have been identified where D1 and D2 are intensive, penetrative and more or less coaxial in nature resulting complex fold interference (hook shaped) (Sarangi and Mohanty, 1998; Goswami and Bhattachrayya, 2008; Samanta and Deb, 2014). The later phases of deformation (D3/D4) were less penetrative in nature. In some portions, the high-grade metamorphic imprints are associated with D1/D2, whereas D3/D4 is associated with retrograde metamorphism. Basic rocks are intruded as small syntectonic bodies within the host granite gneiss while granitoids are emplaced along the axial planes of the synformal to antiformal structures as syn-to late-kinematic with respect to F2. The development of broad warp (F3) of the E–W axial foliation in the north-eastern part is responsible for the third deformation (D3). D4 deformation is characterised by shearing and thrusting. Regional gneissic foliations strike broadly east-west and the trend of cross-cutting elements related to flanking structures varies from 40° to 150°. Flanking structures are associated with the D3 and D4 deformation.

2.2. Types of flanking structures

Varieties of centimeter to meter long flanking structures are observed in Chhotanagpur Granite Gneissic Complex (CGGC) located around Jasidih-Deoghar and Purulia area, which were developed mostly in the

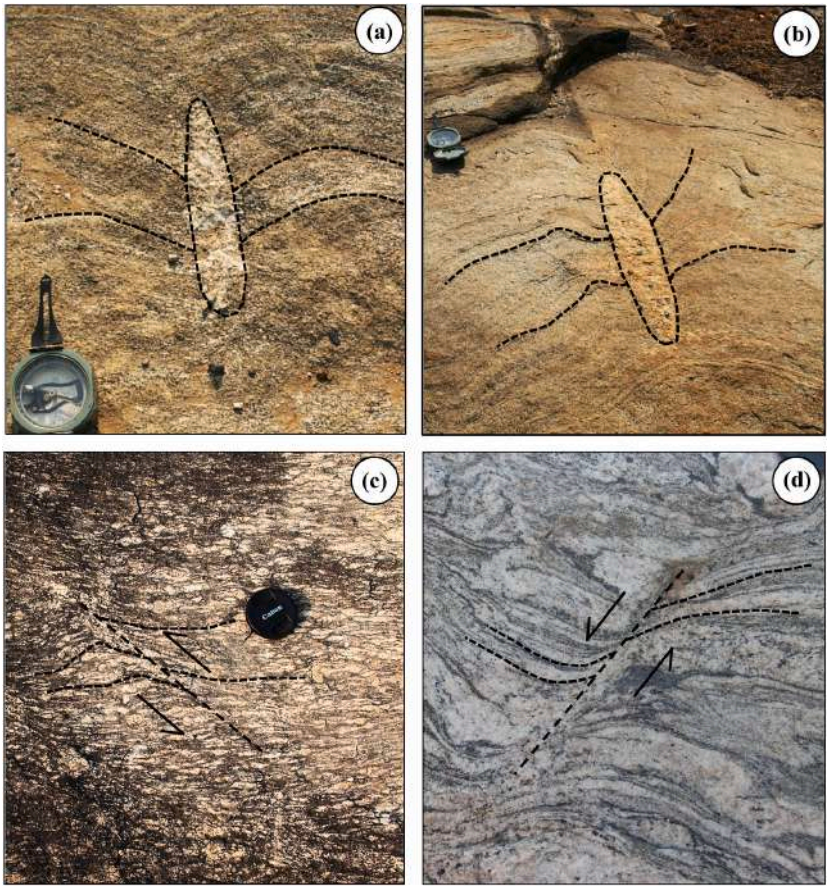

Fig. 3. *Type I* and *Type II* flanking structures in gneissic rock. a) *I-O-O* (*Type I* with no offset and no drag) (Loc.- 24°30.600′ N 86°40.524′ E), b) *I-A-N* (*Type I* with antithetic normal drag) (Loc.- 24°30.722′ N 86°40.578′ E), c) *II-A-R* (*Type II* with antithetic reverse drag) (Loc.- 24°30.722′ N 86°40.578′ E), d) *II-A-N* (*Type II* with antithetic normal drag) (Loc.- 23°16.157′ N 86°22.020′ E). Bulk shear sense is dextral. Diameters of brunton compass and the lens cover are ~6.6 and 6.8 cm. respectively and width of photo-plate (d) is ~35 cm.

last phase of deformation (D4). In the present study, the flanking structures related to isolated cross-cutting element of short length were primarily studied, which are associated with either small elliptical quartzo-feldspathic pegmatitic body or shear fractures without pegmatite. They are broadly described as open-fracture flanking structures (*Type I*) and close-fracture flanking structures (*Type II*) (Fig. 2a and 3), which is completely different from the types described by Mukherjee and Koyi (2009). Geometry of *Type I* and *II* varieties closely matches with the symmetric (orthorhombic symmetry) and asymmetric (monoclinic symmetry) internal boudinage or foliation boudinage structures respectively (Cobbold et al., 1971; Hambrey and Milnes, 1975; Goscombe et al., 2004; Arslan et al., 2008; Arslan et al., 2012). Flanking structures can be associated with either single or multiple cross-cutting elements aligned in a particular trend separated by inter-boudin objects. In this paper, we investigated the structures which are associated with a single cross-cutting element/object. Although, *Type II* is the common flanking structures, reported by many researchers (Passchier, 2001; Grasemann et al., 2003, 2019; Exner et al., 2004), *Type I* structure has not been studied earlier as a part of flanking structures, although dragging of foliations alongside a cross-cutting element are very conspicuous. Specially, when the long axis is oriented at very high angle with the foliation, the dragging near the closure points of cross-cutting element is strong, but at the central portion it shows almost no drag (*O*), similar to neutral (0) roll described by others (Mulchrone, 2007b; Coelho et al., 2005). As classified by early researchers, nature of offset may be synthetic (contractional or *S* type *and* extensional shear-band or *Sh* type) and antithetic (*A*) with respect to the bulk shear direction or with no offset (*O*, equivalent to n-type) (Fig. 2b and 3), whereas, convex and concave geometries of drag of layer with respect to the sense of offset are also termed as normal (*N*), reverse (*R*) respectively (Fig. 2c). In the present study, the nomenclature of flanking structures of natural examples and numerical results is done on the basis of above parameters by the sequential arrangement of those three important features (Shape – Nature of offset – Pattern of drag). For example, in our nomenclature flanking structures associated with small elliptical pegmatitic body showing antithetic offset with normal drag is termed as *I-A-N* geometry.

Spectacular examples of flanking structures from gneissic rocks and their nomenclature are discussed below. *Type I* flanking structures are easily identified from the small elliptical pegmatitic body (Fig. 3a and b and 4). It is also observed that the *Type I* flanking structure of lower aspect ratio is found in biotite-rich rock which may cause higher mechanical anisotropy. *Type II* flanking structures are commonly described as thin shear band associated with planar fracture discontinuity without any pegmatitic body (Fig. 3c and d). The flanking structures may be symmetric or asymmetric with or without offset along the cross-cutting element (Figs. 3 and 4).

3. Numerical modelling

3.1. Model consideration

3.1.1. Material

In order to investigate the effect of layered anisotropy on the development of flanking structures, two-dimensional numerical modelling was performed using Finite Element Method (FEM) (Ramsay and Lisle, 2000; Arslan et al., 2008; Samanta and Deb, 2014; Samanta

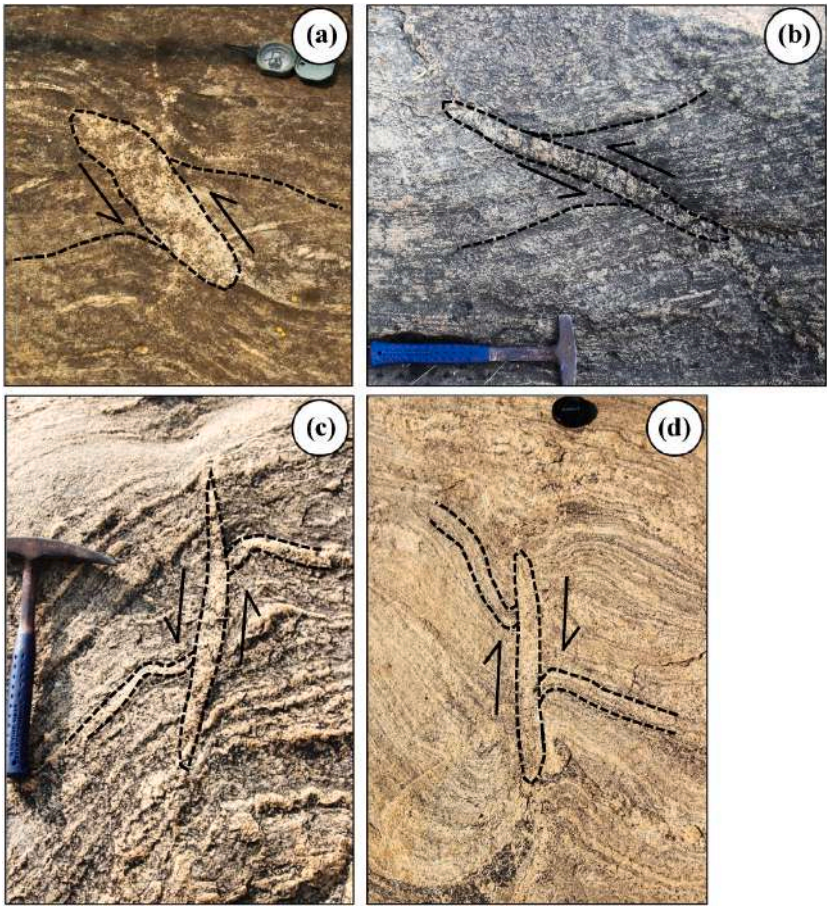

Fig. 4. *Type I* flanking structures in gneissic rock. a) *I-A-R* (*Type I* with antithetic reverse drag) (Loc.- 24°30.393′ N 86°40.766′ E), b) *I-A-R* (*Type I* with antithetic reverse drag) (Loc.- 24°30.923′ N 86°39.375′ E), c) *I-A-N* (*Type I* with Antithetic normal drag) (Loc.- 24°30.874′ N 86°39.344′ E), d) *I-Sh-R* (*Type I* with Shear-band type with reverse drag) (Loc.- 24°30.524′ N 86°40.795′ E). Bulk shear sense is dextral. Diameters of brunton compass and the lens cover are ~6.6 and 6.8 cm. respectively. The length of geological hammer is ~33 cm.

et al., 2017) in plane strain condition. Understandably, the geometry and the values of physical parameters used in the numerical model are not precisely similar to the natural condition. So, the results obtained from the simulations do not reproduce the exact geometry observed in the field. However, it provides first-hand knowledge on the kinematics of flanking structures found in layered gneissic rock. We considered visco-elastic Maxwell rheology in the modelling (cf. Zhang et al., 1996; Mancktelow, 1999; Passchier and Druguet, 2002; Samanta and Deb, 2014) as it simulates the lower crustal deformation where temperature and confining pressure are high (Turcotte and Schubert, 1982). The constitutive equation of this rheology is the following,

$$\frac{d\varepsilon}{dt}=\frac{1}{G}\frac{d\sigma}{dt}+\frac{\sigma}{\eta} \quad (1)$$

where ε and σ are the instantaneous strain (finite, in case of steady state deformation) and stress respectively and G and η are the Maxwell shear modulus and viscosity respectively.

3.1.2. Layered anisotropy

Theoretically, layer parallel anisotropy or layered anisotropy is defined by homogenous alternate competent-incompetent layers (Biot, 1965). The concept was implemented in different applied fields of geology, geophysics and material science etc. (Bayly, 1970; Cobbold et al., 1971; Stromgard, 1973; Treagus, 1973, 1981, 1983, 1985, 1988; Cobbold, 1976; Johnson, 1977; Platt and Vissers, 1980; Cobbold and Watkinson, 1981; Casey and Huggenberger, 1985; Latham, 1985; Allegre and Turcotte, 1986; Christensen, 1987; Nicolas, 1989; Ribe, 1989; Ridley and Casey, 1989; Bose et al., 2020). However, the quantification of layered anisotropy in viscous regime was first introduced by Weijermars (1992) in terms of ratio of normal and shear viscosities ($\delta = \mu_N/\mu_S$), following the concept given by Honda (1986) for planar

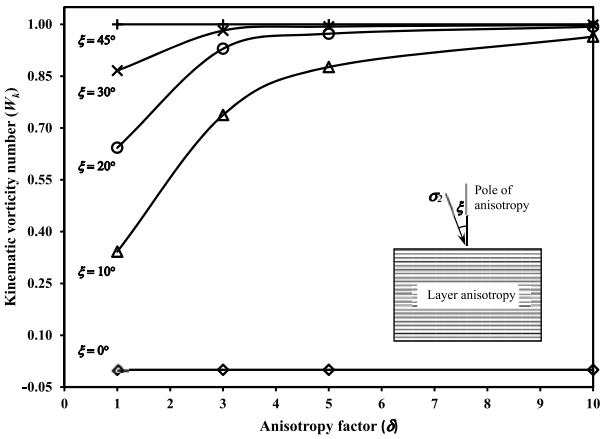

Fig. 5. Variation of kinematic vorticity number (W_k) with anisotropy factor (δ) for different orientation of principal stress axis (ζ) with respect to the pole of anisotropy (A_p). Note that for $\zeta = 0^o$ and 45^o, anisotropy factor does not have any influence on the flow of material.

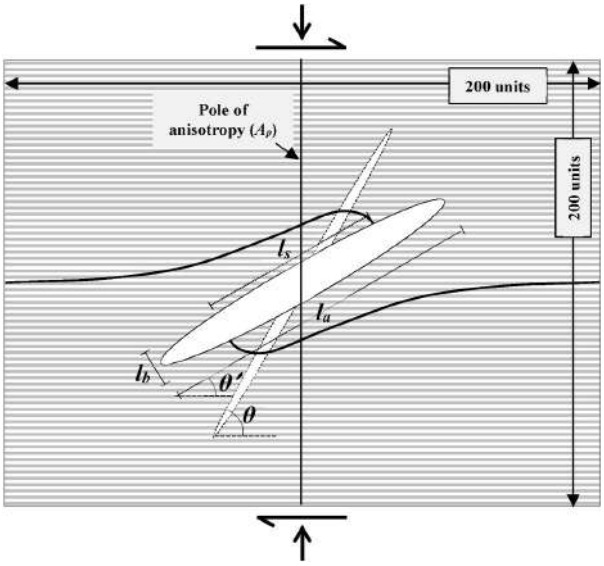

Fig. 6. Geometrical parameters (schematic diagram, not in scale) of flanking structure in layered anisotropic medium. l_a and l_b are the length of major and minor axis of elliptical cut after deformation. l_s is the offset length of marker/layers across the element/fracture/object. θ and θ' are the initial (dashed line) and final (solid line) orientations of the major axis of the cross-cutting element respectively. Width of individual layer is 1 unit. Length and width of the initial elliptical cut element was 40 and 0.2 units respectively.

anisotropy in geophysical layering. Weijermars (1992) also provided theoretical relationship between angle of flow apophyses (α) (Bobyarchick, 1986) or kinematic vorticity number (W_k) with the anisotropic factor (δ) and orientation of principal stress axes (ζ) with respect to the pole of anisotropy (A_p) (Fig. 5, Weijermars, 1992).

$$W_k = \cos\left[tan^{-1}\left\{\frac{cot\ 2\ \xi}{\delta}\right\}\right] \quad (2)$$

Evidently, the amount of kinematic vorticity number (W_k) varies significantly in anisotropy medium for a specific orientation of principal stress axes. Except $\xi = 0^o$ and 45^o the variation of W_k value from isotropic to anisotropic rock decreases with increasing orientation of principal stress axes (ξ) (Fig. 5).

In the present study, two-dimensional mechanical anisotropy is considered as orthotropic (Jaeger and Cook, 1979) or 'transversely isotropic' (Banik, 1987) where viscosities differ in two mutually perpendicular directions. Layers are oriented parallel to the x-axis and the pole of anisotropy (A_p) lies parallel to the y-axis. In numerical modelling, layered anisotropy is simulated by alternate thin competent-incompetent layers of equal thicknesses and equal numbers with coherent interfaces. Considering the steady state deformation and same Poisson's ratio of two layers and Maxwell relaxation time, degree of anisotropy can be defined by the anisotropic factor (Biot, 1957; Weijermars, 1992)

$$\delta = \frac{(\mu_C + \mu_I)^2}{4\mu_C\mu_I} = \frac{(G_C + G_I)^2}{4G_CG_I} = \frac{(E_C + E_I)^2}{4E_CE_I} \quad ,(3)$$

where μ, G and E are the viscosity, shear modulus and elastic modulus. Subscript C and I are used for competent and incompetent layers respectively.

3.1.3. Cross-cutting element/fracture/object

In our numerical modelling, the initial cross-cutting element was simulated with an elliptical cut of high aspect ratio oriented its long axis at different angles with the layers of the host element (Grasemann and Stuwe, 2001; Exner et al., 2004; Kocher and Mancktelow, 2006; Exner and Dabrowski, 2010). During deformation two walls of the cut either slide or move from each other. Layers across the cut generally show offset. In order to save time of simulation, the elliptical cut was kept vacant in compliance with the natural condition assuming it was filled with highly incompetent viscous material, like residual metamorphic melt (viscosity ~ 10^5 Pa s, Holtz et al., 2001) embedded within surrounding quartzo-feldspathic gneissic material (viscosity ~ 10^{22} Pa s, Shi and Cao, 2008). About fifty key simulations were run considering elliptical cut filled with low viscous material and the results were closely similar. The geometry of flanking structures is described by the deformed shape of cross-cutting element, the sense and length of offset/slip along the object and the curvature of drag with respect to the slip sense. Primarily five different initial orientations (θ) of cut were considered in the experiment (Fig. 6). Those are 150^o, 120^o, 90^o, 60^o and 30^o with respect to the layer measured anticlockwise. A few simulations were also run for other initial orientations.

3.1.4. Model specifications

Numerical modelling was performed using ABAQUS (ver. 2020), a commercial FEM software. Following Passchier et al. (2005), we verified numerical results at different model dimensions. To obtain optimal results in reasonable simulation time, a rectangular block (200 × 200 units) consisting 200 number of alternate thin competent and incompetent layers (1 unit each) was taken for the experiment. An elliptical opening of aspect ratio 200 (40/0.2 unit) was inserted at the centre of the model making its long axis at different angle (θ) with the layer (Fig. 6). A thin layer just below the central line was used as marker for measuring offset. A designated formulation for viscoelastic material "VISCO" step is adopted for this simulation with full Newtonian solution technique and direct equation solver method. Total time for deformation was 1×10^{10}s, which is more than the relaxation time (8×10^8 s) of materials assumed for the simulation (Larsen et al., 2005; Samanta et al., 2017). The whole model was meshed by quad-dominated free meshing based on advancing front with approximate global size 0.5 unit, which gives optimum results within reasonable time of simulation. Abaqus Standard element CPE4 (4-node bilinear plane strain quadrilateral) is used throughout the modelling. Total numbers of elements were ~160000.

Considering natural condition of deformation of gneissic rock, the viscosity is set in the range of 10^{17}–10^{23} Pa s (Vergnolle et al., 2003;

Table 1
Material properties used in numerical modelling.

Incompetent layer						
Anisotropic Factor (δ)	Viscosity (Pa.s)	Elastic modulus (Pa)	Shear modulus (Pa)	Bulk Modulus (Pa)	Poisson's Ratio	Relaxation time (s)
1	1×10^{20}	3.13×10^{11}	1.25×10^{11}	2.08×10^{11}	0.25	8×10^8
3	1.01×10^{19}	3.16×10^{10}	1.26×10^{10}	2.10×10^{10}		
5	5.57×10^{18}	1.74×10^{10}	6.97×10^{9}	1.16×10^{10}		
10	2.63×10^{18}	8.23×10^{9}	3.29×10^{9}	5.49×10^{9}		
Competent layer						
1	1×10^{20}	3.13×10^{11}	1.25×10^{11}	2.08×10^{11}	0.25	8×10^8

Table 2
Amount of pure and simple shear for different W_k.

Kinematic vorticity number (W_k)	Pure shear shortening (k in %)	Simple shear (φ in degree)	Effective Finite shear strain (γ)
0.97	10	35.43	0.71
	30	62.95	1.98
0.87	10	18.27	0.33
	30	42.27	0.92
0.71	10	10.79	0.19
	30	27.69	0.53
0.5	10	6.28	0.11
	30	16.85	0.31
0.26	10	2.92	0.05
	30	8	0.14
0	10	0	0
	30	0	0

Copley and McKenzie, 2007; Mukherjee, 2013). In the present study, we take four arbitrary materials by keeping their properties within the established natural values. The values of bulk relaxation modulus, shear relaxation modulus and elastic relaxation modulus are calculated keeping a constant Poisson's ratio of 0.25. The Maxwell relaxation time is taken as 8×10^8 s for all materials (Larsen et al., 2005; Samanta et al., 2017). Anisotropy factor (δ) is taken up to 10 considering real natural conditions (Kocher and Mancktelow, 2006), above which there is little effect of pure shear component. Table 1 presents material properties used in experiments.

3.1.5. Boundary conditions

Although one of the important parameters of the present study is the orientation of principal stress axes, numerical modelling by applying stress from different directions is technically complex to simulate structures in progressive deformation. So, the numerical simulations were run applying displacement at the model boundaries for different anisotropy factors and kinematic vorticity number (W_k) in lieu of varying orientation of principal stress axes. Following the relation between kinematic vorticity number (W_k) and angle between two flow apophyses (α) i.e. $W_k = \cos\alpha$ (Bobyarchick, 1986), the models were deformed pure shear and sub-simple shear (dextral) conditions for $W_k =$ 0, 0.26, 0.5, 0.71, 0.87 and 0.97 corresponding to $\alpha = 90^o$, 75^o, 60^o, 45^o, 30^o and 15^o respectively. Displacements at the four boundaries of the model were employed as below.

$$U_x = k.x + \gamma.y \tag{4}$$

$$U_y = -\frac{k}{(1+k)}.y \tag{5}$$

Where $\gamma = \tan\varphi.\frac{k-\frac{1}{k}}{2.\ln(k)}$, the effective shear strain and φ is the degree of simple shear and k is the percentage of shortening (Merle, 1986; Tikoff and Fossen, 1993). The area of the entire model remained constant throughout the simulation. For all experiments, finite shortening was set up to maximum 30% and degree of simple shear was calculated by using the equation $W_k = \cos\left\{\tan^{-1}\frac{2k}{\tan\varphi}\right\}$ (Tikoff and Fossen, 1993). The values of k and γ for different W_k at 10% and 30% of shortening are as given in Table 2.

3.2. Model results

Interesting results were obtained from 360 number of numerical experiments performed with varying parameters like initial orientation of cross-cutting element (θ), anisotropic factor (δ) and kinematic vorticity number (W_k). The final geometries of the flanking structures are termed on the basis of three important features as proposed in the process of nomenclature (Table-3). Their geometries are quantified by the following parameters, i) shape of cross-cutting element, defined by the normalised aspect ratio of the cut after deformation, R_N ($=\frac{l_a/l_b}{200}$), ii) offset of marker layer normalised to the final object length, L_N ($= l_s/l_a$) with synthetic or antithetic offset to the bulk shear direction and curvature of fabric (Fig. 6). Offset formed due to synthetic movement of marker layer is marked as positive offset (S or Sh), whereas offset formed due to antithetic movement of the marker layer is shown as negative offset (A). In progressive deformation, shape of the cross-cutting element may apparently change by shifting their original tip points and developing a new position of long axis of the cross-cutting element. The original tip points can easily be recognized by the maximum bending of external fabric element near the closures of the elliptical object. Shifting of tip points depends on the degree of anisotropy which may be towards (co-rotation) or opposite (counter-rotation) to bulk shear direction (Fig. 2d). In presence of high degree of anisotropy, the shape of cross-cutting element may even transform to rhombic geometry. Thus, the shape of cross-cutting element, amount of offset and the shifting of tip points (measured by angle between old and new long axis) are considered to be important parameters for determining anisotropic factor.

Progressive development of flanking structure in numerical modelling is described separately for different zones categorizing by the initial

Table 3
Geometry of flanking structures obtained from numerical modelling.

W_k		0		0.26		0.5		0.71		0.87		0.97	
θ	δ	10%	30%	10%	30%	10%	30%	10%	30%	10%	30%	10%	30%
30°	**1**	*II-A-N*	*II-A-N*	*II-A-N*	*II-A-N*	*II-A-N*	*II-A-N*	*II-A-N*	*II-A-N*	*II-S-N*	*II-S-N*	*II-S-N*	*II-S-N*
	3	*I-A-N*	*I-A-R*	*II-A-N*	*I-A-R*	*II-A-N*	*I-A-R*	*II-A-N*	*II-A-N*	*II-A-N*	*II-A-N*	*II-A-N*	*II-A-N*
	5	*I-A-N*	*I-A-R*	*I-A-N*	*I-A-R*	*I-A-N*	*I-A-R*	*II-A-N*	*II-A-N*	*II-A-N*	*II-A-N*	*II-A-N*	*II-A-N*
	10	*I-A-N*	*I-A-R*	*I-A-N*	*I-A-R*	*I-A-N*	*I-A-R*	*I-A-N*	*I-A-R*	*II-A-N*	*II-A-R*	*II-A-N*	*II-A-N*
60°	**1**	*I-A-R*	*I-A-R*	*I-A-R*	*I-A-R*	*II-A-R*	*II-A-R*	*II-A-R*	*II-A-R*	*II-A-R*	*II-A-R*	*II-A-R*	*II-A-R*
	3	*I-A-R*	*I-A-R*	*I-A-R*	*I-A-R*	*I-A-R*	*I-A-R*	*I-A-R*	*I-A-R*	*I-A-R*	*II-A-R*	*II-A-R*	*II-A-R*
	5	*I-A-R*	*I-A-R*	*I-A-R*	*I-A-R*	*I-A-R*	*I-A-R*	*I-A-R*	*I-A-R*	*I-A-R*	*II-A-R*	*II-A-R*	*II-A-R*
	10	*I-A-R*	*I-A-R*	*I-A-R*	*I-A-R*	*I-A-R*	*I-A-R*	*I-A-R*	*I-A-R*	*I-A-R*	*I-A-R*	*II-A-R*	*II-A-R*
90°	**1**	*I-O-O*	*I-O-O*	*I-A-R*	*I-A-R*	*I-A-R*	*I-A-R*	*I-A-R*	*I-A-R*	*I-A-R*	*II-A-R*	*II-A-R*	*II-A-R*
	3	*I-O-O*	*I-O-O*	*I-A-R*	*I-A-R*	*I-A-R*	*I-A-R*	*I-A-R*	*I-A-R*	*I-A-R*	*I-A-R*	*II-A-R*	*II-A-R*
	5	*I-O-O*	*I-O-O*	*I-A-R*	*I-A-R*	*I-A-R*	*I-A-R*	*I-A-R*	*I-A-R*	*I-A-R*	*I-A-R*	*I-A-R*	*II-A-R*
	10	*I-O-O*	*I-O-O*	*I-A-R*	*I-A-R*	*I-A-R*	*I-A-R*	*I-A-R*	*I-A-R*	*I-A-R*	*I-A-R*	*I-A-R*	*II-A-R*
120°	**1**	*I-Sh-R*	*I-Sh-R*	*I-Sh-R*	*I-Sh-R*	*I-Sh-R*	*I-Sh-R*	*I-Sh-R*	*I-Sh-R*	*I-A-N*	*I-A-N*	*I-A-N*	*II-A-N*
	3	*I-Sh-R*	*I-Sh-R*	*I-Sh-R*	*I-Sh-R*	*I-Sh-R*	*I-Sh-R*	*I-Sh-R*	*I-Sh-R*	*I-Sh-R*	*I-A-N*	*I-A-N*	*I-A-N*
	5	*I-Sh-R*	*I-Sh-R*	*I-Sh-R*	*I-Sh-R*	*I-Sh-R*	*I-Sh-R*	*I-Sh-R*	*I-Sh-R*	*I-Sh-R*	*I-A-N*	*I-A-N*	*I-A-N*
	10	*I-Sh-R*	*I-Sh-R*	*I-Sh-R*	*I-Sh-R*	*I-Sh-R*	*I-Sh-R*	*I-Sh-R*	*I-Sh-R*	*I-Sh-R*	*I-A-N*	*I-A-N*	*I-A-N*
150°	**1**	*II-Sh-N*	*II-Sh-N*	*II-Sh-N*	*II-Sh-N*	*II-Sh-N*	*II-Sh-N*	*I-Sh-N*	*I-Sh-N*	*I-Sh-N*	*I-Sh-R*	*I-Sh-R*	*I-Sh-R*
	3	*I-Sh-N*	*I-Sh-R*	*I-Sh-N*	*I-Sh-R*	*I-Sh-N*	*I-Sh-R*	*I-Sh-N*	*I-Sh-R*	*I-Sh-N*	*I-Sh-R*	*I-Sh-R*	*I-Sh-R*
	5	*I-Sh-N*	*I-Sh-R*	*I-Sh-N*	*I-Sh-R*	*I-Sh-N*	*I-Sh-R*	*I-Sh-N*	*I-Sh-R*	*I-Sh-N*	*I-Sh-R*	*I-Sh-R*	*I-Sh-R*
	10	*I-Sh-N*	*I-Sh-R*	*I-Sh-N*	*I-Sh-R*	*I-Sh-N*	*I-Sh-R*	*I-Sh-N*	*I-Sh-R*	*I-Sh-R*	*I-Sh-R*	*I-Sh-R*	*I-Sh-R*

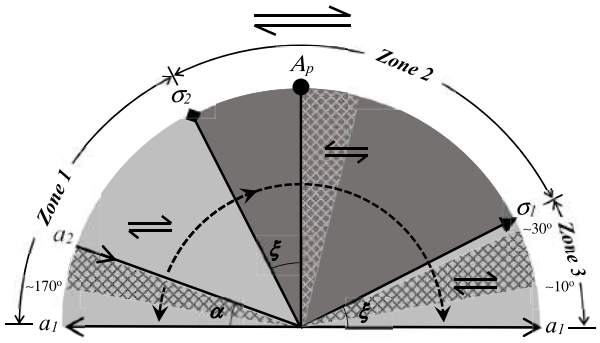

Fig. 7. Zones of synthetic (Zones 1 and 3) and antithetic (Zone 2) offset with respect to the flow apophyses (a_1 and a_2), principal stress axes (σ_1 and σ_2) and pole of anisotropy (A_p). a_1 and a_2 - Extensional and compressional flow apophyses; α- Acute angle between two flow apophyses; ξ – Orientation of principal stress axes. Note that the position of a_2 (α) depends on ξ. Curved dashed lines with arrow indicate the sense of rotation (co-rotation and counter-rotation). Light and dark grey zones indicate zones of synthetic and antithetic offset respectively. Cross-hatched fields indicate zones of normal drag.

orientation of cross-cutting element. Three broad zones are identified, separated by the maximum and minimum principal stress axes (σ_1 and σ_2) based on sense of slip (Fig. 7). Zone 1 and 2 are further subdivided in two subzones separated by the compressional flow apophyse (a_2) and pole of anisotropy (A_p) respectively on the basis of slip and drag pattern. Another two small zones showing normal drag were described by the approximately 30° both clockwise and anticlockwise from the extensional flow apophyse (a_1) (Grasemann et al., 2005; Kocher and Mancktelow, 2006). However, the above zonation was established based on instantaneous flanking structure. So, the final geometry of structures depends on the initial orientation of the cut element, kinematic vorticity number (W_k), the anisotropy factor (δ) and the final orientation of the cut (θ') (indirectly amount of finite strain). For a specific orientation of principal stress axis, the compressional flow apophyse (a_2) deviates away from the pole of anisotropy with increasing anisotropy factor (δ). When the principal stress (ξ) is oriented at high angle with the pole of anisotropy (A_p), there is little or no differences in geometries in both isotropic and anisotropic medium (Fig. 5). However, the difference becomes significant in case of lower orientation of principal stress (ξ), specially at higher finite strain when the cut element crosses pole of anisotropy. When the initial cut does not cross the pole of anisotropy, the drag pattern remains relatively simpler in geometry. To represent natural situation, the final geometries of flanking structures obtained from the numerical modelling for 10% and 30% of shortening are presented in Table 3.

3.2.1. *Shape of cross-cutting element*

One of the most important criteria for classifying flanking structure in layered anisotropic medium is the shape of the cross-cutting element which is quantified by the normalised aspect ratio (R_N). In progressive deformation, the slender elliptical cut changes their shape, resulting apparent rotation of long axis. Deformed shape can be of two geometries. It may either remain perfectly close without any opening, termed as *Type II* structure ($R_N \approx 1$) or may transform to elliptical or circular shape, termed as *Type I* structure ($R_N < 1$) due to opening. *Type I* structures tend to form when the cut element orients initially at a low angle with the compressional flow apophyse (a_2) which varies with the anisotropy factor for same orientation of stress axis. With increasing

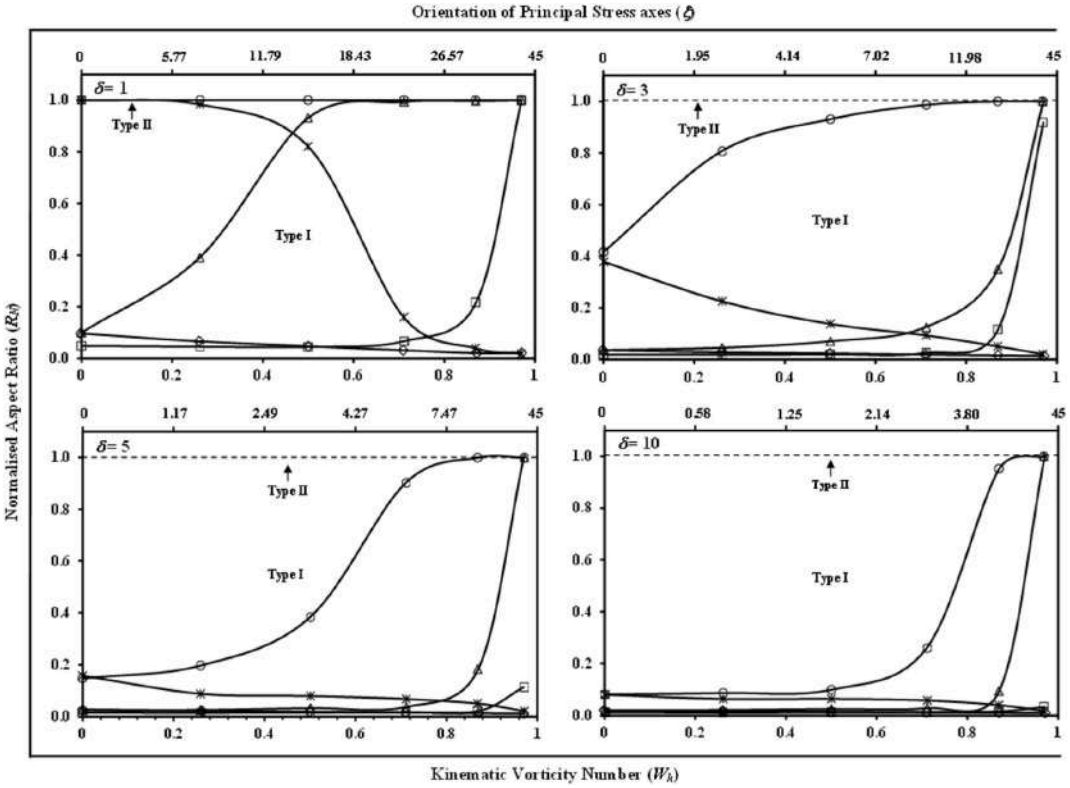

Fig. 8. Variation of normalised aspect ratio (R_N) with kinematic vorticity number (W_k) for different initial orientation of cross-cutting element (θ). Note for *Type I*, $R_N < 1$ and for *Type II*, $R_N \approx 1$. o: $\theta = 30°$, Δ: $\theta = 60°$, □: $\theta = 90°$, ⋄: $\theta = 120°$ and x: $\theta = 150°$. Finite shortening is 10%.

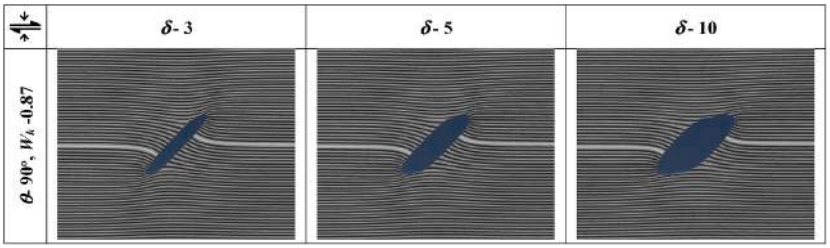

Fig. 9. Development of mica-fish like geometry of cross-cutting element with increasing anisotropy. Finite shortening is 20%.

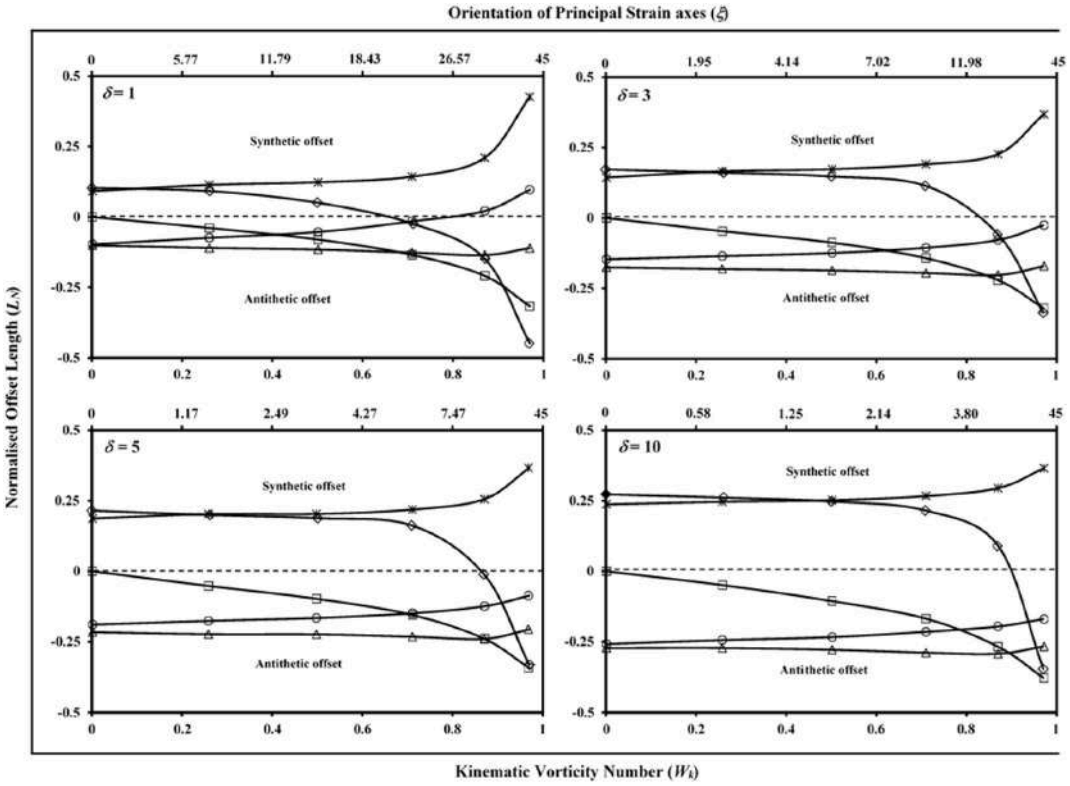

Fig. 10. Variation of normalised offset (L_N) of external fabric with kinematic vorticity number (W_k) for different initial orientation of cross-cutting element (θ). o: $\theta = 30^o$, Δ: $\theta = 60^o$, □: $\theta = 90^o$, ⋄: $\theta = 120^o$ and x: $\theta = 150^o$. Finite shortening is 10%.

anisotropy factor, the direction of compressional flow apophyse (a_2) makes higher angle with the minimum principal stress direction (σ_2). So, the flanking structures with complex drag pattern are relatively rare, but the *Type I* flanking structures are generally more common in higher anisotropic rock. However, at higher W_k value, *Type II* structures form when the initial orientation of cut element is lesser than 90^o i.e. pole of anisotropy. At pure shear dominated deformation ($W_k < 0.8$), R_N value always tends to decrease with increasing anisotropy for all initial orientation (Fig. 8). In Table-3, the shapes are considered as *Type I* when R_N value is lower than 1. In case of higher anisotropic layer, the object (cross-cutting element) shape may even transform to parallelogram similar to mica-fish structure at higher finite strain (Fig. 9).

3.2.2. Amount and sense of offset of planar fabric

Amount of offset, quantified by the parameter normalised offset length (L_N), is measured from the slip shown by the marker line along the long axis of cross-cutting element. The sense of offset (Synthetic, +ve or Antithetic, –ve) is defined by the relative sense of slip with respect to the bulk shear direction. If the cut element lies initially within Zone 2, antithetic offset develops, whereas the offset shows synthetic sense if it lies initially greater than the orientation of the minimum principal stress (σ_2) (Zone 1) or less than the orientation of the maximum principal stress (σ_1) (Zone 3) (Figs. 7 and 10). So, the amount and sense of offset will depend on the progressive rotation of cut element from the initial to the final position with respect to the orientation of principal stress axes and pole of anisotropy.

3.2.3. Drag pattern of planar fabric

Drag pattern of external planar fabrics (especially at the central portion) alongside of cross-cutting element is described as normal or reverse on the basis of convexity pointing towards or opposite to the sense of offset. As evident from the published literatures, there is no such direct relation of geometry of flanking structures with the orientation of flow apophyses, principal stress axes or the pole of anisotropy. Based on

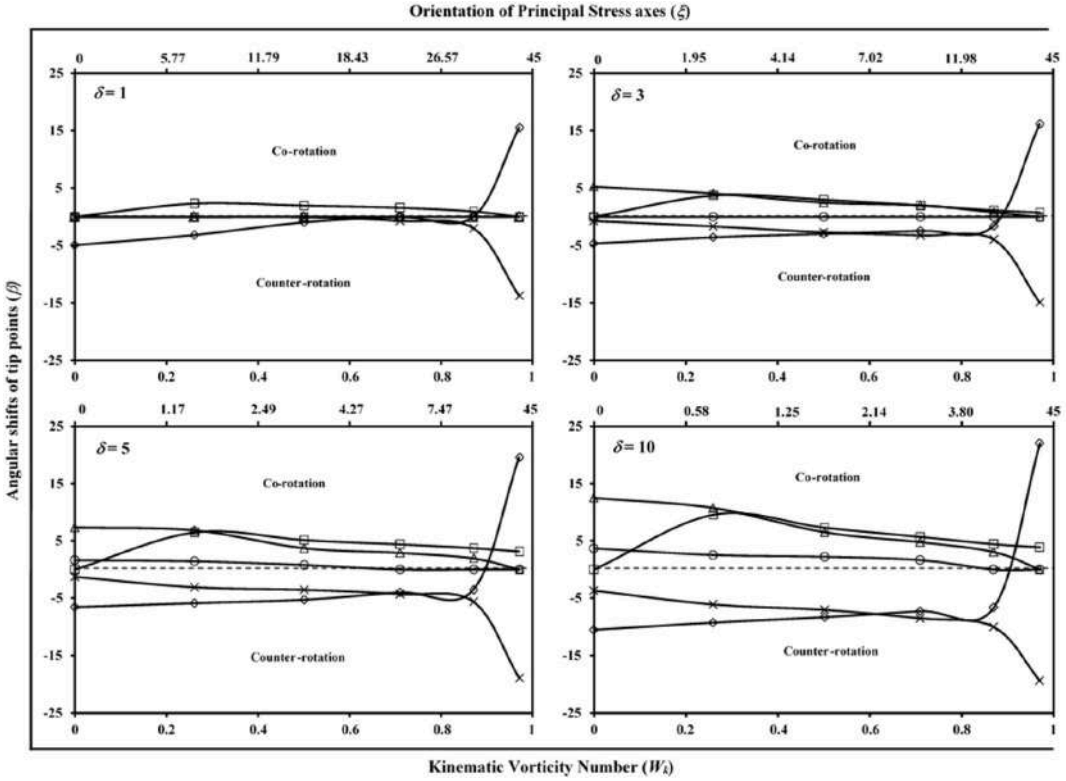

Fig. 11. Variation of angular shift of tip points (β) of cross cutting-object with kinematic vorticity number (W_k) for different initial orientation of cross-cutting element (θ). o: $\theta = 30^o$, **Δ**: $\theta = 60^o$, □: $\theta = 90^o$, ⋄: $\theta = 120^o$ and x: $\theta = 150^o$. Finite shortening is 10%.

instantaneous deformation, the fields of normal drag have been demarcated at an approximately 30° clockwise and anti-clockwise with the extensional flow apophyse and the rest portion shows reverse drag (Grasemann et al., 2005; Kocher and Mancktelow, 2006). However, it is only valid for very low finite strain in case of isotropic medium. The fields of normal-drag in anisotropic medium depends on degree of anisotropy, position of compressional flow apophyse and amount of finite strain. In the regime of co-rotation ($\theta < a_2$ or $\theta < 180^o$-α), two fields of normal drag are found: one starting from A_p toward shear direction and another in between 30° to 10°. Whereas, in the regime of counter-rotation ($\theta > a_2$ or $\theta > 180^o$-α), the lower limit of the field is fixed at approximately 170°, but the upper limit is defined by the position of compressional flow apophyse (a_2) with a maximum limit of 150° (Fig. 7). The drag pattern does not change if the cross-cutting element initiates and remains within the ranges from a_2 to A_p and A_p to 30° during progressive deformation. The drag geometry can be complex if the element crosses the demarcated boundaries. It has been found that the reverse drag transforms to normal drag resulting fold-like complex structure if the cross-cutting element crosses the pole of anisotropy (A_p) during deformation (Fig. 3d, 4c and 7). In this case, complexity increases with increasing anisotropy factor of the layered medium. Interestingly, in progressive deformation normal drag can also transforms to reverse drag when it moves from the field of normal to reverse drag (Fig. 7). Higher anisotropy always prefers reverse drag (Kocher and Mancktelow, 2006).

3.2.4. Shifting of tip points of cross-cutting element

From the numerical results, it is clearly revealed that the *Type I* flanking structure is quite common in strongly anisotropic layered rock (Table-3). During progressive deformation, in case of *Type I* flanking structures, cross-cutting element rotates slightly and gradually changes its shape by migrating the positions of original tip points and developing a new long axis. Initial tip points can be easily identified by the sharp bending of external fabrics near the boundary of the cross-cutting element (Fig. 2d). Amount of shifting depends on the position of cross-cutting element with respect to pole of anisotropy, principal stress axes and the flow apophyses during progressive deformation. At lower finite strain, if the initial orientation of the long axis of cross-cutting element is ≤ 90° (or A_p), the long axis shifts towards the bulk shear sense (co-rotation) and the shifting is opposite (counter-rotation) when it is initially oriented more than 90° (A_p) (Fig. 11). However, the sense of rotation may be reverse in case of simple shear dominated deformation if the cross-cutting element crosses the pole of anisotropy during deformation. Due to shifting of tip points from their original position, the cross-cutting element appears to be rotated synthetically (co-rotation) or antithetically (counter-rotation) to the bulk shear rotation (Fig. 2d and 11). Rotation of axis is only prominent in *Type I* flanking structure. The phenomenon is practically similar to the deformation of low viscous inclusions (Grasemann and Stuwe, 2001; Mancktelow, 2011; Grujic and Mancktelow, 2022) and rotation of rigid object at slip-interface conditions (Mancktelow et al., 2002; Samanta and Bhattacharyya, 2003; Mulchrone, 2007b; Johnson et al., 2009; Mancktelow, 2013; Jiang, 2016), where the estimated mean kinematic vorticity number (W_m) usually is found lower than the actual value.

4. Discussions

4.1. Progressive development of flanking structures

In order to represent the natural condition, numerical simulations were run up to maximum 30% of shortening for different W_k values. Results obtained at 30% of shortening for different anisotropy factors

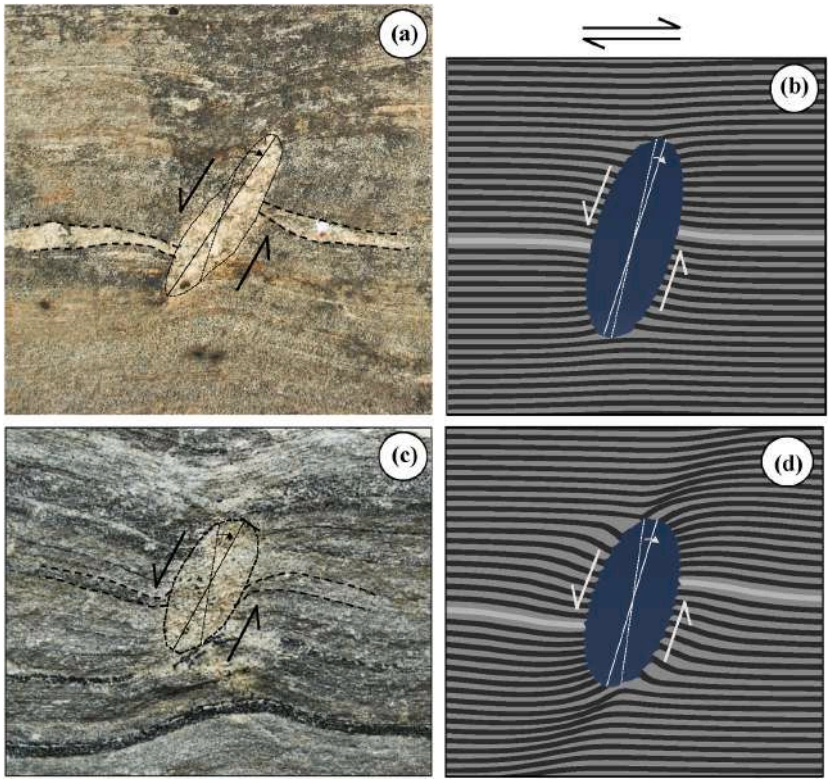

Fig. 12. Comparison of *Type I* flanking structures from gneissic rock in Jasidih area and results obtained from numerical modelling. (a) *I-A-R* flanking structure (Loc.- 24°30.232′ N 86°40.659′ E), (b) Numerical results representing (a) at $\theta = 90^{o}$, $W_k = 0.71$, $\delta = 10$; (c) *I-A-N* flanking structure (Loc.- 24°30.197′ N 86°40.557′ E). (d) Numerical results representing (c) at $\theta = 120^{o}$, $W_k = 0.97$, $\delta = 10$. Note that they have developed in layered medium with higher mechanical anisotropy. The shifting of tip points in all cases is clockwise i.e. co-rotation. Dashed and solid lines indicate initial and final axis of the cross-cutting element. Finite shortening of the numerical results are 10%.

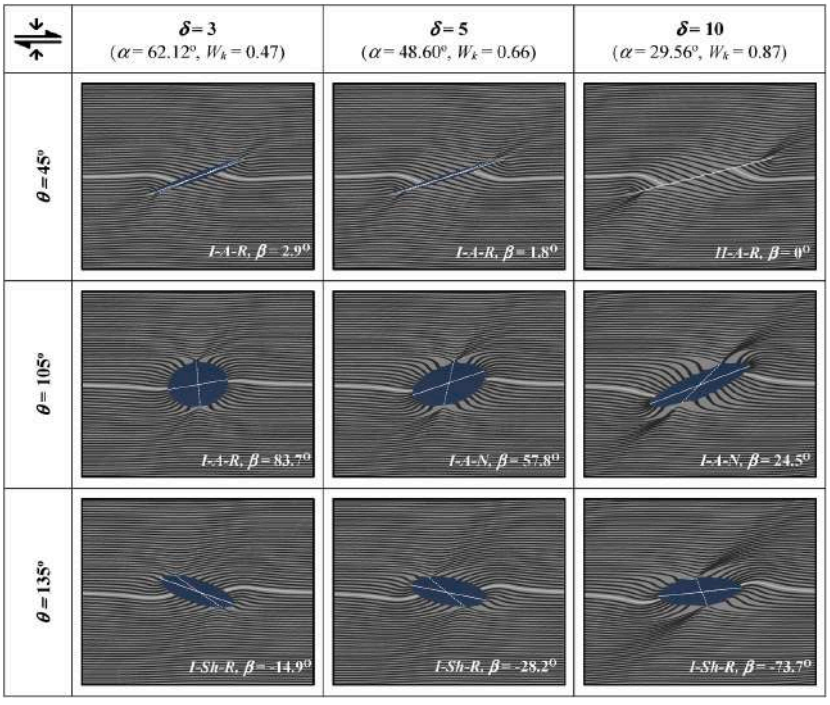

Fig. 13. Flanking structures showing the shape of cross-cutting element, nature of offset, drag pattern and angular shifting of axis (β, acute angle between dashed and solid white lines) with increasing anisotropy factor (δ) and W_k for $\xi = \mathbf{5^{o}}$. Central part (cropped image) of the model is shown. Finite shortening is 30%.

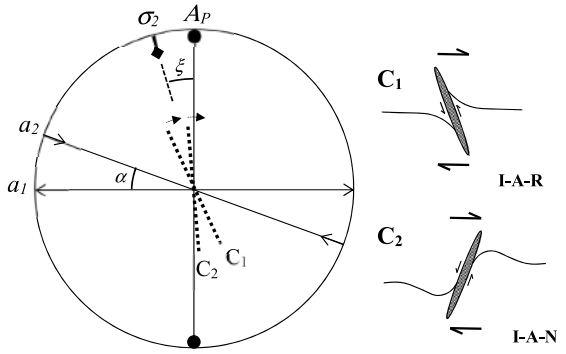

Fig. 14. Progressive development of flanking structures associated with cut elements (shear fractures) of different orientations with respect to minimum principal stress axis (σ_2). Note that $\alpha \approx 19^o$ for $\xi \approx 15^o$ and $\delta \approx 5$. Two sets of fractures (C_1 and C_2) do not necessarily form at same location. See Fig. 7 for the fields of offset and drag pattern.

are compared (Fig. 13). It is revealed that final geometry depends on the progressive change of position of the long axis of cross-cutting element with respect to the flow apophyses, principal stress axes, and pole of anisotropy. Geometry becomes more complex at higher finite strain, resulting from systematic changes of specific parameters when the axis moves from one field to another. At higher finite strain, the *Type II* flanking structures are common as the cross-cutting element rotates from the pole of anisotropy (A_p) to the extensional flow apophyse. In case of higher anisotropy at simple shear dominated deformation, high strain zones localize in the neighborhood of the cross-cutting element originating from the initial tip points (Fig. 13).

In layered anisotropic rock, cross-cutting elements are initially formed in two orientations (C_1 and C_2) at low angle with respect to the minimum principal stress axis (Fig. 14) (Platt and Vissers, 1980; Gomez-Rivas et al., 2015). In progressive deformation, *Type I* structures are evolved through opening of these fractures and successive filling with fluid in favorable condition. Due to their positions with respect to flow apophyses, both fracture-filled objects rotate towards shear direction and their shapes change temporarily depending on the degree of anisotropy and bulk deformation. Flanking structures associated with C_1 fractures initially show synthetic offset with reverse drag, which gradually transforms to antithetic offset in progressive deformation when it crosses the minimum principal stress axis. However, flanking structures associated with C_2 fractures always show antithetic offset. Drag pattern may transform from reverse to normal at higher finite strain when both the fractures cross the pole of anisotropy. Therefore, *Type I* (*I-A-R* and *I-A-N*) flanking structures are very much common in the present gneissic terrain. *Type I* flanking structure without any offset develop when the long axis of fracture are initially oriented almost parallel to the minimum principal stress axis and at low angle to the pole of anisotropy (A_p). However, offset with dragging of external planar fabrics generates when the principal stress axis makes high angle with the pole of anisotropy.

4.2. Estimation of mechanical anisotropy

In Chhotonagpur Gneissic Complex, rocks are characterized by mafic dyke embedded within the gneissic rock containing layers of mafic (pyroxene, amphibole, biotite) and felsic (quartz, feldspar) minerals. Due to infiltration of H_2O through granitic intrusion, pyroxene was transformed to amphibole during progressive deformation. At the later stages of deformations, amphibole converted to biotite due to potassium (K^+)-metasomatism (Ray et al., 2011). Thus, biotitization is more prominent at the marginal part of the pegmatitic body. So, as evident from Sections 3.2.1 and 4.1, *Type I* flanking structures are more common in the neighborhood of the larger pegmatitic body where biotitization is most prominent (Fig. 12c).

In deformed geological terrain, orientation of tectonic stress or principal stress axis remains constant spatially for the layers with similar strike. So, in nature, layered rock having similar strike would exhibit different kinematic vorticity number (W_k) if only the degree of anisotropy differs (Weijermars, 1992; Kocher and Mancktelow, 2006). Layered rock with higher anisotropy will be deformed dominantly under simple shear flow. After analyzing the numerical results and their controlling parameters, it is revealed that the geometry of flanking structure can be an important tool for determining amount of mechanical anisotropy qualitatively in layered rock system. Tendency of developing *Type I* flanking structure becomes more in a layered rock with higher anisotropy factor (Table 3). In nature, effect of layer anisotropy will be preserved more prominently in a deformed terrain with lower paleo-stress direction (ζ) (Fig. 5). Three parameters (R_N, L_N and β) can be used to estimate the degree of anisotropy, depending upon the final orientation (θ') of the cross-cutting element with respect to the foliation plane. If the orientation (θ') is less than 90^o then R_N increases and β decreases with increasing anisotropy. However, the relation is reverse if the orientation (θ') is greater than 90^o. In all cases, L_N increases with increasing anisotropy (Fig. 13).

4.3. Limitations

In migmatitic gneiss, cross-cutting element may grow and change their geometry dynamically depending on the degree of partial melting, which may significantly affect in anisotropic layer at higher finite strain (Druguet and Carreras, 2006; Arslan et al., 2008). To simplify the numerical model, we considered only changes of shape of cross-cutting fracture without any growth during deformation similar to stationary fracture (Arslan et al., 2008). In nature, the geometry of flanking structures may be modified by the later deformation which is needed to be considered before comparing the numerical results with the natural example.

5. Conclusions

Flanking structures documented from layered gneissic rock and numerical modelling lead to following conclusions.

i Mechanical anisotropy has strong influence on the geometry of flanking structures in layered gneissic rock.
ii Geometry of flanking structures in layered anisotropic rock depends on the initial orientation (θ) and final orientation (θ') of cross-cutting element with respect to the principal stress axes and pole of anisotropy in progressive deformation.
iii Shape of cross-cutting element (R_N), shifting of their tip points (β) and the amount of layer offset (L_N) are the most important parameters for estimating anisotropy factor.
iv L_N always increases with increasing anisotropy factor. When $\theta' < 90^o$, R_N increases and β decreases with increasing anisotropy and the relation is reverse when $\theta' > 90^o$.

Declaration of competing interest

The authors declare that they have no known competing financial interests or personal relationships that could have appeared to influence the work reported in this paper.

Data availability

Data will be made available on request.

Acknowledgements

The present work is funded by Ministry of Earth Science, Govt. of

India through the project (MOES/P.O.(Geo.)/185/2018). We thank Professors Bernhard Grasemann and Soumyajit Mukherjee for their thorough reviews that greatly contributed to the improvement of the manuscript. We sincerely acknowledge the constructive suggestions of Prof. Ian Alsop. Subhabrata Das and Masud Rana helped in the field study. Infrastructural facilities provided by the Department of Geological Sciences; Jadavpur University is gratefully acknowledged.

References

Allegre, J.C., Turcotte, D.L., 1986. Implications of a two-component marble-cake mantle. Nature 323, 123–127.
Arslan, A., Passchier, C.W., Koehn, D., 2008. Foliation boudinage. J. Struct. Geol. 30, 291–309.
Arslan, A., Koehn, D., Passchier, C.W., Sachau, T., 2012. The transition from single layer to foliation boudinage- A dynamic modelling approach. J. Struct. Geol. 42, 118–142.
Banerji, A.K., 1991. Presidential address. Geology of the Chotanagpur region. Indian J. Geol. 63, 275–282.
Banik, N.C., 1987. An effective anisotropy parameter in transversely isotropic media. Geophysics 52, 1654–1664.
Barnett, J.A.M., Mortimer, J., Rippon, J.H., Walsh, J.J., Watterson, J., 1987. Displacement geometry in the volume containing a single normal fault. AAPG (Am. Assoc. Pet. Geol.) Bull. 71, 925–937.
Bayly, M.B., 1970. Viscosity and anisotropy estimate from measurements on chevron folds. Tectonophysics 9, 459–474.
Bhattacharya, B.P., 1976. Metamorphism of the Precambrian rocks of the central part of Santhal Parganas district, Bihar. Quaternary Journal of the Geology, Mining and Metallurgical Society of India 48, 183–196.
Biot, M.A., 1957. Folding instability of a layer visco-elastic medium under compression. Proceedings of Royal Society A 242, 444–454.
Biot, M.A., 1965. Mechanics of Incremental Deformations. Wiley, New York.
Bobyarchick, A.R., 1986. The eigenvalues of steady flow in Mohr space. Tectonophysics 122, 35–51.
Bose, N., Dutta, D., Mukherjee, S., 2020. Refraction of micro-fractures due to shear-induced mechanical stratigraphy in a low-grade meta-sedimentary rock. J. Struct. Geol. 133, 103995.
Carreras, J., Cosgrove, J.W., Druguet, E., 2013. Strain partitioning in banded and/or anisotropic rocks: implications for inferring tectonic regimes. J. Struct. Geol. 50, 7–21.
Casey, M., Huggenberger, P., 1985. Numerical modelling of finite-amplitude similar folds developing under general deformation histories. J. Struct. Geol. 7, 103–114.
Christensen, U., 1987. Some geodynamical effects of anisotropic viscosity. Geophys. J. Int. 91, 711–736.
Cobbold, P.R., 1976. Mechanical effects of anisotropy during large finite deformations. Bull. Soc. Geol. Fr. 18, 1497–1510.
Cobbold, P.R., Cosgrove, J.W., Summers, J.M., 1971. Development of internal structures in deformed anisotropic rocks. Tectonophysics 12, 23–53.
Cobbold, P.R., Watkinson, A.J., 1981. Bending anisotropy: a mechanical constraint on the orientation of fold axes in an anisotropic medium. Tectonophysics 72, T1–T10.
Coelho, S., Passchier, C.W., Grasemann, B., 2005. Geometric description of flanking structures. J. Struct. Geol. 27, 597–606.
Copley, A., McKenzie, D., 2007. Models of crustal flow in the India–Asia collision zone. Geophys. J. Int. 169, 683–698.
Cosgrove, J.W., 1976. The formation of crenulation cleavage. J. Geol. Soc. 132, 155–178. London.
Druguet, E., Passchier, C.W., Carreras, J., Victor, P., Den Brock, S., 1997. Analysis of a complex high-strain zone at Cap de Creus, Spain. Tectonophysics 280, 31–45.
Druguet, E., Carreras, J., 2006. Analogue modelling of syntectonic leucosomes in migmatitic schists. J. Struct. Geol. 28, 1734–1747.
Dutta, D., Mukherjee, S., 2019. Opposite shear senses: geneses, global occurrences, numerical simulations and a case study from the Indian Western Himalaya. J. Struct. Geol. 126, 357–392.
Exner, U., Dabrowski, M., 2010. Monoclinic and triclinic 3D flanking structures around elliptical cracks. J. Struct. Geol. 32, 2009–2021.
Exner, U., Grasemann, B., Mancktelow, N.S., 2006. Multiple faults in ductile simple shear: analogue models of flanking structure systems. Geological Society 253, 381–395.
Exner, U., Mancktelow, N.S., Grasemann, B., 2004. Progressive development of s-type flanking folds in simple shear. J. Struct. Geol. 26, 2191–2201.
Gayer, R.A., Powell, D.B., Rhodes, S., 1978. Deformation against metadolerite dykes in the caledonides of finnmark, Norway. Tectonophysics 46, 99–115.
Ghosh, S.K., Sengupta, S., 1999. Boudinage and composite boudinage in superposed deformations and syntectonic migmatisation. J. Struct. Geol. 21, 97–110.
Gomez-Rivas, E., Griera, A., Llorens, M.G., 2015. Fracturing of ductile anisotropic multilayers: influence of material strength. Solid Earth 6, 497.
Goscombe, B.D., Passchier, C.W., Hand, M., 2004. Boudinage classification: end-member boudin types and modified boudin structures. J. Struct. Geol. 26, 739–763.
Goswami, B., Bhattachrayya, C., 2008. Tectonothermal evolution of Chhotanagpur granite gneiss complex from northeastern part of puruliya district, West Bengal, eastern India. Indian J. Geol. 80, 41–54.
Goswami, T., Baruah, S., 2016. Flanking structures as shear sense indicators in the higher himalayan gneisses near tato, west siang district, Arunachal Pradesh, India. In: Mukherjee, S., Mulchrone, K.F. (Eds.), Ductile Shear Zones: from Micro- to Macro-Scales, first ed. John Wiley & Sons, p. 293.
Grasemann, B., Harry, Fritz, Vannay, Jean-Claude, 1999. Quantitative kinematic flow analysis from the Main Central Thrust Zone (NW-Himalaya, India): implications for a decelerating strain path and the extrusion of orogenic wedges. J. Struct. Geol. 21, 837–853.
Grasemann, B., Martel, S., Passchier, C.W., 2005. Reverse and normal drag along a fault. J. Struct. Geol. 27, 999–1010.
Grasemann, B., Stuwe, K., 2001. The development of flanking folds during simple shear and their use as kinematic indicator. J. Struct. Geol. 23, 715–724.
Grasemann, B., Stuwe, K., Vannay, J.C., 2003. Sense and non-sense of shear in flanking structures. J. Struct. Geol. 25, 19–34.
Grasemann, B., Dabrowski, M., Schöpfer, M.P.J., 2019. Sense and non-sense of shear reloaded. J. Struct. Geol. 125, 20–28.
Grujic, D., Mancktelow, N., 2022. Strain-rate- and capillary-number-dependent deformation of weak viscous particles. J. Struct. Geol. 162, 104673.
Hambrey, M.J., Milnes, A.G., 1975. Boudinage in glacier ice e some examples. J. Glaciol. 14, 383–393.
Holtz, F., Johannes, W., Tamic, N., Behrens, H., 2001. Maximum and minimum water contents of granitic melts generated in the crust: a reevaluation and implications. Lithos 56, 1–14.
Honda, S., 1986. Strong anisotropic flow in a finely layered asthenosphere. Geophys. Res. Lett. 13, 1454–1457.
Hudleston, P.J., 1989. The association of folds and veins in shear zones. J. Struct. Geol. 11, 949–957.
Jaeger, J.C., Cook, N.G.W., 1979. Fundamentals of Rock Mechanics, third ed. Chapman & Hall, London.
Jiang, D., 2016. Viscous inclusions in anisotropic materials: theoretical development and perspective applications. Tectonophysics 693, 116–142.
Johnson, A.M., 1977. Styles of Folding. Elsevier, Amsterdam.
Johnson, S.E., Lenferink, H.J., Price, N.A., Marsh, J.H., Koons, P.O., West (Jr), D.P., Beane, R., 2009. Clast-based kinematic vorticity gauges: the effects of slip at matrix/clast interfaces. J. Struct. Geol. 31, 1322–1339.
Kocher, T., Mancktelow, N.S., 2005. Dynamic reverse modelling of flanking structures: a source of quantitative kinematic information. J. Struct. Geol. 27, 1346–1354.
Kocher, T., Mancktelow, N.S., 2006. Flanking structure development in anisotropic viscous rock. J. Struct. Geol. 28, 1139–1145.
Larsen, C.F., Motyka, R.J., Freymueller, J.T., Echelmeyer, K.A., Ivins, E.R., 2005. Rapid viscoelastic uplift in southeast Alaska caused by post-Little Ice Age glacial retreat. Earth Planet Sci. Lett. 237, 548–560.
Latham, J.P., 1985. The influence of nonlinear material properties and resistance to bending on the development of internal structures. J. Struct. Geol. 7, 225–236.
Mahadevan, T.M., 2002. Geology of Bihar & Jharkhand (Text Book Series, 114). Journal of Geological Society of India, Bangalore.
Mancktelow, N.S., 1999. Finite-element modeling of single layer folding in elasto-viscous materials: the effect of the initial perturbation geometry. J. Struct. Geol. 21, 161–177.
Mancktelow, N.S., 2011. Deformation of an elliptical inclusion in two-dimensional incompressible power-law viscous flow. J. Struct. Geol. 33, 1378–1393.
Mancktelow, N.S., 2013. Behaviour of an isolated rimmed elliptical inclusion in 2D slow incompressible viscous flow. J. Struct. Geol. 46, 235–254.
Mancktelow, N.S., Arbaret, L., Pennacchioni, G., 2002. Experimental observations on the effect of interface slip on rotation and stabilisation of rigid particles in simple shear and a comparison with natural mylonites. J. Struct. Geol. 24, 567–585.
Mayrhofer, F., Schöpfer, M.P.J., Adamuszek, M., Dabrowski, M., Grasemann, B., 2022. Transtensional flanking structures. J. Struct. Geol. 161, 104659.
Merle, O., 1986. Patterns of stretch trajectories and strain rates within spreading-gliding nappes. Tectonophysics 124, 211–222.
Mukherjee, S., 2013. Channel flow extrusion model to constrain dynamic viscosity and Prandtl number of the Higher Himalayan Shear Zone. Int. J. Earth Sci. 102, 1811–1835.
Mukherjee, S., 2014. Review of flanking structures in meso- and micro-scales. Geol. Mag. 151, 957–974.
Mukherjee, S., Koyi, H.A., 2009. Flanking microstructures. Geol. Mag. 146, 517–526.
Mulchrone, K.F., 2007a. Modelling flanking structures using deformable high axial ratio ellipses: insights into finite geometries. J. Struct. Geol. 29, 1216–1228.
Mulchrone, K.F., 2007b. An analytical solution in 2D for the motion of rigid elliptical particles with a slipping interface under a general deformation. J. Struct. Geol. 29, 950–960.
Nicolas, A., 1989. Structures of Ophiolites and Dynamics of Oceanic Lithosphere. Kluwer, Dordrecht.
Passchier, C.W., 2001. Flanking structures. J. Struct. Geol. 23, 951–962.
Passchier, C.W., Mancktelow, N.S., Grasemann, B., 2005. Flow perturbations: a tool to study and characterize heterogeneous deformation. J. Struct. Geol. 27, 1011–1026.
Passchier, C.W., Trouw, R.A.J., 2005. Microtectonics. Springer-Verlag, Berlin, p. 366.
Passchier, C.W., Druguet, E., 2002. Numerical modelling of asymmetric boudinage. J. Struct. Geol. 24, 1789–1803.
Passchier, C., Heesakkers, V., Coelho, S., 2008. Two mechanisms for forming flanking folds. In: Declan De Paor, Journal of the Virtual Explorer 30.
Platt, J.P., Vissers, R.L.M., 1980. Extensional structures in anisotropic rocks. J. Struct. Geol. 2, 397–410.
Price, N.J., Cosgrove, J.W., 1990. Analysis of Geological Structures. Cambridge University Press, Cambridge.
Ramsay, J.G., Lisle, R.J., 2000. Applications of Continuum Mechanics in Structural Geology. Academic Press, London.

Ray, S., Sanyal, S., Sengupta, P., 2011. Mineralogical control on rheological inversion of a suite of deformed mafic dykes from parts of the Chottanagpur granite gneiss complex of eastern India. In: Srivastava, R.K. (Ed.), Dyke Swarms: Keys for Geodynamic Interpretation. Springer, Berlin, Heidelberg.
Reches, Z., Eidelman, A., 1995. Drag along faults. Tectonophysics 247, 145–156.
Ribe, N.M., 1989. Seismic anisotropy and mantle flow. J. Geophys. Res. 94, 4213–4223.
Ridley, J., Casey, M., 1989. Numerical modeling of folding in rotational strain histories: strain regimes expected in thrust belts and shear zones. Geology 17, 875–878.
Samanta, S.K., Basu Majumder, D., Sarkar, G., 2017. Geometry of torn boudin–An indicator of relative viscosity. J. Struct. Geol. 104, 21–30.
Samanta, S.K., Bhattacharyya, G., 2003. Modes of Detachment at the Inclusion–Matrix Interface, vol. 25, pp. 1107–1120.
Samanta, S.K., Deb, I., 2014. Development of concave-face boudin in Chhotanagpur Granite Gneiss Complex of Jasidih-Deoghar area, eastern India: insight from finite element modeling. J. Struct. Geol. 62, 38–51.
Sarangi, S., Mohanty, S., 1998. Structural studies in the Chhotanagpur gneissic complex near Gomoh, Dhanbad district, Bihar. Indian J. Geol. 70, 73–80.
Saroglou, H., Tsiambaos, G., 2007. Classification of anisotropic rocks. In: Proceedings of the 11th ISRM Congress, pp. 9–13. Lisbon, Portugal.
Sharma, R.S., 2009. Cratons and fold belts of India. In: Lecture Notes in Earth Sciences. Springer-Verlag, Berlin Heidelberg, p. 41, 127.
Shi, Y.L., Cao, J.L., 2008. Effective viscosity of China continental lithosphere. Earth Sci. Front. 15, 82–95.
Stromgard, K.E., 1973. Stress distribution during formation of boudinage and pressure shadows. Tectonophysics 16, 215–248.
Tikoff, B., Fossen, H., 1993. Simultaneous pure and simple shear: the unified deformation matrix. Tectonophysics 217, 267–283.
Treagus, S.H., 1973. Buckling stability of a viscous single-layer system, oblique to the principal compression. Tectonophysics 19, 271–289.
Treagus, S.H., 1981. A theory of stress and strain variations in viscous layers, and its geological implications. Tectonophysics 72, 75–103.
Treagus, S.H., 1983. A theory of finite strain variation through contrasting layers, and its bearing on cleavage refraction. J. Struct. Geol. 5, 351–368.
Treagus, S.H., 1985. The relationship between foliation and strain: an experimental investigation: discussion. J. Struct. Geol. 7, 119–121.
Treagus, S.H., 1988. Strain refraction in layered systems. J. Struct. Geol. 10, 517–527.
Turcotte, D.L., Schubert, G., 1982. Geodynamics: Applications of Continuum Physics to Geological Problems. Wiley, New York.
Vergnolle, M., Pollitz, F., Calais, E., 2003. Constraints on the viscosity of the continental crust and mantle from GPS measurements and postseismic deformation models in western Mongolia. J. Geophys. Res. 108, 2502.
Weijermars, R., 1992. Progressive deformation in anisotropic rocks. J. Struct. Geol. 14, 723–742.
Wiesmayr, G., Grasemann, B., 2005. Sense and non -sense of shear in flanking structures with layer-parallel shortening: implications for fault related folds. J. Struct. Geol. 27, 249–264.
Zhang, Y., Hobbs, B.E., Ord, A., Muhlhaus, H.B., 1996. Computer simulation of single layer buckling. J. Struct. Geol. 18, 643–655.

APPENDICES

A.3 Presented Conference Abstracts

Geometry of flanking structures in layer anisotropic medium: an insight from numerical modelling

Debojyoti Basu Majumder*, Susanta Kumar Samanta

Department of Geological Sciences, Jadavpur University, Kolkata-700032

Email ID*: d.b.majumder2014@gmail.com

Flanking structures, generally defined as deflection of planar and linear fabrics alongside of any cross-cutting fracture/object, are commonly observed in layered and/or foliated metamorphic rock in the wide range of micro- to tectonic scales. In last two decades, number of analogue and numerical modelling were attempted to understand the evolution of the structures because of their importance in using as good kinematic indicator of any deformed rock. However, most of the previous researchers modelled it considering the medium as either elastic or viscous homogeneous isotropic with a passive cut element without considering the effect of active layering within the medium. In high grade gneissic rock at the lower crustal geological regime, these deflected structures are found against any thin shear bands or pegmatitic body where the alternative layering of leucosome and melanosome create mechanical anisotropy at different scales due to heterogeneously slipping interfaces. In schistose rocks, the effect of mechanical anisotropy is brought by flaky minerals which defines the slip surfaces. In the present study, the effect of layer anisotropy is investigated with the help of finite element modelling considering maxwell viscoelastic medium and deformable cut element to simulate more naturalistic flanking structures. Three parameters, we considered here, are: i) anisotropy factor ($d = m_N/m_S$, the ratio of normal and shear viscosity), ii) Kinematic vorticity number (W_k, function of pure and simple shear ratio) and iii) initial orientation of the cut with respect to layering (q) (Fig. 1). Mechanical anisotropy was simulated by alternate hard and soft layers of equal thicknesses with different viscosities. The cut element filled with very low viscous material, was replicated with an elliptical (aspect ratio of 200) opening with a frictionless, non-overlapping interface condition. Using ABAQUS (Ver. 2020) 80 numbers of numerical simulations were run for different initial cut orientation (q = 30, 60, 90, 120 and 150 degree) at d = 1 (isotropic), 3, 5 and 10; and W_k = 0, 0.5, 0.71 and 0.87. The finite shortening was fixed at 10% for all W_k value. The final geometries of the flanking structures are described by the following parameters, i) Shape, defined by normalized aspect ratio, $R_N = (l_a/l_b)/200$, of the cut after deformation ii) Orientation of the long axis of the cut after deformation (θ'), iii) offset of layers (l_s) normalised to the final cut length ($L_N = l_s/l_a$) with synthetic or antithetic offset to the bulk shear direction. From the numerical results it is observed that apart from the initial orientation of the cut, both the anisotropic factor (d) and Kinematic vorticity number (W_k) have significant influences on the overall geometry or types of flanking structures.

The geometry of the flanking structures primarily controlled by the normalized aspect ratio (R_N) of the cut element and the neighbourhood layer curvature and offset along the cut. With increasing anisotropy, R_N decreases (degree of opening increases) resulting the curvature more symmetric across the cut irrespective of the value of W_k. However, the symmetricity of curvature reduces from tip to centre of the cut. Asymmetric curvatures are common when the cut shows offset of layer without opening (higher R_N value). In most of the cases, the normalized length of offset (L_N) increases with increasing anisotropy factor (d). Sense of offset (antithetic or synthetic to the bulk shear) depends on the initial orientation of the cut. At higher W_k, when the cut element initially verges toward the shear direction, sense of offset varies from synthetic to antithetic with increasing anisotropy factor, whereas it is reverse when the cut element initially verges opposite to the shear direction. So, the value of R_N and L_N can be used as a good tool for determining the degree of mechanical anisotropy within the rock.

Keywords: Flanking structures, Anisotropic medium, Numerical modelling

RDS8-P14

Estimation of viscosity contrast from single layer fold amplitude

Debojyoti Basu Majumder*, Subhabrata Das, Susanta Kumar Samanta
Dept. of Geological Sciences, Jadavpur University, Kolkata – 700032
d.b.majumder2014@gmail.com*

Abstract

In nature, layered rocks, subjected to deform under contractional ductile regime, produce various large to small scale folded structures. Previous researchers worked on the development of folding of single layer embedded within rheologically similar and/or different medium under various kinematic conditions. The study of single layer fold is important for its utility in estimation of rheological parameters from its geometry. In nature, the rocks are assumed to be viscoelastic and the process of folding commonly occurs in lower crustal region. A series of numerical experiments have been performed in order to simulate folding of single layer with different thicknesses and viscosity ratio of layer and matrix. Numerical results reveal that during progressive deformation, the wavelength show a linear relationship with its corresponding amplitude of the fold train. As the initial wavelength of the fold depends on viscosity contrast and layer thickness, viscosity contrast can be estimated from the ratio of fold amplitude to layer thickness. To support this method, a few analogue experiments have been performed using plasticine layer of varying thicknesses and home-made putty as matrix. The results are comparable with the numerical results and overall give a similar relationship between the amplitude and layer thickness. As, continuous fold train is rarely found in field, viscosity contrast is difficult to estimate from the fold wavelength. Instead of measuring the wavelength, the amplitude is much easier to obtain by considering the half of the normal distance between two enveloping surfaces of the fold. In nature, when the fold geometry varies spatially, this approach can be more suitable for estimating viscosity contrast. In conclusion, estimation of viscosity contrast from the fold amplitude would further aid us in validating the viscosity contrast obtained from the finite wavelength and thus strengthen the study about the influence of rheology on formation of folds.

Keywords: Fold geometry, Qualitative rheology, Numerical modelling, Analogue modelling

APPENDICES

A.4 Certificates of Conference Presentations

BHU
Capital of Knowledge

बी एच यू
सर्व विद्या की राजधानी

7th RDS Conference

A national conference under the aegis of
Structural Geology and Tectonic Studies Group India (SGTSGI)

This is to certify that

Debojyoti Basu Majumder of Jadavpur University, Kolkata,

attended the 7th National Conference on Rock Deformation and Structures (RDS 7) organised by Department of Geology, Banaras Hindu University between 13th to 15th October, 2022 and made ~~Oral~~ / Poster presentation.

Dr. Sayandeep Banerjee
Convener
RDS 7

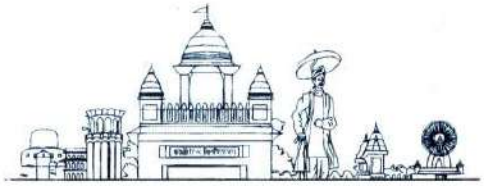

Prof. Santanu Bose
Secretary
SGTSGI

8th National Conference

on

ROCK DEFORMATION AND STRUCTURES

(RDS 8)

October 22-24, 2024

ORGANIZED BY:

DEPARTMENT OF EARTH AND ENVRONMENTAL SCIENCES, IISER BHOPAL

UNDER THE AEGIS OF

STRUCTURAL GEOLOGY AND TECTONIC STUDIES GROUP, INDIA

CERTIFICATE OF PARTICIPATION

This is to certify that Prof./Dr./~~Mr.~~/Ms.

DEBOJYOTI BASU MAJUMDER

have participated in the National Conference on Rock Deformation and Structures/and ~~Post conference~~ ~~field trip~~.

DR.JYOTIRMOY MALLIK

CONVENER (RDS 8)

PROF.SANTANU BOSE

SECRETARY (SGTSGI)